Synthesis of Anodic Alumina Nanotubes for Drug Delivery and Nanotoxicity Study:

understanding of bio-nano interactions by a nanomaterial model

Ye Wang

A thesis submitted for the degree of Doctor of Philosophy

The University of Adelaide

School of Chemical Engineering

August 2015

Table of Contents

Acknowledgements

This thesis not only presents my work on the keyboard, but also epitomizes a milestone of a 3-year journey embraced with warmness and care. I'm grateful to acknowledge those remarkable individuals who academically and emotionally supported me to finish the rough road of a PhD.

First, I wish to thank my supervisors Prof. Dusan Losic, Prof. Andreas Evdokiou and Dr. Abel Santos. Their respectful personalities, dedication to research and passion for science enlighten me to keep pushing my upper limit to become a better scientist. Prof. Dusan Losic as my principle supervisor provided me invaluable research resources and freedom I needed to explore bio-nanotechnology. Dr. Abel Santos has been a mainstay throughout my PhD study, who generously supported me in all respects of my life both professionally and personally. I would not have finished this PhD without the guidance of Prof. Andreas Evdokiou, who has been a steady hand to steer me to through my cancer research at Basil Hetzel Institute. I will always be indebted to Dusan, Andreas and Abel for their life-time mentorships and friendships.

I am thankful to my colleagues and friends in Dusan and Andreas' groups, who are willing to help me particularly during the difficult times. I want to thank especially Gagandeep Kaur, Irene Zinonos, Aneta Zysk, Vasilios Liapis, Vasilios Panagopoulos, Shelley Hay and Tushar Kumeria. I could not have accomplished my PhD study without your assistance. My time at Adelaide was enjoyable in large part due to many friends, including Steve Amos, Anne Philcox, Ji Lang and Sheena Chen. The good memories that we have together mean so much to me, and I will treasure our friendship forever. I would like to specially thank Abel again as my dear friend, and I wish all the best of his life and career.

I cannot finish this acknowledgement without expressing my deepest gratitude to my parents and girlfriend for their sacrifice, support and encouragement. It is their unselfish love that gives me strength to finish my overseas study. Finally, I acknowledge China Scholarship Council and The University of Adelaide for the offer of my scholarship.

Thesis Declaration Statement

I certify that this work contains no material which has been accepted for the award of any other degree or diploma in my name, in any university or other tertiary institution and, to the best of my knowledge and belief, contains no material previously published or written by another person, except where due reference has been made in the text. In addition, I certify that no part of this work will, in the future, be used in a submission in my name, for any other degree or diploma in any university or other tertiary institution without the prior approval of the University of Adelaide and where applicable, any partner institution responsible for the joint-award of this degree.

I give consent to this copy of my thesis when deposited in the University Library, being made available for loan and photocopying, subject to the provisions of the Copyright Act 1968.

The author acknowledges that copyright of published works contained within this thesis resides with the copyright holder(s) of those works.

I also give permission for the digital version of my thesis to be made available on the web, via the University's digital research repository, the Library Search and also through web search engines, unless permission has been granted by the University to restrict access for a period of time.

Name: Ye Wang

Signature:

Date: 12/8/2015

Abstract

Nanomedicines, which utilize nano-sized drug-carriers so-called nanoparticles to load therapeutic drugs for selective cancer targeting and treatment, are promising therapeutics for fighting cancer. Unfortunately, although achieving commercial success, the first generation of nanomedicines only showed limited improvement of cancer therapy in clinical practice. In this situation, the fabrication of novel nanomedicines has been and will continue to be an important approach for improving cancer therapeutics. It is equally important to understand the paradigms and mechanisms of nanotoxicity in order to minimize or eliminate the potential toxicological consequence of synthetic nanomaterials to the living organism and environment.

In this thesis, a new model nanomaterial, so-called anodic alumina nanotubes (AANTs) were synthesised for the study of nanotoxicity and drug delivery. Firstly, an advanced nanofabrication technique so-called pulse anodization was intensively studied in this thesis for structurally engineering anodic aluminium oxide (AAO) nanostructures. This enabled the production of AAO-based nanophotonics (i.e. microcavities) as well as AANTs. Then, systematic studies were conducted on the toxicological properties and drug delivery applicability of AANTs toward cancer therapy. This 3-year PhD project not only sheds new light on the fabrication of novel AAO-based nanostructures by pulse anodization, but also expands our knowledge and understanding in the field of nanotechnology, cancer biology, drug delivery and nanotoxicity. The AANTs-based nanotoxicity and drug delivery studies also highlight the potential of this novel nanomaterial for biomedical applications.

Key word: drug delivery, nanotoxicity, cancer therapy, nanotube, anodic aluminium oxide, anodization, cancer biology

PhD PUBLICATIONS

Summary: Book Chapter: **1**; Published Journal Articles: **10**; Submitted Journal Articles: **3**; Paper in preparation: **1**; Conferences: **12**.

Book Chapter

1. **Wang, Y.**; Liu, J.; Cui, L.; Losic, D., Cytotoxicity, drug delivery and photothermal therapy of functionalized carbon nanomaterials, Eds. L. Dai, R.R. Naik, and M. Zhang, Springer Series in Biomaterials Science and Engineering, Carbon Nanomaterials and Nanotechnology for Biomedical Applications, 2015 (in press)

Peer Review Journal Articles

2. **Wang, Y.**; Kaur, G.; Zysk, A.; Liapis, V.; Hay, S.; Santos, A.; Losic, D.; Evdokiou, A.: Systematic in vitro nanotoxicity study on anodic alumina nanotubes with engineered aspect ratio: Understanding nanotoxicity by a nanomaterial model. *Biomaterials* 2015, 46,117-130. (IF=8.557)
3. **Wang, Y**.; Chen, Y.; Kumeria, T.; Ding, F.; Evdokiou, A.; Losic, D. and Santos, A. (2015): Facile synthesis of optical microcavities by a rationally designed anodization approach: Tailoring photonic signals by nanopore structure, *ACS Applied Materials & Interfaces* 2015, *7* (18), pp 9879–9888 (IF=6.723)
4. **Wang, Y.**; Santos, A.; Evdokiou, A.; Losic, D., Rational Design of Ultra-Short Anodic Alumina Nanotubes by Short-Time Pulse Anodization. *Electrochimica Acta*. 2015, 154, 379-386. (IF=4.504)
5. **Wang, Y.**; Santos, A.; Evdokiou, A.; Losic, D. (2015): An Overview on Nanotoxicity and Nanomedicine Research: Principles, Progresses and Implications *Journal of Materials Chemistry B*, 2015, DOI: 10.1039/C5TB00956A (IF=4.726)
6. **Wang, Y.**; Santos, A.; Kaur, G.; Evdokiou, A.; Losic, D., Structurally engineered anodic alumina nanotubes as nano-carriers for delivery of anticancer therapeutics. *Biomaterials* 2014, 35, 5517-5526. (IF=8.557)
7. Chen, Y. Santos, A. **Wang, Y**. Kumeria, T. Ho, D. Li, J. Wang, C. and Losic, D. (2015): Rational design of photonic dust from nanoporous anodic alumina films: A versatile photonic nanotool for visual sensing, Scientific Reports, 5, article number 12893, DOI:10.1038/srep12893 (IF= 5.578)

8. Chen, Y.; Santos, A**.**; **Wang, Y**.; Kumeria, T.; Wang, C.; Li, J. and Losic, D., Interferometric nanoporous anodic alumina photonic coatings for optical sensing. *Nanoscale* 2015, 7, 7770-7779. (IF=7.394)
9. Chen, Y.; Santos, A**.** ; Ho, D.; **Wang, Y**.; Kumeria, T.; Li, J.; Wang, C. and Losic, D. (2015): On the generation of interferometric colors in aluminum: Colored aluminum as a photonic sensing tool. *Electrochimica Acta*. 2015, 174, 672-681 (IF=4.504)
10. Santos, A.; Sinn Aw, M. †; Bariana, M. †; Kumeria, T. †; **Wang, Y.** †; Losic, D., Drug-releasing implants: current progress, challenges and perspectives. *Journal of Materials Chemistry B* 2014, 2, 6157-6182. † **Equal Contribution** (IF=4.726)
11. Santos, A.; Kumeria, T. †; **Wang, Y.** †**.** Losic, D., In situ monitored engineering of inverted nanoporous anodic alumina funnels: on the precise generation of 3D optical nanostructures. *Nanoscale* 2014, 6, 9991-9999 (Journal Cover). † **Equal Contribution**

Submitted Papers

12. **Wang, Y.**; Kaur, G.; Chen, Y.; Santos, A**.**; Evdokiou, A. and Losic, D. (2015): Pharmacological targeting of autophagic and endoplasmic reticulum stress signaling by a nanotube-based combinatorial delivery system (submitted to Journal of Material Chemistry B).
13. Chen, Y. Santos, A**. Wang, Y**. Kumeria, T. Ho, D. Li, J. Wang, C. and Losic, D. (2015): Engineering of Interferometric Colors in High Purity and Technical Aluminum By Biomimetic Anodic Oxide Films: A Comparison (submitted to *ACS Applied Materials & Interfaces, in reversion*)
14. Santos, A; Yoo, JH; Rohatgi, C; Kumeria, T; **Wang, Y** and Losic, D (2015): Realisation and Advanced Engineering of True Optical Rugate Filters Based on Nanoporous Anodic Alumina by Sinusoidal Pulse Anodisation (submitted to *Nanoscale)*

Paper in Progress

15. **Wang, Y.**; Zinonos, I.; Zysk, A.; Hay, S.; Kaur, G.; Santos, A.; Evdokiou, A.; Losic, D., The *in vivo* Compatibility of Anodic Alumina Nanotubes (to be submitted to Biomaterials)

CONFERENCES (**12** conferences: **5** oral**, 7** posters)

1. **Y. Wang**, G. Kaur, A. Santos, A. Evdokiou, D. Losic, A study of nanotoxicity and targeting of autophagic and endoplasmic reticulum stress signaling networking by a

nanotube-based delivery system， 6th International NanoMedicine Conference 2015, Sydney (oral presentation)

2. **Y. Wang**, G. Kaur, A. Santos, D. Losic, A. Evdokiou, A study of nanotoxicity and cancer targeting of cell signaling networking by a nanotube-based delivery system, ANN ECR Workshop 2015(poster)
3. **Y. Wang**, G. Kaur, A. Santos, D. Losic, A. Evdokiou, Understanding bio-nano interaction by a nanomaterial model: toward nanomaterial-based cancer therapeutics, ASMR SA Annual Scientific Meeting 2015(poster)
4. **Y. Wang**, G. Kaur, A. Santos, A. Evdokiou, D. Losic, Electrochemically Synthetized Anodic Alumina Nanotubes as Novel Drug Carriers for Cancer Therapy: A Toxicity Study, 5th International NanoMedicine Conference, Sydney, JUN 2014 (oral presentation)
5. **Y. Wang**, A. Santos, G. Kaur, A. Evdokiou, D. Losic, Synthesis of structurally engineered anodic alumina nanotubes for drug delivery applications, RACI National Congress 2014, Adelaide, DEC 2014 (oral presentation)
6. **Y. Wang**, A. Santos, G. Kaur, A. Evdokiou, D. Losic, Fabrication of anodic alumina nanotube for drug delivery and nanotoxicity study, CRS student workshop 2014, Adelaide, OCT 2014 (oral presentation)
7. Losic, D. Sinn Aw, M. Gulati, M. **Wang, Y**. Kaur, G. Rahman, S. Santos, A. Findlay, D. Evdokiou, A.: Electrochemically nanoengineered drug-releasing implants for localized drug delivery and advanced bone and cancer therapies. Taishan Academic Forum 2014, Qingdao-China, 22-23 (oral presentation)
8. **Y. Wang**, A. Santos, G. Kaur, A. Evdokiou, D. Losic, Synthesis of Structurally Engineered Anodic Alumina Nanotubes as Novel Drug Nano-carriers for Drug Delivery Applications, ANN ECR Workshop 2014, Sydney, JUL 2014 (poster)
9. **Y. Wang**, Abel Santos, Andreas Evdokiou, Dusan Losic, Synthesis of Alumina Nanotubes as Novel Drug Nano-carriers for Drug Delivery Applications, ACMM23 & ICONN 2014, Adelaide, FEB 2014 (poster)
10. A. Santos. **Y. Wang.** T. Kumeria. and D. Losic. Inverted nanoporous anodic alumina funnels: Towards three-dimensional optical nanostructures. International Conference on Nanoscience and Nanotechnology, Adelaide-Australia, 292. FEB 2014 (poster)
11. **Y. Wang**, T. Altalhi, A. Santos, D. Losic Synthesis and Characterization of Carbon Nanocapsules for Drug Delivery Applications, CHEMECA 2013, Brisbane, SEP 2013 (poster)

12. **Y. Wang**, T. Altalhi, A. Santos and D. Losic Synthesis tunable morphology of Carbon Nanocapsules by non-catalyst approach, OZcarbon 2013, Melbourne, DEC 2013 (poster)

Chapter 1 Literature Review and Thesis Outline

1.1 Introduction of Aluminium Anodization and Anodic Aluminium Oxide

Aluminium anodization is a well-established electrochemical process that converts aluminium surfaces into nanoporous alumina by electrochemical oxidization. This technique has long been established over a hundred years in aluminium industry as a surface finishing method for preventing metal corrosion and allowing colouring.[1] Beside the numerous applications in the aluminium industry, aluminium anodization also showed significant applications in nanotechnology during the past 30 years.[3] The anodic aluminium oxide (AAO) films produced by industrialized conditions have irregular nanopore arrangements and uncontrolled geometry, which are unfavourable for nanotech research and application. To control the morphology of nanopore at nanoscale, Masuda and co-workers developed a ground-breaking technique so-called two-step anodization in 1995. This technique takes advantage of the pre-patterning effect of first-step anodization at optimized conditions to fabricate self-organized AAO nanostructures.[2] The resulting porous oxide films have close-compacted hexagonal arrangement and long-range straight channels (**Scheme 1**). Under specific electrochemical conditions, the pore diameter can be feasibly tuned from 10 to 400nm. Due to their confined geometry, AAO nanostructures have been widely used as templates for fabricating other nanostructures such as nanotubes, nanorods, nanowires.[3] Other outstanding properties of AAO such as thermo/ chemical stability, dielectric and optical properties also attracted intensive research to explore the application of this nanomaterial in different areas, including but not limited to optical sensing, catalysis, biomedical implant, solar cells and energy storage.

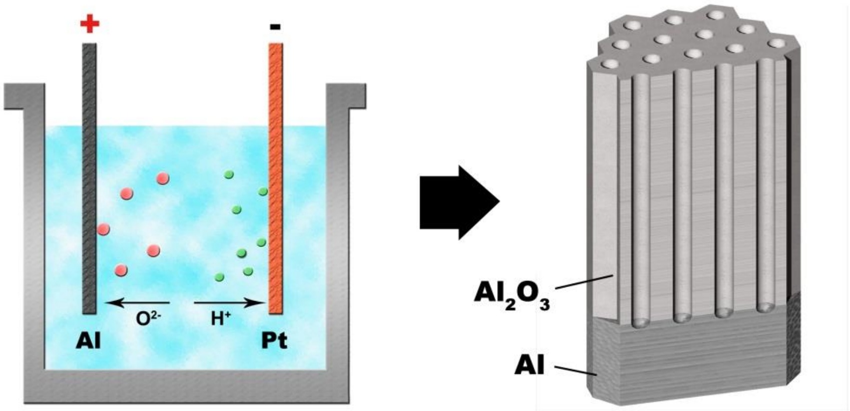

Scheme 1 Schematic illustration of aluminium anodization process. Anodization is conducted by passing direct current through acidic electrolyte solution, where aluminium is used as anode. During anodization, the oxygen ions driven by the current will move to the anode to oxide the surface of aluminium into alumina. At certain electrochemical conditions so-called self-organised regimes, self-assembled nanopores will form on the anodic film.

Porous AAO nanostructures with straight cylindrical geometry are conventionally fabricated by a technique so called mild anodization (MA) in regard to the slow growth rate of the oxide film (2–7 μm/h) under low current density (j=1-5 mA/cm^2).[2] Experimental studies and theoretical models have confirmed that the formation of such self-organized nanoporous anodic film is due to the mechanical stress driven by the migration of ions (i.e. Al^{3+} and O^{2-}) across the oxide barrier layer as well as field-enhanced dissolution of oxide.[4-8] Since the mechanical stress and electrochemical oxidation rate are proportional to the current passing through the oxide layer, not only does the current density applied during anodization govern the growth rate of nanopore, but also the geometric features of the resulting nanoporous film such as the nanopore size and shape.[7] For example, AAO with high growth rates and large pore diameters can be achieved when the anodization process is carried out under high current densities (j > 30 mA/cm^2) so-called hard anodization (HA).[9]

AAO nanostructures fabricated by MA and HA with straight channels generated numerous interest and applications in nanotechnology.[3] The current challenge is the difficulty of structural engineering AAO with well-controlled morphology. Such precisely controlled morphology at nanoscale is expected to generate new properties and potential applications that straight nanopore structures do not have. Thanks to the elucidation of the electrochemistry of anodization process, the structural engineering of AAO can be feasibly conducted by using pulse anodization (PA) approach[10-14].

It is known that the grow rate of oxide film and features of nanopores (i.e. porous diameter, interporous distance) are mainly governed by the applied current density and voltage at a given electrolyte system.[1-7] Anodization conducted at constant voltage (potentiostatic anodizaiton) or constant current (galvanostatic anodization) can form straight nanopore along the channel wall with a steady growth rate. The terminology of PA is related to the application of periodic voltage or current pulses during anodization, which are referred as potentiostatic PA and galvanostatic PA respectively. The programmed periodic electrochemistry during PA can control the nanopore geometry in real time, and consequently enable the continuous structure engineering of AAO into stack-layered AAO nanostructure. The resulted nanostructures have distinct properties as compared to AAO with straight nanopores. For instance, the development of PA technique makes it possible to precisely tailor the effective refractive index profile of AAO along the depth of nanopore in order to generate photonic crystals (e.g. distributed Bragg reflectors). In addition, novel one-dimensional and three-dimensional (3D) nanostructures can be produced by replicating nanostructures from pulse-anodized AAO. More importantly, PA can be used to directly produce anodic alumina nanotubes (AANTs) at specific conditions, in which stack-layered AAO nanostructures are fabricated and then broken down into individual nanotubes.[13] This fabrication process enhances the productivity of nanotube by taking advantage of 3D stack-layer AAO structures as starting materials instead of using monolayer AAO structures.[12]

Although the fabrication of AAO and AANTs has been reported, detailed fabrication mechanisms of AANTs associated with PA are not well understood. The length control of AANTs has only been demonstrated within a narrow range so far[13], while attempts of improving length control of AANTs are yet to come. In addition, the applicability of AANTs for drug delivery application has never been explored. The benefits of using non-spherical nanomaterials for drug delivery have been confirmed by theoretical models and experimental studies based on their effects on cellular internalization and vascular dynamics.[15-16] Furthermore, AANTs should have low toxicity since they have the same material composition with bulk-sized anodic alumina, which have been used as biomedical implants due to its excellent biocompatibility.[17] Based on the above statement about the background and research gaps of aluminium anodization, it can be envisioned that studies of PA and AANTs should generate new research opportunities for advanced applications such as nanofabrication (e.g. nanophotonics), optical sensing, and drug delivery.

References

1. Md Jani, A. M.; Losic, D.; Voelcker, N. H., Nanoporous anodic aluminium oxide: Advances in surface engineering and emerging applications. *Progress in Materials Science* **2013,** *58* (5), 636-704.
2. Masuda, H.; Fukuda, K., Ordered metal nanohole arrays made by a 2-step replication of honeycomb structures of anodic alumina, *Science* **1995,** *268* (5216), 1466-1468.
3. Lee, W.; Park, S.-J., Porous Anodic Aluminum Oxide: Anodization and Templated Synthesis of Functional Nanostructures. *Chemical Reviews* **2014**.
4. Houser, J. E.; Hebert, K. R., The role of viscous flow of oxide in the growth of self-ordered porous anodic alumina films. *Nat Mater* **2009,** *8* (5), 415-420.

5. Hebert, K. R.; Albu, S. P.; Paramasivam, I.; Schmuki, P., Morphological instability leading to formation of porous anodic oxide films. *Nat Mater* **2012,** *11* (2), 162-166.

6. Nielsch, K.; Choi, J.; Schwirn, K.; Wehrspohn, R. B.; Gösele, U., Self-ordering Regimes of Porous Alumina: The 10 Porosity Rule. *Nano Letters* **2002,** *2* (7), 677-680.

7. Lee, W.; Kim, J.-C.; Gösele, U., Spontaneous Current Oscillations during Hard Anodization of Aluminum under Potentiostatic Conditions. *Advanced Functional Materials* **2010,** *20* (1), 21-27.

8. Thompson, G. E.; Wood, G. C., Porous anodic film formation on aluminium. *Nature* **1981,** *290* (5803), 230-232.

9. Lee, W.; Ji, R.; Gosele, U.; Nielsch, K., Fast fabrication of long-range ordered porous alumina membranes by hard anodization. *Nat Mater* **2006,** *5* (9), 741-747.

10. Losic, D.; Lillo, M.; Losic, D., Jr., Porous Alumina with Shaped Pore Geometries and Complex Pore Architectures Fabricated by Cyclic Anodization. *Small* **2009,** *5* (12), 1392-1397.

11. Losic, D.; Losic, D., Preparation of Porous Anodic Alumina with Periodically Perforated Pores. *Langmuir* **2009,** *25* (10), 5426-5431.

12. Lee, W.; Schwirn, K.; Steinhart, M.; Pippel, E.; Scholz, R.; Gosele, U., Structural engineering of nanoporous anodic aluminium oxide by pulse anodization of aluminium. *Nat Nano* **2008,** *3* (4), 234-239.

13. Lee, W.; Scholz, R.; Gösele, U., A Continuous Process for Structurally Well-Defined Al2O3 Nanotubes Based on Pulse Anodization of Aluminum. *Nano Letters* **2008,** *8* (8), 2155-2160.

14. Woo, L.; Jae-Cheon, K., Highly ordered porous alumina with tailor-made pore structures fabricated by pulse anodization. *Nanotechnology* **2010,** *21* (48), 485304.

15. Gratton, S. E. A.; Ropp, P. A.; Pohlhaus, P. D.; Luft, J. C.; Madden, V. J.; Napier, M. E.; DeSimone, J. M., The effect of particle design on cellular internalization pathways. *Proceedings of the National Academy of Sciences* **2008,** *105* (33), 11613-11618.

16. Decuzzi, P.; Godin, B.; Tanaka, T.; Lee, S. Y.; Chiappini, C.; Liu, X.; Ferrari, M., Size and shape effects in the biodistribution of intravascularly injected particles. *Journal of Controlled Release* **2010,** *141* (3), 320-327.

17. Ingham, C. J.; ter Maat, J.; de Vos, W. M., Where bio meets nano: The many uses for nanoporous aluminum oxide in biotechnology. *Biotechnology Advances* **2012**, 30 (5), 1089-1099.

1.2 An Overview on Nanotoxicity and Nanomedicine Research: Principles, Progresses and Implications

1.2.1 Introduction, Significance and Commentary

This section is a comprehensive overview on the basic principles and progress of nanomaterial-based drug delivery and nanotoxicity research. First, the basic concepts and mechanism of nanomaterial-medicated drug delivery and nanotoxicity are summarized individually. Second, the classification of drug delivery strategies and nanotoxicity paradigms are presented in detail supported by the most recent research cases. Importantly, interconnection of nanotoxicity and drug delivery research are highlighted to address the future opportunities for developing advanced therapeutic approaches by utilizing intrinsic nanotoxicity. Finally, the review is summarized with conclusions and future prospects of utilizing nanoparticles for manipulating the behaviour of cells *in vitro* and *in vivo*. The scope and vision of this review covers a wide-range of bioengineering research including material chemistry, nanotechnology, cancer biology, toxicology and immunology, which underpin the fundamental knowledge and methodologies of this PhD project.

1.2.2 Publication

This section is a research paper published by Ye Wang, Abel Santos, Andreas Evdokiou, Dusan Losic, An Overview on Nanotoxicity and Nanomedicine Research: Principles, Progresses and Implications, Journal of Materials Chemistry B, 2015, DOI: 10.1039/C5TB00956A.

Statement of Authorship

Title of Paper	An Overview on Nanotoxicity and Nanomedicine Research: Principles, Progress and Implications on Cancer Therapy
Publication Status	☑ Published ☐ Accepted for Publication ☐ Submitted for Publication ☐ Publication Style
Publication Details	Wang, Y.; Santos, A.* Evdokiou, A.*; and Losic, D.*, An Overview on Nanotoxicity and Nanomedicine Research: Principles, Progress and Implications on Cancer Therapy J. Mater. Chem. B, 2015, DOI: 10.1039/C5TB00956A

Principal Author

Name of Principal Author (Candidate)	Ye Wang		
Contribution to the Paper	Conducted literature review and prepared manuscript draft		
Overall percentage (%)	80		
Signature		Date	31/7/15

Co-Author Contributions

By signing the Statement of Authorship, each author certifies that:

i. the candidate's stated contribution to the publication is accurate (as detailed above);

ii. permission is granted for the candidate in include the publication in the thesis; and

iii. the sum of all co-author contributions is equal to 100% less the candidate's stated contribution.

Name of Co-Author	Abel Santos		
Contribution to the Paper	Supervised development of work and manuscript evaluation		
Signature		Date	31/07/15

Name of Co-Author	Andreas Evdokiou		
Contribution to the Paper	Supervised development of work and manuscript evaluation		
Signature		Date	**11/8/2015**

Name of Co-Author	Dusan Losic		
Contribution to the Paper	Supervised development of work and manuscript evaluation		
Signature		Date	10/01/2015

Journal of
Materials Chemistry B

REVIEW

View Article Online
View Journal

Cite this: DOI: 10.1039/c5tb00956a

An overview of nanotoxicity and nanomedicine research: principles, progress and implications for cancer therapy

Ye Wang,[ab] Abel Santos,*[a] Andreas Evdokiou*[b] and Dusan Losic*[a]

Received 19th May 2015,
Accepted 29th June 2015

DOI: 10.1039/c5tb00956a

www.rsc.org/MaterialsB

The toxic paradigms of chemotherapeutic drugs and nanoparticles are tightly linked. Whereas uncontrolled exposure of living systems to therapeutics/nanomaterials leads to toxicity, selective induction of cytotoxicity in cancer cells helps in the fight against cancer. The increasing understanding of nanotoxicity paradigms has recently resulted in important benchmarks for the safe design of nanomaterial-based drug delivery systems aiming to fight cancer. In this context, this review aims to compile and present recent advances, outcomes and interconnections between nanomaterial-based drug delivery and nanotoxicity disciplines in order to provide a comprehensive guidance for future research. First, the basic concepts and mechanisms of nanomaterial-based drug delivery and nanotoxicity are introduced. Second, we present a detailed classification of drug delivery strategies and nanotoxicity paradigms, supported by the most recent research studies with a special focus on the interconnections between nanotoxicity and drug delivery research, which are highlighted in order to explore future opportunities for developing advanced therapeutic approaches. Finally, this review is concluded with future prospects on the use of nanoparticles for manipulating the behavior of cells and animals.

1. Introduction

Cancer is one of the world's most devastating diseases with high resilience to conventional treatments.[1] Since P. Ehrlich postulated his visionary concept of "magic bullet" based on the use of targeted medicines to efficaciously attack pathogens

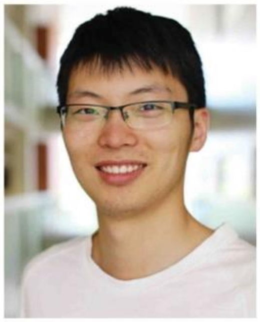

Ye Wang

Ye Wang is a PhD candidate studying at the School of Chemical Engineering, The University of Adelaide. He received his Bsc degree in Biological Engineering from Nanjing Agricultural University (China) in 2012. He is currently carrying out his PhD degree under the supervision of Prof. Dusan Losic, Prof. Andreas Evdokiou and Dr. Abel Santos. His research focuses on developing novel nanomaterials for cancer therapy and nano-toxicity study.

Abel Santos

Dr. Abel Santos received his Bsc degree in Chemical Engineering from the Universitat Jaume I (Castelló de la Plana, Spain) in 2005 and Msc and PhD degrees in Electronic Engineering from the Universitat Rovira i Virgili (Tarragona, Spain) in 2011. He joined the Prof. Losic's Nano-Research Group at The University of Adelaide in 2012. He received an ARC-DECRA award in 2014 in the School of Chemical Engineering at The University of Adelaide, where he works on structural engineering of nanoporous materials by means of electrochemical approaches, optical biosensing based on nanoporous materials and smart nanocarriers and implants for drug delivery applications.

---

[a] School of Chemical Engineering, The University of Adelaide, Engineering North Building, 5005 Adelaide, Australia. E-mail: abel.santos@adelaide.edu.au, dusan.losic@adelaide.edu.au
[b] School of Medicine, Discipline of Surgery, The University of Adelaide, Australia. E-mail: andreas.evdokiou@adelaide.edu

without affecting healthy tissues, various chemotherapeutic drugs (*e.g.* synthetic chemicals, proteins, peptides, *etc.*) have been used to treat cancer together with other approaches, including surgery and radiotherapy.[2] However, these strategies may not always succeed mainly due to the unfavorable drug pharmacokinetics, strong side effects of drugs, tumor metastasis, and the development of multi-drug resistance.[3] The unprecedented discoveries of cancer targets and cancer genome mapping have dramatically stimulated the development of new chemicals, inhibitors, therapeutic genes and bioactive peptides/antibodies for targeted cancer therapy.[4,5] Unfortunately, these novel drugs still face biological barriers when delivered systemically into the body, which greatly reduce the targeting efficiency and potentially increase side-effects. At the beginning of the new millennium, we have witnessed intensive multidisciplinary research on nanotechnology across almost all disciplines. In particular, nanotechnology when confronted with cancer biology has triggered new opportunities for improving targeted cancer therapy.

Nanomaterials are commonly defined as those materials with very small components and/or structural features (such as particles and fibers) with at least one dimension in the range of 1–100 nm.[6,7] Nanomaterials can be metals, metal oxides, ceramics, polymers, or composite materials and present novel properties when compared to conventional materials due to their nanoscale features. These materials have enabled promising new opportunities in oncology for treatment of cancer by nanomaterial-based drug delivery strategies, in which anti-cancer drugs are loaded directly onto nanomaterials and transported to specific tumor tissues for killing cancer cells.[8] Since nanomaterials as drug carriers are programmed to target cancer cells actively, the drug delivery efficiency should be significantly improved when compared to passive targeting of tumor by free diffusion of drug molecules. Although nanomaterial-based drug delivery strategies provide superior advantages over traditional chemotherapy, the potential cytotoxicity associated with nanomaterials still raises significant concerns.[9] Nanoparticles have distinct toxicity patterns as compared with their larger counterparts. The reduced size of materials at nano-scale increases the number of surface molecules and their surface area exponentially, leading to complex biophysicochemical interactions at the bio–nano interfaces when exposed to physiological environments.[10,11] Understanding these interactions and their consequence is of fundamental importance for the identification of potential paradigms of nanotoxicity. It should be noted that drug delivery and nanotoxicity have strong correlations. Induction of toxicity in cancer cells in a selective manner by nanomaterial-based drug delivery strategies eliminates tumors, whereas unfavourable toxicity of nanomaterials, therapeutic drugs, and the combination of both, often termed as nanomedicines, causes side-effects and dysfunctions. More importantly, since nanoparticles, therapeutic drugs and nanomedicines share similar biological fates/responses in the body, understanding the interconnections between nanotoxicity and drug delivery profoundly broadens our vision and increases the possibilities for improving cancer therapy. Statistically, the number of publications related to the scope of nanomaterial-based drug delivery and nanotoxicity has increased sharply since 2000 (Fig. 1). In 2014, over 14 200 and 2120 research studies were published on these two areas, respectively, which were approximately two hundred times more than the number of studies reported in 2000. That means, more than 44 papers per day have been published in these two areas during 2014. To address the significance of research in drug delivery and nanotoxicity, this review aims to provide a comprehensive view about the fundamental principles, concepts as well as the most recent research progress in these two areas. The scope and structure of this review is shown in Fig. 2.

Andreas Evdokiou

He is Professor of Breast Cancer Research and Head of Breast Cancer Research Unit (BCRU), Department of Surgery, Basil Hetzel Institute, The QEH, University of Adelaide (2011–2016) His cancer research is focused on cancer cell biology, particularly to understand the mechanisms involved in the development, progression and metastatic spread of bone related malignancies and the mode of action of novel therapeutics for the treatment of metastatic disease and pathologic bone loss.

Dusan Losic

Prof. Dusan Losic is an Australian Future Fellow and Research Professor at the School of Chemical Engineering, The University of Adelaide, where he is leading the NanoResearch Group. He completed his PhD in Nanoscience and Nanotechnology at Flinders University (2003), where he worked as a Research Fellow, followed by a 5-year ARC Research Fellowship (2007) in the Ian Wark Research Institute at The University of South Australia. His multidisciplinary nanotechnology research involves fundamental, engineering and applied aspects across several disciplines, including chemistry, materials science, engineering, biology and medicine working on diverse topics, namely, molecular separations, biosensing and drug delivery.

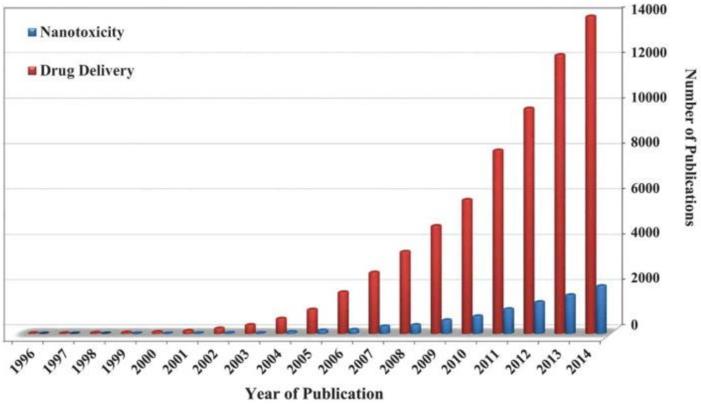

Fig. 1 The number of published papers on drug delivery and nanotoxicity from 1996 to 2014 according to the statistics on Google Scholar. Note that the key word "drug delivery" here only refers to the notion of nanomaterial-based drug delivery.

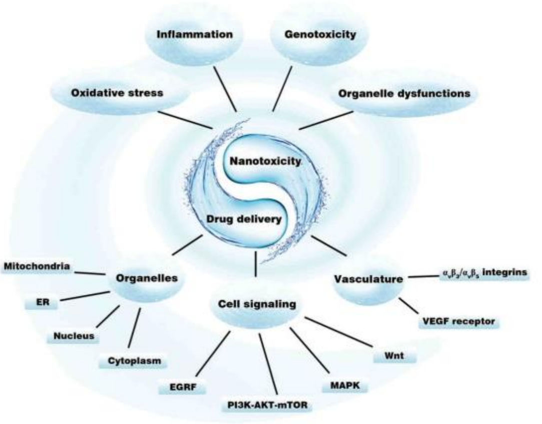

Fig. 2 Scheme of the correlations between nanotoxicity and nanomaterial-based drug delivery research. The studies of nanomaterial-based drug delivery and nanotoxicity are closely interconnected, which is presented as a TaiChi shown in the middle of the scheme. Nanotoxicity research provides direct benchmarks for the safe-design of novel nanomaterial-based drug delivery systems, while selective induction of toxicity in cancer cells by nanomaterial-based drug delivery approaches cures cancer. The major nanotoxicity paradigms and specific site-targeting strategies will be discussed in this review.

2. Site-targeted drug delivery: engineered drug targeting approaches by nanomaterials

Conventional drug therapies suffer from many drawbacks and intrinsic limitations such as low drug solubility of hydrophobic drugs, poor biodistribution, lack of selectivity and unfavourable pharmacokinetics.[7,12,13] The importance of controlling drug pharmacokinetics has been realized since 1950, but challenges still exist for delivering cytotoxic anti-cancer drugs with minimum side-effects.[14] For example, one of the most widely used anthracyclines, doxorubicin, has a rapid plasma clearance and short half-life (5–10 min in the first phase, and 29 h in the terminal phase) when administered intravenously.[15] In addition, doxorubicin, like other anthracyclines, potentially induces cardiotoxicity, limiting the therapeutic dosage that can be administered in clinical applications.[16] Comorbid conditions, such as impaired liver or renal functions, can further limit the dose tolerance of these cytotoxic drugs.[14] Biocompatible and bioactive drugs, including proteins, nucleic acids, enzymes and genes, face other problems as they degrade prematurely by metabolism when administered through oral or intravenous routes.[17] Unfortunately, the problems of dosing and off-site targeting of cytotoxic drugs are just some of the issues that patients suffering from cancer must face. Prolonged exposure to drugs may cause cancer cells to develop cross-resistance to several structurally unrelated chemotherapeutic agents, a phenomenon known as multi-drug resistance, which significantly diminishes the therapeutic outcomes.[18,19] Therefore, effective treatment of cancer requires a full understanding of cancer biology in order to adjust the features of medicines.

Nanomaterial-based site-targeted drug delivery systems are promising approaches to overcome the inherent limitations of conventional drugs. These systems present several attractive properties, including reduced off-target toxicity, enhanced efficiency of drug delivery by enhanced permeability and retention (EPR) effect and site-targeting strategies. Other advantages such as improved drug-circulation times, controlled drug-release kinetics, and superior dose scheduling for improved patient compliance also highlight the potential of nanomedicines in clinical applications.[20] It is noteworthy that micro-sized drug formulations, such as iron and aluminium salt-based drug crystals, were established almost a century ago.[21,22] However, the widespread application of nano-sized drug formulations emerged in the early 1990s along with the flourishing of nanotechnology.[23] Thus far, numerous nanomaterial-based drug delivery systems have been developed, including liposomes,[24] polymers,[25] metal and metal oxides[26] and composite nanomaterials.[27] More than 40 nanomaterial-based

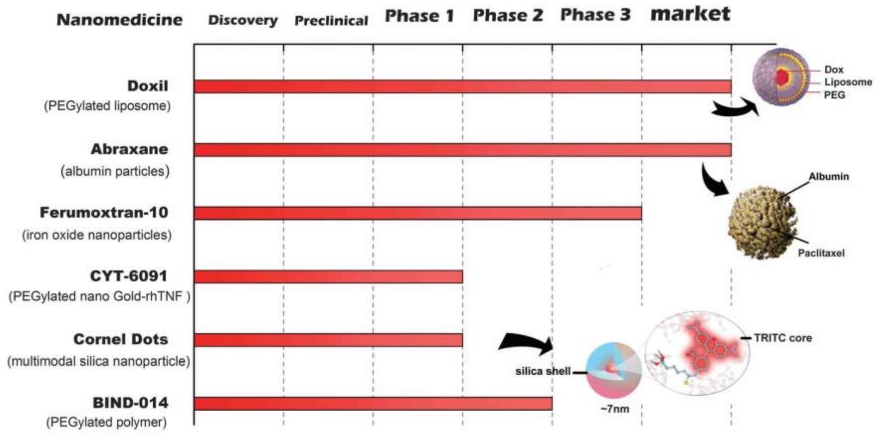

Fig. 3 Selected nanoparticle-based programs in clinical development.

products have been approved by the Food and Drug Administration (FDA) for clinical use (Fig. 3). For example, Doxil®, a polyethylene glycol (PEG) functionalized liposomal formulation of doxorubicin, was approved in 1995 for the clinical treatment of cancer and sarcoma.[28] Unfortunately, although the first generation of nanomedicines (*e.g.* Doxil®) achieved commercial success, these formulations utilizing the EPR effect to passively target tumors only showed limited improvement of cancer therapy in clinical practice.[20,24] Recently, a polymer-based site-targeted nanomedicine, BIND-014, demonstrated positive phase II results for the treatment of non-small cell lung cancer.[29,30] As the first example of a site-targeted nanomedicine, BIND-014 actively targets prostate-specific membrane antigens expressed on prostate cancer cells and the neovasculature of most non-prostate solid tumors. The promising clinical trials of BIND-014 clearly demonstrate the bright future of site-targeted nanomedicines due to their improved ability to target tumors. In this section, we will highlight the mechanisms, methodologies and recent research progress of nanomaterial-based site-targeted drug delivery strategies.

2.1 Mechanisms and concept of nanomaterial-based site-targeted drug delivery

As mentioned above, the first generation of nanomedicines utilized the EPR effect to target tumors. The earliest report of an EPR effect showed that the accumulation of anti-cancer protein at a tumor site is caused by the enhanced permeability in tumors due to the abnormal blood vessels and lymphatic drainage.[31] Such angiogenic blood vessel gaps, as large as 600 nm between adjacent endothelial cells, allow nanoparticles (NPs) to preferentially accumulate in tumors rather than spread into healthy tissues. In addition, cancer cells use high rates of glycolysis to obtain extra energy, resulting in a relatively acidic micro-environment when compared with normal tissues.[32] These characteristics of tumor cells provide a strong rationale for releasing drugs as a function of their pK_as and the cellular pH gradient. In this passive-targeting protocol, the anti-cancer drug loaded on nano-carriers is engineered to be stable within microenvironments at physiological pH (*i.e.* during transport), while the release of drug can be triggered at the tumor site, where the pH is lower than that of normal cells.

The EPR effect provides several benefits when compared to free diffusion of drug molecules into tumor tissues. However, EPR-based drug delivery systems as a passive targeting approach also face challenges. For instance, the EPR effect is limited to specific stages and types of tumors.[33] In addition, the complexity of the tumor micro-environment offers many barriers (*e.g.*, high interstitial fluid pressure, dense collagen matrix, *etc.*) that hamper the effect of passively delivered drugs into the tumor. Besides, the longer circulation times of the PEGylated liposomal doxorubicin are associated with several chemotherapy-induced side effects, such as stomatitis and palmar-plantar erythrodysesthesia.[20] A more promising way to overcome these limitations is to use site-targeted delivery systems. In these systems, nano-carriers functionalized with a homing molecule, such as ligands and monoclonal antibodies, are used to deliver drugs to solid tumors or cross biological barriers by a specific molecular recognition process (Fig. 4).

The internalization of nanomaterials occurs *via* endocytosis pathways, which are initiated by the formation of the endosome through the invaginating plasma membrane to envelop the conjugates formed by cell receptors and nanomaterials. Subsequently, newly formed endosomes are transported through endosomal–lysosomal–autophagy pathways. Besides entry into endosomal, lysosomal and autophagosomal compartments, it is believed that nanomaterials can escape from endosomes based on the so-called "proton sponge hypothesis",[34] which is the key for NPs to intracellularly deliver therapeutics to their targets and avoid drug degradation inside acidic lysosomes (Fig. 5). Meanwhile, the receptor released from the conjugate returns to the cell membrane to start a second round of transport through endocytic recycling pathways.[35] To increase the specificity, the corresponding antigen or receptor should be expressed exclusively on all tumor cells but not present on

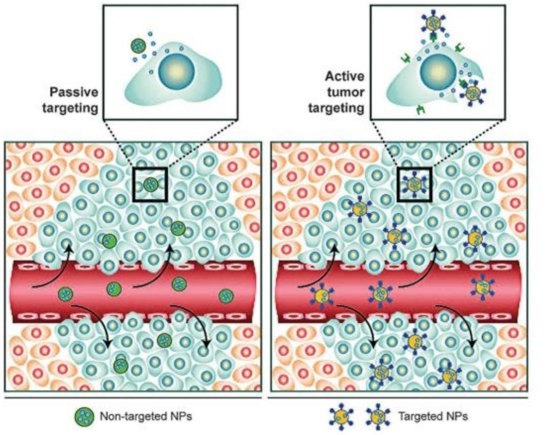

Fig. 4 Schematic illustration of passive and targeted drug delivery. (left) Non-targeted nanoparticles (NPs) end in passively extravasating through the leaky vasculature, which is characteristic of solid tumors and inflamed tissue, and preferentially accumulate through the EPR effect. (right) Targeted NPs containing surface ligands can recognize the receptor located on tumor cell surfaces.[8]

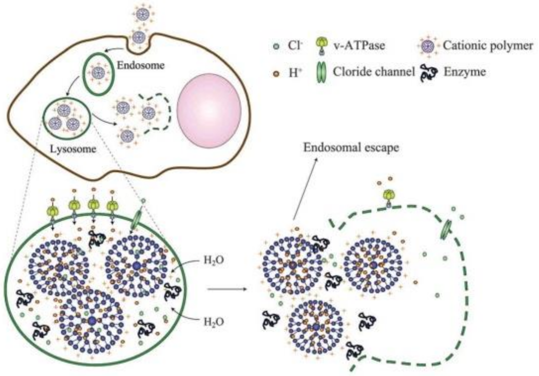

Fig. 5 Schematic of the proton sponge effect by cationic nanoparticles. Cationic nanoparticles with positive surface charges are capable of sequestering protons when internalized into the acidic lysosomal compartment. This function keeps the v-ATPase (proton pump) functioning and leads to the continuous reduction of pH and passive entry of chloride ions. Such high osmotic pressure subsequently causes the swelling and rupture of endosomes.[10]

normal tissues. For example, the folate receptor is overexpressed on tumor cells to increase the nutritional uptake, and thus folate is widely used as the homing molecule. But folate is also supplied by food, which might compete with ligands present on nano-carriers.[35] To date, tumor-associated biomarkers such as transferring receptors, growth factors and other overexpressed proteins have been widely used as cancer targets.[36] The application of novel biomarkers is the way envisaged for increasing the therapeutic efficacy and specificity of nanomaterial-based site-targeted therapeutics.[29]

2.2 Recent advances of nanomaterial-based site-targeted drug delivery

2.2.1 Intracellular targeting strategies. Intracellular targeting is of great interest for gene therapies, molecular imaging and treatment of organelle-specific diseases. Previous understanding of intracellular dynamics and cell uptake of nanomaterials showed that NPs enter the cell through various endocytosis pathways, including macropinocytosis, clathrin-mediated endocytosis, caveolin-mediated endocytosis, clathrin/caveolin-independent endocytosis and phagocytosis (Fig. 6). Specific organelle targeting can be realized by utilizing the endosomal escape of nanoparticles after cell uptake. The first intracellular delivery system was created and driven by the development of synthetic vectors for gene delivery.[37] Cationic NPs are ideal nanocarriers to deliver and accumulate cargos (*e.g.* genes and drugs) into the peri-nuclear region. For example, recently Zhou *et al.* developed a co-delivery system of doxorubicin and siRNA for *in vivo* preclinical breast cancer treatment. siRNA was efficiently loaded onto polystyrene nanoparticles through layer-by-layer deposition.[38] The siRNA loading was optimized to be 3500 siRNA molecules per particle in order to overcome the loss of siRNA during endosomal escape. The nanoparticles achieved a long circulating time with a half time of 28 h without triggering inflammatory responses, and significantly reduced the target gene expression (luciferase gene) in tumors by four-fold. In a combinatorial approach, tailored siRNAs that target multi-drug resistance proteins were loaded onto the surface of doxorubicin-loaded liposomes for achieving synergistic effects. This novel system successfully induced an eight-fold decrease in tumor volume within 15 days as compared to the control treatment.

In contrast to passive nuclear targeting, the active targeting strategy relies on the selective functionalization of NPs with nuclear localization signals for targeting the nuclear pore complexes (NPCs).[39] NPCs are large proteinaceous structures, which act as selective gates for nucleoplasmic transport of macromolecules.

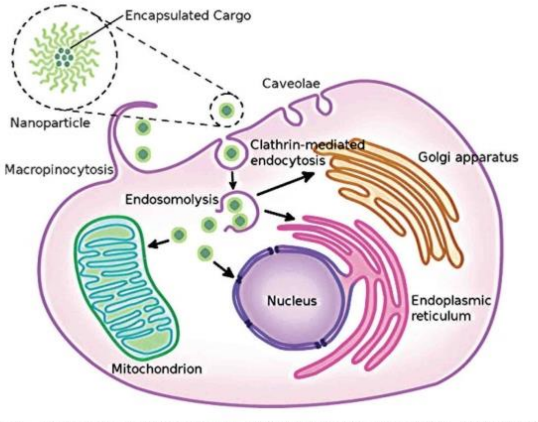

Fig. 6 Schematic representation of nanoparticle-meditated delivery of cargo. After endosomal escape, the nanoparticle can be engineered to target various cellular compartments such as mitochondria, endoplasmic reticulum, Golgi, nucleus, and cytoplasm.[36]

Table 1 Examples of nanoparticles for intracellular targeting delivery

Targeting moieties	Target organelle	Ref.
Mitochondrial localization signal	Mitochondria	39, 41, 43 and 55
ER-insertional sequence	ER	44, 56 and 57
Nuclear localization signals	Nucleus	39–42
P-gp inhibitor or bypass P-gp	Cytoplasm	44–52
Enhancing endocytosis and intracellular accumulation		

The transport is mediated by recognizing nuclear transport receptors and nuclear localization signals. Utilizing this feature enables the translocation of NPs with a maximum size of up to 39 nm into the nucleus.[39–42] Similarly, other targeting peptides that are recognized by the cytosolic transport systems, such as the mitochondrial localization signal, endoplasmic reticulum (ER) signal peptide and the ER retrieval sequence, have also been used for translocation of nanoparticles (Table 1). For example, mitochondriotropic triphenylphosphonium functionalized drug-loaded liposomes exhibited enhanced uptake and cancer cell killing both *in vitro* and *in vivo* due to the efficient mitochondria-targeting capability.[43] Entrapping an ER-insertion signal sequence into poly(γ-glutamic acid) NPs exhibited enhanced cellular immune responses as a result of the elevated antigen transport to ER, which is responsible for the antigen presentation process.[44] In addition, cytoplasmic targeting is of critical importance to overcome MDR in cancer cells. It is known that MDR is mainly caused by the complex interplay of cell survival pathways, which facilitate cell survival by various mechanisms, including enhanced drug transport,[18] over-expression of anti-apoptotic proteins,[19] increased DNA damage repair[45] and autophagy.[46] So far, various strategies have been employed to design drug delivery systems for effective transport of anti-cancer drugs into the targeted intracellular compartment.[16] The chemotherapy-induced up-regulation of P-glycoprotein (P-gp), a broad-specificity trans-membrane drug efflux pump, is considered a major event in the establishment of MDR in cancer cells. Inhibition of P-gp by anionic liposomes/lipids,[47,48] conjugation of NPs with P-gp antibodies and P-gp inhibitors[49] have shown promising preclinical and clinical results for reversing MDR. Another feasible approach is to enhance the cellular uptake (*i.e.* facilitate endocytosis to bypass P-gp) to achieve the rapid accumulation and controlled intracellular release of cytotoxic drugs.[47,50–53] In this approach, anti-cancer drugs, such as doxorubicin, can be conjugated on the surface of NPs through a stimuli-responsive linker so that the drug release can be activated by changes of physiological microenvironments.[54]

2.2.2 Cell signalling targeting strategies. Delivery of specific proteins, peptides and molecules that influence signaling pathways and manipulate cell functions is another approach for cancer killing. Such strategies not only require a good understanding of the cell survival mechanisms, but also an optimal design of drug cocktails and the pharmacokinetics of drug delivery systems. However, the transition of this approach is still rare, and a systematic review on this strategy is yet to come. Herein, we summarize the latest research results on cell signaling targeting strategies that have been demonstrated in recent years.

The phosphatidylinositol 3-kinase (PI3K)/Akt/mammalian target of rapamycin (mTOR) (PI3K/Akt/mTOR) pathways are important intracellular signaling pathways that regulate cell cycle, proliferation and longevity. These signaling pathways are frequently overactive in many types of cancer cells, and thus make the inhibitors of PI3K, Akt and mTOR useful candidates for molecular-targeted therapy. Rapamycin is a clinically available mTOR inhibitor (trade name: Rapamune) for chemotherapy, but the intrinsic drug resistance of rapamycin in cancer cells hampered the therapeutic effect.[58] Combination delivery of rapamycin with other drugs can reverse such resistance and achieve synergistic therapeutic effects *in vitro*. Unfortunately, such synergy was not always translated into good clinical performances because of the unfavorable pharmacokinetic parameters of drug combinations. To address this challenge, Elvin *et al.* developed a polymer micelle-based combination system for the co-delivery of rapamycin and paclitaxel *in vivo* by using poly(ethylene glycol)-*block*-poly(D,L-lactide) polymer micelles. After carefully optimizing the drug loading ratio and release profile, the nanoparticles could accumulate in tumors within 24 hours and effectively suppressed tumor growth due to the inhibition of mTOR and Akt downstream signaling (Fig. 7). A similar approach aiming to manipulate Akt signaling is to deliver Akt inhibitors for blocking the phosphorylation of Akt, which can activate apoptosis signaling to kill cancer cells.[59] In this study, anti-pAkt was conjugated with silica nanoparticles

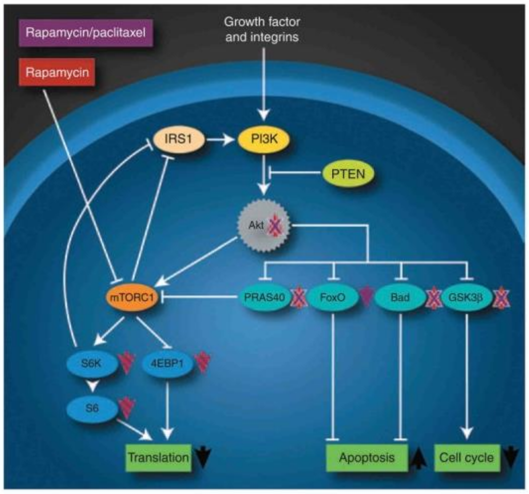

Fig. 7 Rapamycin and paclitaxel nanoparticles synergistically target the PI3K/Akt/mTOR pathway by suppressing feedback loop Akt-phosphorylation.[60]

followed by delivery to MCF-7 breast cancer cells. *In vitro* results confirmed the enhanced apoptosis and cell death after 24 h treatment.

Recent cell signalling studies demonstrated that the sequential delivery of different drugs for targeting signaling networks has a significant effect on cancer cell killing. Mitogen-activated protein kinase (MAPK) signalling and epidermal growth factor receptor (EGRF) signalling are both critical for regulating cellular functions.[61,62] Dysregulation of these signalling pathways is correlated with tumor progression, invasion and metastasis in a variety of cancer types. Previous research showed that delivery of the MAPK inhibitor PD98059 conjugated with poly(lactide-*co*-glycide) (PLGA) NPs inhibited tumor growth *in vivo* and enhanced the anti-tumor efficacy of cisplatin-based chemotherapy.[63] Note that in this research PD98059-loaded NPs were administered before cisplatin to achieve the scheduled inhibition and sensitization of tumor cells. Time-staggered inhibition of epidermal growth factor receptor (EGFR) was also shown to dramatically sensitise cancer cells to genotoxic drugs such as doxorubicin.[64] Translating this knowledge into drug delivery systems, Morton *et al.* developed a liposome-based combination delivery system to sequentially deliver a hydrophobic EGFR inhibitor and the DNA-damaging agent doxorubicin.[45] By using the lipid shell for storage of the hydrophobic drug and the aqueous interior to load the hydrophilic drug, liposomes enable incorporation of high concentrations of both therapeutics for their sequential release: the hydrophobic EGFR inhibitor on the shell is released first followed by doxorubicin from the core of the liposome (Fig. 8). The nanocarrier functionalized with PEG and folic acid had enhanced cell uptake and cancer killing *in vitro* and effectively produced tumor regression *in vivo*. More importantly, these investigators explored a number of drug cocktails with EGRF inhibitors in this drug delivery system, which further strengthened their preclinical results for future clinical transition.[45]

In another interesting work, a designed inhibitor of glycogen synthase kinase-3b (GSK-3b), so-called GFP-FRATtide, was delivered into stem cells for the manipulation of the Wnt–β-catenin signalling pathway.[65] This pathway is an evolutionarily conserved pathway that regulates crucial aspects of cell fate determination, cell migration, cell polarity, neural patterning and organogenesis during embryonic development.[66] GSK-3β is a key component of the Wnt signalling pathways and has long been treated as a target for molecular therapy.[67] In this work, the delivery of the GSK-3β inhibitor by hydrophobic silica NPs was tested in human and rat stem cells. The delivery of GFP-FRATtide induced Wnt signalling, resulting in the elevation of β-catenin levels due to GSK-3b inhibition. Accumulation of β-catenin up-regulated the transcription of Wnt target genes, which manipulated cellular proliferation and maintained cells in an undifferentiated state. Taken together, the emerging development of nanomaterial-based cell signalling targeting strategies as novel molecular therapeutics presented new possibilities for precisely manipulating cellular behaviour, which is ideally envisaged for providing personalized and dynamic cancer therapies (Table 2).

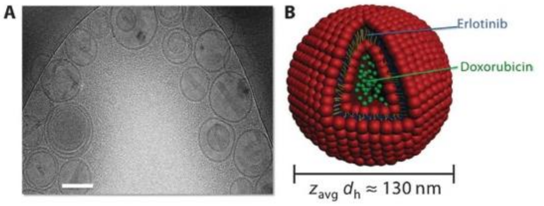

Fig. 8 Characterization of the combination therapeutic-loaded liposomal system. (A) Cryogenic transmission electron micrograph of dual drug-loaded liposomes. Scale bar, 100 nm. (B) Schematic of dual loading of a small-molecule inhibitor (erlotinib, blue) into the hydrophobic, vesicular wall compartment and of a cytotoxic agent (doxorubicin, green) into the aqueous, hydrophilic interior.[45]

Table 2 Examples of nanoparticles for cell signaling targeting delivery[a]

Targeting signaling[b]	Ref.
PI3K–AKT–mTOR signaling	60, 68 and 69
EGFR signaling	45, 70 and 71
Wnt signaling	65
MAPK/ERK signaling	63, 72 and 73

[a] Note that nanoparticles as a cytotoxic paradigm can intrinsically regulate cell signalling. The related work will be discussed in the nanotoxicity section to distinguish the concepts. [b] This table only summarizes the delivery of signalling regulators by nanoparticles. Delivery of cytotoxic drugs also activates various signaling pathways such as apoptosis signaling, which is not included here.

2.2.3 Vasculature targeting strategies. The transport of therapeutic agents from the systemic circulation to cancer cells requires three steps: (1) the drug molecules or NPs need to reach the tumor tissue *via* the blood vessels, (2) then cross the vessel wall and (3) penetrate through interstitial spaces to target cancer cells (Fig. 9). However, many barriers exist in each step for tumor targeting. Unlike normal tissues, blood velocity in tumors is independent of vessel diameter and unevenly distributed. This heterogeneous micro-environment creates poorly perfused or even unperfused regions, which makes NPs, or even small molecules, difficult to reach the tumor homogeneously.[20,74] Furthermore, the lack of functional lymphatic vessels and vascular hyperpermeability inside tumors result in interstitial hypertension (elevated interstitial fluid pressure), which in turn reduces the convective transport of drugs and NPs.[20]

Tumor vasculature targeting is a promising strategy to circumvent the barriers encountered by nanoparticles. All solid tumors depend on angiogenesis – the formation of new blood vessels – to support tumor growth.[76] Tumor blood vessels tend to express or overexpress extracellular matrix proteins on endothelial cell surface when compared to normal blood vessels, making them ideal as potential targets.[77] For example, vascular endothelial growth factor (VEGF) and its receptors (VEGFRs) as major angiogenic regulators have long been considered as tumor imaging and cancer therapeutic targets.[78,79] To translate this strategy into a nanomedicine approach, quantum dots were conjugated with VEGF and dual labelled with ^{64}Cu for VEGFR-targeted

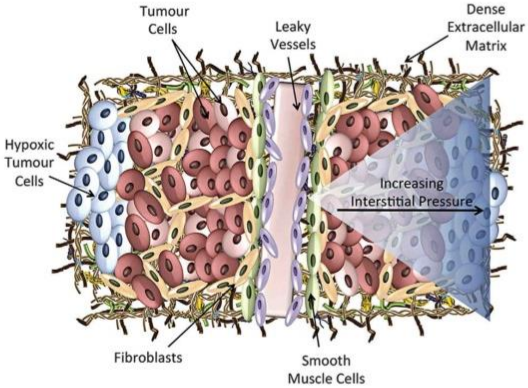

Fig. 9 Complexity of the tumor microenvironment prevents nanoparticles from effectively penetrating deeply into and effectively accessing tumor cells. (1) The leaky nature of the endothelium can be variable thereby restricting access to certain areas of the tumor. (2) Once nanoparticles have exited the vessels, they usually have to pass through other cellular layers including smooth muscle cells and fibroblasts before gaining access to tumor cells. (3) Interstitial pressure increases with increasing distance from the vessel which can prevent nanoparticles from penetrating deeply into the tumor. (4) Dense extracellular matrix can present an additional barrier to movement of nanoparticles into the tumor with stiffer tumors more difficult to penetrate. (5) High cell density of tumor cells is difficult to penetrate with most chemotherapy drugs only able to travel 3–5 cell diameters into the tumor and larger nanoparticles hindered to an even greater extent. Heterogeneity in tumor cells creates challenges for active targeting as they can possess highly varied cell surface molecule expression.[75]

PET/near-infrared fluorescence imaging.[80] The nanoparticles exhibited high VEGFR-2-specific binding affinity *in vitro* and *in vivo*, with a tumor accumulation of ≈4% ID g^{-1} (injected dose per gram of tissue) at 24 h post-injection, which was significantly higher than that of NPs without VEGF conjugation (<1% ID g^{-1}). Besides VEGFR, $\alpha_v\beta_3$ and $\alpha_v\beta_5$ integrins, which are overexpressed in angiogenic vessels, are also frequently used as targets. Ruoslahti *et al.* demonstrated the strategy of using iRGD peptide conjugated doxorubicin and NPs for targeting vasculature, in which the drugs/NPs could bind specifically to integrin $\alpha_v\beta_3$ and $\alpha_v\beta_5$ *via* the RGD motif.[81,82] Upon binding, the sequence undergoes proteolytic cleavage of the peptide exposing a new binding motif specific for neutrophilin-1 and allowing for deep penetration of the tumor tissue. Similar protocols have also been demonstrated by conjugating RGD with quantum dots,[83] single-wall carbon nanotubes,[84] zinc oxide nanowires,[85] superparamagnetic iron oxide nanoparticles,[86] gold nanorods,[87] dendrimers[88] and other NPs.

In addition to the modification of moieties for targeting vasculature, the physicochemical properties of NPs, such as size, shape and surface charge, also affect the ability of nanoparticles to penetrate tumors. As an example, *in vivo* experiments with gold NPs have demonstrated that only those NPs with sizes smaller than 10 nm can efficiently penetrate tumors (Fig. 10).[89] Nonetheless, the "size dilemma" becomes a concern when facing the fact that small sized NPs rapidly go through renal clearance, and thus are unlikely to effectively accumulate within the tumor.[90] To address this challenge, Wong *et al.* developed a 100 nm "multistage" gelatin quantum dots (QDGelNPs), which were designed to be broken down into smaller 10 nm nanoparticles for efficient tumor penetration by utilizing tumor-associated proteases to degrade gelatin.[91] These particles consist of a gelatine core with amino-PEG functionalized quantum dots conjugated onto the surface. The larger NPs can be cleaved by a matrix metalloproteinase (MMP), which is a protease present in high abundance within the tumor microenvironment. They demonstrated that only 25 ng of proteases (MMP-2) was required to release 50% of quantum dots *in vitro*. Furthermore, they found that the serum half-life of QDGelNPs (22.0 ± 3.4 h) is two-fold higher than that of the control group (silica NPs, 12.9 ± 2.4 h), which successfully extended the half-time of quantum dots. After 6 h post-injection, the QDGelNPs had penetrated up to ≈300 μm from the injection site while the silica NPs exhibited little or no dissemination from their initial location.

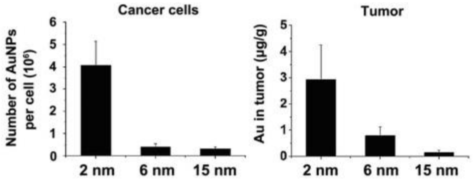

Fig. 10 Uptake of 2, 6, and 15 nm gold nanoparticles in MCF-7 monolayer cells and *in vivo* tumor tissues. 2 nm gold nanoparticles showed significantly enhanced tumor penetration as compared to larger nanoparticles.[89]

3. Nanotoxicity: mechanisms and implications for safe design of nanomaterials

Bio-safety of nanomaterials is a critical prerequisite to be considered when developing nano-carriers. Increasing attention has been focused on nanotoxicity since 2000 (Fig. 1). It should be noted that the purpose of nanotoxicological research is to provide evaluations of adverse effects associated with a nanomaterial for its safe use in the workplace, especially to establish the safe working dosage in different exposure pathways such as ingestion, inhalation or skin absorption.[9,92,93] According to this definition, however, most of the previous research studies were mechanistic studies rather than nanotoxicological assessments. Nonetheless, these studies provide meaningful guidance and implications for the safe design of nanomaterials.

Among numerous synthetic NPs, several types of inorganic nanomaterials (*e.g.* quantum dots, gold, silver, iron oxide NPs) and polymeric NPs have gained particular interest for their clinical applications. However, conflicting results of these and other types of nanomaterials have been found when analysing the effect of physicochemical parameters of NPs on their toxicity. Besides the issues of reproducibility and analysis techniques, the major problems in nanotoxicity studies are the intrinsic complexity of evaluating NPs' physicochemical

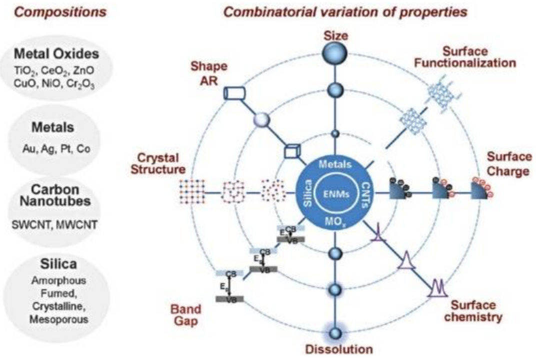

Fig. 11 Key paradigms of nanotoxicity of the library of nanomaterials, including metals, metal oxides, carbon nanotubes, and silica-based nanomaterials.[94]

factors and their toxicological consequence. The identified major physicochemical factors are size, surface chemistry, surface charge, aspect ratio and compositions (Fig. 11). Each of these parameters has a specific impact on the toxicological consequences associated with a given nanomaterial.

As one of the most important factors, size plays a critical role in nanotoxicity. The surface area and volume ratio of NPs increase exponentially with size reduction at nano-scale. Such "quantum size effect" leads to complex interactions between nanomaterials and biomolecules (*i.e.* protein, DNA) inside the biological milieu. It is reasonable to conclude that the size difference of NPs leads to variations of toxicological patterns. Such size-dependent effects were confirmed in cell-culture and animal experiments using various materials, such as gold[95] and silica NPs,[97–99] in which the smaller sized NPs are more toxic than bigger sized NPs. However, this conclusion is not true for all types of nanomaterials as other toxicity paradigms, such as crystal structure and surface reactivity, also change with the NPs' size. For instance, Warheit and co-workers have shown in a pulmonary instillation study that the toxicity of TiO_2 is independent of their size.[96] Concurrently, Karlsson *et al.* found out that Fe_2O_3, Fe_3O_4 and TiO_2 NPs with nano and micro-size showed similar toxicity with no size-dependent effect.

The aspect ratio, the ratio of the nanomaterial' size in two dimensions, also directly impacts the toxicity associated with one dimensional materials (*e.g.* nanowires) since it dramatically changes the fate of cell-uptake, biodistribution and the subsequent toxicity patterns of nanoparticles.[100] One-dimensional nanomaterials with high aspect ratios, such as magnetic nanowires,[101] alumina nanotubes,[102,103] CeO_2 nanorods,[104] silica NPs,[106] silicon[107] and silver nanowires,[108] displayed length-dependent acute toxicity (*i.e.* inflammatory response, lung fibrosis and organelle damage) as shown in both *in vitro* and *in vivo* model systems as compared to their sphere forms. However, the impact of the aspect ratio on toxicity is hard to determine individually due to the interference factors generated from the nanofabrication process. For example, the toxicity of gold nanorods comes from the use of growth-directing surfactant cetyltrimethylammonium bromide (CTAB),[105] while carbon nanotubes contain catalyst NPs as impurities, which also, at least in part, contribute to the length-dependent toxicity. In that respect, studies on other bio-inert inorganic fibre-like nanomaterials would make it possible to determine the role of the aspect ratio in nanotoxicity. For example, we recently reported the toxicity study of anodic alumina nanotubes with aspect ratios ranging from 7.8 to 63.3, in which we confirmed the toxic paradigms of high aspect ratio nanomaterials such as changes in cell morphology, pro-inflammatory responses and induction of apoptosis/necrosis.[102]

Surface chemistry and surface charge are two key parameters that determine the interactions of NPs with physiological environments. Considering the effect of surface chemistry, the reduced size of NPs down to nano-scale increases the number of atoms and crystal lattice defects on the surface of NPs, and thus enhances the surface energy and reactivity. The high surface energy can be released again by the formation of radicals such as reactive oxygen species (ROS) that causes DNA and protein damage.[118] The dissolution of toxic ions from NPs' surface, such as Zn^{2+},[113] Cu^{2+},[114] and Ag^{2+},[115] also generates serious organelle damage and cellular dysfunction. Nonetheless, the surface generation of ROS and dissolution of toxic ions are also dependent on the composition of nanomaterials. For example, CeO_2 NPs can suppress the ROS toxicity through surface oxidation of Ce^{3+} to Ce^{4+}.[109] Surface charges mainly contribute to the colloidal stability of nanomaterials, which is dominated by the colloidal forces (*i.e.* attractive van der Waals forces and repulsive electrostatic forces) at the solid–liquid interface. It is worth stressing that the charged surface with high surface energy adsorbs serum proteins, which constitutes a primary bio–nano interface determining the fate of the nanomaterials.[97] In cell culture experiments, adsorption of serum proteins was found to facilitate particle dispersion and change the cell uptake of NPs from serum-independent to serum dependent, while animal studies have proved that the adsorption of proteins contributes to the rapid clearance of NPs as well as toxicity in major organs depending on the dose.[111,112]

Compared to single parameter analysis, more complicated is the combination of these factors (*e.g.* size, surface charge, *etc.*) together on a certain nanomaterial. Since each nanomaterial has its distinct toxicity pattern, it is difficult to generate a general principle for nanotoxicity evaluation. Furthermore, conflicting results between nanotoxicity studies are produced due to the inconsistency of experimental procedures employed in different laboratories. Therefore, the optimization and standardization of toxicological analysis is crucial to establish a comprehensive and coherent methodology for nanotoxicity studies. This problem has been reasonably addressed in the recent years by improving *in vitro* and *in vivo* high throughput sequence technologies and platforms, which have enabled a more coherent methodology to analyse complex nanotoxicity scenarios. These technologies provide powerful tools for the rapid establishment of the hierarchical toxic levels of each toxic paradigm on a given nanomaterial.[94,116,117] In this section, we focus on the elucidation of mechanisms of nanotoxicity, aiming to shed light on the safe design of nanomaterials for clinical applications. In addition, the recent research utilizing intrinsic nanotoxicity for strategic cancer therapy will also be highlighted.

3.1 Mechanisms of nanotoxicity

3.1.1 Oxidative stress, inflammation and genotoxicity. Oxidative stress, defined as an imbalance between production and elimination of intracellular ROS, can lead to chronic inflammation and genotoxicity, which in turn mediate most of chronic diseases including cancer, diabetes, and cardiovascular and pulmonary diseases.[118] As the product of a normal cellular metabolism (*i.e.* O^{2-}, H_2O_2, $OH^{\bullet}$ and NO), ROS play vital roles in signalling pathways of plant and animal cells in response to the intra- and extracellular environmental conditions.[119] ROS toxicity is one of the first identified predictive toxicity paradigms of nanomaterials, which has been extensively studied in the last two decades. Four different ROS generation routes by nanomaterials have been identified so far: (1) ROS are generated directly from the surface of NPs;[120] (2) transition metal ions catalyse oxygen metabolic products into more reactive hydroxyl radicals (*i.e.* $OH^{\bullet}$);[121–124] (3) NPs trigger mitochondrial dysfunction, leading to an imbalance of the respiratory chain and disturbed ROS signalling;[125,126] (4) macrophages and neutrophils produce ROS when activated by NPs.[127] To eliminate the harmful pre-oxidant, cells utilize a complex system consisting of enzymatic antioxidants (*e.g.*, glutathione peroxidase, glutathione reductase, catalase) and non-enzymatic antioxidants (*e.g.*, glutathione, vitamins C and D).[118,128] However, unbalanced capability of intracellular ROS scavenging unavoidably leads to inflammatory reactions and DNA damage (Fig. 12).

Inflammation is a physiological process in response to cell/tissue injury and it is mediated by immune cells (*i.e.* macrophages, neutrophils and dendritic cells) that secrete signalling cytokines, reactive nitrogen species. Although inflammation is an important protective defence against infection and injury, mechanistic studies revealed that the immunotoxicity of nanomaterials can trigger the activation of the inflammasomes (a group of intracellular multi-protein complexes that respond to exogenous stimuli) and immune responses.[129,130] Receptor meditated immune responses, including toll-like receptors (TLRs), NOD-like receptors (NLRs) and their related downstream signalling, are also involved in inflammation induction by various nanomaterials such as graphene oxide.[131] Once activated, the inflammation response is characterized by the increased production of a number of cytokines such as tumor necrosis factor-α and interleukins, which lead to a cascade of immune reactions.[132–134] Severe consequences such as fibrosis and bronchial granulomas have been observed in test animals after instillation or inhalation of toxic nanomaterials such as carbon nanotubes at high doses due to the inflammation response.[127,135,136]

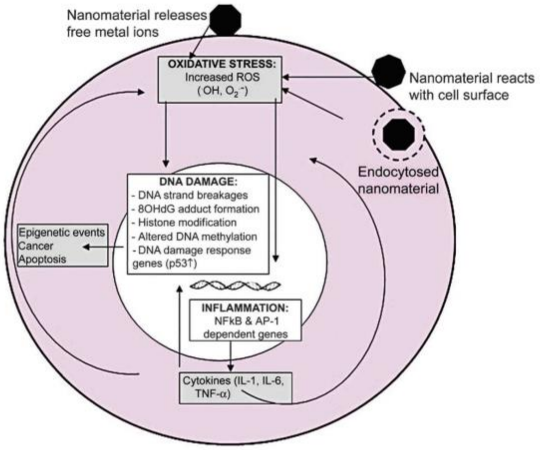

Fig. 12 Schematic of cross-talks of mechanisms of oxidative stress, inflammation and genotoxicity. Nanomaterials may result in oxidative stress or inflammatory responses that in turn have the potential to damage DNA and alter transcriptional patterns.[137]

Genotoxicity is another critical toxic paradigm of nanomaterials. NPs with small sizes (<10 nm) can directly enter the cell nucleus and influence the function of DNA, which can cause genotoxic responses, such as chromosomal fragmentation, DNA strand breakage, point mutations, oxidative DNA adducts and alterations in gene expression profiles.[138] Larger NPs may access the cell nucleus during mitosis when the nuclear membrane dissolves. In addition, ROS generation induced by nanomaterials also contributes to DNA damage when the DNA repair machinery cannot counteract the ROS damage.[137] Recent comprehensive reviews have systematically documented the methodologies and research process of nanomaterial-associated genotoxicity.[137,139,140]

3.1.2 Dysfunction of major organelles: autophagosomes, lysosomes, mitochondria and endoplasmic reticulum. The elucidation of the intracellular fate of nanomaterials shows that the transport of NPs is initiated by endocytosis pathways followed by the fusion of endosomes with lysosomes for digestion. The lysosomal degradation pathway plays a vital role in balancing cellular homeostasis and cell function in that the hydrolytic enzymes and acidic environment in the lysosome degrade intracellular pathogens (*i.e.* nanomaterials), damaged organelles and long-lived proteins.[141] Lysosomotropic agents, such as primary amine-based chemicals used to target lysosomes, have long been envisaged as chemotherapeutic agents due to their capability to rupture lysosomes through the proton sponge effect.[153] In the context of nanotoxicity, however, nanomaterials with proton buffering capabilities can serve as lysosomotropic agents to induce non-selective toxicity when taken up by healthy cells. As a major toxic paradigm, a number of nanomaterials were documented to induce lysosomal dysfunctions, so-called lysosomal membrane permeabilization (LMP). The release of lysosomal hydrolases such as cathepsin B, D and L is harmful to cells by initiating indiscriminate degradation of cellular components, which potentially leads to apoptosis. The lysosomal breakdown may also induce cytosolic acidification, which in turn induces cell death by necrosis.[142,143] Many studies have observed nanomaterial-induced LMP, including carbon nanomaterials,[98,144] metal/metal oxide nanoparticles[145,146] and cationic NPs.[147]

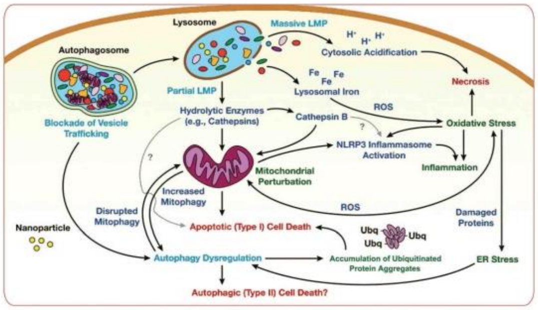

Fig. 13 Mechanisms of autophagy and lysosomal dysfunction toxicity. The initiators of autophagy and lysosomal dysfunction toxicity, displayed in light blue text in the figure, include blockade of vesicle trafficking, lysosomal membrane permeabilization (LMP), and autophagy dysregulation. Toxic effectors (ROS, cytosolic acidification, hydrolytic enzymes, reactive oxygen species, and the NLRP3 inflammasome) are displayed in dark blue. Conditions resulting from effector-mediated loss of homeostasis (oxidative stress, inflammation, ER stress, disrupted mitophagy, accumulation of ubiquitinated protein aggregates, and mitochondrial perturbation) are displayed in green. Finally, this loss of homeostasis can result in cell death pathways necrosis and apoptotic (type I) and autophagic (type II) cell death (displayed in red).[150]

After endosomal escape or LMP, the released nanomaterials and lysosomal hydrolases can further generate inflammation, ROS and subsequently damage other major organelles including mitochondria and endoplasmic reticulum (ER) (Fig. 13). Mitochondria as the intracellular ROS generators and mediators play critical roles in many cell functions including ROS signaling, ROS generation/detoxification and programmed cell death.[53,148] Nanomaterial-induced mitochondrial dysfunction can cause the release of cytochrome *c* and activate caspase (caspase-9), which eventually leads to cell apoptosis. Different from the function of mitochondria, ER as the machinery of biosynthesis is responsible for intracellular calcium homeostasis, lipid synthesis and protein secretion. Interruption of ER leads to the accumulation of unfolded proteins on ER, which activates a cell-rescue pathway, the so-called ER stress. The biomarker of ER stress was first identified in the early 2000, which generated great interest in the study of ER stress-related disease. However, it was not until 2011 when researchers realized about the importance of ER stress in nanotoxicity. So far, ER stress has been treated as a biomarker of nanotoxicity in several nanomaterial models, including silver, gold, zinc oxide, polymeric NPs, and anodic alumina nanotubes.[95,102,126,151,152] Similar to the dysfunctions of lysosomes and mitochondria, the interruption of ER can also lead to the disruption of cellular homeostasis such as mitochondrial-dependent apoptosis due to the up-regulation of cytosolic Ca^{2+} and ROS levels.

Finally, macro-autophagy, herein referred to as autophagy, is a homeostatic, catabolic degradation process which regulates the degradation of cytoplasmic material in response to various stress signals including those resulting from nanomaterial internalization.[154,155] The role of autophagy in nanotoxicity, however, can be either cyto-protective or cyto-destructive, since autophagic and apoptotic machineries share common signaling pathways. The formation of autophagosomes can isolate toxic nanomaterials from other organelles. Nonetheless, the accumulation of non-degradable nanomaterials inside autophagosomes may lead to autophagy dysfunction, defined as excessive autophagy induction or blockade of autophagy flux. Excessive cyto-protective autophagy transforms into autophagic cell death, which is characterized by the accumulation of autophagosomes and caspase-independent cell death pattern.[156] Recent studies have identified that the outcome of nanomaterial-induced autophagy (cyto-protective or cyto-destructive) is highly dependent on the physiological properties of nanomaterials (*i.e.* size and surface chemistry) and experimental factors such as cell models, working dose and treatment time.[147,150,155,157] Therefore, autophagy research should be carefully optimized to minimize the experimental variation. A comprehensive review of nanomaterial-induced autophagy can be found elsewhere.[150,155,158]

In summary, the overall mechanism of nanotoxicity is related to ROS production, inflammation, genotoxicity and major organelle dysfunctions. Once the cellular homeostasis cannot counteract the hostile impact of nanomaterials, a "domino effect" of the cell signaling cascade and organelles' dysfunctions will follow, which will eventually lead to programmed cell death. The major mechanisms of nanotoxicity that we discussed above are summarized in Table 3.

3.2 Design of materials for safe and efficient drug delivery application

3.2.1 Strategies of making non-toxic nano-carriers. The toxicity of nano-carriers influences their maximum tolerance doses (MTDs) that can be used in practice. The elucidation of nanotoxicity paradigms provides direct benchmarks for designing non-toxic nanomaterials as drug carriers. The successful design of safe nanomaterials requires full consideration of nanotoxicity paradigms, such as surface charge, surface chemistry, *etc.* (Fig. 11). It is worth stressing that since nanomaterials have distinct physical and chemical properties, strategies to reduce the toxicity of nanomaterials should be discussed on a case-by-case basis.

In general, non-degradable inorganic NPs (*e.g.* gold, iron, silica and quantum dots) generate toxicity mainly due to three paradigms: (1) organelle dysfunctions caused by the intracellular accumulation of NPs, (2) ROS generation/oxidative stress and (3) dissolution of toxic ions. A recent review has systematically compiled the key effects of cytotoxicity induced by inorganic NPs, including gold, silver, iron oxide, zinc oxide and quantum dots.[207] After summarizing numerous results of nanotoxicity studies, the methods developed to overcome the cytotoxicity of inorganic NPs are found to be virtually similar. Firstly, to avoid the unfavourable accumulation of non-degradable NPs inside cells and organs, working doses of NPs should be optimized according to their corresponding MTDs or median lethal doses. In addition, the physical sizes and hydrodynamic diameters of NPs are recommended to be less than 10 nm to permit complete and rapid elimination from the body.[167,168] Secondly, to prevent ROS generation, NPs' aggregation and dissolution of toxic ions, surface coatings are essentially required to

Table 3 Summary of major mechanisms of the nanotoxicity-associated paradigms

Paradigms	Cause	Consequence	Ref.
Oxidative stress	Nanoparticle (reactive surface, dissolution of toxic ions); LMP; mitochondrial dysfunctions; activation of immune cells	ROS toxicity; damage of other organelles; induction of inflammation and genotoxicity; apoptosis	120, 124, 159 and 160
Inflammation	Activation of TLRs and NLRs; uptake by immune cells; release of alarmins	NLRP3 inflammasome activation; release of cytokines	132–134
Genotoxicity	Nanoparticle interruption; ROS accumulation; dissultion of toxic ions; inflammation	Chromosomal fragmentation, DNA strand breakages, point mutations, oxidative DNA adducts and alterations in gene expression profiles	137–139
Lysosomal dysfunction (LMP)	Proton sponge hypothesis; ROS toxicity; increase of lysosomal pH; distruption of lysosomal trafficking	NLRP3 inflammasome activation; release of ROS, ions and hydrolytic enzymes; induction of dysfunction of other organelles; apoptosis	145, 150 and 161
Mitochondrial dysfunction	Mitochondrial outer membrance depolarization; release of ROS	NLRP3 inflammasome activation; autophagy induction; apoptosis	95, 125, 151 and 162
ER stress	Unfolded protein accumulation of ER	Activation of the ER stress signaling pathway and autophagy to balance homeostasis; apoptosis	152 and 163–165
Autophagy dysfunction	Blockage of autophagy reflex caused by particle overloading; excessive autophagy induction	Apoptotic and autophagic cell death	150, 155 and 166

Table 4 Representative surface chemistry strategies for modifying carbon nanomaterials

Functionalization type	Methods	Ref.
Covalent	Polyethylene glycol	170–172
	Polyacrylic acid	173 and 174
	Polyethylenimine	175–177
	Poly(*N*-isopropylacrylamide)	178
	Chitosan	179–181
Non-covalent	van der Waals force	182 and 183
	Electrostatic	184 and 185
	Hydrogen bonding	182 and 186–188
	Coordination bonding	189

cap the surface of NPs with a biocompatible layer *via* surface functionalization approaches. For example, PEGylation (the process of attaching PEG chains) is a well-established protocol used for surface functionalization. PEG polymers are FDA approved polymers formed by ethylene oxide in linear or branched structures. PEGylation of NPs can efficiently prevent the direct contact of biological interfaces with reactive surfaces of inorganic NPs. Other surface functionalization strategies, including covalent and non-covalent functionalization, have also been widely used in the past decades (Table 4). These versatile approaches not only make nanomaterials biocompatible, but also enable the attachment of other functional chemical groups for preparing multimodal nanomaterials, in which the nanomaterials perform several functions such as bio-imaging, disease diagnosis, cell targeting (selective binding/uptake through functional groups) and stimuli-responsive drug release.[169]

Unlike inorganic NPs, polymeric NPs have attracted great interest for gene and drug delivery due to their excellent biocompatibility and biodegradability. Biodegradable polymeric NPs (*e.g.* PLGA) can degrade into lactic acid and glycolic acid after administration. These degradation by-products can be eliminated by metabolic reaction cycles without inducing significant toxicity, although ROS generation and pro-inflammatory response were found at high working doses *in vitro*.[208] Note that biodegradable cationic NPs, such as cationic lipids, liposomes and polymers, can trigger toxicity by acidifying the endosomal–lysosomal compartment through the proton sponge effect (Fig. 5). The dysfunction of liposome structure has potential to cause other cellular organelles' stress, trigger inflammation as well as programmed cell death. Another cytotoxic paradigm associated with lipid is that some lipids, such as derivatives of cholesterol, are protein kinase C (PKC) inhibitors, which may interfere with normal PKC enzyme functions.[209] To overcome these problems, strategies have been developed to reduce the cationic charge density and replace the small molecule end-groups of lipid chains.[209,210] Non-degradable cationic polymers, such as polyethylenimine (PEI), are also promising materials as non-viral vectors for gene delivery. However, the non-degradable nature significantly hampered their practical application.[211] To facilitate the clearance of non-degradable cationic polymers, the size of polymers can be programmed to be reduced by using biodegradable linkers (*i.e.* acid labile ester) to bind short polymer chains into a longer chain.[212] Modification of cationic polymers by addition of hydrophilic monomers and/or polymers, such as PEG, is also an efficient way to reduce the excessive surface charges and prevent unfavourable interactions with serum proteins and red blood cells.

3.2.2 Optimization of pharmacological factors to enhance drug delivery efficiency. Our understanding of nanotoxicity in the last decade enabled the fabrication of non-toxic nanocarriers for drug delivery. However, the clinical success of nanomedicines requires further engineered designs for the optimization of pharmacological performances. The *in vivo* performance of nanomedicines has been mainly limited by their low stability and rapid clearance.[213] These two issues consequently lead to short circulation half-life, low efficiency of targeting and toxicity.

Driven by the motivation of improving pharmacokinetics of nanomedicine, numerous studies have been conducted to explore the impact of various physicochemical factors of nanomaterials on their biodistribution.[214] Recent studies have made key findings about the identification of protein corona to the biological fate of nanomaterials. Currently, it is well-accepted that the interactions of nanomaterials with biological barriers (*e.g.* reticuloendothelial system (RES)) are dominated by the bio–nano interfaces between the surface of nanomaterials and the physiological environment. The surface of nanomaterials will be modified by proteins that existed in biological fluids (*e.g.* blood plasma) once nanomaterials are administered into the bloodstream.[215] Since nano-sized materials have high free energy on the surface, their surfaces tend to adsorb biomolecules in order to reach an equilibrium low-energy state. The formation of protein shells, so-called protein corona directly medicates the dispersion and distribution of nanomaterials *in vivo*. Bio-analytical studies have revealed that protein corona contains a hard corona and a soft corona depending on the affinity and binding strength of proteins present in plasma. Proteins with strong affinities bind tightly the nanoparticle surface, forming a relatively stable hard shell, while proteins with weak affinities will form soft corona on the top of the hard one. Current studies of protein corona have revealed that the protein identities of the corona are dynamic in nature, which depend on the environments through which the nanomaterials are transported (*e.g.* bloodstream and cell membranes).[216] As a result, the patterns of protein corona significantly differ from various types of plasmas and species. In addition, the features of protein corona are also distinct based on the physiological properties of nanomaterials (*e.g.* size, surface chemistry, surface charge, *etc.*). The impact of these parameters on protein corona has recently been systematically reviewed.[217] The complexity of protein corona, similar to the patterns of nanotoxicity, creates difficulties in generating a general rule to control the biological consequences associated with nanomaterials, since each type of nanomaterial in each biological fluid will have a distinct pattern of corona. The inconsistent reproducibility of nanofabrication and bioanalytical results is the major obstacle for the fundamental study of protein–corona and bio–nano interactions. Therefore, high-throughput and high sensitivity characterizations such as nuclear analytical techniques[218] will be required in the future to establish a complete library of protein coronas as a function of different nanomaterials and biological milieus. Such understanding will provide a powerful guidance for the precise manipulation of protein corona in order to better control the biological responses (*e.g.* cell uptake, targeting and immune response) at the bio–nano interfaces.

Although protein corona may favour the stability and biocompatibility of nanomaterials within biological fluids, it may have a negative impact on nanomaterials' biodistribution.[219,220] Binding of complement and immunoglobulin promotes macrophage phagocytosis and activates the immune system.[217] The complement system is part of innate immune system that assists phagocytic clearance of pathogens through a number of small proteins served as opsonin. Complement proteins, such as C3 and C5, will identify nanomaterials as foreign pathogens when adsorbed on their surface, resulting in a high rate of hepatic uptake and clearance. In addition, protein corona may also inhibit the recognition of ligands (*i.e.* antibodies, proteins and peptides) that are grafted on the surface of nanomaterials as homing agents for active site-targeting. Therefore, reducing the formation of protein corona is required for the long time circulation of nanoparticles *in vivo*.

Overall, PEGylation is the most widely used approach for improving the serum half-life of therapeutics and nanomaterials. The concept of PEGylation was first introduced in the late 1970s, and reached widespread application in the 1990s for liposome and polymeric NP-based drug delivery systems. Besides the benefits of reducing toxicity of nanomaterials as we discussed above, the non-ionic hydrophilic property of PEG can provide stealth behaviour of NPs by minimizing the adsorption of opsonin and consequently diminish RES uptake.[110] Grafting PEG brushes onto the surface of NPs also prolongs blood circulation by increasing the hydrodynamic diameters of nanomateials for slowing renal clearance.[213] Many solid results have identified that the chain length/molecular weight of PEG and grafting density considerably influence the formation of protein corona and particle biodistribution. For example, one of the earliest reports from Gref *et al.* studied the influence of PEG layer thickness and grafting density on three different biodegradable nanoparticles, including PLGA, poly(lactic acid) (PLA) and poly(*o*-caprolactone). Their pioneering results showed that PEGylation significantly reduced protein adsorption ($>50\%$) especially that of apolipoprotein (A-IV and E) and complement protein C3. In addition, a steep decrease in protein adsorption was observed when increasing the molecular weight of PEG from 2000 to 5000. When discussing the impact of PEG density, they found that even 0.5 wt% PEG on the surface was able to reduce protein adsorption by half as compared to the PLA reference particles. The most significant reduction of protein absorption was found in particles containing 5 wt% PEG.[221] Ten years later, Walkey *et al.* systematically studied the effect of macrophage uptake on gold NPs with differing particle size and grafted PEG densities. By using label-free liquid chromatography tandem mass spectrometry, they mapped over 70 most abundant proteins from protein corona. Their results showed that increased PEG density led to a monotonic decrease in total protein adsorption as well as a shift of the cell-uptake pathway from serum dependent to serum independent.[222] Recently Lee *et al.* studied the impact of PEGylation on biodistribution of filamentous NPs by using plant virus filamentous NPs as models. In their studies, PEGylation of high aspect ratio virus-like NPs effectively reduced RES clearance, minimized inflammation and improved overall half-life.[223] In summary, PEGylation as the most successful surface modification method has been applied in the majority of nanomaterial-based drug formulations used in clinical practice. No other synthetic polymer has reached this status.[224] A deeper insight of the pros and cons of PEGylation can be found in a review paper written by Knop *et al.*[224] Since the biodistribution and pharmacokinetics of nanomaterials directly impact the toxicity and therapeutic outcomes, the physicochemical parameters of nanomaterials need to be carefully engineered on a case-by-case basis according to the specific requirements.

3.3 Engineered nanotoxicity for advanced disease therapy

Uncontrolled nanotoxicity leads to side-effects. Induction of nanotoxicity in a selective manner by engineering nanomaterials, in contrast, may serve as advanced therapeutics. As we discussed above, autophagy as an intrinsic catabolic degradation pathway plays an important role in the development of MDR, cell longevity and programmed cell death. Precise regulation of autophagy behaviour by nanoparticles enables novel therapeutic concepts. Ling *et al.* demonstrated that the induction of autophagy can be manipulated by controlling the surface chemistry of carbon nanotubes. Autophagy induced by mTOR dependent and independent pathways has been realized by using a full library of 81 surface-modified carbon nanotubes.[111] Wei *et al.* recently reported the *in vitro* regulation of autophagy by europium hydroxide [$\mathrm{Eu^{III}(OH)_3}$] nanorods for reducing protein aggregation. It is known that autophagy dysfunction contributes to neurogenerative diseases due to the lack of clearance of protein aggregates.[190] Their result, although not supported by *in vivo* studies, provides proof-of-concept evidence that nanomaterials can regulate the longevity of cells for the therapy of neurodegenerative diseases such as Alzheimer's and Parkinson's disease.[149,162] Note that the nanomaterial-induced autophagy is not always of benefit for the longevity of brain cells. As an example, Chen *et al.* reported that CdSe/ZnS quantum dots induced autophagy-dependent synaptic dysfunction in mouse brains after intrahippocampal infusion. Treatment with autophagy inhibitors (wortmannin and chloroquine) can reverse toxicity by suppressing nanoparticle-induced autophagy flux and down-regulating synapsin impairments.[157] In addition, nano-alumina was found to trigger cerebrovascular toxicity by up-regulating autophagy activity in the brain and elevating blood–brain barrier permeability.[191]

Autophagy has also gained increased attention in the area of chemotherapy. Autophagy is intrinsically activated by cytotoxic drugs, and is one of the origins of MDR. The application of autophagy inhibitors such as chloroquine (CQ) in combination with other therapies is currently in clinical trials and has recently been translated into nanoparticle-based drug delivery systems.[192–194] In one study, nano-sized manganese(II) oxide (MnO) nanocrystals were utilized for magnetic resonance imaging (MRI) and combination chemotherapy (Fig. 14). The MnO nanoparticles can induce significant T_1-MRI contrast enhancement as well as high levels of autophagy, which is shown to be independent of tumor suppressor p53. In addition, suppression of autophagy by an inhibitor (*i.e.* 3-methylamphetamine) or inhibition of apoptosis by z-VAD-fmk reduced the cytotoxicity of MnO, providing evidence that autophagy is responsible for the MnO nanoparticle-induced cytotoxicity. More importantly, autophagy triggered by MnO was shown to have a synergistic effect when co-administered with doxorubicin *in vitro* and *in vivo*. Such a synergistic effect of nanomaterial-medicated autophagy and anti-cancer drugs provides new concepts for cancer therapy. In another study, drug loaded PLGA nanoparticles were co-administered with the autophagy inhibitor CQ for cancer therapy. PLGA nanoparticles were found to localize in the autophagosome for degradation after internalization. After autophagy inhibition, the drug delivery system showed significantly enhanced cancer killing ability *in vitro* and tumor suppression *in vivo*.[193,195] Recently, an interesting study demonstrated the anti-tumor effect of graphene oxide when injected intratumorally *in vivo*. Such effect was shown to be due to the cytotoxic autophagy induction through TLR signalling, in which the activation of TLR-4/9 up-regulates the autophagy machinery including Beclin-1 and microtubule-associated protein 1A/1B-light chain 3 (LC3).[196]

Fig. 14 Schematic illustration of the preparation of MnO nanocrystals for the integration of MRI and autophagy induction for chemotherapy.[194] Left: MnO prepared by microwave synthesis showed enhanced MRI and induced cytotoxic autophagy, which is synergistic with the effect of doxorubicin for chemotherapy. Right: The process of autophagy consists of the formation of autolysosomes to engulf nanoparticles and damaged organelles, which can be inhibited by 3-MA, wortmannin (inhibits the formation of autophagosomes) and bafilomycin A1 (inhibits fusion of autophagosomes and lysosomes).

Finally, autophagy plays a critical role in immunotherapy by nanoparticle-induced tumor vaccination. Tumors escape defensive immune attack by a variety of mechanisms of immunosuppression, which inhibits the activity of antigen presenting cells, mainly dendritic cells (DCs) and cytotoxic T lymphocytes ($\mathrm{CD^{8+}}$ T cells). Anti-tumor immune responses must go through a process, so called cross-presentation, in order to generate protective T-cell responses to kill cancer cells. Cross-presentation of DC requires three distinctive steps to trigger adaptive immune responses, including antigen internalization, protein degradation and loading of antigen-derived peptides into major histocompatibility complex class I molecules (MHC I) presented at the surface of DCs. Autophagy as a protein degradation process facilitates MHC I presentation; fusion of autophagosomes with the MHC II-containing compartment, such as late endosomes and lysosomes, also enhances MHC II presentation of cytosolic proteins and viral antigens (Fig. 15).[197,198] Based on this mechanism, a novel therapeutic vaccine was developed by utilizing alumina nanoparticles to transport conjugated antigens (ovalbumin) to autophagosomes of DCs.[199] Nano-alumina with 60 nm diameter triggered significant $\mathrm{CD^{8+}}$ T cell production as compared to TiO_2 and Fe_2O_3 nanoparticles. Importantly, autophagy suppression by 3-MA or wortmannin, knockdown of Beclin 1 and autophagy gene silencing (Atg 12) nearly abolished the cross-presentation of OVA, proving the essential role of autophagy in antigen presentation. Mice injected with nano-alumina-OVA completely rejected tumors and remained tumor-free for more than 40 days. This study further demonstrated the advantage of using nano-alumina conjugated autophagosomes to suppress tumor growth due to the high content of antigens than nano-alumina-OVA. Note that nanomaterial-based tumor vaccination has been extensively reported in the last ten years.

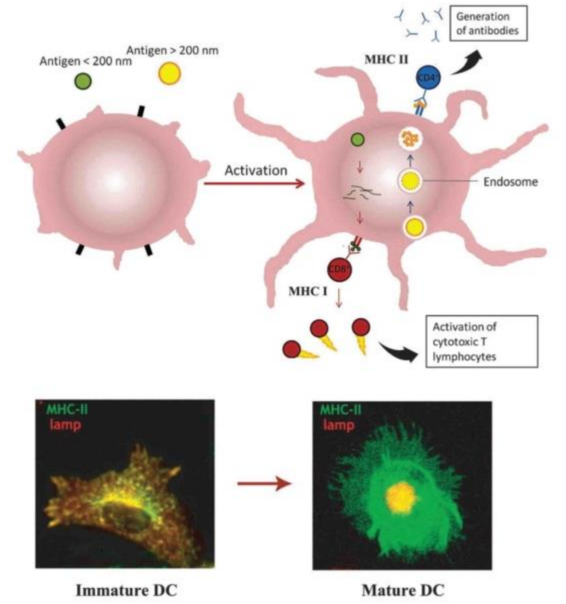

Immature DC Mature DC

Fig. 15 Scheme of induction of immune response by dendritic cells. Top: Antigens which enter cells *via* endosomal pathways (blue arrows) are typically degraded within a vesicle before the contents are displayed on the cellular surface by MHC II receptors and recognized by CD^{4+} T cells. Alternatively, antigens present in the cytosol (red arrows) are broken down and presented on MHC I receptors, which are recognized by CD^{8+} T cells. Bottom: Immunofluorescence images of the mutation of DC, which showed a dramatic reorganization of cell formation and function. MHC-II-GFP is shown in green, and the lysosomal membrane protein Lamp is shown in red. Immature DCs are highly endocytic and accumulate most of MHC-II molecules inside the cell in lysosomal compartments. On maturation, MHC-II is transported to the plasma membrane to activate T helper cells (CD^{4+} T cells).[202]

Numerous nanoparticles have demonstrated the capability for effective immune activation by utilizing nanoparticle-induced immunotoxicity. Comprehensive strategies and mechanisms of this application can be found elsewhere.[200,201]

4. Conclusion and future perspective

This review has summarized the concepts, mechanisms and recent progress in drug delivery and nanotoxicity research. From proof-of-concept to commercialization, our increasing understanding of drug delivery has dramatically promoted the commercial transition of nanomaterial-based drug delivery systems into the market for improving our well-being. After the success of the first generation of nanomedicines, the next generation of nanomedicines with improved site-targeting, stimuli-responsive drug release, and multimodal capacities are currently undergoing clinical trials.[24,54,203] However, the biosafety issue and the complex bio–nano interactions in the human body could hamper the development of nanomedicines, and thus will continually gain interest from both researchers and pharmaceutical business in the future. With the maturity of nanofabrication and drug delivery techniques, personalized nanomaterial-based cancer therapy may address the future requirements of individual cancer patients such as drug cocktail selection, dynamic dose schedule and specialized nano-carrier design according to disease symptoms. Furthermore, nanoparticles as a nano-sized tool provide new opportunities in dealing with biological science. Besides fighting cancer and disease, recent findings showed remote manipulation of glucose homeostasis in mice by using 5 nm iron nanoparticles to control ion channels through radio-wave heating with major implications in the fight against diabetes.[204–206] It can be envisioned that controlling advanced animal behaviour by bioengineered nanoparticles will be possible and highly influential in the future.

Acknowledgements

This research was supported by the Australian Research Council (ARC) through the grants DP120101680, FT110100711, and DE14010054, the National Health and Medical Research Council (NHMRC) of Australia through grant APP627015, the Australian Breast Cancer Research (ABCR), The Hospital Research Foundations (THRF) and the University of Adelaide Interdisciplinary Research Fund (DVC IRF-2014). Ye Wang has appreciated the scholarship provided by the China Scholarship Council.

Notes and references

1 R. Siegel, J. Ma, Z. Zou and A. Jemal, *Ca-Cancer J. Clin.*, 2014, **64**, 9–29.
2 E. B. C. T. C. Group, *Lancet*, 2005, **365**, 1687–1717.
3 C. Holohan, S. Van Schaeybroeck, D. B. Longley and P. G. Johnston, *Nat. Rev. Cancer*, 2013, **13**, 714–726.
4 A. S. Paparella, T. P. Soares da Costa, M. Y. Yap, W. Tieu, M. C. Wilce, G. W. Booker, A. D. Abell and S. W. Polyak, *Curr. Trends Med. Chem.*, 2014, **14**, 4–20.
5 T. Li, H.-J. Kung, P. C. Mack and D. R. Gandara, *J. Clin. Oncol.*, 2013, **31**, 1039–1049.
6 D. Peer, J. M. Karp, S. Hong, O. C. Farokhzad, R. Margalit and R. Langer, *Nat. Nanotechnol.*, 2007, **2**, 751–760.
7 A. Santos, M. Sinn Aw, M. Bariana, T. Kumeria, Y. Wang and D. Losic, *J. Mater. Chem. B*, 2014, **2**, 6157–6182.
8 O. C. Farokhzad and R. Langer, *ACS Nano*, 2009, **3**, 16–20.
9 H. F. Krug, *Angew. Chem., Int. Ed.*, 2014, **53**, 12304–12319.
10 A. E. Nel, L. Madler, D. Velegol, T. Xia, E. M. V. Hoek, P. Somasundaran, F. Klaessig, V. Castranova and M. Thompson, *Nat. Mater.*, 2009, **8**, 543–557.
11 A. Nel, T. Xia, L. Mädler and N. Li, *Science*, 2006, **311**, 622–627.
12 D. Losic and S. Simovic, *Expert Opin. Drug Delivery*, 2009, **6**, 1363–1381.
13 M. Sinn Aw, M. Kurian and D. Losic, *Biomater. Sci.*, 2014, **2**, 10–34.
14 B. Chertok, M. J. Webber, M. D. Succi and R. Langer, *Mol. Pharmaceutics*, 2013, **10**, 3531–3543.

15 A. Gabizon, H. Shmeeda and Y. Barenholz, *Clin. Pharmacokinet.*, 2003, **42**, 419–436.
16 P. Ma and R. J. Mumper, *Nano Today*, 2013, **8**, 313–331.
17 P. van Hoogevest, X. Liu and A. Fahr, *Expert Opin. Drug Delivery*, 2011, **8**, 1481–1500.
18 P. Borst, R. Evers, M. Kool and J. Wijnholds, *JNCI, J. Natl. Cancer Inst.*, 2000, **92**, 1295–1302.
19 L. M. Thai, A. Labrinidis, S. Hay, V. Liapis, S. Bouralexis, K. Welldon, B. J. Coventry, D. M. Findlay and A. Evdokiou, *Cancer Res.*, 2006, **66**, 5363–5370.
20 R. K. Jain and T. Stylianopoulos, *Nat. Rev. Clin. Oncol.*, 2010, **7**, 653–664.
21 M. Auerbach and H. Ballard*ASH Education Program Book*, 2010, pp. 338–347.
22 P. Marrack, A. S. McKee and M. W. Munks, *Nat. Rev. Immunol.*, 2009, **9**, 287–293.
23 F. Ehmann, K. Sakai-Kato, R. Duncan, D. H. Pérez de la Ossa, R. Pita, J.-M. Vidal, A. Kohli, L. Tothfalusi, A. Sanh, S. Tinton, J.-L. Robert, B. Silva Lima and M. P. Amati, *Nanomedicine*, 2013, **8**, 849–856.
24 Y. Barenholz, *J. Controlled Release*, 2012, **160**, 117–134.
25 J. Cui, M. P. van Koeverden, M. Müllner, K. Kempe and F. Caruso, *Adv. Colloid Interface Sci.*, 2014, **207**, 14–31.
26 H. Alhmoud, B. Delalat, R. Elnathan, A. Cifuentes-Rius, A. Chaix, M.-L. Rogers, J.-O. Durand and N. H. Voelcker, *Adv. Funct. Mater.*, 2015, **25**, 1137–1145.
27 E.-K. Lim, T. Kim, S. Paik, S. Haam, Y.-M. Huh and K. Lee, *Chem. Rev.*, 2015, **115**, 327–394.
28 J. D. Heidel and M. E. Davis, *Pharm. Res.*, 2011, **28**, 187–199.
29 M. Srinivasarao, C. V. Galliford and P. S. Low, *Nat. Rev. Drug Discovery*, 2015, **14**, 203–219.
30 J. Hrkach, D. Von Hoff, M. M. Ali, E. Andrianova, J. Auer, T. Campbell, D. De Witt, M. Figa, M. Figueiredo, A. Horhota, S. Low, K. McDonnell, E. Peeke, B. Retnarajan, A. Sabnis, E. Schnipper, J. J. Song, Y. H. Song, J. Summa, D. Tompsett, G. Troiano, T. Van Geen Hoven, J. Wright, P. LoRusso, P. W. Kantoff, N. H. Bander, C. Sweeney, O. C. Farokhzad, R. Langer and S. Zale, *Sci. Transl. Med.*, 2012, **4**, 128ra139.
31 Y. Matsumura and H. Maeda, *Cancer Res.*, 1986, **46**, 6387–6392.
32 L. E. Gerweck and K. Seetharaman, *Cancer Res.*, 1996, **56**, 1194–1198.
33 Y. Yan, G. K. Such, A. P. R. Johnston, J. P. Best and F. Caruso, *ACS Nano*, 2012, **6**, 3663–3669.
34 W. Liang and J. K. W. Lam, *Endosomal Escape Pathways for Non-Viral Nucleic Acid Delivery Systems*, INTECH Open Access Publisher, 2012, pp. 421–467.
35 R. Misra, S. Acharya and S. K. Sahoo, *Drug Discovery Today*, 2010, **15**, 842–850.
36 J. G. Huang, T. Leshuk and F. X. Gu, *Nano Today*, 2011, **6**, 478–492.
37 D. Luo and W. M. Saltzman, *Nat. Biotechnol.*, 2000, **18**, 33–37.
38 Z. J. Deng, S. W. Morton, E. Ben-Akiva, E. C. Dreaden, K. E. Shopsowitz and P. T. Hammond, *ACS Nano*, 2013, **7**, 9571–9584.
39 A. M. Derfus, W. C. W. Chan and S. N. Bhatia, *Adv. Mater.*, 2004, **16**, 961–966.
40 N. Panté and M. Kann, *Mol. Biol. Cell*, 2002, **13**, 425–434.
41 A. Hoshino, K. Fujioka, T. Oku, S. Nakamura, M. Suga, Y. Yamaguchi, K. Suzuki, M. Yasuhara and K. Yamamoto, *Microbiol. Immunol.*, 2004, **48**, 985–994.
42 B. Kang, M. A. Mackey and M. A. El-Sayed, *J. Am. Chem. Soc.*, 2010, **132**, 1517–1519.
43 S. V. Boddapati, G. G. M. D'Souza, S. Erdogan, V. P. Torchilin and V. Weissig, *Nano Lett.*, 2008, **8**, 2559–2563.
44 K. Matsuo, T. Yoshikawa, A. Oda, T. Akagi, M. Akashi, Y. Mukai, Y. Yoshioka, N. Okada and S. Nakagawa, *Biochem. Biophys. Res. Commun.*, 2007, **362**, 1069–1072.
45 S. W. Morton, M. J. Lee, Z. J. Deng, E. C. Dreaden, E. Siouve, K. E. Shopsowitz, N. J. Shah, M. B. Yaffe and P. T. Hammond, *Sci. Signaling*, 2014, **7**, 44.
46 D. C. Rubinsztein, P. Codogno and B. Levine, *Nat. Rev. Drug Discovery*, 2012, **11**, 709–730.
47 C. Riganti, C. Voena, J. Kopecka, P. A. Corsetto, G. Montorfano, E. Enrico, C. Costamagna, A. M. Rizzo, D. Ghigo and A. Bosia, *Mol. Pharmaceutics*, 2011, **8**, 683–700.
48 Y. Chen, S. R. Bathula, J. Li and L. Huang, *J. Biol. Chem.*, 2010, **285**, 22639–22650.
49 R. Krishna and L. D. Mayer, *Cancer Res.*, 1997, **57**, 5246–5253.
50 J. Shen, Q. He, Y. Gao, J. Shi and Y. Li, *Nanoscale*, 2011, **3**, 4314–4322.
51 Y.-J. Gu, J. Cheng, C. W.-Y. Man, W.-T. Wong and S. H. Cheng, *Nanomedicine*, 2012, **8**, 204–211.
52 F. Wang, Y.-C. Wang, S. Dou, M.-H. Xiong, T.-M. Sun and J. Wang, *ACS Nano*, 2011, **5**, 3679–3692.
53 N. Hardy, H. M. Viola, V. P. A. Johnstone, T. D. Clemons, H. Cserne Szappanos, R. Singh, N. M. Smith, K. S. Iyer and L. C. Hool, *ACS Nano*, 2015, **9**, 279–289.
54 S. Mura, J. Nicolas and P. Couvreur, *Nat. Mater.*, 2013, **12**, 991–1003.
55 Y. Yamada, H. Akita, H. Kamiya, K. Kogure, T. Yamamoto, Y. Shinohara, K. Yamashita, H. Kobayashi, H. Kikuchi and H. Harashima, *Biochim. Biophys. Acta, Biomembr.*, 2008, **1778**, 423–432.
56 G.-E. Costin, M. Trif, N. Nichita, R. A. Dwek and S. M. Petrescu, *Biochem. Biophys. Res. Commun.*, 2002, **293**, 918–923.
57 H. Sneh-Edri, D. Likhtenshtein and D. Stepensky, *Mol. Pharmaceutics*, 2011, **8**, 1266–1275.
58 S.-Y. Sun, L. M. Rosenberg, X. Wang, Z. Zhou, P. Yue, H. Fu and F. R. Khuri, *Cancer Res.*, 2005, **65**, 7052–7058.
59 S. S. Bale, S. J. Kwon, D. A. Shah, A. Banerjee, J. S. Dordick and R. S. Kane, *ACS Nano*, 2010, **4**, 1493–1500.
60 E. Blanco, T. Sangai, S. Wu, A. Hsiao, G. U. Ruiz-Esparza, C. A. Gonzalez-Delgado, F. E. Cara, S. Granados-Principal, K. W. Evans, A. Akcakanat, Y. Wang, K.-A. Do, F. Meric-Bernstam and M. Ferrari, *Mol. Ther.*, 2014, **22**, 1310–1319.
61 A. S. Dhillon, S. Hagan, O. Rath and W. Kolch, *Oncogene*, 2007, **26**, 3279–3290.

62 S. V. Sharma, D. W. Bell, J. Settleman and D. A. Haber, *Nat. Rev. Cancer*, 2007, **7**, 169–181.

63 S. Basu, R. Harfouche, S. Soni, G. Chimote, R. A. Mashelkar and S. Sengupta, *Proc. Natl. Acad. Sci. U. S. A.*, 2009, **106**, 7957–7961.

64 M. J. Lee, A. S. Ye, A. K. Gardino, A. M. Heijink, P. K. Sorger, G. MacBeath and M. B. Yaffe, *Cell*, 2012, **149**, 780–794.

65 D. A. Shah, S.-J. Kwon, S. S. Bale, A. Banerjee, J. S. Dordick and R. S. Kane, *Biomaterials*, 2011, **32**, 3210–3219.

66 H. Clevers and R. Nusse, *Cell*, 2012, **149**, 1192–1205.

67 S. Frame and P. Cohen, *Biochem. J.*, 2001, **359**, 1–16.

68 D. Cirstea, T. Hideshima, S. Rodig, L. Santo, S. Pozzi, S. Vallet, H. Ikeda, G. Perrone, G. Gorgun, K. Patel, N. Desai, P. Sportelli, S. Kapoor, S. Vali, S. Mukherjee, N. C. Munshi, K. C. Anderson and N. Raje, *Mol. Cancer Ther.*, 2010, **9**, 963–975.

69 R. Harfouche, S. Basu, S. Soni, D. Hentschel, R. Mashelkar and S. Sengupta, *Angiogenesis*, 2009, **12**, 325–338.

70 S. K. Kim and L. Huang, *J. Controlled Release*, 2012, **157**, 279–286.

71 D. Zheng, D. A. Giljohann, D. L. Chen, M. D. Massich, X.-Q. Wang, H. Iordanov, C. A. Mirkin and A. S. Paller, *Proc. Natl. Acad. Sci. U. S. A.*, 2012, **109**, 11975–11980.

72 Y. Chen, X. Zhu, X. Zhang, B. Liu and L. Huang, *Mol. Ther.*, 2010, **18**, 1650–1656.

73 S. Kang, H.-J. Cho, G. Shim, S. Lee, S.-H. Kim, H.-G. Choi, C.-W. Kim and Y.-K. Oh, *Pharm. Res.*, 2011, **28**, 3069–3078.

74 P. Ruenraroengsak, J. M. Cook and A. T. Florence, *J. Controlled Release*, 2010, **141**, 265–276.

75 S. M. Sagnella, J. A. McCarroll and M. Kavallaris, *Nanomedicine*, 2014, **10**, 1131–1137.

76 J. Folkman, *Annu. Rev. Med.*, 2006, **57**, 1–18.

77 E. Ruoslahti, S. N. Bhatia and M. J. Sailor, *J. Cell Biol.*, 2010, **188**, 759–768.

78 D. Neri and R. Bicknell, *Nat. Rev. Cancer*, 2005, **5**, 436–446.

79 N. Ferrara, *Nat. Rev. Cancer*, 2002, **2**, 795–803.

80 K. Chen, Z.-B. Li, H. Wang, W. Cai and X. Chen, *Eur. J. Nucl. Med. Mol. Imaging*, 2008, **35**, 2235–2244.

81 W. Arap, R. Pasqualini and E. Ruoslahti, *Science*, 1998, **279**, 377–380.

82 M. E. Åkerman, W. C. W. Chan, P. Laakkonen, S. N. Bhatia and E. Ruoslahti, *Proc. Natl. Acad. Sci. U. S. A.*, 2002, **99**, 12617–12621.

83 W. Cai and X. Chen, *Nat. Protoc.*, 2008, **3**, 89–96.

84 Z. Liu, W. Cai, L. He, N. Nakayama, K. Chen, X. Sun, X. Chen and H. Dai, *Nat. Nanotechnol.*, 2007, **2**, 47–52.

85 H. Hong, J. Shi, Y. Yang, Y. Zhang, J. W. Engle, R. J. Nickles, X. Wang and W. Cai, *Nano Lett.*, 2011, **11**, 3744–3750.

86 H.-Y. Lee, Z. Li, K. Chen, A. R. Hsu, C. Xu, J. Xie, S. Sun and X. Chen, *J. Nucl. Med.*, 2008, **49**, 1371–1379.

87 Y. Xiao, H. Hong, V. Z. Matson, A. Javadi, W. Xu, Y. Yang, Y. Zhang, J. W. Engle, R. J. Nickles and W. Cai, *Theranostics*, 2012, **2**, 757.

88 A. Almutairi, R. Rossin, M. Shokeen, A. Hagooly, A. Ananth, B. Capoccia, S. Guillaudeu, D. Abendschein, C. J. Anderson, M. J. Welch and J. M. J. Fréchet, *Proc. Natl. Acad. Sci. U. S. A.*, 2009, **106**, 685–690.

89 K. Huang, H. Ma, J. Liu, S. Huo, A. Kumar, T. Wei, X. Zhang, S. Jin, Y. Gan, P. C. Wang, S. He, X. Zhang and X.-J. Liang, *ACS Nano*, 2012, **6**, 4483–4493.

90 T. Lammers, F. Kiessling, W. E. Hennink and G. Storm, *J. Controlled Release*, 2012, **161**, 175–187.

91 C. Wong, T. Stylianopoulos, J. Cui, J. Martin, V. P. Chauhan, W. Jiang, Z. Popović, R. K. Jain, M. G. Bawendi and D. Fukumura, *Proc. Natl. Acad. Sci. U. S. A.*, 2011, **108**, 2426–2431.

92 G. Oberdörster, E. Oberdörster and J. Oberdörster, *Environ. Health Perspect.*, 2005, **113**, 823–839.

93 H. F. Krug and P. Wick, *Angew. Chem., Int. Ed.*, 2011, **50**, 1260–1278.

94 A. Nel, T. Xia, H. Meng, X. Wang, S. Lin, Z. Ji and H. Zhang, *Acc. Chem. Res.*, 2012, **46**, 607–621.

95 R. Coradeghini, S. Gioria, C. P. García, P. Nativo, F. Franchini, D. Gilliland, J. Ponti and F. Rossi, *Toxicol. Lett.*, 2013, **217**, 205–216.

96 D. B. Warheit, T. R. Webb, C. M. Sayes, V. L. Colvin and K. L. Reed, *Toxicol. Sci.*, 2006, **91**, 227–236.

97 R. Wottrich, S. Diabaté and H. F. Krug, *Int. J. Hyg. Environ. Health*, 2004, **207**, 353–361.

98 S. K. Sohaebuddin, P. T. Thevenot, D. Baker, J. W. Eaton and L. Tang, *Part. Fibre Toxicol.*, 2010, **7**, 22.

99 T. Yu, K. Greish, L. D. McGill, A. Ray and H. Ghandehari, *ACS Nano*, 2012, **6**, 2289–2301.

100 S. E. A. Gratton, P. A. Ropp, P. D. Pohlhaus, J. C. Luft, V. J. Madden, M. E. Napier and J. M. DeSimone, *Proc. Natl. Acad. Sci. U. S. A.*, 2008, **105**, 11613–11618.

101 M. Safi, M. Yan, M.-A. Guedeau-Boudeville, H. Conjeaud, V. Garnier-Thibaud, N. Boggetto, A. Baeza-Squiban, F. Niedergang, D. Averbeck and J.-F. Berret, *ACS Nano*, 2011, **5**, 5354–5364.

102 Y. Wang, G. Kaur, A. Zysk, V. Liapis, S. Hay, A. Santos, D. Losic and A. Evdokiou, *Biomaterials*, 2015, **46**, 117–130.

103 Y. Wang, A. Santos, G. Kaur, A. Evdokiou and D. Losic, *Biomaterials*, 2014, **35**, 5517–5526.

104 Z. Ji, X. Wang, H. Zhang, S. Lin, H. Meng, B. Sun, S. George, T. Xia, A. E. Nel and J. I. Zink, *ACS Nano*, 2012, **6**, 5366–5380.

105 A. M. Alkilany, P. K. Nagaria, C. R. Hexel, T. J. Shaw, C. J. Murphy and M. D. Wyatt, *Small*, 2009, **5**, 701–708.

106 J. R. Roberts, R. R. Mercer, R. S. Chapman, G. M. Cohen, S. Bangsaruntip, D. Schwegler-Berry, J. F. Scabilloni, V. Castranova, J. M. Antonini and S. S. Leonard, *J. Nanomater.*, 2012, **2012**, 2.

107 C. A. Poland, F. Byrne, W.-S. Cho, A. Prina-Mello, F. A. Murphy, G. L. Davies, J. M. D. Coey, Y. Gounko, R. Duffin, Y. Volkov and K. Donaldson, *Nanotoxicology*, 2012, **6**, 899–911.

108 A. Schinwald and K. Donaldson, *Part. Fibre Toxicol.*, 2012, **9**, 34.

109 T. Xia, M. Kovochich, M. Liong, L. Mädler, B. Gilbert, H. Shi, J. I. Yeh, J. I. Zink and A. E. Nel, *ACS Nano*, 2008, **2**, 2121–2134.

110 J. Cui, R. De Rose, K. Alt, S. Alcantara, B. M. Paterson, K. Liang, M. Hu, J. J. Richardson, Y. Yan, C. M. Jeffery, R. I. Price, K. Peter, C. E. Hagemeyer, P. S. Donnelly, S. J. Kent and F. Caruso, *ACS Nano*, 2015, **9**, 1571–1580.
111 L. Wu, Y. Zhang, C. Zhang, X. Cui, S. Zhai, Y. Liu, C. Li, H. Zhu, G. Qu, G. Jiang and B. Yan, *ACS Nano*, 2014, **8**, 2087–2099.
112 R. Tang, D. F. Moyano, C. Subramani, B. Yan, E. Jeoung, G. Y. Tonga, B. Duncan, Y.-C. Yeh, Z. Jiang, C. Kim and V. M. Rotello, *Adv. Mater.*, 2014, **26**, 3310–3314.
113 K. H. Müller, J. Kulkarni, M. Motskin, A. Goode, P. Winship, J. N. Skepper, M. P. Ryan and A. E. Porter, *ACS Nano*, 2010, **4**, 6767–6779.
114 Z. Chen, H. Meng, G. Xing, C. Chen, Y. Zhao, G. Jia, T. Wang, H. Yuan, C. Ye, F. Zhao, Z. Chai, C. Zhu, X. Fang, B. Ma and L. Wan, *Toxicol. Lett.*, 2006, **163**, 109–120.
115 P. V. AshaRani, G. Low Kah Mun, M. P. Hande and S. Valiyaveettil, *ACS Nano*, 2009, **3**, 279–290.
116 T. Xia, D. Malasarn, S. Lin, Z. Ji, H. Zhang, R. J. Miller, A. A. Keller, R. M. Nisbet, B. H. Harthorn, H. A. Godwin, H. S. Lenihan, R. Liu, J. Gardea-Torresdey, Y. Cohen, L. Mädler, P. A. Holden, J. I. Zink and A. E. Nel, *Small*, 2013, **9**, 1428–1443.
117 C. Chen, Y.-F. Li, Y. Qu, Z. Chai and Y. Zhao, *Chem. Soc. Rev.*, 2013, **42**, 8266–8303.
118 S. Reuter, S. C. Gupta, M. M. Chaturvedi and B. B. Aggarwal, *Free Radicals Biol. Med.*, 2010, **49**, 1603–1616.
119 I. Fridovich, *Science*, 1978, **201**, 875–880.
120 L. Risom, P. Møller and S. Loft, *Mutat. Res., Fundam. Mol. Mech. Mutagen.*, 2005, **592**, 119–137.
121 L. Gao, J. Zhuang, L. Nie, J. Zhang, Y. Zhang, N. Gu, T. Wang, J. Feng, D. Yang, S. Perrett and X. Yan, *Nat. Nanotechnol.*, 2007, **2**, 577–583.
122 W. He, Y. Liu, J. Yuan, J.-J. Yin, X. Wu, X. Hu, K. Zhang, J. Liu, C. Chen, Y. Ji and Y. Guo, *Biomaterials*, 2011, **32**, 1139–1147.
123 K. Fan, C. Cao, Y. Pan, D. Lu, D. Yang, J. Feng, L. Song, M. Liang and X. Yan, *Nat. Nanotechnol.*, 2012, **7**, 459–464.
124 L. K. Limbach, P. Wick, P. Manser, R. N. Grass, A. Bruinink and W. J. Stark, *Environ. Sci. Technol.*, 2007, **41**, 4158–4163.
125 Y. Pan, A. Leifert, D. Ruau, S. Neuss, J. Bornemann, G. Schmid, W. Brandau, U. Simon and W. Jahnen-Dechent, *Small*, 2009, **5**, 2067–2076.
126 L.-R. Wang, X. Xue, X.-M. Hu, M.-Y. Wei, C.-Q. Zhang, G.-L. Ge and X.-J. Liang, *Small*, 2014, **10**, 2859–2869.
127 P. Wang, X. Nie, Y. Wang, Y. Li, C. Ge, L. Zhang, L. Wang, R. Bai, Z. Chen, Y. Zhao and C. Chen, *Small*, 2013, **9**, 3799–3811.
128 M. O. DeNichilo, V. Panagopoulos, T. E. Rayner, R. A. Borowicz, J. E. Greenwood and A. Evdokiou, *Am. J. Pathol.*, 2015, **185**, 1372–1384.
129 B. Sun, X. Wang, Z. Ji, R. Li and T. Xia, *Small*, 2013, **9**, 1595–1607.
130 K. Donaldson and C. L. Tran, *Inhalation Toxicol.*, 2002, **14**, 5–27.
131 G.-Y. Chen, H.-J. Yang, C.-H. Lu, Y.-C. Chao, S.-M. Hwang, C.-L. Chen, K.-W. Lo, L.-Y. Sung, W.-Y. Luo, H.-Y. Tuan and Y.-C. Hu, *Biomaterials*, 2012, **33**, 6559–6569.
132 M. A. Dobrovolskaia and S. E. McNeil, *Nat. Nanotechnol.*, 2007, **2**, 469–478.
133 X. Wang, S. P. Reece and J. M. Brown, *Toxicol. Mech. Methods*, 2013, **23**, 168–177.
134 M. A. Dobrovolskaia, D. R. Germolec and J. L. Weaver, *Nat. Nanotechnol.*, 2009, **4**, 411–414.
135 C. A. Poland, R. Duffin, I. Kinloch, A. Maynard, W. A. H. Wallace, A. Seaton, V. Stone, S. Brown, W. MacNee and K. Donaldson, *Nat. Nanotechnol.*, 2008, **3**, 423–428.
136 J. P. Ryman-Rasmussen, M. F. Cesta, A. R. Brody, J. K. Shipley-Phillips, J. I. Everitt, E. W. Tewksbury, O. R. Moss, B. A. Wong, D. E. Dodd, M. E. Andersen and J. C. Bonner, *Nat. Nanotechnol.*, 2009, **4**, 747–751.
137 N. Singh, B. Manshian, G. J. S. Jenkins, S. M. Griffiths, P. M. Williams, T. G. G. Maffeis, C. J. Wright and S. H. Doak, *Biomaterials*, 2009, **30**, 3891–3914.
138 Z. Magdolenova, A. Collins, A. Kumar, A. Dhawan, V. Stone and M. Dusinska, *Nanotoxicology*, 2014, **8**, 233–278.
139 N. Golbamaki, B. Rasulev, A. Cassano, R. L. Marchese Robinson, E. Benfenati, J. Leszczynski and M. T. D. Cronin, *Nanoscale*, 2015, **7**, 2154–2198.
140 L. Gonzalez, D. Lison and M. Kirsch-Volders, *Nanotoxicology*, 2008, **2**, 252–273.
141 A. Folick, H. D. Oakley, Y. Yu, E. H. Armstrong, M. Kumari, L. Sanor, D. D. Moore, E. A. Ortlund, R. Zechner and M. C. Wang, *Science*, 2015, **347**, 83–86.
142 W. Fiers, R. Beyaert, W. Declercq and P. Vandenabeele, *Oncogene*, 1999, **18**, 7719–7730.
143 P. Boya and G. Kroemer, *Oncogene*, 2008, **27**, 6434–6451.
144 A. H. Ringwood, N. Levi-Polyachenko and D. L. Carroll, *Environ. Sci. Technol.*, 2009, **43**, 7136–7141.
145 X. Ma, Y. Wu, S. Jin, Y. Tian, X. Zhang, Y. Zhao, L. Yu and X.-J. Liang, *ACS Nano*, 2011, **5**, 8629–8639.
146 W.-S. Cho, R. Duffin, S. E. M. Howie, C. J. Scotton, W. A. H. Wallace, W. Macnee, M. Bradley, I. L. Megson and K. Donaldson, *Part. Fibre Toxicol.*, 2011, **8**, 27.
147 C. Loos, T. Syrovets, A. Musyanovych, V. Mailänder, K. Landfester and T. Simmet, *Biomaterials*, 2014, **35**, 1944–1953.
148 F. T. Andón and B. Fadeel, *Acc. Chem. Res.*, 2012, **46**, 733–742.
149 I. Kim, W. Xu and J. C. Reed, *Nat. Rev. Drug Discovery*, 2008, **7**, 1013–1030.
150 S. Stern, P. Adiseshaiah and R. Crist, *Part. Fibre Toxicol.*, 2012, **9**, 20.
151 M. I. Khan, A. Mohammad, G. Patil, S. A. H. Naqvi, L. K. S. Chauhan and I. Ahmad, *Biomaterials*, 2012, **33**, 1477–1488.
152 Y.-Y. Tsai, Y.-H. Huang, Y.-L. Chao, K.-Y. Hu, L.-T. Chin, S.-H. Chou, A.-L. Hour, Y.-D. Yao, C.-S. Tu, Y.-J. Liang, C.-Y. Tsai, H.-Y. Wu, S.-W. Tan and H.-M. Chen, *ACS Nano*, 2011, **5**, 9354–9369.
153 R. A. Firestone, J. M. Pisano and R. J. Bonney, *J. Med. Chem.*, 1979, **22**, 1130–1133.

154 B. Levine, N. Mizushima and H. W. Virgin, *Nature*, 2011, **469**, 323–335.
155 K. Peynshaert, B. B. Manshian, F. Joris, K. Braeckmans, S. C. De Smedt, J. Demeester and S. J. Soenen, *Chem. Rev.*, 2014, **114**, 7581–7609.
156 M. C. Maiuri, E. Zalckvar, A. Kimchi and G. Kroemer, *Nat. Rev. Mol. Cell Biol.*, 2007, **8**, 741–752.
157 L. Chen, Y. Miao, L. Chen, P. Jin, Y. Zha, Y. Chai, F. Zheng, Y. Zhang, W. Zhou, J. Zhang, L. Wen and M. Wang, *Biomaterials*, 2013, **34**, 10172–10181.
158 A. B. Djurišić, Y. H. Leung, A. M. C. Ng, X. Y. Xu, P. K. H. Lee, N. Degger and R. S. S. Wu, *Small*, 2015, **11**, 26–44.
159 T. Xia, M. Kovochich, J. Brant, M. Hotze, J. Sempf, T. Oberley, C. Sioutas, J. I. Yeh, M. R. Wiesner and A. E. Nel, *Nano Lett.*, 2006, **6**, 1794–1807.
160 H. Meng, T. Xia, S. George and A. E. Nel, *ACS Nano*, 2009, **3**, 1620–1627.
161 Y. Tahara, M. Nakamura, M. Yang, M. Zhang, S. Iijima and M. Yudasaka, *Biomaterials*, 2012, **33**, 2762–2769.
162 M. T. Lin and M. F. Beal, *Nature*, 2006, **443**, 787–795.
163 R. Chen, L. Huo, X. Shi, R. Bai, Z. Zhang, Y. Zhao, Y. Chang and C. Chen, *ACS Nano*, 2014, **8**, 2562–2574.
164 Y. Chen and F. Brandizzi, *Trends Cell Biol.*, 2013, **23**, 547–555.
165 J. Wang, X. Fang and W. Liang, *ACS Nano*, 2012, **6**, 5018–5030.
166 E. Panzarini and L. Dini, *Mol. Pharmaceutics*, 2014, **11**(8), 2527–2538.
167 H. Soo Choi, W. Liu, P. Misra, E. Tanaka, J. P. Zimmer, B. Itty Ipe, M. G. Bawendi and J. V. Frangioni, *Nat. Biotechnol.*, 2007, **25**, 1165–1170.
168 H. S. Choi, Y. Ashitate, J. H. Lee, S. H. Kim, A. Matsui, N. Insin, M. G. Bawendi, M. Semmler-Behnke, J. V. Frangioni and A. Tsuda, *Nat. Biotechnol.*, 2010, **28**, 1300–1303.
169 J. K. Pokorski and N. F. Steinmetz, *Mol. Pharmaceutics*, 2011, **8**, 29–43.
170 Z. Liu, X. Sun, N. Nakayama-Ratchford and H. Dai, *ACS Nano*, 2007, **1**, 50–56.
171 Z. Liu, J. T. Robinson, X. M. Sun and H. J. Dai, *J. Am. Chem. Soc.*, 2008, **130**, 10876–10877.
172 X. M. Sun, Z. Liu, K. Welsher, J. T. Robinson, A. Goodwin, S. Zaric and H. J. Dai, *Nano Res.*, 2008, **1**, 203–212.
173 G. Gollavelli and Y. C. Ling, *Biomaterials*, 2012, **33**, 2532–2545.
174 Y. J. Lu, H. W. Yang, S. C. Hung, C. Y. Huang, S. M. Li, C. C. M. Ma, P. Y. Chen, H. C. Tsai, K. C. Wei and J. P. Chen, *Int. J. Nanomed.*, 2012, **7**, 1737–1747.
175 L. M. Zhang, Z. X. Lu, Q. H. Zhao, J. Huang, H. Shen and Z. J. Zhang, *Small*, 2011, **7**, 460–464.
176 B. A. Chen, M. Liu, L. M. Zhang, J. Huang, J. L. Yao and Z. J. Zhang, *J. Mater. Chem.*, 2011, **21**, 7736–7741.
177 Y. Liu, D.-C. Wu, W.-D. Zhang, X. Jiang, C.-B. He, T. S. Chung, S. H. Goh and K. W. Leong, *Angew. Chem.*, 2005, **117**, 4860–4863.
178 Y. Z. Pan, H. Q. Bao, N. G. Sahoo, T. F. Wu and L. Li, *Adv. Funct. Mater.*, 2011, **21**, 2754–2763.
179 V. K. Rana, M. C. Choi, J. Y. Kong, G. Y. Kim, M. J. Kim, S. H. Kim, S. Mishra, R. P. Singh and C. S. Ha, *Macromol. Mater. Eng.*, 2011, **296**, 131–140.
180 H. Q. Bao, Y. Z. Pan, Y. Ping, N. G. Sahoo, T. F. Wu, L. Li, J. Li and L. H. Gan, *Small*, 2011, **7**, 1569–1578.
181 D. Depan, J. Shah and R. D. K. Misra, *Mater. Sci. Eng., C*, 2011, **31**, 1305–1312.
182 J. Shen, M. Shi, N. Li, B. Yan, H. Ma, Y. Hu and M. Ye, *Nano Res.*, 2010, **3**, 339–349.
183 M. C. Duch, G. R. S. Budinger, Y. T. Liang, S. Soberanes, D. Urich, S. E. Chiarella, L. A. Campochiaro, A. Gonzalez, N. S. Chandel and M. C. Hersam, *Nano Lett.*, 2011, **11**, 5201–5207.
184 L. Feng, S. Zhang and Z. Liu, *Nanoscale*, 2011, **3**, 1252–1257.
185 W. Hu, C. Peng, M. Lv, X. Li, Y. Zhang, N. Chen, C. Fan and Q. Huang, *ACS Nano*, 2011, **5**, 3693–3700.
186 X. T. Zheng and C. M. Li, *Mol. Pharmaceutics*, 2012, **9**, 615–621.
187 X. Huang, X. Qi, F. Boey and H. Zhang, *Chem. Soc. Rev.*, 2012, **41**, 666–686.
188 W. Chen, P. Yi, Y. Zhang, L. Zhang, Z. Deng and Z. Zhang, *ACS Appl. Mater. Interfaces*, 2011, **3**, 4085–4091.
189 X. Y. Yang, X. Y. Zhang, Y. F. Ma, Y. Huang, Y. S. Wang and Y. S. Chen, *J. Mater. Chem.*, 2009, **19**, 2710–2714.
190 F. Madeo, N. Tavernarakis and G. Kroemer, *Nat. Cell Biol.*, 2010, **12**, 842–846.
191 L. Chen, B. Zhang and M. Toborek, *Nanomedicine*, 2013, **9**, 212–221.
192 Z. J. Yang, C. E. Chee, S. Huang and F. A. Sinicrope, *Mol. Cancer Ther.*, 2011, **10**, 1533–1541.
193 X. Zhang, Y. Dong, X. Zeng, X. Liang, X. Li, W. Tao, H. Chen, Y. Jiang, L. Mei and S.-S. Feng, *Biomaterials*, 2014, **35**, 1932–1943.
194 Y. Lu, L. Zhang, J. Li, Y.-D. Su, Y. Liu, Y.-J. Xu, L. Dong, H.-L. Gao, J. Lin, N. Man, P.-F. Wei, W.-P. Xu, S.-H. Yu and L.-P. Wen, *Adv. Funct. Mater.*, 2013, **23**, 1534–1546.
195 X. Zhang, X. Zeng, X. Liang, Y. Yang, X. Li, H. Chen, L. Huang, L. Mei and S.-S. Feng, *Biomaterials*, 2014, **35**, 9144–9154.
196 G.-Y. Chen, C.-L. Chen, H.-Y. Tuan, P.-X. Yuan, K.-C. Li, H.-J. Yang and Y.-C. Hu, *Adv. Healthcare Mater.*, 2014, **3**, 1486–1495.
197 Y. Li, L.-X. Wang, G. Yang, F. Hao, W. J. Urba and H.-M. Hu, *Cancer Res.*, 2008, **68**, 6889–6895.
198 L. English, M. Chemali, J. Duron, C. Rondeau, A. Laplante, D. Gingras, D. Alexander, D. Leib, C. Norbury, R. Lippe and M. Desjardins, *Nat. Immunol.*, 2009, **10**, 480–487.
199 H. Li, Y. Li, J. Jiao and H.-M. Hu, *Nat. Nanotechnol.*, 2011, **6**, 645–650.
200 D. J. Irvine, M. A. Swartz and G. L. Szeto, *Nat. Mater.*, 2013, **12**, 978–990.
201 M. A. Swartz, S. Hirosue and J. A. Hubbell, *Sci. Transl. Med.*, 2012, **4**, 148rv149.

202 E. S. Trombetta and I. Mellman, *Annu. Rev. Immunol.*, 2005, **23**, 975–1028.
203 C. Sheridan, *Nat. Biotechnol.*, 2012, **30**, 471–473.
204 H. Huang, S. Delikanli, H. Zeng, D. M. Ferkey and A. Pralle, *Nat. Nanotechnol.*, 2010, **5**, 602–606.
205 S. A. Stanley, J. E. Gagner, S. Damanpour, M. Yoshida, J. S. Dordick and J. M. Friedman, *Science*, 2012, **336**, 604–608.
206 S. A. Stanley, J. Sauer, R. S. Kane, J. S. Dordick and J. M. Friedman, *Nat. Med.*, 2015, **21**, 92–98.
207 S. J. Soenen, W. J. Parak, J. Rejman and B. Manshian, *Chem. Rev.*, 2015, **115**, 2109–2135.
208 R. P. Singh and P. Ramarao, *Toxicol. Sci.*, 2013, **136**, 131–143.
209 H. Lv, S. Zhang, B. Wang, S. Cui and J. Yan, *J. Controlled Release*, 2006, **114**, 100–109.
210 J. C. Sunshine, D. Y. Peng and J. J. Green, *Mol. Pharmaceutics*, 2012, **9**, 3375–3383.
211 X. Gao, L. Yao, Q. Song, L. Zhu, Z. Xia, H. Xia, X. Jiang, J. Chen and H. Chen, *Biomaterials*, 2011, **32**, 8613–8625.
212 S. K. Samal, M. Dash, S. Van Vlierberghe, D. L. Kaplan, E. Chiellini, C. van Blitterswijk, L. Moroni and P. Dubruel, *Chem. Soc. Rev.*, 2012, **41**, 7147–7194.
213 F. Alexis, E. Pridgen, L. K. Molnar and O. C. Farokhzad, *Mol. Pharmaceutics*, 2008, **5**, 505–515.
214 M. Longmire, P. L. Choyke and H. Kobayashi, *Nanomedicine*, 2008, **3**, 703–717.
215 M. P. Monopoli, C. Aberg, A. Salvati and K. A. Dawson, *Nat. Nanotechnol.*, 2012, **7**, 779–786.
216 T. Cedervall, I. Lynch, S. Lindman, T. Berggård, E. Thulin, H. Nilsson, K. A. Dawson and S. Linse, *Proc. Natl. Acad. Sci. U. S. A.*, 2007, **104**, 2050–2055.
217 C. Gunawan, M. Lim, C. P. Marquis and R. Amal, *J. Mater. Chem. B*, 2014, **2**, 2060–2083.
218 C. Chen, Y.-F. Li, Y. Qu, Z. Chai and Y. Zhao, *Chem. Soc. Rev.*, 2013, **42**, 8266–8303.
219 C. Ge, J. Du, L. Zhao, L. Wang, Y. Liu, D. Li, Y. Yang, R. Zhou, Y. Zhao, Z. Chai and C. Chen, *Proc. Natl. Acad. Sci. U. S. A.*, 2011, **108**, 16968–16973.
220 S. Wan, P. M. Kelly, E. Mahon, H. Stöckmann, P. M. Rudd, F. Caruso, K. A. Dawson, Y. Yan and M. P. Monopoli, *ACS Nano*, 2015, **9**, 2157–2166.
221 R. Gref, M. Lück, P. Quellec, M. Marchand, E. Dellacherie, S. Harnisch, T. Blunk and R. H. Müller, *Colloids Surf., B*, 2000, **18**, 301–313.
222 C. D. Walkey, J. B. Olsen, H. Guo, A. Emili and W. C. W. Chan, *J. Am. Chem. Soc.*, 2012, **134**, 2139–2147.
223 K. L. Lee, S. Shukla, M. Wu, N. R. Ayat, C. E. El Sanadi, A. M. Wen, J. F. Edelbrock, J. K. Pokorski, U. Commandeur, G. R. Dubyak and N. F. Steinmetz, *Acta Biomater.*, 2015, **19**, 166–179.
224 K. Knop, R. Hoogenboom, D. Fischer and U. S. Schubert, *Angew. Chem., Int. Ed.*, 2010, **49**, 6288–6308.

1.3 Thesis outline

The aim of this thesis is to structurally engineering anodic aluminium oxide (AAO), and to fabricate a new nanomaterial, so-called anodic alumina nanotubes (AANTs) for the study of drug delivery and nanotoxicity. The scheme of the thesis structure is shown in **Figure 1**.

(1) In **chapter 3**, in-depth mechanistic studies of pulse anodization (i.e. potentiostatic and galvanostatic pulse anodization) were conducted for the fabrication of advanced anodic aluminium oxide (AAO) nanostructures, including AANTs and AAO-microcavities. These studies enabled an improved understanding of structurally engineering AAO by pulse anodization. Importantly, these fundamental nanofabrication studies allow the feasible fabrication of AANTs with different aspect ratio, paving the way for the following nanotoxicity and drug delivery study.

(2) A systematic *in vitro* nanotoxicity study of high aspect ratio AANTs was performed in **chapter 4**. This is the first toxicological study of AANTs, which characterized seven criteria of toxic paradigms of AANTs with different aspect ratio ranging from 7.8 to 63.3. These results highlighted the aspect ratio-associated nanotoxicity paradigm as well as the methodologies of using high-throughput toxicological screening platform for nanotoxicity studies.

(3) In **chapter 5**, AANTs were used as drug carriers to deliver a pro-apoptotic receptor agonist, tumor necrosis factor-related apoptosis-inducing ligand (Apo2L/TRAIL) for cancer therapy. AANTs showed exceptional drug loading capacity (104 ± 14.4 μg per mg of AANTs) and demonstrated efficient cancer killing *in vitro* due to the apoptosis induction by Apo2L/TRAIL.

(4) To further understand the nanotoxicity mechanism and develop novel therapeutic approach, the effect of autophagy and endoplasmic reticulum (ER) stress on AANTs-associated toxicity was studied in **chapter 6**. Targeting of autophagic and ER stress

signaling networking by using AANTs to deliver drugs (i.e. thapsigargin and 3-Methyladenine) successfully achieved synergistic effect of cancer killing.

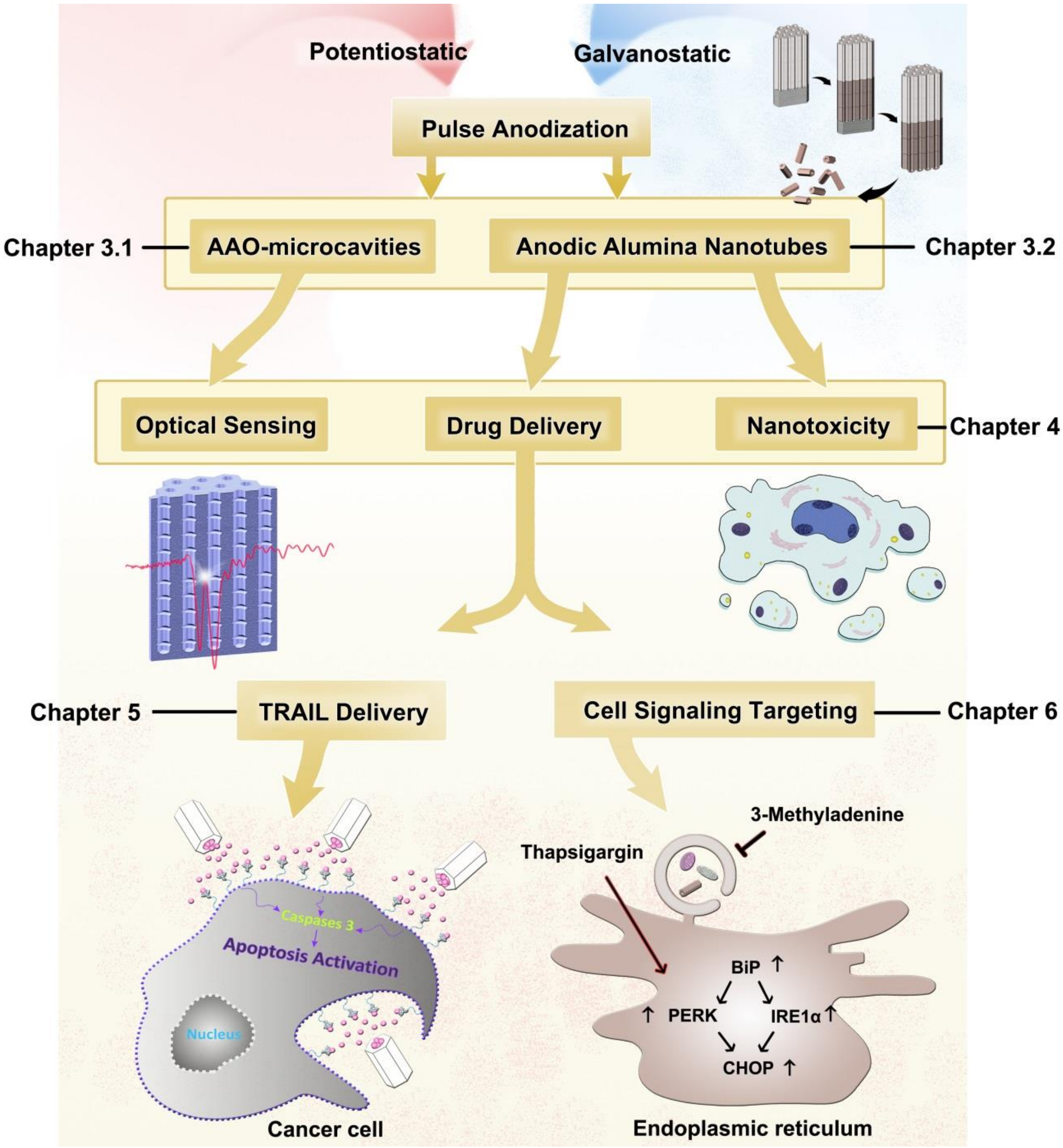

Figure 1 Scheme of the thesis outline. This thesis started with pulse anodization, which consisted of potentiostatic and galvanostatic anodization. Understanding the mechanism of this technique enables the feasible fabrications of AAO-microcavities and AANTs. Then AANTs were used as nanomaterial models for the research of drug delivery and nanotoxicity. In particular, novel cancer therapy concepts were demonstrated in regard to the delivery of TRAIL or cell signaling modulators for efficient cancer targeting and killing.

Chapter 2 Experimental Protocol

Materails/Chemicals

Aluminum (Al) foils of thickness 0.32mm and purity 99.9997% were supplied by Goodfellow Cambridge Ltd. (UK). Sulfuric acid (H_2SO_4), copper(II) chloride ($CuCl_2$), hydrochloric acid (HCl), perchloric acid ($HClO_4$), hydrogen peroxide (H_2O_2), chromium trioxide (CrO_3), paraformaldehyde, Fluorescein isothiocyanate–dextran (average mol wt 70,000), 2′,7′-Dichlorofluorescein diacetate, 4',6-diamidino-2-phenylindole ($C_{16}H_{15}N_5$ – DAPI) and Alizarin Red S were purchased from Sigma-Aldrich (Australia). PE annexin V apoptosis detection kit, JC 1 detection kit and TNF-α ELISA detection set were purchased from BD science. Western blot antibodies were purchased from Cell Signaling. Dulbecco's modified Eagle's medium, RPMI 1640 media, fetal calf serum (FCS), penicillin/streptomycin, and glutamine were purchased from Biosciences (Australia). Trypsin (Gibco); phosphate buffer solution (PBS) (HyClone Laboratories, Inc); Culture flasks, 96-well plate, 24-well plate and 6-well plate (greiner Bio-One); 8-well glass chamber slide (Thermo Fisher); AlamarBlue® and ER-Tracker Blue-White DPX (Life Technologies Corporation); Ultrapure water Option Q–Purelabs (Australia) was used for preparation of all the relevant solutions.

Anodization: Anodization was conducted with a customer-designed setup as described in literature.[1] (**Scheme 1**) Briefly, Al chip was in contact with a copper plate used as anode, and platinum wire was used as cathode. The copper plate was connected with a powerful cooling stage in order to maintain the electrolyte temperature. The surface area of Al exposure to the electrolyte was confined by a window with the size of 0.95 cm^2. During anodization, the electrolyte solution was vigorously stirred to stabilize the reaction. Keithley 2400 / 2612 source-meter unit was used to control the electrochemical parameters via Labview interfaces. To start anodization, Al chips 1.5 cm in diameter were first sonicated in ethanol and ultrapure water. Then, Al chips were electro-polished prior to anodization in a mixture of ethanol and $HClO_4$ 4:1 (v:v) at 20 V and 5 ℃ for 3 min. After electropolishing, surface-finished Al chips were thoroughly washed by deionized water and dried for future use. The fabrication of anodic aluminum oxide (AAO) nanostructures was performed through different anodization technique including mild anodization, hard anodization or pulse anodization. The detailed conditions of material fabrication have been fully addressed in each chapter.

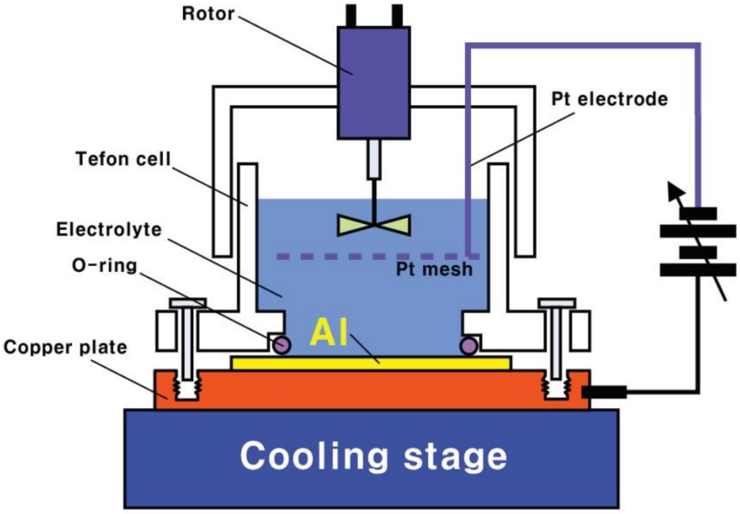

Scheme 1 Schematic illustration of the anodization set-up used in this thesis**.** [1]

Material characterization: Briefly, transmission electron microscope (FEI Tecnai G2 Spirit TEM), field emission gun scanning electron microscope (FEG-SEM FEI Quanta 450), confocal microscope (Leica SP5 spectral scanning confocal microscope), UV-VIS-NIR spectroscopy (Cary 5000, Agilent), thermogravimetric (TGA) analysis (Auto TGA Q500, TA Instruments) and Fourier transform infrared spectroscopy (Spectrum 400 FT-IR Spectrometer, PerkinElmer) were routinely used. ZetaSizer Nano (Malvern Instruments Ltd., Worcestershire, UK) was used for measuring hydrodynamic diameter and zeta-potential of nanomaterials. A XS analytical balance with readability 0.01mg (Mettler-

Toledo International, Inc.) was used for sample weight measurement in all the experiments. The frequently used settings of each above mentioned facility has been summarized in **Table 1**.

Table 1 Summary of major parameter settings of instruments used for material characterization

Instrument Name	Major Parameter Settings
TEM	High Tension: 100kV Spot size: 1-4
SEM	High Vaccum: Chamber Pressure: 130Pa Spot size: 3-5 High Voltage: 10 – 30 kV
Confocal Microscope	Excitation lazers: 405-nm, 488-nm, and 561-nm Band-pass filters: 420–480 nm, 505–530 nm, and 570–700 nm. Pinhole: default setting
TGA	N_2 flow rate: 23 – 60 ml/min Ramp: 10 ^oC/min to 600 degree Pan Type: Platinum
FITR	Wavenumber (nm): 650 – 4000 Scan resolution: 4 cm^{-1} Accumulation: 10 scans
UV-VIS-NIR spectroscopy	Scan range: 300 – 3000 nm Scan rate: 600nm/min Data interval (nm): 0.1 to 5
ZetaSizer Nano	Refractive Index: 1.670 (Aluminum hydroxide) Adsorption: 0.030 Temperature: 25 ^oC Cell: DTS1060C

Cell Culture: Cells were cultured in Dulbecco's modified Eagle's medium (DMEM), supplemented with glutamine (2 mM), penicillin (100 IU mL^{-1}), streptomycin (100 μg mL^{-1}) and 10 % fetal bovine serum at 37 ℃ in a 5% CO_2-containing humidified atmosphere.[2-3] Prior to each test, cells were harvested using trypin-EDTA-PBS and $1 \cdot 10^4$ cells were plated in each well in 96-well plate setup with 200 μL of growth media. Unless otherwise indicated, cells were allowed to attach overnight before inducing treatment. (e.g. AANTs) All the cell experiments were repeated three times.

Biochemical assays: cell toxicity assay (e.g. trypan blue, alarmar blue etc.), flow cytometry assays and immunoassays (e.g. ELISA, western blot) are conducted by standard protocols.[4-8] The detailed methodologies of bioassays used in this thesis have been illustrated in related publications. For immunostaining and confocal microscopy characterization, cells after treatment were fixed with 4 % paraformaldehyde on the 8-well chamber slide.[9] The chamber was then visualized under a confocal microscopy.

TEM microtome sample preparation: To prepare microtome cells samples, $1 \cdot 10^5$ cells/well were seeded in a 6-well plate and allowed to attach overnight. After treatment, cells were carefully washed with sterile phosphate-buffered saline (PBS) two times, and transferred into 1.5 mL eppendorf tubes. Collected cell pellets were re-suspended in a solution of 4 *vol* % paraformaldehyde and 1.25 *vol* % glutaraldehyde and were fixed overnight. Then, all samples were post-fixed in a 2 *vol* % osmium tetroxide solution for 45 min. After this, cells were fully dehydrated and embedded in epoxy resin. Ultrathin sections of 70 nm were cut and post-stained with uranyl acetate and lead citrate. Cell samples were analyzed by TEM at 100 kV**.**

Statistical analysis: Data were analyzed using Origin pro and Microsoft Excel software and presented as mean values ± standard deviation (SD) from three independent measurements. Statistical comparisons between different treatments were assessed by two-tailed t-tests. The criterion for significance was $p < 0.05$ for *, $p < 0.01$ for **, and $p < 0.001$ for ***. The effect of drug combinations on cytotoxicity was assessed by the median-effect method as previously described. Combination index (CI) values were calculated from median results of cytotoxicity assays, which were done in triplicate. CI values significantly >1 indicate drug antagonism. CI = 1 indicated summation, CI < 1 indicated synergism.[10]

References

1. Lee, W.; Ji, R.; Gosele, U.; Nielsch, K., Fast fabrication of long-range ordered porous alumina membranes by hard anodization. *Nat Mater* **2006,** *5* (9), 741-747.

2. Wang, Y.; Kaur, G.; Zysk, A.; Liapis, V.; Hay, S.; Santos, A.; Losic, D.; Evdokiou, A., Systematic in vitro nanotoxicity study on anodic alumina nanotubes with engineered aspect ratio: Understanding nanotoxicity by a nanomaterial model. *Biomaterials* **2015,** *46* (0), 117-130.

3. Nel, A.; Xia, T.; Meng, H.; Wang, X.; Lin, S.; Ji, Z.; Zhang, H., Nanomaterial Toxicity Testing in the 21st Century: Use of a Predictive Toxicological Approach and High-Throughput Screening. *Accounts of Chemical Research* **2012,** *46* (3), 607-621.

4. Bimbo, L. M.; Sarparanta, M.; Santos, H. A.; Airaksinen, A. J.; Mäkilä, E.; Laaksonen, T.; Peltonen, L.; Lehto, V.-P.; Hirvonen, J.; Salonen, J., Biocompatibility of Thermally Hydrocarbonized Porous Silicon Nanoparticles and their Biodistribution in Rats. *ACS Nano* **2010,** *4* (6), 3023-3032.

5. Ji, Z.; Wang, X.; Zhang, H.; Lin, S.; Meng, H.; Sun, B.; George, S.; Xia, T.; Nel, A. E.; Zink, J. I., Designed Synthesis of CeO2 Nanorods and Nanowires for Studying Toxicological Effects of High Aspect Ratio Nanomaterials. *ACS Nano* **2012,** *6* (6), 5366-5380.

6. Xia, T.; Kovochich, M.; Liong, M.; Mädler, L.; Gilbert, B.; Shi, H.; Yeh, J. I.; Zink, J. I.; Nel, A. E., Comparison of the Mechanism of Toxicity of Zinc Oxide and Cerium Oxide Nanoparticles Based on Dissolution and Oxidative Stress Properties. *ACS Nano* **2008,** *2* (10), 2121-2134.

7. Axe, E. L.; Walker, S. A.; Manifava, M.; Chandra, P.; Roderick, H. L.; Habermann, A.; Griffiths, G.; Ktistakis, N. T., Autophagosome formation from membrane compartments enriched in phosphatidylinositol 3-phosphate and dynamically connected to the endoplasmic reticulum. *The Journal of Cell Biology* **2008,** *182* (4), 685-701.

8. Chen, R.; Huo, L.; Shi, X.; Bai, R.; Zhang, Z.; Zhao, Y.; Chang, Y.; Chen, C., Endoplasmic Reticulum Stress Induced by Zinc Oxide Nanoparticles Is an Earlier Biomarker for Nanotoxicological Evaluation. *ACS Nano* **2014**.

9. Kiernan, J., Making and using aqueous mounting media. *Microsc. Today* **1997,** *97*, 16-17.

10. Chou, T.-C., Drug Combination Studies and Their Synergy Quantification Using the Chou-Talalay Method. *Cancer Research* **2010,** *70* (2), 440-446.

Chapter 3 Mechanistic Study of Electrochemical Pulse Anodization for Synthesis of Novel Anodic Aluminium Oxide Nanostructures

3.1 Fabrication of AAO-based Nanophotonics by Potentiostatic Pulse Anodization

3.1.1 Introduction, Significance and Commentary

Pulse anodization is a powerful technique to control the geometry of nanopore on anodic films by programming electrochemical parameters (e.g. current density and voltage) during anodization. However, fabricating nano-architectures of anodic alumina oxide (AAO) is still challenging due to the complexity of electrochemical oxidation. The aim of this section is to understand the mechanism of structurally engineering of AAO by pulse anodization, and to produce novel AAO-based nanophotonics. Herein potentiostatic pulse anodization was used to engineer the geometry of nanopores in real time, which for the first time produced a novel AAO-based nanophotonics so called AAO-microcavities. The elucidation of the pulse anodization mechanism is of fundamental importance for the fabrication of novel AAO-based nanostructures, especially for advanced applications such as optical sensing.

3.1.2 Publication

This section is a research paper published by Ye Wang, Yuting Chen, Tushar Kumeria, Fuyuan Ding, Andreas Evdokiou, Dusan Losic, Abel Santos, Facile Synthesis of Optical Microcavities by a Rationally Designed Anodization Approach: Tailoring Photonic Signals by Nanopore Structure, *ACS applied materials & interfaces*, 2015, *7* (18), pp 9879–9888.

Statement of Authorship

Title of Paper	Facile Synthesis of Optical Microcavities by a Rationally Designed Anodization Approach: Tailoring Photonic Signals by Nanopore Structure
Publication Status	☑ Published ☐ Accepted for Publication ☐ Submitted for Publication ☐ Publication Style
Publication Details	Wang, Y.; Chen, Y.; Kumeria, T.; Ding, F.; Evdokiou, A.*; Losic, D.* and Santos, A.* (2015): Facile synthesis of optical microcavities by a rationally designed anodization approach: Tailoring photonic signals by nanopore structure, ACS Applied Materials & Interfaces 2015, 7 (18), pp 9879–9888 (IF=5.900)

Principal Author

Name of Principal Author (Candidate)	Ye Wang		
Contribution to the Paper	Designed project and accomplished 80% of experiments, performed data analysis and prepared manuscript		
Overall percentage (%)	80%		
Signature		Date	31/7/2015

Co-Author Contributions

By signing the Statement of Authorship, each author certifies that:

i. the candidate's stated contribution to the publication is accurate (as detailed above);

ii. permission is granted for the candidate in include the publication in the thesis; and

iii. the sum of all co-author contributions is equal to 100% less the candidate's stated contribution.

Name of Co-Author	Yuting Chen		
Contribution to the Paper	Assisted in part of experiment		
Signature		Date	1. 8. 2015.

Name of Co-Author	Tushar Kumeria		
Contribution to the Paper	Assisted in part of experiment		
Signature		Date	10/7/15

Name of Co-Author	Fuyuan Ding		
Contribution to the Paper	Assisted in part of experiment		
Signature		Date	31/07/15

Name of Co-Author	Andreas Evdokiou		
Contribution to the Paper	Supervised development of work, helped in data interpretation and manuscript evaluation		
Signature		Date	**11/8/2015**

Name of Co-Author	Dusan Losic		
Contribution to the Paper	Supervised development of work, helped in data interpretation and manuscript evaluation		
Signature		Date	10/07/2015

Name of Co-Author	Abel Santos		
Contribution to the Paper	Supervised development of work, helped in data interpretation and manuscript evaluation		
Signature		Date	31/07/15

Name of Co-Author			
Contribution to the Paper			
Signature		Date	

ACS APPLIED MATERIALS & INTERFACES

Research Article

www.acsami.org

Facile Synthesis of Optical Microcavities by a Rationally Designed Anodization Approach: Tailoring Photonic Signals by Nanopore Structure

Ye Wang,[†,‡] Yuting Chen,[†] Tushar Kumeria,[†] Fuyuan Ding,[†] Andreas Evdokiou,*[,‡] Dusan Losic,*[,†] and Abel Santos*[,†]

[†]School of Chemical Engineering, The University of Adelaide, Adelaide, SA 5005, Australia

[‡]Discipline of Surgery, Basil Hetzel Institute, The University of Adelaide, Adelaide, SA 5005, Australia

Supporting Information

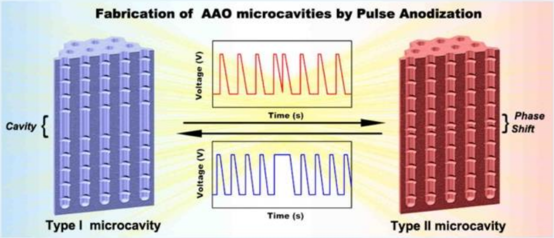

ABSTRACT: Structural engineering of porous anodic aluminum oxide (AAO) nanostructures by anodization has been extensively studied in the past two decades. However, the transition of this technique into the fabrication of AAO-based one-dimensional photonic crystal is still challenging. Herein, we report for the first time on the fabrication of AAO optical microcavities by a rationally designed anodization approach. In our study, two feasible methods are used to fabricate microcavities with tunable resonance peak across the visible and near-infrared spectra. Distributed Bragg reflector (DBR) nanostructures are first fabricated by pulse anodization approach, in which the anodization voltage was periodically manipulated to achieve pseudosinusoidal modulation of the effective refractive index gradient along the depth of the AAO nanostructures. Microcavities were created by creating a nanoporous layer of constant porosity between two AAO−DBR nanostructures, and by introducing a shift of the phase of the porosity gradient along the depth of AAO. The position of the resonance peak in these microcavities can be linearly tuned by means of the duration of the high voltage anodization. These optical nanostructures are sensitive to alterations of the effective media inside the nanopores. The AAO microcavity shows a central wavelength shift of 2.58 ± 0.37 nm when exposed to water vapor. Our research highlights the feasibility of anodization technique to fabricate AAO-based photonic nanostructures for advanced sensing applications.

KEYWORDS: *electrochemical anodization, anodic aluminum oxide, nanopores, photonic crystal, distributed Bragg reflectors, microcavities, chemical sensing*

■ INTRODUCTION

Intensive and extensive research studies on nanoporous anodic aluminum oxide (AAO) prepared by self-ordering electrochemical anodization have stimulated numerous advanced applications in recent decades such as nanofabrication, optical sensing, energy storage, and drug delivery.[1−4] In particular, AAO has gained considerable interests in recent years for chemical sensing and biosensing mainly due to its scalable and cost-competitive fabrication process, high surface area, excellent chemical and mechanical stability, and tunable pore geometry.[5] High aspect ratio AAO nanostructures with straight cylindrical geometry are conventionally fabricated by a technique of so-called mild anodization (MA) with regard to the slow growth rate of the oxide film (2−7 μm/h) under low current density (j = 1−5 mA/cm^2).[6] Experimental studies and theoretical models have confirmed that the formation of self-organized nanoporous anodic films is due to the mechanical stress driven by the migration of ions (i.e., Al^{3+} and O^{2-}) across the oxide barrier layer as well as field-enhanced dissolution of oxide.[7−11] Since the mechanical stress and electrochemical oxidation rate are proportional to the ionic current passing through the oxide layer, the current density applied during anodization governs the growth rate of the anodic oxide and also the geometric features of the resulting nanoporous film such as the nanopore's size and its shape.[10] For example, AAO with high growth rates and large pore diameters can be produced when the anodization process is carried out under high current densities (j > 30 mA/cm^2).[12] Importantly, the elucidation of the formation mechanism of AAO has recently boosted numerous studies on the fabrication of novel AAO-based photonic nanostructures. AAO structures based on stacks of periodic dielectric nanoporous layers with sinusoidally patterned effective refractive index display tunable photonic stop bands (i.e., wavelength ranges where the material present high reflectivity and low/limited transmittance of light).[13] In contrast to straight nanopores, AAO with modulated or

Received: March 2, 2015
Accepted: April 22, 2015
Published: April 22, 2015

DOI: 10.1021/acsami.5b01885
ACS Appl. Mater. Interfaces 2015, 7, 9879−9888

Scheme 1. Illustration of Fabrication Process of AAO Microcavities by Pulse Anodization[a]

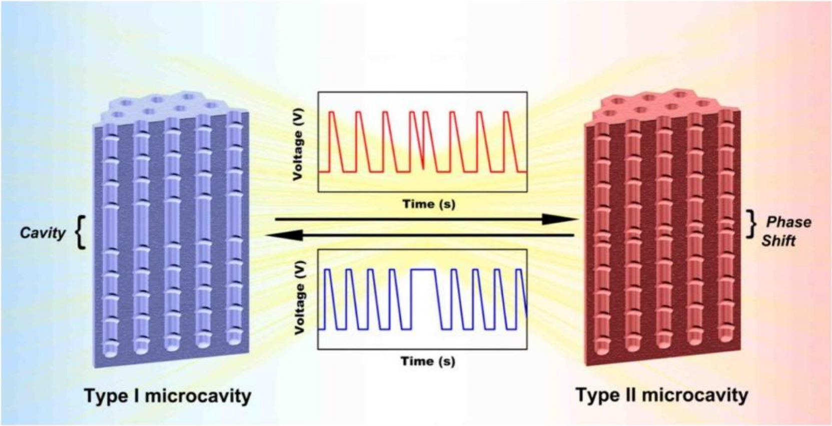

[a]Type I microcavities are prepared by inserting a cavity layer between two AAO−DBR structures (left side). Type II microcavities are fabricated by shifting the phase of anodization profile to achieve the phase modulation of effective refractive index in the bottom DBR structures (right side).

hierarchically branched nanopores can be fabricated by continuous periodic manipulation of the current density/voltage during anodization. This electrochemical approach, so-called pulse anodization,[14−18] makes it possible to precisely tailor the effective refractive index profile of AAO in depth in order to generate distributed Bragg reflectors (DBR).[19−23] Several recent studies have demonstrated the potential of AAO-based DBR nanostructures for chemical and biological sensing applications.[24−26]

The understanding of the anodization mechanism has tremendously enhanced our ability to fabricate AAO featuring sophisticated nanostructures. However, more extensive fundamental research must be carried out in order to develop novel AAO-based photonic structures with optimized optical properties. In this scenario, here we report on a rationally designed synthesis approach aimed to fabricate AAO-based optical microcavities for potential chemical vapor sensing. AAO microcavities are prepared by pulse anodization, in which the nanostructure of AAO is directly manipulated by the anodization voltage in order to modulate the effective refractive index of the nanoporous structure in depth. The AAO microcavities, similar to other thin-film microcavities,[27−30] are formed by inserting a thin layer of nanopores with constant effective refractive index between two highly reflective DBR structures (type I microcavities) as well as by shifting the phase of the refractive index along the depth of AAO (type II microcavities) (Scheme 1). We demonstrate that both strategies are feasible solutions for fabricating AAO microcavities with tunable position of the resonance peak. The sensing capabilities of the AAO microcavities are tested by using water vapor as a model gas. Our result provides promising opportunities for preparing more sophisticated AAO-based photonic nanostructures for advanced applications, such as optical interference filters, light harvesting devices, and environmental sensors.

■ EXPERIMENTAL SECTION

Materials and Chemicals. Aluminum (Al) foils of thickness 0.32 mm and purity 99.9997% were supplied by Goodfellow Cambridge Ltd. (Wrexham, U.K.). Oxalic acid ($H_2C_2O_4$), copper(II) chloride ($CuCl_2$), hydrochloric acid (HCl), ethanol (denatured; C_2H_5OH), perchloric acid ($HClO_4$), chromium trioxide (CrO_3), and phosphoric acid (H_3PO_4) were purchased from Sigma-Aldrich (Castle Hill, Australia) and used without further processing. Ultrapure water Option Q-Purelabs (Castle Hill, Australia) was used for preparing all of the solutions used in this study.

Table 1. Summary of Anodization Conditions Used to Fabricate the Two Types of Microcavities Produced in This Study

	type I microcavities		type II microcavities	
serial no.	HVA duration (s)	cavity anodization duration (min)	phase change	HVA duration (s)
1	140	20	1/2 π	140
2	180	20	π	140
3	240	10−20	3/2 π	140
4	300	20	7/4 π	140
5	360	20		

Fabrication of AAO Microcavities by Pulse Anodization. The AAO microcavities were synthesized by a modified pulse anodization process.[21,31] Briefly, Al chips 1.5 cm in diameter were first sonicated in ethanol and ultrapure water. Al chips were electropolished prior to anodization in a mixture of ethanol and $HClO_4$ 4:1 (v:v) at 20 V and 5 °C for 3 min. After this, the first anodization step was carried out in an electrolyte of 0.3 M $H_2C_2O_4$ at 40 V and 6 °C for 20 h. The resulting AAO layer was dissolved by wet chemical etching in a solution of 0.2 M chromic acid (H_2CrO_4) and 0.4 M H_3PO_4 at 70 °C for 3 h. Subsequently, pulse anodization was conducted at 5 °C with vigorous stirring. A Keithley 2400 source-meter unit was used to control the pulse parameters. The area exposed to the electrolyte solution was 0.95 cm^2, and the current density (j) was calculated by dividing the input current by the anodized sample area. In general, a pulse cycle contains three steps: (1) a constant high voltage step, named high voltage anodization (HVA), was first conducted at 50 V for a certain period of time, which ranged from 140 to 360 s. (2) Then the voltage was gradually reduced to 20 V at a rate of 0.078 V/s. (3) Finally, the anodization voltage was kept at 20 V, stage named low voltage anodization (LVA), for 8 min. A typical AAO−DBR nanostructure was first fabricated by applying 40 pulse cycles of anodization following the aforementioned protocol. To fabricate AAO microcavities with cavity layers (type I microcavities), an AAO−DBR structure was first created by 20 pulse anodization cycles. Then, the anodization process was continued at 50 V under a designed duration to achieve an optimum thickness of the cavity layer. This was followed by another set of 20

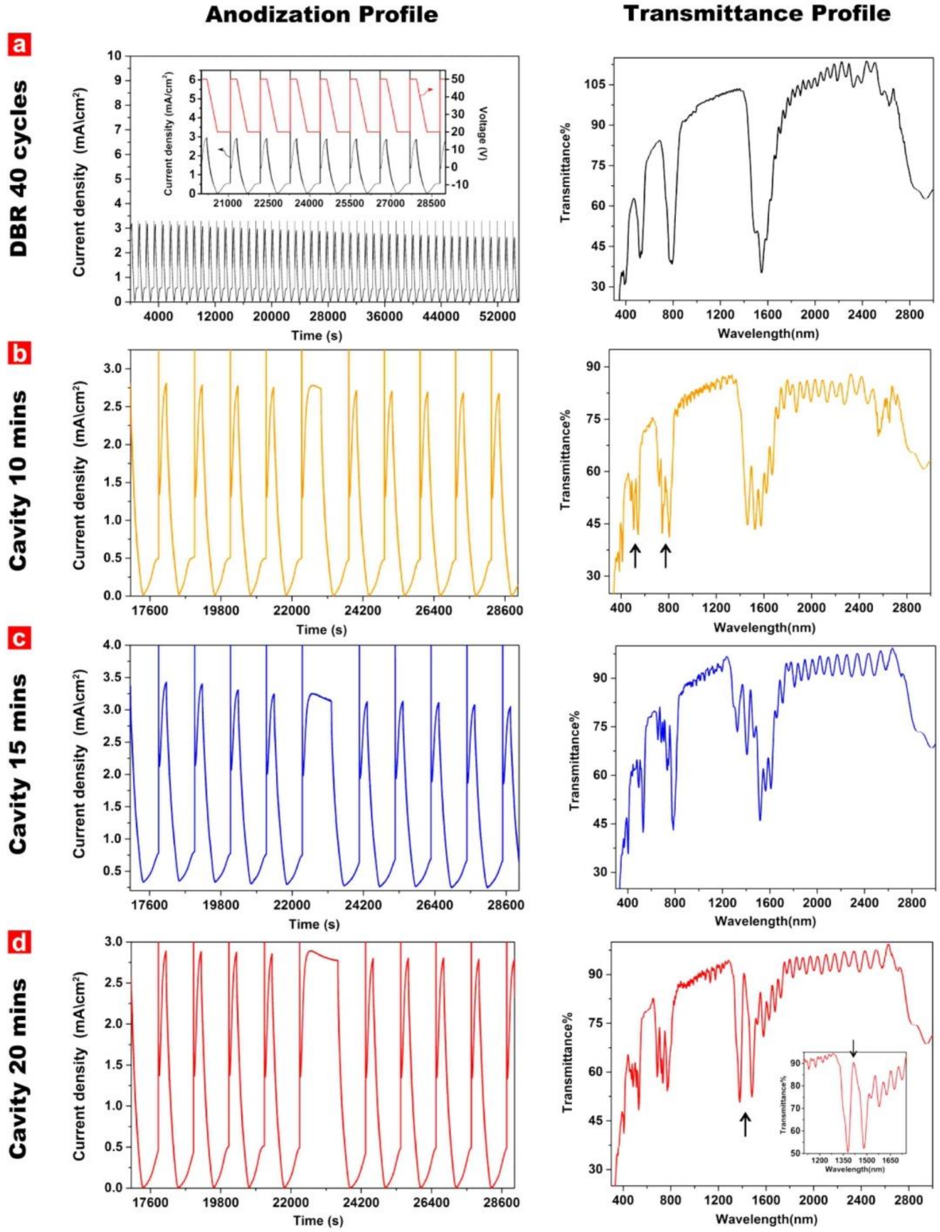

Figure 1. Anodization profiles and transmittance spectra of AAO−DBR and AAO microcavities (type I). (a) AAO−DBR is prepared by 40 cycles' pulse anodization. Each pulse cycle consisted of a 240 s anodization at 50 V, a programmed reduction of voltage to 20 V at the rate of 0.078 V/s, and a 480 s anodization at 20 V. Inset represents an enlarged anodization profile. (b−d) Optimization of cavity layer thickness for preparing microcavities. The cavity layer was sandwiched between two DBR nanostructures anodized continuously with 20 cycles' pulse, respectively. The cavity layer thickness was controlled by anodization at 50 V for (b) 10, (c) 15 min and (d) 20 min, respectively. Black arrows denote the positions of the resonance peaks of microcavities.

cycles of pulse anodization to form another AAO−DBR structure at the bottom of the resulting AAO film (Scheme 1, left side). The synthesis conditions of type II AAO microcavities are the same as those used to produce microcavities of type I (i.e., 5 °C; HVA of 140 s/50 V; LVA of 480 s/20 V; and 40 pulse cycles in total) except that a phase change is introduced at the 20th pulse cycle instead of growing cavity layers (Scheme 1, right side). For instance, after fabrication of the first DBR structure, the pulse phase was shifted 1/2 π at the 20th pulse. Then, the process was continued with a series of 20 pulses at 1/2 π phase shift. This process makes it possible to create an optical microcavity (i.e., optical interface) between the two DBR structures without any physical layer between both DBRs. Once the anodization process was finished, the remaining aluminum substrate was selectively removed from the backside of these Al chips by wet chemical etching through an etching mask in a saturated solution of HCl/$CuCl_2$. A pore-widening process was performed by wet chemical etching in

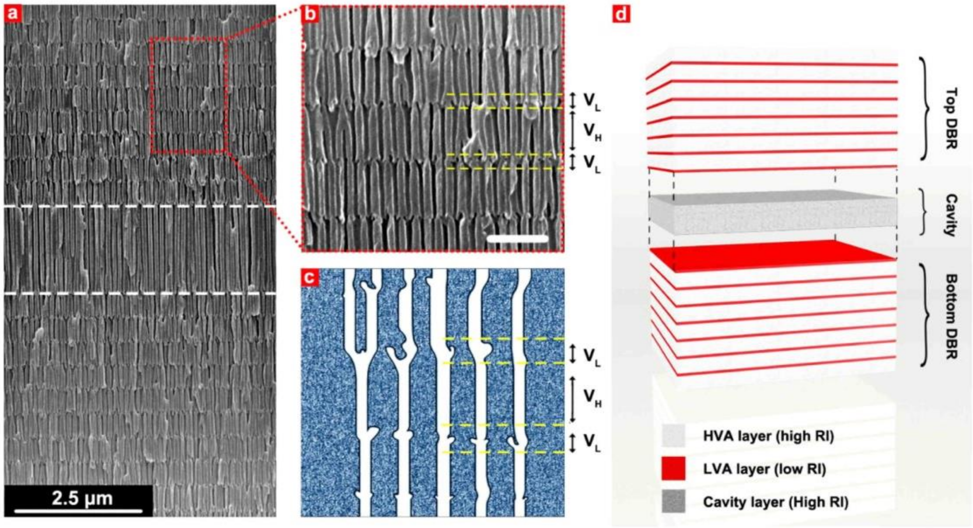

Figure 2. Structural characterization of AAO microcavities (type I). (a) SEM cross-section image of the AAO microcavities with cavity layer thickness of 1.770 ± 0.014 μm after 20 min anodization at 50 V. White dashed line denotes the boundary of the cavity layer. (b) Magnified view of the DBR layer indicated in panel a by a red rectangle. The yellow dashed line denotes the boundaries of the high voltage anodization (HVA) layer and low voltage anodization (LVA) layer. V_L is low voltage, while V_H denotes high voltage. Scale bar: 500 nm. (c) Schematic illustration of the nanopore structure, which contains straight pores in the HVA layer and a branched structure at the LVA layer. (d) Scheme of the structure of AAO microcavities (type I) containing a cavity layer sandwiched between two DBR layers. The modulation of refractive index (RI) is achieved by alternating HVA and LVA layers in a sequential manner.

freshly prepared H_3PO_4 solution at a concentration of 5 wt % at 35.0 ± 0.1 °C for 12 min. The fabrication conditions used to produce the previously mentioned microcavities are summarized in Table 1.

Structural Characterizations. The structural characteristics of the AAO microcavities were established from SEM images acquired by a field emission gun scanning electron microscope (FEG-SEM FEI Quanta 450). The transmission spectra were obtained by using UV−vis−near-IR spectroscopy (Cary 5000, Agilent). The spectra were collected from 300 to 3000 nm at a resolution of 5 nm. To conduct the Lorentzian fit of the resonance peak, the spectra resolution was adjusted to 0.1 nm. The optical images of AAO microcavities were captured by a digital camera (Nikon D3100).

Water Vapor Sensing. To test the sensitivity of AAO microcavities to chemical vapors, 3 mL of ultrapure water was added in a 5 mL hydrothermal autoclave reactor and preheated to 70 °C. Since this process was conducted in such conditions that water vapor was in thermodynamic equilibrium with its condensed state, the vapor pressure as a function of temperature can be determined by the Clausius−Clapeyron relation, which is estimated to be 31.1760 KPa at 70 °C. Type II AAO microcavities prepared by a 7/4 π phase shift was placed on the top of the reactor and faced down to allow the infiltration of vapor into its nanopores. After certain accumulated time course (i.e 10, 30, 60, 120, and 240 s), the sample was assessed immediately by UV−vis−near-IR spectroscopy at the wavelength range from 850 to 1100 nm with a resolution of 1 nm.

Unless otherwise indicated, all of the aforementioned experiments were repeated three times, and the obtained values of the different characteristic parameters were statistically treated by calculating averages and standard deviations.

■ RESULTS AND DISCUSSION

Synthesis of AAO Microcavities (Type I) by Optimizing the Thickness of the Cavity Layer. For a DBR structure containing dielectric stacks with alternated effective refractive indexes, the optical thickness of each stack should be equal to a quarter of the wavelength at which the light reflection is maximum in order to achieve constructive interference of light according to the Bragg condition,

$$n_H d_H = \lambda/4 = n_L d_L \tag{1}$$

where n_H/d_H and n_L/d_L are the effective refractive indices and thicknesses of the corresponding layers with high and low effective refractive index, respectively.[27,32,33] To create a narrow resonance (microcavity) in the stop band of a DBR, a cavity layer with half-wavelength optical thickness is inserted in the middle of the dielectric stacks. This makes it possible to create destructive interferences at a certain wavelength, which is established by the characteristics of the cavity layer. Therefore, the design of thin-film optical microcavities requires a precise control over the thickness and effective refractive index of each layer on the DBR and the cavity layer, since very slight deviations of these structures will lower the quality of the optical cavity. Note that long-term aluminum anodization (>24 h) unavoidably decreased the electrolyte concentration and consequently reduced the current density, which makes the quality control of each stack layer a challenge.[34]

AAO microcavities (type I) with a physical cavity layer sandwiched in between two AAO-DBR structures were produced by pulse anodization of aluminum (Figure 1). Figure 1a shows the anodization profile and transmittance spectrum of an AAO−DBR pulse anodized by 40 cycles. To achieve the variation of effective refractive index, the voltage was engineered from 50 to 20 V in a periodic fashion. Note that direct switching voltage from 50 to 20 V blocks the growth of nanopore due to the delayed current recovery caused by the thick oxide barrier layer formed during previous HVA. In a given electrolyte, the barrier layer thickness increases with the anodization potential (U) with a proportional rate of 1.3 nm V^{-1} for MA process.[12] However, at voltage control condition,

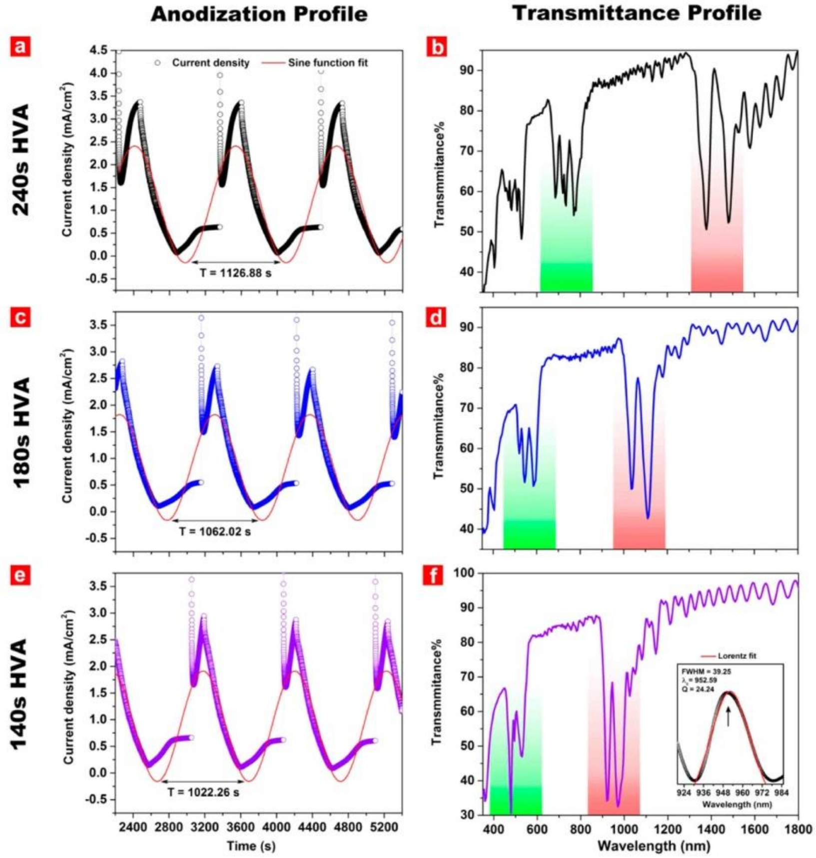

Figure 3. Manipulation of the AAO microcavities stop band position by changing high voltage anodization (HVA) duration. (a, c, e) Current density−time profile of pulse anodization with HVA duration of 240, 180, and 140 s, respectively. Sine function fitting was applied as an illustration of pseudosinusoidal current density profile. (b, d, f) Transmittance profiles of the resulting AAO microcavities prepared under different HVA durations. Red color region denotes the position of the first order stop band. Green region denotes the position of the second order stop band. The blue shift of stop band is evident when the HVA duration is decreased. Inset is a magnification of the cavity resonance of AAO microcavities prepared by 140 s HVA. Lorentz fit was applied, and the quality factor of these AAO microcavities was determined to be 24.24.

the current density is inversely proportional to the logarithm of the barrier layer thickness according to the high field conduction theory,

$$j = j_0 \exp(\beta \Delta U / t_b) \tag{2}$$

where j is current density, j_0 and β are material-dependent constants at a given temperature, and $\Delta U/t_b$ is the effective electric field strength across the barrier thickness, t_b.[2] From this expression we can infer that when the voltage is reduced from high to low with a large potential difference, the thickness of the barrier layer remains at a thick level, while the effective field strength at LVA is not strong enough to keep the ionic flow (i.e., Al^{3+} and O^{2-}) through the thick oxide barrier layer at the pore bottom tips. To overcome this limitation, a decreasing voltage ramp was applied at a rate of 0.078 V/s, which is the fastest possible according to our results. After 12 min of pore widening treatment, the porosity contrast between layers increases, and the transmittance spectra of the AAO−DBR presents three characteristic resonance peaks at the wavelengths of 1550, 790, and 520 nm. To create a microcavity resonance peak, a cavity layer was fabricated by HVA at designed duration (i.e., 10, 15, and 20 min) as shown in Figure 1b−d. The resulting transmittance spectra clearly showed the evolution of the resonance peaks with regard to the thickness of the cavity layer, in which the first order resonance peak at the wavelength of 1415 nm was formed completely with a HVA cavity layer of 20 min. SEM characterization revealed that the thickness of the cavity layer after 20 min of HVA was 1.770 ± 0.014 μm (Figure 2a). Figure 2b shows a magnified view of the DBR structure. It is evident that straight pores were formed at the HVA section while branching structure appeared during LVA. Previous studies on pore branching phenomenon in AAO showed that the number of branched nanopores can be precisely engineered by reducing the voltage by a factor of $1/\sqrt{n}$, where n is the number of branches per pore.[39−41]

Note that this condition cannot be accomplished unless a chemical etching step is performed to reduce the oxide barrier layer thickness and allow the flow of ions (i.e., Al^{3+} and O^{2-}) at reduced voltage. In our protocol, the potential was reduced approximately by a factor of $1/\sqrt{6}$. However, we only observed two-branch structure in a competitive growth pattern (Figure 2b,c and Supporting Informaton (SI) Figure S1). This phenomenon is thought to be associated with the uneven distribution of the electric field at the bottom of nanopores due

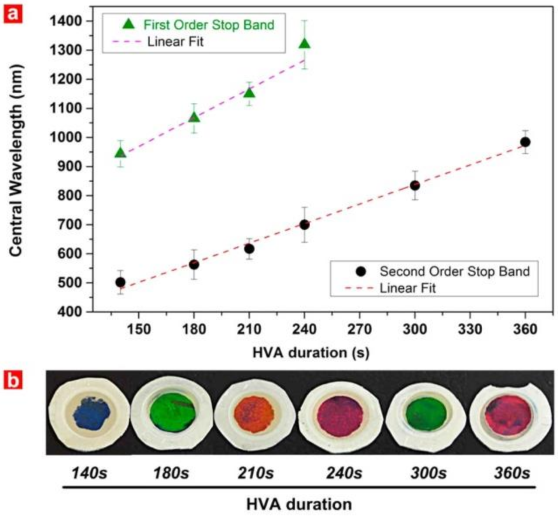

Figure 4. Relation of central wavelength position and resulting color of AAO microcavities against high voltage anodization duration. (a) Linear fitting of central wavelength position against the HVA duration. The first and second order stop band positions can be tailored across the range of visible and near-infrared wavelength. (b) The color of AAO microcavities can be precisely controlled by HVA duration.

to the continuous reduction of voltage.[36] Interestingly, the branching nanopores did not grow steadily but formed as tips at the interfaces of HVA and LVA layers. This phenomenon is due to the unregulated growth of nanopore at the disordered growth regime. In the condition of LVA, the anodization was conducted at 20 V/0.3 M oxalic acid, which is far from the self-organized regime in oxalic acid (40 V).[9] In addition, although the duration of LVA was twice longer than HVA, the growth rate of nanopore was slow due to the delayed current recovery as well as reduced ion current density according to eq 2. Therefore, such undeveloped branching pores increased the porosity in the LVA layer, thus leading to low effective refractive index. In contrast, HVA led to a relatively lower porosity, which generates higher effective refractive index as compared to LVA (Figure 2d). Accordingly, the programmed anodization profile creates a periodically modulated porosity, which in turn results in a DBR structure.[35,36] This engineered periodical porosity pattern enabled the accumulation of in phase interference from each dielectric stack, thus achieving the sharp characteristic reflection peak of the DBR as shown in Figure 1a. Since pulse anodization is frequently used to produce AAO-based photonic nanostructures, clarifying the mechanism of porous growth pattern during voltage shifting is of fundamental importance for controlling the porosity of dielectric stacks. Another advantage of this fabrication approach is that the performance of microcavities is mainly determined by the thickness of the cavity layer as illustrated in Figure 2d. Therefore, one can precisely design the cavity structure by HVA, in which the growth rate of pores is linear with the duration of anodization.

Tuning Resonance Peak Position by Engineering HVA Duration. From SEM structural characterization, the layer thickness of the HVA layer is considerably thicker than that of the LVA layer. We reasoned that tuning the HVA layer thickness may affect the stop band position of the DBR, as the stop band wavelength is proportional to the effective media of dielectric stacks according to eq 1. As shown in Figure 3, reducing HVA duration from 240 to 140 s without changing the cavity structure readily shifted the position of the first order resonance peak from 1415 to 945 nm. The resonance wavelength value of the sample of 140 s HVA was determined by fitting a Lorentzian curve to the experimental data, which had a quality factor of 24.24 with full width at half-maximum (FWHM) of 39.25 nm (Figure 3f). Note that the current density profile in our condition can be treated as a pseudosinusoidal profile when fitted to a sine function (Figure 3a,c,e). As we discussed earlier, the anodization voltage influences the barrier layer thickness, while it is the ionic current density that dominates the geometry of the nanopore such as nanopore diameter and branching feature. It is known that the nanopore geometry is influenced by the mechanical stress over the barrier layer, which is governed by the ionic current density passed through the barrier layer at a given potential according to eq 2.[10,42] When the potential drops from a high to a low value, the concurrently reduced current density will decrease the compressive stress over the barrier layer due to retarded ionic migration moved from cell bottom toward cell boundary, which leads to the uneven distribution of current density at the bottom, and consequently result in the modulation of nanopore geometry and branching structure.[7,8] Therefore, the periodical current density pattern engineered the effective refractive index profile into a pseudosinusoidal pattern, which makes it possible to manipulate the photonic stop band position by changing the anodization period.[37,38,43]

This strategy enables us for the first time to control the resonance peak of AAO microcavities and tune its position across the visible and near-infrared spectra. The positions of the resonance peak are linear with the duration of HVA (Figure 4). The visual color of these photonic structures is dominated by the second order stop band when HVA is below 240 s, while the third order of the stop band starts to induce color when the HVA is higher than 300 s. Note that the features of cavities (i.e., thickness and effective refractive indexes) were maintained constant in all of these experiments, which causes the variation of the qualities of the resulting resonance peak (SI Figure S2). Since the performance of microcavities is mainly dependent on the cavity structure, it is expected that higher quality cavities can be obtained after further optimization of the cavity thickness.

Fabrication of AAO Microcavities (Type II) by Continuously Modifying the Phase of Effective Refractive Index in DBR Structure. The technique of inserting cavity layers is commonly used to fabricate high quality microcavities. A more challenging method is to utilize the phase difference of effective refractive index profiles of DBRs for achieving destructive interferences. Such protocol requires a precise control of the modulation of the effective refractive index profile perpendicular to the surface of the thin film, and the experimental realizations are rare in thin-film photonics technology.[28] To address this challenge, we engineered the anodization profile by introducing a phase change of pulse profile started at the 20th pulse cycle (SI Figure S3). Herein, we chose the condition of 140 s HVA as an example, in which the period of a single pulse was determined to be 1022.26 s (Figure 3e). Since the anodization profiles are translated into the effective refractive index of AAO, the phase of effective refractive index at the bottom DBR was shifted by programmed anodization profiles, resulting in the narrow resonance peak

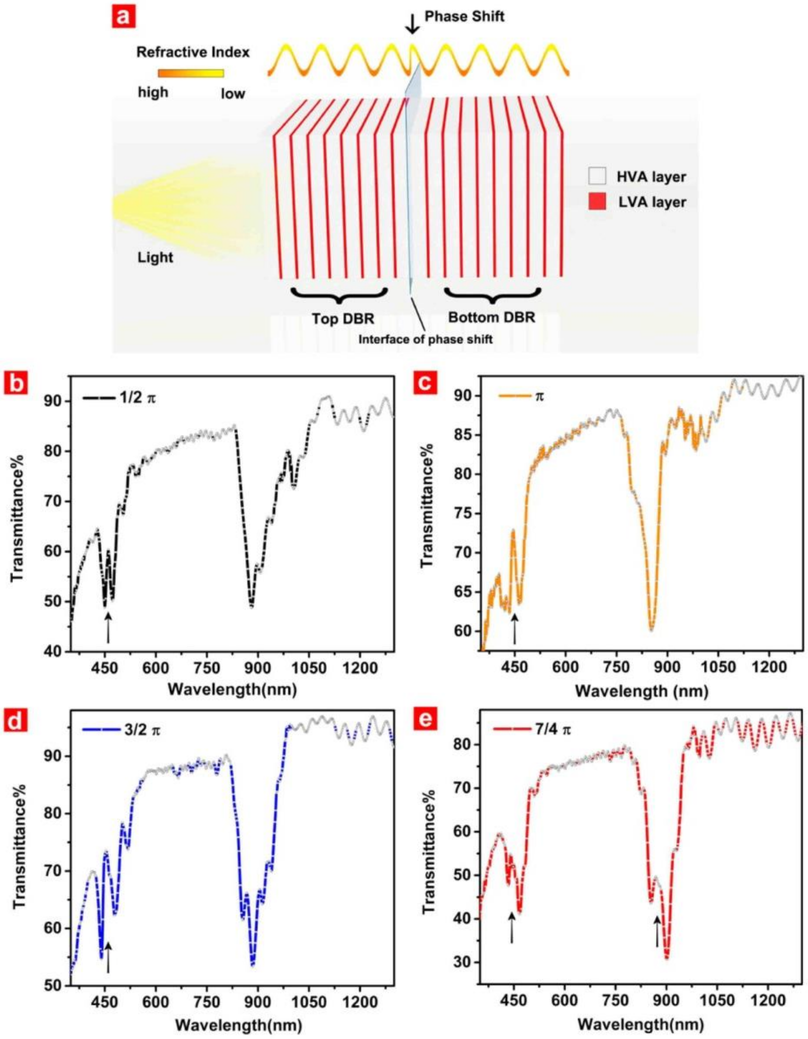

Figure 5. Phase shift of refractive index profile for preparation of AAO microcavities (type II). (a) Scheme of type II AAO microcavities prepared by continuous pulse anodization. The graded refractive index profile of the bottom DBR structure has a phase shift from 1/2 to 7/4 π to achieve the resonance with top DBR structure. (b−e) Transmittance profiles of AAO microcavities prepared by phase shift method. Black arrows denote the positions of resonance peaks.

within the stop band (Figure 5d−b). The second order resonance peak appeared with a 1/2 π phase shift and became stronger with a π phase shift due to the stronger destructive interferences between the upper and lower DBRs. In contrast, the first order resonance peak did not appear until the 7/4 π phase shift. From structural analysis, the modulation of pore geometry by 1/2 π phase shift is virtually undetectable by SEM characterization: straight pores were identified at the interface of the phase shift. However, branching of nanopores and variation of nanopore diameter appeared at the interface of the 7/4 π phase shift (SI Figure S4). We hypothesize that the absence of the first order resonance peak at 1/2 π−3/2 π phase shift is due to the delayed current recovery effect when anodization was switched from HVA to LVA. Although compromised by slowly reduced voltage to enable the continuous anodization at low voltage, the slow current recovery retarded the formation of nanopores at the beginning stage of LVA, thus delaying the translation of the phase profile into effective refractive index profile along the depth of AAO. It can be expected that anodization profiles aimed at facilitating the current recovery by increasing the electrolyte temperature and the use of sulfuric acid as electrolyte will efficiently address this limitation.[2,42]

Vapor Sensing Performance of AAO Microcavities. As a proof of applicability, we decided to demonstrate and asses the sensitivity of AAO microcavities toward water vapor. To this end, we exposed an AAO microcavity to a water vapor environment. It is known that the resonance peaks of microcavities structures are sensitive to changes in the refractive index of the medium inside the nanopores due to the photon confinement effect.[29,36] Since water vapor has higher refractive index than air, the accumulation of water molecules inside the nanopores will increase the effective refractive index of the AAO microcavity and thus will lead to a red shift of its

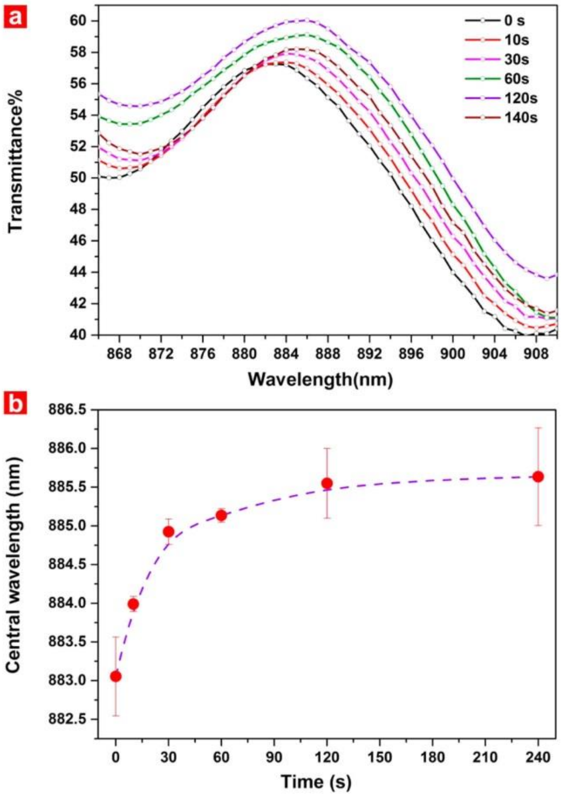

Figure 6. Water vapor sensing performance of AAO microcavities (type II) prepared with 7/4 π phase shift. (a) Transmittance profile of the resonance peak of AAO microcavities when exposed to water vapor at different time intervals. (b) Peak shift of the central wavelength against time after exposure to water vapor.

resonance peak. Transmittance spectra were recorded after vapor exposure at certain time points, and the shifts of the resonance peak were monitored as a function of time (Figure 6). We chose AAO microcavities (type II) with a 7/4 π phase shift as a sensor model. A red shift of the first order resonance peak appeared with a time-dependent fashion when the water vapor was condensed inside the nanopores of these AAO microcavities (Figure 6a). The resonance peak showed a central wavelength shift of 2.58 ± 0.37 nm in total after exposure to water vapor for 120 s, at which the saturation of the sensor was achieved. It is expected that AAO microcavities can be used for other gas sensing applications as well as biological/chemical sensing when combined with surface functionalization strategies.[25,44]

■ CONCLUSION

Although anodization of aluminum is a well-developed technique, the fabrication of advanced AAO-based photonic structures requires precise control over the nanoporous geometry for efficient light guiding. Herein, we have addressed this challenge by putting forward facile and rationally designed strategies for the fabrication of AAO microcavities by pulse anodization. Two types of AAO microcavities were synthesized by intercalating a cavity layer with constant refractive index between two AAO−DBR nanostructures and by programming phase shifts of effective refractive index profiles of AAO−DBR continuously along the depth of AAO. These methods not only enable a versatile tunability of the resonance peaks across the visible and near-infrared spectra but also open up new opportunities toward the design of more advanced AAO-based photonic nanostructures such as Thue−Morse, Fibonacci, and the combination of both, which potentially exhibit the novel patterns of resonance peaks and stop bands.[45] The resulting AAO microcavities presented in our study contained the features of Bragg stacks structures, making these structures easy to reproduce and exhibit good sensing potential. More importantly, these AAO optical structures when combined with other nanofabrication strategies such as atomic layer deposition and template replica offer solid foundations to prepare more sophisticated optical devices for a broad range of applications.[46]

■ ASSOCIATED CONTENT

Ⓢ Supporting Information

Further information about the branching structure characterization by SEM, transmission spectra of AAO microcavities (type I) prepared by different HVA durations, voltage and current density profiles, and the anodization profile/SEM images of AAO microcavities (type II). The Supporting Information is available free of charge on the ACS Publications website at DOI: 10.1021/acsami.5b01885.

■ AUTHOR INFORMATION

Corresponding Authors

*(A.S.) Tel.: +61 8 8313 1535. Fax: +61 8 8303 4373. E-mail: abel.santos@adelaide.edu.au. Web page: http://www.adelaide.edu.au/directory/abel.santos.
*(A.E.) Tel.: +618 8222 7451. Fax: +618 8222 7872. E-mail: andreas.evdokiou@adelaide.edu.au.
*(D.L.) Tel.: + 61 8 8313 4648 Fax: +61 8 8303 4373. E-mail: dusan.losic@adelaide.edu.au. Personal web page: http://www.adelaide.edu.au/directory/dusan.losic.

Author Contributions

Y.W. designed and conducted the experiments assisted by Y.C. The obtained results were discussed and analyzed by all of the authors. The final version of the manuscript was written through contributions of all the authors. All the authors have given approval to the final version of the manuscript.

Funding

This research was supported by the Australian Research Council (ARC) through Grants DE14010054 and FT110100711, the National Health and Medical Research Council (NHMRC) of Australia through Grant APP627015, the Australian Breast Cancer Research (ABCR), and the University of Adelaide Interdisciplinary Research Fund (DVC IRF-2014).

Notes

The authors declare no competing financial interest.

■ ACKNOWLEDGMENTS

We are thankful for Adelaide Microscopy for providing microscopy facilities. Y.W. appreciates the scholarship support from China Scholarship Council. This work was performed in part at the OptoFab node of the Australian National Fabrication Facility utilizing Commonwealth and SA State Government funding.

■ ABBREVIATIONS

DBR, distributed Bragg reflectors
FWHM, full width at half-maximum
HVA, high voltage anodization
LVA, low voltage anodization
MA, mild anodization
RI, refractive index

■ REFERENCES

(1) Md Jani, A. M.; Losic, D.; Voelcker, N. H. Nanoporous anodic aluminium oxide: Advances in surface engineering and emerging applications. *Prog. Mater. Sci.* **2013**, *58* (5), 636−704.

(2) Lee, W.; Park, S.-J. Porous Anodic Aluminum Oxide: Anodization and Templated Synthesis of Functional Nanostructures. *Chem. Rev.* **2014**, *114* (15), 7487−7556.

(3) Losic, D.; Simovic, S. Self-ordered nanopore and nanotube platforms for drug delivery applications. *Expert Opin. Drug Delivery* **2009**, *6* (12), 1363−1381.

(4) Wang, Y.; Santos, A.; Kaur, G.; Evdokiou, A.; Losic, D. Structurally engineered anodic alumina nanotubes as nano-carriers for delivery of anticancer therapeutics. *Biomaterials* **2014**, *35* (21), 5517−5526.

(5) Santos, A.; Kumeria, T.; Losic, D. Nanoporous anodic aluminum oxide for chemical sensing and biosensors. *TrAC, Trends Anal. Chem.* **2013**, *44*, 25−38.

(6) Masuda, H.; Fukuda, K. Ordered Metal Nanohole Arrays Made by A 2-step Replication of Honeycomb Structures of Anodic Alumina. *Science* **1995**, *268* (5216), 1466−1468.

(7) Houser, J. E.; Hebert, K. R. The role of viscous flow of oxide in the growth of self-ordered porous anodic alumina films. *Nat. Mater.* **2009**, *8* (5), 415−420.

(8) Hebert, K. R.; Albu, S. P.; Paramasivam, I.; Schmuki, P. Morphological instability leading to formation of porous anodic oxide films. *Nat. Mater.* **2012**, *11* (2), 162−166.

(9) Nielsch, K.; Choi, J.; Schwirn, K.; Wehrspohn, R. B.; Gösele, U. Self-ordering Regimes of Porous Alumina: The 10 Porosity Rule. *Nano Lett.* **2002**, *2* (7), 677−680.

(10) Lee, W.; Kim, J.-C.; Gösele, U. Spontaneous Current Oscillations during Hard Anodization of Aluminum under Potentiostatic Conditions. *Advanc. Funct. Mater.* **2010**, *20* (1), 21−27.

(11) Thompson, G. E.; Wood, G. C. Porous anodic film formation on aluminium. *Nature* **1981**, *290* (5803), 230−232.

(12) Lee, W.; Ji, R.; Gosele, U.; Nielsch, K. Fast fabrication of long-range ordered porous alumina membranes by hard anodization. *Nat. Mater.* **2006**, *5* (9), 741−747.

(13) Yablonovitch, E. Photonic band-gap structures. *J. Opt. Soc. Am. B* **1993**, *10* (2), 283−295.

(14) Lee, W.; Schwirn, K.; Steinhart, M.; Pippel, E.; Scholz, R.; Gosele, U. Structural engineering of nanoporous anodic aluminium oxide by pulse anodization of aluminium. *Nat. Nanotechnol.* **2008**, *3* (4), 234−239.

(15) Lee, W.; Scholz, R.; Gösele, U. A Continuous Process for Structurally Well-Defined Al_2O_3 Nanotubes Based on Pulse Anodization of Aluminum. *Nano Lett.* **2008**, *8* (8), 2155−2160.

(16) Wang, Y.; Santos, A.; Evdokiou, A.; Losic, D. Rational Design of Ultra-Short Anodic Alumina Nanotubes by Short-Time Pulse Anodization. *Electrochim. Acta* **2015**, *154*, 379−386.

(17) Wang, K.; Liu, G.; Hoivik, N.; Johannessen, E.; Jakobsen, H. Electrochemical engineering of hollow nanoarchitectures: Pulse/step anodization (Si, Al, Ti) and their applications. *Chem. Soc. Rev.* **2014**, *43* (5), 1476−1500.

(18) Losic, D.; Lillo, M.; Losic, D., Jr. Porous Alumina with Shaped Pore Geometries and Complex Pore Architectures Fabricated by Cyclic Anodization. *Small* **2009**, *5* (12), 1392−1397.

(19) Zheng, W. J.; Fei, G. T.; Wang, B.; Jin, Z.; Zhang, L. D. Distributed Bragg reflector made of anodic alumina membrane. *Mater. Lett.* **2009**, *63* (8), 706−708.

(20) Biao, W.; Guang Tao, F.; Min, W.; Ming Guang, K.; De, Li Z.. Preparation of photonic crystals made of air pores in anodic alumina. *Nanotechnology* **2007**, *18* (36), No. 365601.

(21) Rahman, M. M.; Marsal, L. F.; Pallarès, J.; Ferré-Borrull, J. Tuning the Photonic Stop Bands of Nanoporous Anodic Alumina-Based Distributed Bragg Reflectors by Pore Widening. *ACS Appl. Mater. Interfaces* **2013**, *5* (24), 13375−13381.

(22) Grzegorz, D. S.; Katarzyna, H. Distributed Bragg reflector based on porous anodic alumina fabricated by pulse anodization. *Nanotechnology* **2012**, *23* (7), No. 075303.

(23) Zheng, W.; Fei, G.; Wang, B.; De Zhang, L. Modulation of Transmission Spectra of Anodized Alumina Membrane Distributed Bragg Reflector by Controlling Anodization Temperature. *Nanoscale Res. Lett.* **2009**, *4* (7), 665−667.

(24) Guo, D.-L.; Fan, L.-X.; Wang, F.-H.; Huang, S.-Y.; Zou, X.-W. Porous Anodic Aluminum Oxide Bragg Stacks as Chemical Sensors. *J. Phys. Chem. C* **2008**, *112* (46), 17952−17956.

(25) Kumeria, T.; Santos, A.; Losic, D. Ultrasensitive Nanoporous Interferometric Sensor for Label-Free Detection of Gold(III) Ions. *ACS Appl. Mater. Interfaces* **2013**, *5* (22), 11783−11790.

(26) Chen, Y.; Santos, A.; Wang, Y.; Kumeria, T.; Wang, C.; Li, J.; Losic, D. Interferometric nanoporous anodic alumina photonic coatings for optical sensing. *Nanoscale* **2015**, DOI: 10.1039/C5NR00369E.

(27) Furchi, M.; Urich, A.; Pospischil, A.; Lilley, G.; Unterrainer, K.; Detz, H.; Klang, P.; Andrews, A. M.; Schrenk, W.; Strasser, G.; Mueller, T. Microcavity-Integrated Graphene Photodetector. *Nano Lett.* **2012**, *12* (6), 2773−2777.

(28) Hawkeye, M. M.; Brett, M. J. Narrow bandpass optical filters fabricated with one-dimensionally periodic inhomogeneous thin films. *J. Appl. Phys.* **2006**, *100* (4), No. 044322-1.

(29) Jenie, S. N. A.; Pace, S.; Sciacca, B.; Brooks, R. D.; Plush, S. E.; Voelcker, N. H. Lanthanide Luminescence Enhancements in Porous Silicon Resonant Microcavities. *ACS Appl. Mater. Interfaces* **2014**, *6* (15), 12012−12021.

(30) Böcking, T.; Kilian, K. A.; Reece, P. J.; Gaus, K.; Gal, M.; Gooding, J. J. Substrate Independent Assembly of Optical Structures Guided by Biomolecular Interactions. *ACS Appl. Mater. Interfaces* **2010**, *2* (11), 3270−3275.

(31) Kumeria, T.; Rahman, M. M.; Santos, A.; Ferré-Borrull, J.; Marsal, L. F.; Losic, D. Structural and Optical Nanoengineering of Nanoporous Anodic Alumina Rugate Filters for Real-Time and Label-Free Biosensing Applications. *Anal. Chem.* **2014**, *86* (3), 1837−1844.

(32) Auguié, B.; Fuertes, M. C.; Angelomé, P. C.; Abdala, N. L.; Soler Illia, G. J. A. A.; Fainstein, A. Tamm Plasmon Resonance in Mesoporous Multilayers: Toward a Sensing Application. *ACS Photonics* **2014**, *1* (9), 775−780.

(33) Brudieu, B.; Bris, A. L.; Teisseire, J.; Guillemot, F.; Dantelle, G.; Misra, S.; Cabarrocas, P. R. i.; Sorin, F.; Gacoin, T. Sol−Gel Route Toward Efficient and Robust Distributed Bragg Reflectors for Light Management Applications. *Adv. Opt. Mater.* **2014**, *2* (11), 1105−1112.

(34) Han, H.; Park, S.-J.; Jang, J. S.; Ryu, H.; Kim, K. J.; Baik, S.; Lee, W. In Situ Determination of the Pore Opening Point during Wet-Chemical Etching of the Barrier Layer of Porous Anodic Aluminum Oxide: Nonuniform Impurity Distribution in Anodic Oxide. *ACS Appl. Mater. Interfaces* **2013**, *5* (8), 3441−3448.

(35) Fang, C.-Y.; Liu, Y.-L.; Lee, Y.-C.; Chen, H.-L.; Wan, D.-H.; Yu, C.-C. Nanoparticle Stacks with Graded Refractive Indices Enhance the Omnidirectional Light Harvesting of Solar Cells and the Light Extraction of Light-Emitting Diodes. *Adv. Funct. Mater.* **2013**, *23* (11), 1412−1421.

(36) Jalkanen, T.; Mäkilä, E.; Suzuki, Y. I.; Urata, T.; Fukami, K.; Sakka, T.; Salonen, J.; Ogata, Y. H. Studies on Chemical Modification of Porous Silicon-Based Graded-Index Optical Microcavities for Improved Stability Under Alkaline Conditions. *Adv. Funct. Mater.* **2012**, *22* (18), 3890−3898.

(37) Yan, P.; Fei, G. T.; Shang, G. L.; Wu, B.; De Zhang, L. Fabrication of one-dimensional alumina photonic crystals with a

narrow band gap and their application to high-sensitivity sensors. *J. Mater. Chem. C* **2013**, *1* (8), 1659−1664.

(38) Macias, G.; Ferré-Borrull, J.; Pallarès, J.; Marsal, L. 1-D nanoporous anodic alumina rugate filters by means of small current variations for real-time sensing applications. *Nanoscale Res. Lett.* **2014**, *9* (1), 1−6.

(39) Meng, G.; Jung, Y. J.; Cao, A.; Vajtai, R.; Ajayan, P. M. Controlled fabrication of hierarchically branched nanopores, nanotubes, and nanowires. *Proc. Natl. Acad. Sci. U. S. A.* **2005**, *102* (20), 7074−7078.

(40) Xing, H.; Zhiyuan, L.; Kai, W.; Yi, L. Fabrication of three dimensional interconnected porous carbons from branched anodic aluminum oxide template. *Electrochem. Commun.* **2011**, *13* (10), 1082−1085.

(41) Chen, B.; Xu, Q.; Zhao, X.; Zhu, X.; Kong, M.; Meng, G. Branched Silicon Nanotubes and Metal Nanowires via AAO-Template-Assistant Approach. *Adv. Funct. Mater.* **2010**, *20* (21), 3791−3796.

(42) Woo, L.; Jae-Cheon, K. Highly ordered porous alumina with tailor-made pore structures fabricated by pulse anodization. *Nanotechnology* **2010**, *21* (48), No. 485304.

(43) Su, Y.; Fei, G. T.; Zhang, Y.; Yan, P.; Li, H.; Shang, G. L.; Zhang, L. D. Controllable preparation of the ordered pore arrays anodic alumina with high-quality photonic band gaps. *Mater. Lett.* **2011**, *65* (17−18), 2693−2695.

(44) Kumeria, T.; Rahman, M. M.; Santos, A.; Ferré-Borrull, J.; Marsal, L. F.; Losic, D. Nanoporous Anodic Alumina Rugate Filters for Sensing of Ionic Mercury: Toward Environmental Point-of-Analysis Systems. *ACS Appl. Mater. Interfaces* **2014**, *6* (15), 12971−12978.

(45) Agarwal, V.; Miguel, E. M.-R. Optical characterization of polytype Fibonacci and Thue−Morse quasiregular dielectric structures made of porous silicon multilayers. *J. Phys. D: Appl. Phys.* **2007**, *40* (10), No. 3203.

(46) Martín, J.; Martín-González, M.; Francisco Fernández, J.; Caballero-Calero, O. Ordered three-dimensional interconnected nanoarchitectures in anodic porous alumina. *Nat. Commun.* **2014**, *5*, No. 5130.

Supporting Information

Facile Synthesis of Optical Microcavities by a Rationally Designed Anodization Approach: Tailoring Photonic Signals by Nanopore Structure

Ye Wang, [1, 2] *Yuting Chen,* [1] *Tushar Kumeria,* [1] *Fuyuan Ding,* [1]*Andreas Evdokiou,* [2*] *Dusan Losic,* [1*] *Abel Santos,* [1*]

1. School of Chemical Engineering, The University of Adelaide, Adelaide, SA, 5005
2. Discipline of Surgery, The University of Adelaide, Basil Hetzel Institute, Adelaide, SA, 5005

*Corresponding authors: andreas.evdokiou@adelaide.edu, dusan.losic@adelaide.edu.au, abel.santos@adelaide.edu.au

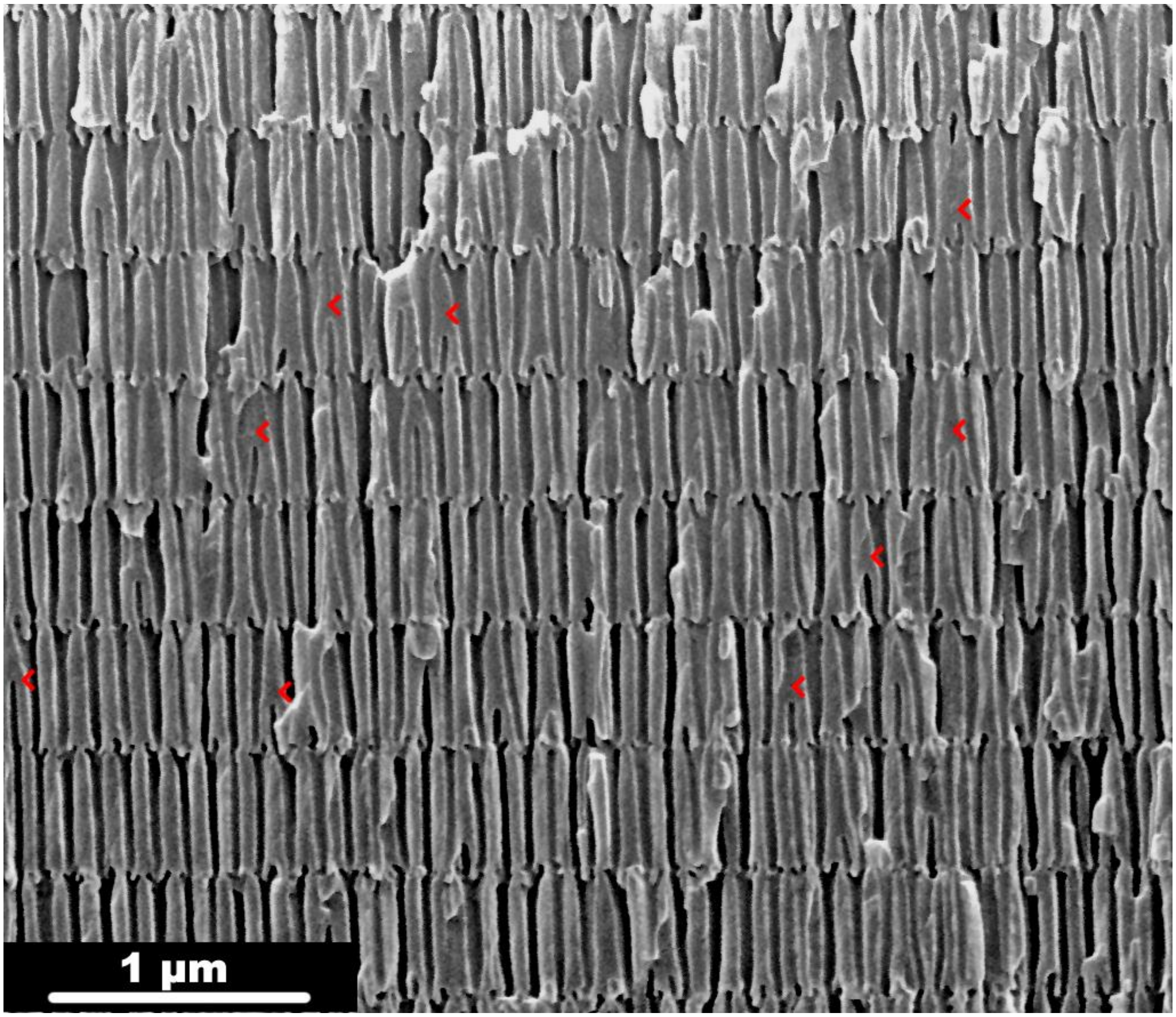

Figure S1 SEM cross-section image of AAO-DBR structure. Red arrow heads denote the end of branching nanopore.

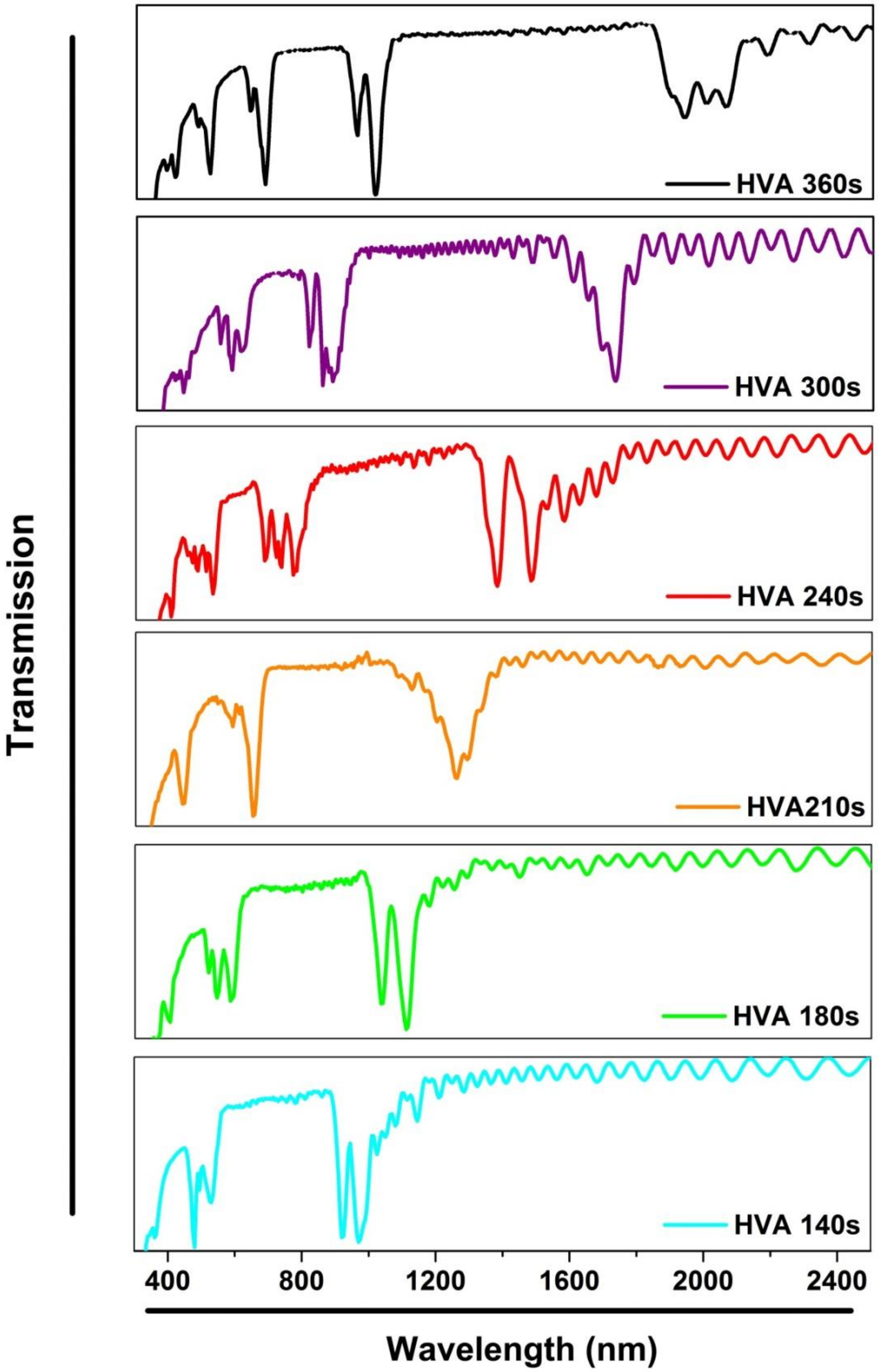

Figure S2 Transmission spectra of AAO microcavities (type I) prepared by different HVA durations.

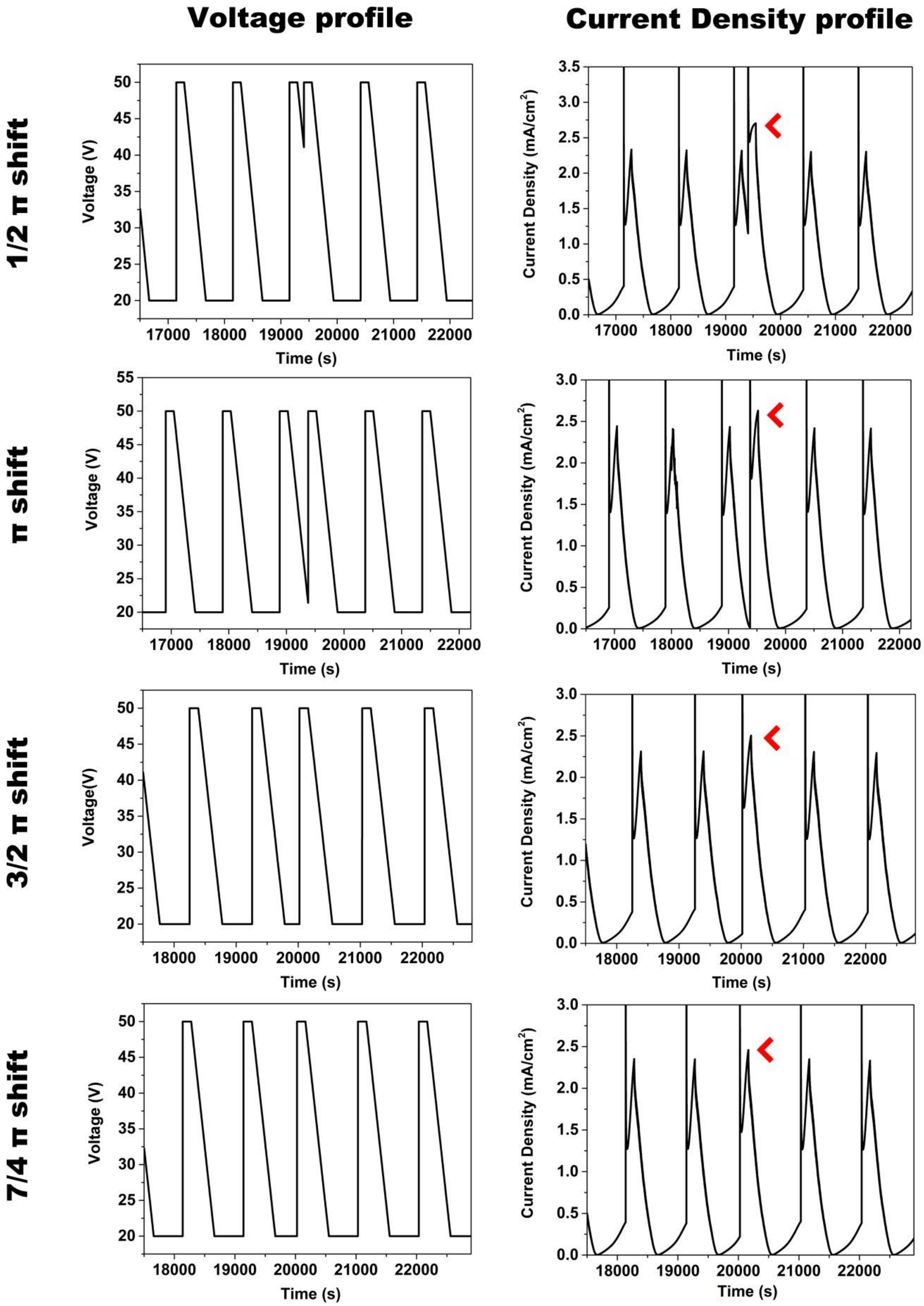

Figure S3 Voltage and current density profile of pulse anodization with programmed phase change after 20 cycles' pulse. Red arrow heads denote the transition of current density corresponding to the phase change of voltage profile.

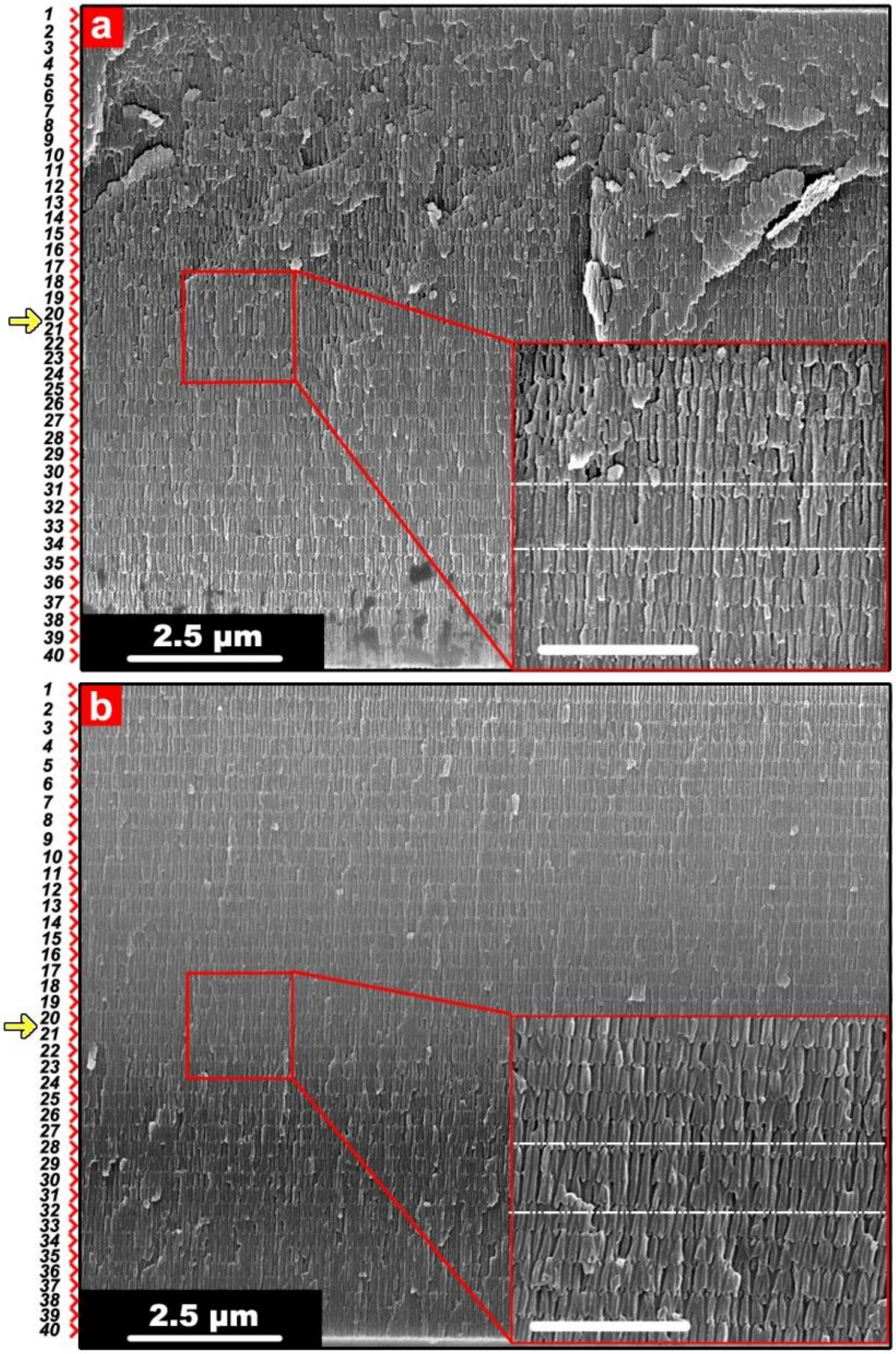

Figure S4 Cross-section SEM images of AAO microcavities (type II) produced by phase shift of refractive index profile at (a) 1/2 π and (b) 7/4 π. The series number of layers islabeled at the left side of images. The induction of phase shift is at the 20th layer. Magnified images are inserted, in which the interfaces of phase shift have been denoted by white dash-line. Inserted scale bar: 1 μm.

3.2 Fabrication of Ultra-Short Anodic Alumina Nanotubes by Galvanostatic Pulse Anodization

3.2.1 Introduction, Significance and Commentary

The aim of this topic is to understand the mechanism of galvanostatic pulse anodization (PA) for the fabrication of anodic alumina nanotubes (AANTs). We found that AANTs can only be produced by PA with high current density, which generates significant heat during PA. Based on this phenomenon, we hypothesized that Joule's heat plays a critical role on the fabrication of AANTs. In this study, we proved that the heat evolution results in an enhanced oxygen generation and a rapid voltage recovery during PA, which consequently facilitated the production of AANTs. The understanding of AANTs fabrication mechanism enables us for the first time to fabricate ultra-short AANTs by reducing pulse duration to one second, and using ethanol modified electrolyte to enhance heat generation. The resulting AANTs with controlled dimensions offer new opportunities for advanced applications such as catalysis, template-assisted nanofabrication and drug delivery.

3.2.2 Publication

This section is a research paper published by Ye Wang, Andreas Evdokiou, Dusan Losic, Abel Santos, Rational Design of Ultra-Short Anodic Alumina Nanotubes by Short-Time Pulse Anodization, *Electrochimica Acta*, **2015**, 154, 379-386.

Statement of Authorship

Title of Paper	Rational Design of Ultra-Short Anodic Alumina Nanotubes by Short-Time Pulse Anodization
Publication Status	☑ Published ☐ Accepted for Publication ☐ Submitted for Publication ☐ Publication Style
Publication Details	Wang, Y.; Santos, A*.; Evdokiou, A.*; Losic, D.*, Rational Design of Ultra-Short Anodic Alumina Nanotubes by Short-Time Pulse Anodization. Electrochimica Acta. 2015, 154, 379-386. (IF=4.086)

Principal Author

Name of Principal Author (Candidate)	Ye Wang		
Contribution to the Paper	Designed project and accomplished 80% of experiments, performed data analysis and prepared manuscript		
Overall percentage (%)	80%		
Signature		Date	31/7/2015

Co-Author Contributions

By signing the Statement of Authorship, each author certifies that:

i. the candidate's stated contribution to the publication is accurate (as detailed above);
ii. permission is granted for the candidate in include the publication in the thesis; and
iii. the sum of all co-author contributions is equal to 100% less the candidate's stated contribution.

Name of Co-Author	Abel Santos		
Contribution to the Paper	manuscript evaluation		
Signature		Date	31/07/15

Name of Co-Author	Andreas Evdokiou		
Contribution to the Paper	manuscript evaluation		
Signature		Date	**11/8/2015**

Name of Co-Author	Dusan Losic		
Contribution to the Paper	manuscript evaluation		
Signature		Date	10/07/2015

Electrochimica Acta 154 (2015) 379–386

Contents lists available at ScienceDirect

Electrochimica Acta

journal homepage: www.elsevier.com/locate/electacta

Rational Design of Ultra-Short Anodic Alumina Nanotubes by Short-Time Pulse Anodization

Ye Wang [a,b], Abel Santos [a,*], Andreas Evdokiou [b,*], Dusan Losic [a,*]

[a] School of Chemical Engineering, The University of Adelaide, Engineering North Building, 5005 Adelaide, Australia
[b] School of Medicine, Discipline of Surgery, The University of Adelaide, Australia

ARTICLE INFO

Article history:
Received 16 November 2014
Received in revised form 9 December 2014
Accepted 9 December 2014
Available online 11 December 2014

Keywords:
anodic aluminum oxide
pulse anodization
anodic alumina nanotube
current density

ABSTRACT

Herein, we report on a rational electrochemical approach based on pulse anodization (PA) of aluminum for the fabrication of ultra-short anodic alumina nanotubes (AANTs) with exquisitely controlled dimensions. AANTs with average length 485 ± 180 nm and outer diameter 90 ± 10 nm were fabricated by PA with 0.3 M sulfuric acid and 10% ethanol. Our findings suggest that extensive Joule's heat generation at the nanopore's base is critical for optimized AANTs' liberation from pulse-anodized anodic aluminum oxide (AAO) nanostructure. The heat evolution results in an enhanced oxygen generation and a rapid voltage recovery during PA. While oxygen generation weakens the conjunction between cells, rapid voltage recovery generates asynchronous inner/outer wall structural modulation, which consequently facilitates structural cleavage of nanotubes along mild anodization/hard anodization (MA/HA) interfaces after acid etching. The understanding of AANTs fabrication mechanism enables us for the first time to fabricate ultra-short AANTs by reducing HA duration down to 1 second and using ethanol for enhancing heat generation. The resulting AANTs with controlled dimensionse and high liberation yield offer new opportunities for advanced applications such as catalysis, template-assisted nanofabrication, optical sensing and drug delivery.

1. Introduction

Aluminum anodization is a well-established nanofabrication technique used to produce a broad range of anodic aluminum oxide (AAO) nanostructures [1,2]. The resulting self-ordered AAO nanostructures have a wide variety of applications in many fields such as sensing, drug delivery, energy storage, medical devices and molecular separation due to their excellent physiochemical properties [3–6]. Another important application of AAO is to be used as a starting material for fabricating other nanotubular structures by template replica technique [7]. AAO template has many unique properties as compared to other hard templates such as controlled pore size/density, high aspect ratio of long-range pores and excellent chemical/thermal stability. Various organic and inorganic nanotube structures have been successfully fabricated by AAO-assisted template approach [8–11]. However, the production yield of this synthesis approach is critically limited by the total area of the AAO template and the time-consuming template fabrication process itself. The most widely used fabrication method of AAO is the so-called mild anodization (MA), which usually takes more than one day to get ordered nanoporous structure with limited self-ordering windows [12]. To achieve simple and fast fabrication of AAO with wide range of pore size, an industrialized anodization technique so-called hard anodization (HA) has been recently utilized in nanotechnology to get high aspect ratio AAO nanostructures within a short time [13,14]. However, HA process is relatively less stable as compared to MA process mainly due to the extensive heat generation as high voltage or current are required.

To overcome these limitations and to fabricate novel nanotube structures from AAO templates, recently Lee et al. developed a facile route for fabricating anodic alumina nanotubes (AANTs) by pulse anodization (PA) [15]. This method significantly improved the yield of nanotube production by creating stack-layered AAO structures during PA and subsequently breaking down the pulse-anodized AAO into individual AANTs under precisely designed condition. Although large quantities of nanotube can be fabricated by this electrochemical approach, the detailed formation mechanism of AANTs has not been exhaustively investigated yet. A better understanding of the generation

---

* Corresponding author.
E-mail addresses: abel.santos@adelaide.edu.au (A. Santos), andreas.evdokiou@adelaide.edu (A. Evdokiou), dusan.losic@adelaide.edu.au (D. Losic).

http://dx.doi.org/10.1016/j.electacta.2014.12.056
0013-4686/

mechanism of AANTs would enable better control over the dimensions, morphology and geometric features of this novel one-dimensional nanomaterial. AANTs have unique hollow lumen structure and stable physiochemical properties, which have great potential to be used as templates for nanofabrication or directly be used as nanocontainer for advanced applications such as drug delivery. Our recent work also demonstrated that as-prepared AANTs with average length 600 nm have excellent biocompatibility and can efficiently deliver high amount of therapeutic drugs for potential cancer therapy [16].

In this article, we report for the first time on the synthesis of ultra-short AANTs by a rationally designed short-time PA. The fabrication of short AANTs (i.e. length < 600 nm) is important to reduce their cytotoxicity given that the reduced length can improve macrophage clearance and reduce intracellular stress [17,18]. A precise control over the AANTs dimensions and geometry can also provide a versatile platform for other advanced applications such as template-assisted nanofabrication. However, the fabrication of ultra-short AANTs has not been achieved yet due to the lack of understanding of this fabrication process. To shed light on this gap, we systematically investigated the impact of the starting layer thickness, the current density, the pulse duration and the electrolyte composition during AANTs fabrication (Scheme 1). The understanding of the intrinsic formation mechanism of AANTs not only provides us a new insight to structurally engineer AAO by PA, but also makes it possible to successfully reduce the resulting length of AANTs down to 485 nm, which is not achievable by the existing nanofabrication methods.

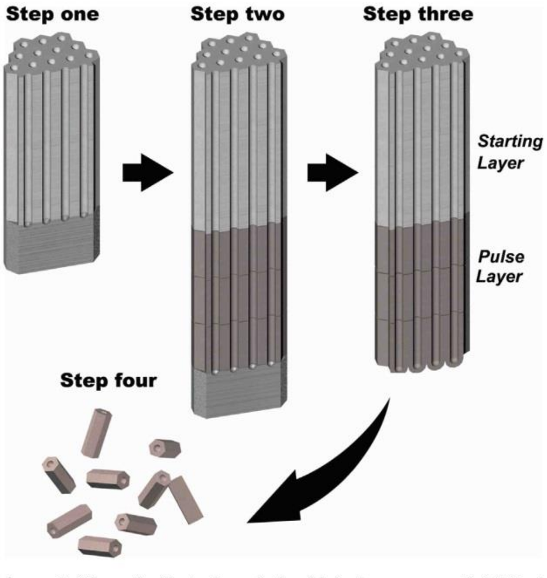

Scheme 1. Schematic illustration of the fabrication process of AANTs by galvanostatic pulse anodization. Electrochemically polished aluminum was first anodized at MA conditions to grow a certain thickness of oxide layer (starting layer). Afterwards, galvanostatic pulse anodization was performed by applying a series of current density pulses to switch the anodization regime between MA and HA conditions. Finally, the remaining aluminum substrate was removed by selective acid etching and liberated AANTs were obtained by acid etching and gentle sonication.

2. Experimental

2.1. Materials and chemicals

Aluminum (Al) foils of thickness 0.32 mm and purity 99.9997% were supplied by Goodfellow Cambridge Ltd. (UK). Sulfuric acid (H_2SO_4), copper(II) chloride ($CuCl_2$), hydrochloric acid (HCl), ethanol (denatured) (C_2H_5OH), perchloric acid ($HClO_4$), chromium trioxide (CrO_3) and phosphoric acid (H_3PO_4) were purchased from Sigma-Aldrich (Australia) and used without further processing. Ultrapure water Option Q–Purelabs (Australia) was used for preparing all the solutions used in this study.

2.2. Fabrication of anodic alumina nanotubes by pulse anodization

AANTs were synthesized by a modified pulse anodization process [15]. Briefly, Al chips 1.5 cm in diameter were first sonicated in ethanol and ultrapure water. Al chips were electropolished prior to anodization in a mixture of ethanol and $HClO_4$ 4:1 (v:v) at 20 V and 5 °C for 3 min. After this, the first anodization step was carried out in an electrolyte of 0.3 M H_2SO_4 at 25 V and 6 °C for 5 h, 10 h, 15 h and 20 h to obtain starting layer thicknesses of 33 μm, 65 μm, 90 μm and 110 μm, respectively. Subsequently, pulse anodization was conducted under galvanostatic conditions at 1 °C with vigorous stirring. The area exposed to the electrolyte solution was 0.95 cm^2 and the current density (j) calculated by dividing the input current by the anodized sample area. This anodization step consisted of a periodic combination of MA and HA pulses in 0.3 M H_2SO_4 electrolyte, which was modified with various concentrations of ethanol ranging from 0% to 25%. After that, the remaining aluminum substrate was removed by wet chemical etching in a mixture of 0.2 M $CuCl_2$ and 6.1 M HCl. Free-standing AANTs were obtained by immersion in the same acid solution for 5 to 30 mins at room temperature followed by gentle ultrasonic treatment for one hour.

2.3. Structural characterizations

The shape and structure of prepared AANTs and pulse-anodized AAO structure were characterized by a transmission electron microscope (FEI Tecnai G2 Spirit TEM) and a field emission gun scanning electron microscope (FEG-SEM FEI Quanta 450). The size distribution of AANTs was calculated by counting approximately 500 AANTs from three independent experiments and their geometric features (i.e. length and inner and outer diameters) established by image analysis using ImageJ software.

3. Result and discussion

3.1. The thickness of starting layer influences the structural modulation of the outer wall of nanopores

Self-ordered AAO films were traditionally fabricated by MA process, in which a slow oxide growth rate (i.e. 2–7 μm/h) is achieved under low current density ($j = 1–5$ mA/cm^2) conditions [12]. In contrast, HA conditions at high current density (i.e. $j > 30$ mA/cm^2) made it possible to produce self-ordered AAO films at high growth rates (i.e. 40–60 μm/h) [13]. Unlike conventional MA process, an oxide layer must be formed on the surface of the aluminum substrate before HA process to suppress breakdown effects, avoid plastic deformation, achieve self-organization and improve the mechanical integrity of the resulting AAO film. For the same reason, a protective oxide layer (i.e. starting layer) is necessary before galvanostatic PA is started due to the high current density at HA condition.

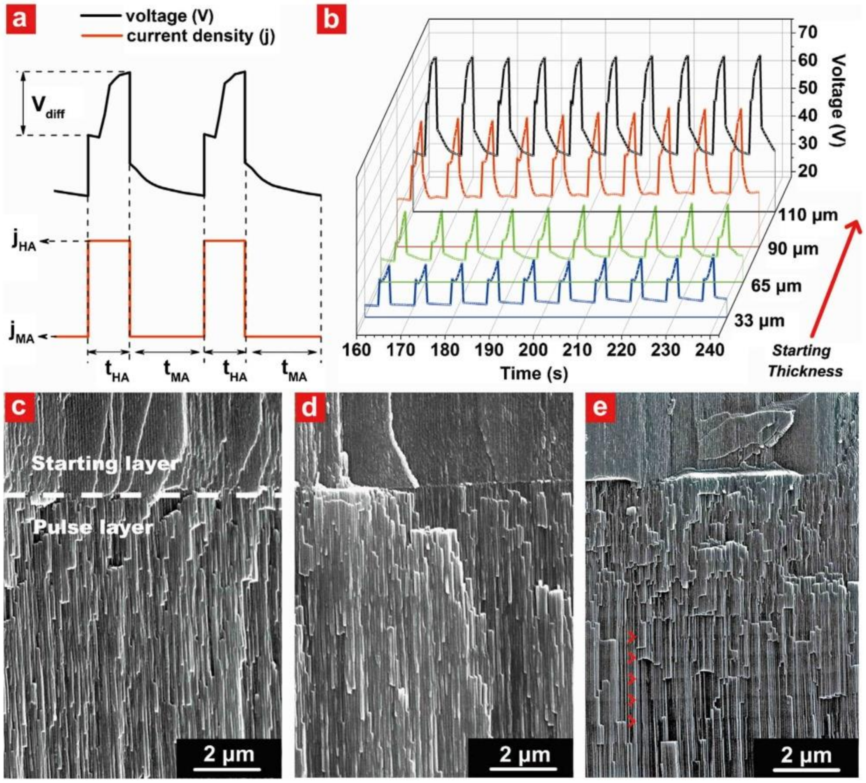

Fig. 1. The fabrication of stack-layer nanostructure by pulse anodization is depend on the starting thickness of AAO. (a) Scheme of HA/MA pulse used for pulse anodization. j_{HA}/j_{MA} is the current density applied to achieve HA/MA conditions; t_{HA}/t_{MA} is pulse durations, and V_{diff} denotes the anodization voltage difference between the starting and ending stage of each HA-pulse. (b) Representative voltage-time profile of pulse anodization with different starting layer thickness. The anodization condition was maintained at $j_{MA} = 3.26$ mA/cm^2/$t_{MA} = 5$ s and $j_{HA} = 368.52$ mA/cm^2 and $t_{HA} = 2$ s. (c–e) Cross-section SEM images of AAO nanostructure with starting layer thickness of 33 µm (c), 65 µm (d) and 110 µm (e). White dash line indicates the interface formed by the transition from MA to HA. Red arrow heads showed the resulting spaced layer structure.

Strikingly, we found that the starting layer thickness directly influences the structural modulation of the outer wall of nanopores during PA (Fig. 1). To study the impact of the starting layer thickness, we first conducted potentiostatic MA instead of HA in order to have a better control over the starting layer thickness. The next step of PA pulses consisted of 30 cycles of current pulses. Each pulse constitutes a HA-pulse followed by a MA pulse as illustrated in Fig. 1a. The voltage-time profiles in Fig.1b clearly showed thickness-dependent voltage recovery effect, where the value of the voltage difference between the starting and ending stage of each HA-pulse (V_{diff}) gradually increased with the starting layer thickness from approximately 5 V at 33 µm to 17 V at 110 µm. Correspondingly, the resulting pulse-anodized AAO nanostructure with starting layer thicknesses of 33 µm and 65 µm did not show significant outer wall modulation, although the space-layered nanostructure could be recognized (Fig. 1c and d); the structural modulation become evident with the starting layer thickness of 110 µm, as shown in Fig. 1e. This structural modulation pattern can directly influence the AANTs fabrication: AANTs can only be obtained from AAO structure with starting layer thickness of 110 µm after acid etching and sonication treatment (Fig. S 1 supporting information).

From these results, we infer that the generation of extensive Joule's heat at the nanopore's bottom during PA might contribute to this thickness-dependent voltage recovery pattern. According to Joule's law of heat, the Joule's heat (Q) at a given time (t) can be expressed as:

$$Q = Rj^2t \tag{1}$$

where R is the electronic resistance of the barrier layer and j is the applied current density. HA conducted at high current density is accompanied by a large evolution of heat as compared to MA. The extensive heat generation can cause the dissolution of aluminum oxide in the acid electrolyte and thus enhance the ionic flow across the oxide barrier layer at the pore bottom, which will eventually lead to electric breakdown [19,20]. Pulse anodization is an effective method to dissipate the Joule's heat by introducing a MA step after HA [21–23]. However, with the increasing thickness of the starting layer, the convective heat transfer in the electrolyte might not be efficient enough to dissipate the generated heat due to the confinement of long-ranged nanopores. Such heat generation at the nanopore bottom can unavoidably lead to the partial dissolution of the oxide barrier layer, thus facilitating the rapid voltage recovery.

Note that so far there is no direct method to measure the *in situ* Joule's heat generation at the nanopore bottom. To verify our hypothesis about the role of heat evolution on AANTs' fabrication, we lowered the HA current density down to 210.52 mA/cm^2 to reduce the heat generation during HA pulse while maintaining the starting layer thickness at 110 µm. Interestingly, no AANTs were obtained within 2 s HA pulse, while AANTs can be readily fabricated by extending HA duration to 10 s. The anodization

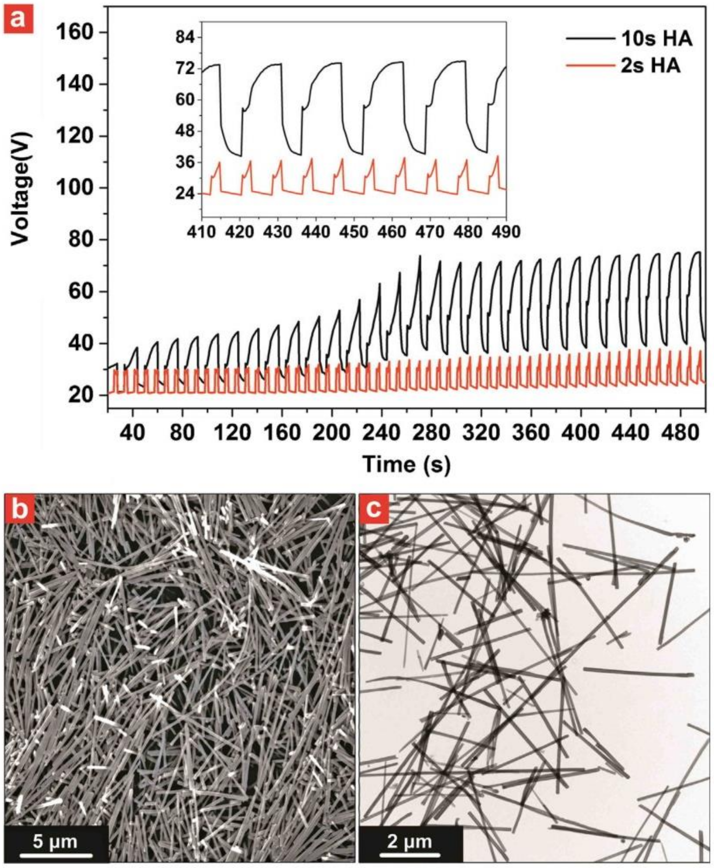

Fig. 2. The effect of reduced current density and extended HA pulse duration on the AANTs fabrication. (a) Representative voltage-time profile at j_{HA} = 210.52 mA/cm^2 and starting layer thickness of 110 μm. HA duration was set to 2 s and 10 s, respectively, followed by 5 s MA pulse at j_{MA} = 3.26 mA/cm^2. A magnified voltage-time profile at the late stage of anodization is shown in the inset. (b) TEM and (c) SEM characterization of AANTs fabricated by 10 s HA with j_{HA} = 210.52 mA/cm^2.

profile in Fig. 2a showed that the reduction of current density significantly retarded the voltage recovery pattern within 2 s HA pulse, which is similar to the pattern of 33 μm and 65 μm starting thicknesses at j_{HA} = 368.52 mA/cm^2. Extending HA duration to 10 s showed a complete voltage recovery pattern with a HA potential difference of approximately 17 V at the late stage of the PA process. In addition, voltage gradually increased with the anodization time during this process and stabilized at 74 V. However, the maximum voltage of 2 s HA pulse did not increase significantly after a number of pulse cycles. This voltage-time pattern strongly indicated that the continuous heat generation during 10 s HA pulse contributes to the sufficient voltage recovery pattern as well as the increasing of anodization voltage to a maximum value. The Joule's heat evolution was significantly reduced at j_{HA} = 210.52 mA/cm^2 as compared to the case of j_{HA} = 368.52 mA/cm^2. Therefore, the generated Joule's heat during a 2 s HA pulse can be efficiently dissipated by the following 5 s MA pulse, which lead to a relative stable anodization voltage at a low value as well as the retarded voltage recovery pattern. Nevertheless, this drawback can be overcome by extending the duration of HA pulse to achieve sufficient voltage recovery and consequently to trigger the modulation of the wall structure (Fig. S 2 supporting information). As a result, AANTs with average length 3.64 ± 1.53 μm can be obtained at the condition of 10 s HA pulse with j_{HA} = 210.52 mA/cm^2 (Fig. 2b and c), while no AANTs was produced under the 2 s HA pulse at j_{HA} = 210.52 mA/cm^2.

3.2. Sufficient oxygen evolution is required for AANTs liberation

The fabrication of AANTs from pulse-anodized AAO film requires the cleavage of the AAO nanostructure at the conjunction of layers as well as between the cell boundaries. Therefore, understanding the mechanism of cell separation effect is of critical importance to improve the liberation of AANTs from pulse anodized AAO films. To characterize the inner porous structure, we prepared microtome sections of pulse anodized AAO nanostructure. As shown in Fig. 3a, a clearly modulation of inner pore structure was observed at the interface of each layer, which is created by the transition of current density between HA and MA regime [22,24]. While the inner diameter of nanopores at the modulation point (i.e. transition between MA and HA pulse) is 8.5 ± 1.8 nm, it becomes 24.5 ± 4.8 nm during the HA pulse. Note that the areas between two adjacent cells appeared to be brighter than the nanopore's wall structure in TEM, indicating the existence of material with less atomic density along cell boundaries (Fig. 3b and c). The generation of gas voids and aluminum hydroxide has long been considered as the main cause of cell separation effect at HA performed under high current density or voltage conditions

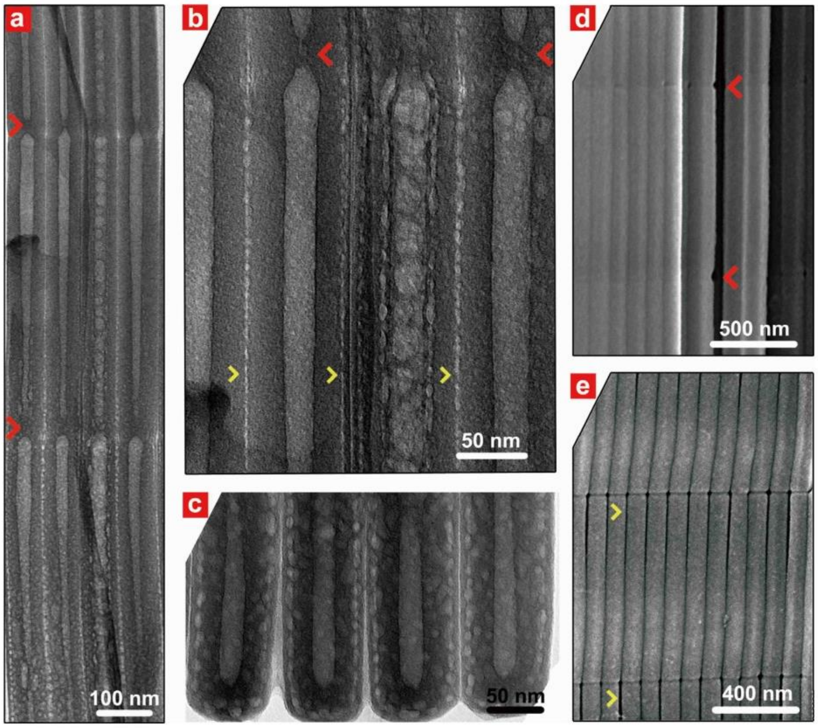

Fig. 3. Evidence of oxygen evolution during pulse anodization. (a-c) TEM characterization of resulting AAO nanostructure fabricated by pulse anodization at the condition of $j_{MA} = 3.26\ mA/cm^2/t_{MA} = 5$ s and $j_{HA} = 368.52\ mA/cm^2$ and $t_{HA} = 2$ s. The cross section image (a) and the bottom image (c) clearly show air voids along the cell boundaries. A magnified cross-section image is shown in (b). (d and e) SEM images of AAO nanostructure before (d) and after (e) acid etching. Red arrow heads show the modulation of the nanoporous structure. Yellow arrow heads show the voids and gaps along the cell boundaries.

[25–27]. We hereby assumed that the compositions of bright layers are possibly aluminum hydroxide and voids generated by the oxygen evolution during PA process. After immersing the AAO film in $HCl/CuCl_2$ solution for a short time, a clear gap along adjacent cell boundaries can be observed, indicating the dissolution of aluminum hydroxide after acid etching (Fig. 3d and e). Therefore, our results are in good agreement with previously published studies, confirming that the generation of aluminum hydroxide and oxygen bubbles along cell boundaries are critical to induce the cell separation during pulse anodization. Since the electrochemical reaction of oxygen evolution is controlled by the current density, it is expected that HA pulses with high current density would produce cell separation effect more efficiently than low HA current density pulses.

3.3. Fabrication of ultra-short AANTs by modifying electrolyte

Fabricating ultra-short AANTs is of great interest to improve their future application such as drug delivery. We attempted to reduce HA pulse duration to shorten the resulting length of AANT. However, the resulting voltage-time pattern showed an incomplete voltage recovery during short-time PA, which led to the failure of AANTs production (Fig. 4a). As shown in the above sections, the fabrication of AANTs is controlled by current density, HA duration and heat generation during PA. Although reduced HA duration can shorten the resulting thickness of HA layer section at a given current intensity, it unavoidably leds to a reduced heat generation during HA, which is unfavorable for AANTs fabrication. Therefore, other strategies need to be established to maintain the heat generation during short time PA.

We found that adding certain amount of ethanol (EtOH) (5–10%v) is necessary for obtaining liberated AANTs when short-time HA pulses are used. Fig. 4a shows the representative current-voltage profiles with 1 s HA pulse at $j_{HA} = 368.52\ mA/cm^2$. The addition of 10% EtOH to the electrolyte can generate efficient voltage recovery within 1 second HA pulse as compared to the PA with 0.3 M H_2SO_4. The resulting pulse-anodized AAO clearly showed spaced-layer structure with approximately 500 nm thickness (Fig. 4b). After liberation, AANTs with average length 485 ± 180 nm can be obtained (Fig. 4c and d). Note that the average inner wall diameter is 33.0 ± 8.0 nm, which is slightly bigger than that of the pore diameter before liberation. This can be associated to acid dissolution effect during the liberation process.

We assume that EtOH can promote heat generation during short-time PA, which facilitated the liberation of AANTs from pulse-anodized AAO nanostructure. To understand the function of ethanol during short-time PA, we performed galvanostatic HA at $j_{HA} = 368.52\ mA/cm^2$ with a starting layer thickness of 110 μm (Fig. 5). HA in 0.3 M H_2SO_4 showed a typical voltage profile characteristic of galvanostatic anodization [1]. Voltage reaches a maximum value during the initial stage of this process and becomes stable at appromixtely 69 V. Then, after this initial stage, voltage increases gradually due to the intensive Joule's heat generation during HA. Finally, the local breakdown of the AAO film takes place after 16 mins, which is characterized by the abrupt increament of the anodization voltage. Note that we observed plastic deformation and non-uniform thickness distribution of the anodic film after long time HA, which is caused by uneven-distributed heat generation and current flow at the pore bottom (Fig. S 3 supporting information) [19,20]. In contrast, when HA was

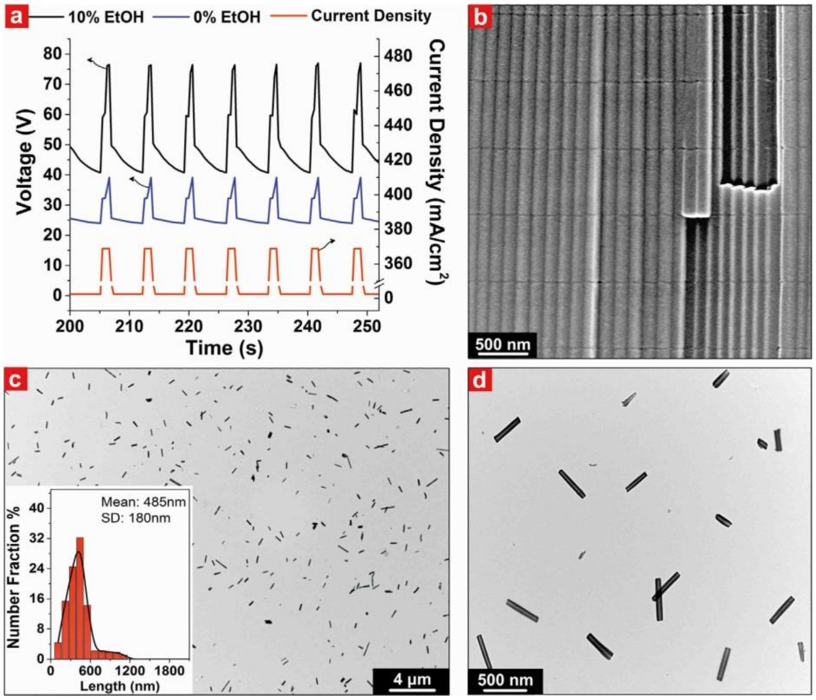

Fig. 4. Fabrication of ultra-short AANTs by manipulating electrolyte composition. (a) A representative voltage-current anodization profile under the condition of 1 s HA pulse. The electrolyte with 0.3 M H_2SO_4 did not create rapid voltage recovery. The addition of 10% ethanol can efficiently induce around 17 V voltage difference during 1 s HA pulse (b) SEM cross-section view of the AAO nanostructure fabricated by the condition of 1 s HA pulse. (c and d) TEM characterization and size distribution of resulting ultra-short AANTs.

performed in EtOH-modified H_2SO_4 electrolyte, a significant faster breakdown pattern was observed as compared to the electrolyte system without ethanol. HA with 5%v EtOH showed steady porous growth pattern at the beginning, but electric breakdown happened after 362 ± 10 s. HA with 10%v EtOH showed a rapid breakdown pattern after 130 ± 20 s. Furthemore, we found out that the breakdown effect can happen in a few seconds when the concentration of EtOH is increased up to 20%v. From these results we hypothesize that the ethanol concentration-dependant breakdown effect is caused by the rapid heat generation at the bottom of the nanopores, which leads to the catastrophic local flow of current across the oxide barrier layer. EtOH has been frequently used as a coolant to achieve HA condition under high electric field conditions at temperatures below 0 °C [28–30]. However, our result demonstrated that EtOH is not efficient to dissipate the heat generated during HA process when the temperature of the electrolyte is relatively high. The rapid heat generation at the bottom of the nanopores, however, can be efficiently dissipated by PA, and thus a steady growth of the anodic film can be achieved. As discussed above, the voltage recovery rate during HA is directly associated with localized heat generation. Therefore, the rapid heat generation in EtOH-modified electrolyte contributed to the fast voltage recovery within a short-time HA pulse (1 s), which generated sufficient structural modulation and cell separation for successful AANT liberation.

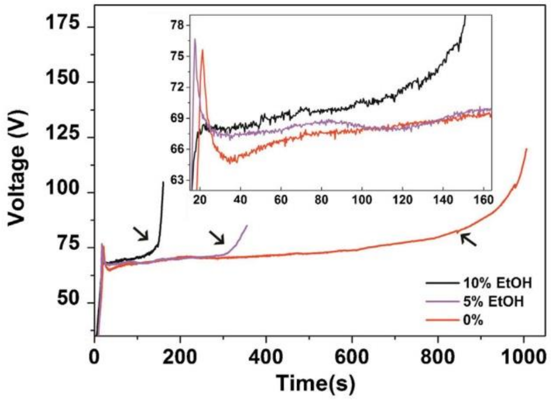

Fig. 5. HA anodization profile with ethanol-modified electrolyte. AAO film with starting layer thickness of 110 μm was directly anodized at a constant current density of 368.52 mA/cm². Ethanol addition can significantly shorten the breakdown time. Black arrows indicate the breakdown time point for each percentage of ethanol. Insert depicts an enlarged voltage-time profile of HA during the anodization time between 20 s to 160 s.

We also found that as-prepared ultra-short AANTs have a unique narrow ending at one side (Fig. 6c). This structure is engineered by switching the current density between HA and MA regimes, as illustrated in Fig. 3. Nonetheless, AANTs should have narrow structures on both ends if nanotubes were evenly cleaved at the site of structural modulation of outer wall. To investigate the liberation mechanism of AANTs, we performed SEM characterization of the pulse-anodized AAO nanostructures after extensive acid etching. It is evident that the connection between layers were completely removed and the nanotubes started to detach from the AAO film after long time etching (Fig. 6a). At higher magnification,

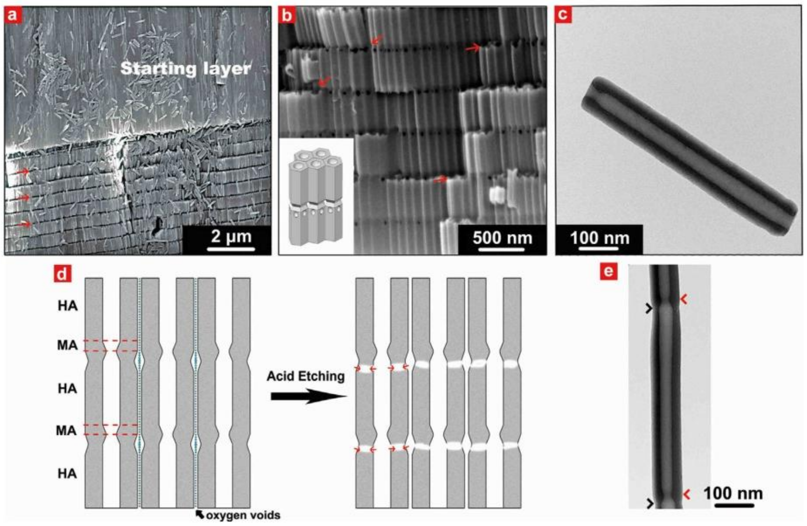

Fig. 6. Effect of chemical etching of pulse-anodized AAO structure on AANTs liberation. (a) A SEM cross-section image and schematic (bottom inset) of pulse anodized AAO structure after extensive acid etching. The anodization condition was $j_{MA} = 3.26\ mA/cm^2/t_{MA} = 5s$ and $j_{HA} = 368.52\ mA/cm^2/t_{HA} = 1s$. (b) A representative magnified SEM cross-section image showed that periodically perforated pores appeared at the region close to the modulated wall structure, which corresponded to the starting stage of HA pulse. Red arrows show the cleavage of AANTs after etching. (c) A representative TEM image of single a AANTs, showing a unique narrow ending structure at one side of the nanotubes. (d) Schematic illustration of chemical etching process. The asynchronous inner/outer wall structural modulation generates a weak conjunction along the interface of HA/MA segment, which can be preferably removed after acid etching. (e) TEM characterization of a single liberated AANTs with joint connection. The back/red arrow heads show outer/inner wall modulation respectively.

periodically perforated pores can be seen at the area close to the modulated wall structure, which corresponds to the starting stage of HA pulse (Fig. 6b). The formation of perforated pores is due to the selective chemical dissolution at the position where the thickness of the pore wall structure is the thinnest [31]. As discussed above, the modulation of the inner pore diameter happened at the time point when current density was switched between HA and MA regimes [22,24], while the outer pore modulation was engineered by the voltage recovery effect at the beginning of HA pulse. Therefore, the structural modulation of outer pore wall should happen after the inner wall modulation, which created a thinner wall structure as compared to the HA-segment and MA-segment (Fig. 6d). This thin layer can be etched faster than other area, and thus created the perforated pores and weakness conjunction along the interface of HA-MA segment. This liberation mechanism is well supported by the finding that AANTs with joint connections have asynchronous inner/outer wall structural modulation (Fig. 6e). The elucidation of AANTs' liberation mechanism is of fundamental importance for AANTs fabrication. It can be expected that more sophisticated AANTs structure can be fabricated by using PA to engineer inner pore geometry and simultaneously generate structural modulation of outer pore for AANTs liberation.

4. Conclusion

In summary, we have reported an innovative approach for fabricating ultra-short AANTs by galvanostatic PA. Out results proved that the heat generation plays a key role for AANTs fabrication. Sufficient heat generation at the pore bottom is necessary to achieve the rapid voltage recovery and oxygen evolution for creating weakened conjunctions along cell boundaries as well as along MA/HA interfaces. We have demonstrated that creating the starting porous layer with specific thickness (110 µm) and manipulating the electrolyte composition with EtOH are essential factors to produce ultra-short AANT under short-time PA. These findings not only improve our understanding of PA of aluminum, but also provide a facile, comprehensive and cost-competitive method to fabricate large quantities of well-defined ultra-short AANTs nanostructures with average length 485 ± 180 nm. These nanostructures afford great opportunities in a broad field of applications such as catalysis, sensing, template-assisted nanofabrication, energy storage and drug delivery due to their unique hollow nanostructure and superior thermal/biological stability.

ACKNOWLEDGMENTS

This research was supported by the Australian Research Council (ARC) and the National Health and Medical Research Council (NHMRC) through the grants DP120101680,FT110100711, DE14010054 and APP627015. Authors thank Mr. Jason Peak, Mr. Michael Jung and Mr. Jeffrey Hiorns from the mechanical workshop for their help and support with the fabrication of the experimental set-ups used in this study. Authors appreciate the Adelaide Microscopy (AM) centre for FEG-SEM and TEM characterization. Ye Wang appreciate the scholarship support from China Scholarship Council.

Appendix A. Supplementary data

Supplementary data associated with this article can be found, in the online version, at http://dx.doi.org/10.1016/j.electacta.2014.12.056.

References

[1] W. Lee, S.-J. Park, Porous Anodic Aluminum Oxide: Anodization and Templated Synthesis of Functional Nanostructures, Chem.Rev. 114 (15) (2014) 7487–7556.
[2] A.M. Jani, D. Losic, N.H. Voelcker, Nanoporous anodic aluminium oxide: Advances in surface engineering and emerging applications, Prog. Mater. Sci. 58 (5) (2013) 636–704.

[3] A. Santos, M.S. Aw, M. Bariana, T. Kumeria, Y. Wang, D. Losic, Drug-releasing implants: current progress, challenges and perspectives, J. Mater. Chem. B 2 (2014) 6157–6182.
[4] T. Kumeria, M.M. Rahman, A. Santos, J. Ferré-Borrull, L.F. Marsal, D. Losic, Nanoporous Anodic Alumina Rugate Filters for Sensing of Ionic Mercury: Toward Environmental Point-of-Analysis Systems, ACS Appl. Mater. Interfaces 6 (2014) 12971–12978.
[5] P. Banerjee, I. Perez, L. Henn-Lecordier, S.B. Lee, G.W. Rubloff, Nanotubular metal-insulator-metal capacitor arrays for energy storage, Nat Nano 4 (2009) 292–296.
[6] G.D. Sulka, K. Hnida, A. Brzózka, pH sensors based on polypyrrole nanowire arrays, Electrochim. Acta 104 (2013) 536–541.
[7] Y. Liu, J. Goebl, Y. Yin, Templated synthesis of nanostructured materials, Chem. Soc. Rev 42 (2013) 2610–2653.
[8] G.D. Sulka, A. Brzózka, L. Liu, Fabrication of diameter-modulated and ultrathin porous nanowires in anodic aluminum oxide templates, Electrochim. Acta 56 (2011) 4972–4979.
[9] J. Martín, M. Martín-González, J. Francisco Fernández, O. Caballero-Calero, Ordered three-dimensional interconnected nanoarchitectures in anodic porous alumina, Nat Commun 5 (2014) , doi:http://dx.doi.org/10.1038/ncomms6130.
[10] H. Masuda, K. Fukuda, Ordered Metal Nanohole Arrays Made By a 2-Step Replication Of Honeycomb Structures Of Anodic Alumina, Science 268 (5216) (1995) 1466–1468.
[11] G. Meng, Y.J. Jung, A. Cao, R. Vajtai, P.M. Ajayan, Controlled fabrication of hierarchically branched nanopores, nanotubes, and nanowires, Proc. Natl. Acad. Sci. U. S. A. 102 (20) (2005) 7074–7078.
[12] K. Nielsch, J. Choi, K. Schwirn, R.B. Wehrspohn, U. Gösele, Self-ordering Regimes of Porous Alumina: The 10 Porosity Rule, Nano Lett. 2 (2002) 677–680.
[13] W. Lee, R. Ji, U. Gosele, K. Nielsch, Fast fabrication of long-range ordered porous alumina membranes by hard anodization, Nat Mater 5 (2006) 741–747.
[14] A. Santos, J.M. Montero-Moreno, J. Bachmann, K. Nielsch, P. Formenti'n, J. Ferre'-Borrull, J. Pallarès, W.L.s.F Marsal, Understanding Pore Rearrangement during Mild to Hard Transition in Bilayered Porous Anodic Alumina Membranes, ACS Appl. Mater. Interfaces 3 (2011) 1925–1932.
[15] W. Lee, R. Scholz, U. Gösele, Nano Letters, A Continuous Process for Structurally Well-Defined Al_2O_3 Nanotubes Based on Pulse Anodization of Aluminum, Nano Lett. 8 (2008) 2155–2160.
[16] Y. Wang, A. Santos, G. Kaur, A. Evdokiou, D. Losic, Structurally engineered anodic alumina nanotubes as nano-carriers for delivery of anticancer therapeutics, Biomaterials 35 (2014) 5517–5526.
[17] A.E. Nel, L. Madler, D. Velegol, T. Xia, E.M.V. Hoek, P. Somasundaran, F. Klaessig, V. Castranova, M. Thompson, Understanding biophysicochemical interactions at the nano-bio interface, Nat Mater 8 (2009) 543–557.
[18] K. Kostarelos, The long and short of carbon nanotube toxicity, Nat Biotech 26 (2008) 774–776.
[19] S. Tajima, Luminescence: breakdown and colouring of anodic oxide films on aluminium, Electrochim. Acta 22 (1977) 995–1011.
[20] J.M. Albella, I. Montero, J.M. Martinez-Duart, A theory of avalanche breakdown during anodic oxidation, Electrochim. Acta 32 (1987) 255–258.
[21] W. Lee, K. Schwirn, M. Steinhart, E. Pippel, R. Scholz, U. Gosele, Structural engineering of nanoporous anodic aluminium oxide by pulse anodization of aluminium, Nat Nano 3 (2008) 234–239.
[22] L. Woo, K. Jae-Cheon, Highly ordered porous alumina with tailor-made pore structures fabricated by pulse anodization, Nanotechnology 21 (2010) 485304.
[23] C.K. Chung, W.T. Chang, M.W. Liao, H.C. Chang, C.T. Lee, Fabrication of enhanced anodic aluminum oxide performance at room temperatures using hybrid pulse anodization with effective cooling, Electrochim. Acta 56 (2011) 6489–6497.
[24] W. Lee, J.-C. Kim, U. Gösele, Spontaneous Current Oscillations during Hard Anodization of Aluminum under Potentiostatic Conditions, Adv. Funct. Mater. 20 (2010) 21–27.
[25] L. Yi, L. Zhiyuan, H. Xing, L. Yisen, C. Yi, Investigation of intrinsic mechanisms of aluminium anodization processes by analyzing the current density, RSC Adv. 2 (2012) 5164–5171.
[26] S.Z. Chu, K. Wada, S. Inoue, M. Isogai, A. Yasumori, Fabrication of Ideally Ordered Nanoporous Alumina Films and Integrated Alumina Nanotubule Arrays by High-Field Anodization, Adv. Mater. 17 (2005) 2115–2119.
[27] S. Zhao, K. Chan, A. Yelon, T. Veres, Novel Structure of AAO Film Fabricated by Constant Current Anodization, Adv. Mater. 19 (2007) 3004–3007.
[28] L. Yanbo, Z. Maojun, M. Li, S. Wenzhong, Fabrication of highly ordered nanoporous alumina films by stable high-field anodization, Nanotechnology 17 (2006) 5101.
[29] Y.B. Li, M.J. Zheng, L. Ma, High-speed growth and photoluminescence of porous anodic alumina films with controllable interpore distances over a large range, Appl. Phys. Lett. 91 (2007) 073109-073109-073103.
[30] L. Yi, L. Zhiyuan, C. Shuoshuo, H. Xing, H. Xinhua, Novel AAO films and hollow nanostructures fabricated by ultra-high voltage hard anodization, Chem. Commun. 46 (2010) 309–311.
[31] D. Losic, D. Losic, Preparation of Porous Anodic Alumina with Periodically Perforated Pores, Langmuir 25 (2009) 5426–5431.

Supporting Information

Rational Design of Ultra-Short Anodic Alumina Nanotubes by Short-Time Pulse Anodization

Ye Wang, [a, b] Abel Santos,* [a] Andreas Evdokiou,* [b] Dusan Losic,* [a]

[a] School of Chemical Engineering, The University of Adelaide, Engineering North Building, 5005 Adelaide, Australia.

[b] School of Medicine, Discipline of Surgery, The University of Adelaide

* E-mails: abel.santos@adelaide.edu.au / dusan.losic@adelaide.edu.au / andreas.evdokiou@adelaide.edu

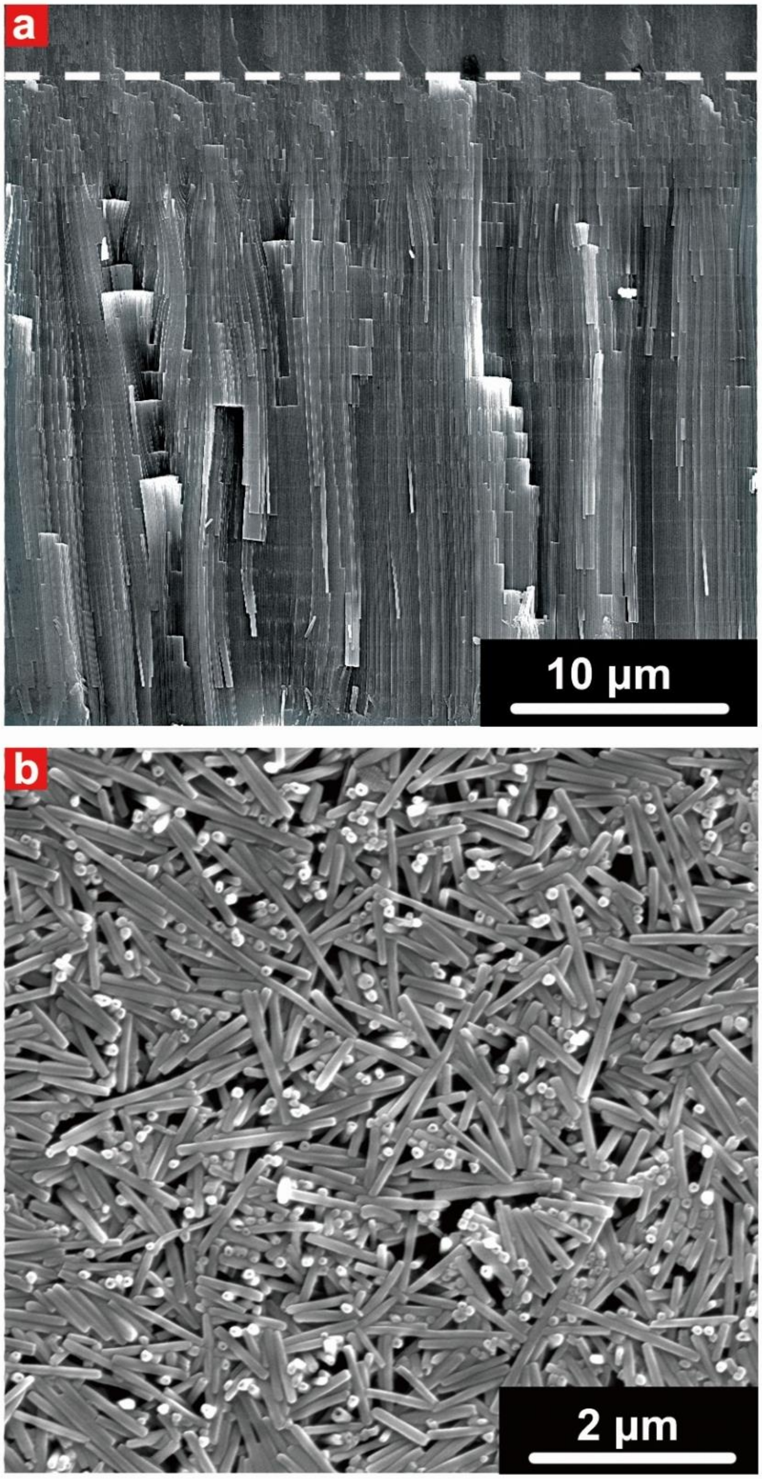

Figure S 1 (a) Cross-section SEM image of pulse anodized AAO nanostructure synthesised at the condition of j_{MA} = 3.26 mA/cm^2/ t_{MA} = 5s and j_{HA}= 368.52 mA/cm^2 / t_{HA}= 2 s. White dash line denotes the interface between MA layer and pulse layer. (b) SEM images of AANTs after liberation.

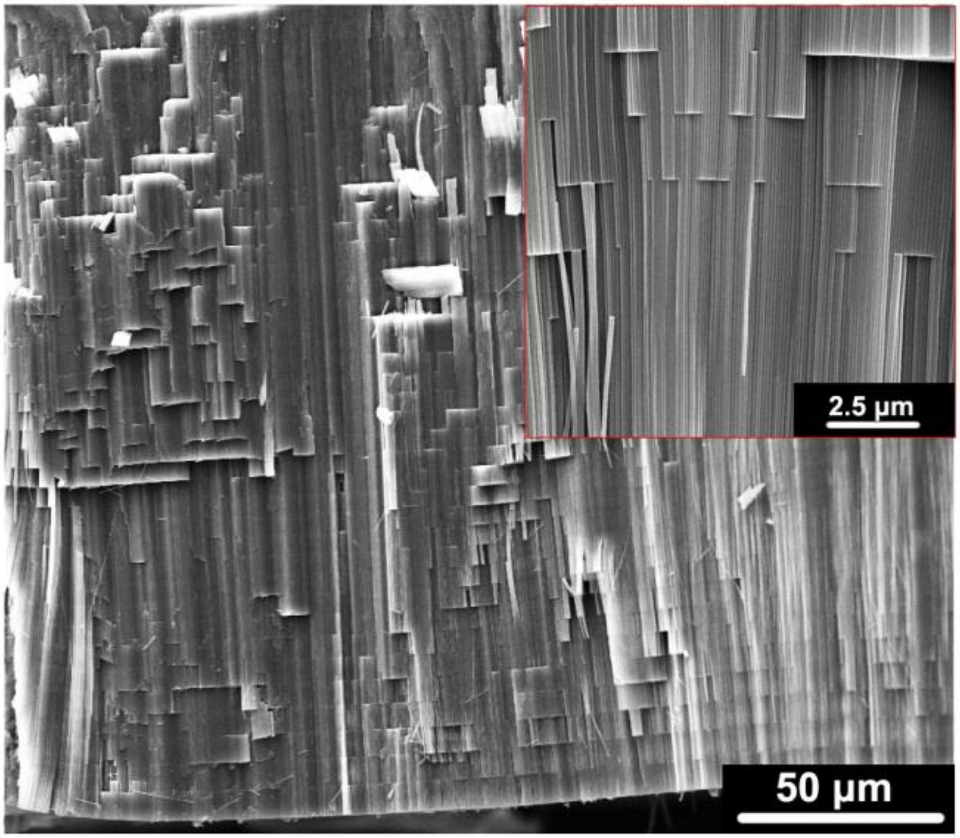

Figure S 2 Cross-section SEM image of pulse anodized AAO nanostructure synthesised at the condition of j_{MA} = 3.26 mA/cm^2/ t_{MA} = 5 s and j_{HA} = 210.52 mA/cm^2 / t_{HA} = 10 s. Inset is an enlarged view of cross-section SEM image.

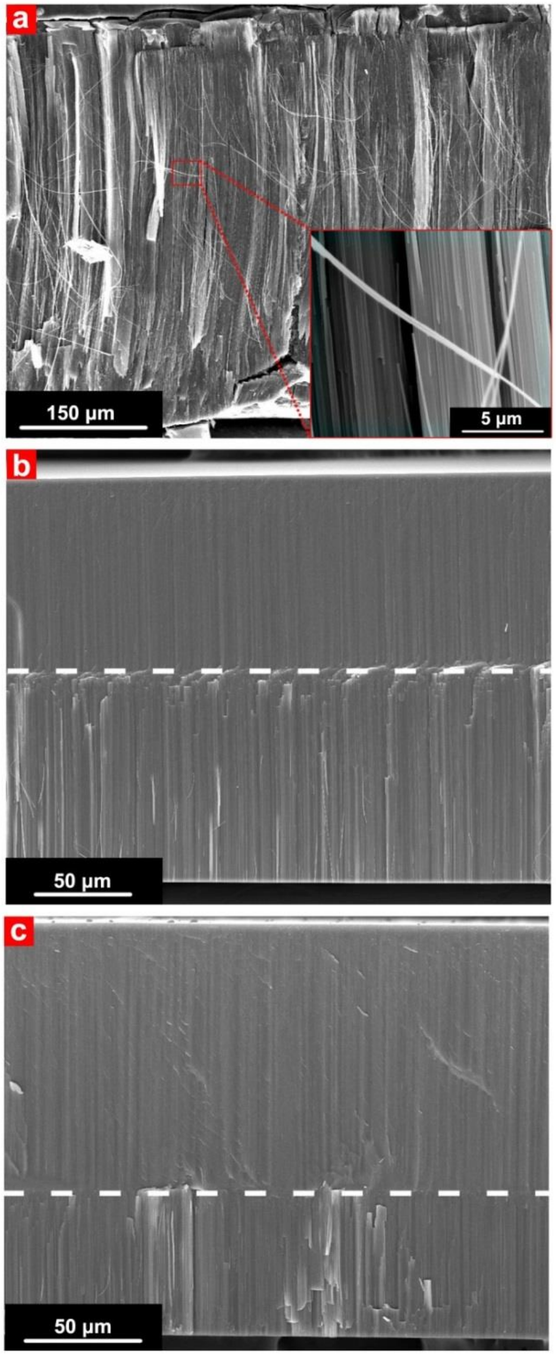

Figure S 3 Hard anodization (HA) with a starting layer thickness of 110 μm at constant current intensity of 368.52 mA/cm^2. (a and b) SEM image of AAO after (a) 16 mins HA and (b) 6 mins under 0.3 M H_2SO_4 condition. Inset shows a magnified SEM image of AAO after 16 mins HA, showing significant cell sepeartion effect. (c) SEM cross-section characterization of AAO after 150 s HA with 0.3 M H_2SO_4 and 10% ethanol. HA was stopped when electri-breakdown happened. The resulting layer thickness is approximately 50 μm. It is evident that the HA duration and resulting AAO thickness is limited by ethanol mixture. White dash line denotes the interface between MA layer and pulse layer.

Chapter 4 Cytotoxicity Study of Anodic Alumina Nanotubes

4.1 Introduction, Significance and Commentary

In the previous chapter, the mechanisms of structurally engineering AAO and the fabrication of anodic alumina nanotubes (AANTs) have been discussed. AANTs are ideal nanomaterial models to study bio-nano interactions and drug delivery due to their intrinsic bio-inert property and well-controlled morphology. However, the toxicity of AANTs is still unknown. The aim of this chapter is to understand the toxicity paradigms of anodic alumina nanotubes (AANTs) regarding to the aspect ratios. Aspect ratio is defined as the ratio of the length and width of a nanomaterial in two dimensions. In this study AANTs with different aspect ratio (AR) ranging from 7.8 to 63.3 are used to study toxicity *in vitro*. Cytotoxicity studies were conducted *in vitro* with mouse macrophage cell line RAW 264.7 and human breast cancer cell line MDA-MB 231-TXSA. The presented results successfully identified the aspect ratio-dependent toxicity patterns of AANTs, in which the toxic AR threshold of AANTs was determined to be 7.8. This study demonstrated the impact of nanomaterials' AR to cell functions at the level of sub-cellular organelles, and also highlighted the significance of using high-throughput toxicity screening platform for rapid establishing hierarchical nanotoxicity assessment.

4.2 Publication

This section is a research paper published by Ye Wang, Gagandeep Kaur, Aneta Zysk, Vasilios Liapis, Shelley Hay, Abel Santos, Dusan Losic, Andreas Evdokiou, Systematic in vitro nanotoxicity study on anodic alumina nanotubes with engineered aspect ratio: Understanding nanotoxicity by a nanomaterial model, *Biomaterials*, **2015**, 46, 117-130.

Statement of Authorship

Title of Paper	Systematic in vitro nanotoxicity study on anodic alumina nanotubes with engineered aspect ratio: Understanding nanotoxicity by a nanomaterial model
Publication Status	☑ Published ☐ Accepted for Publication ☐ Submitted for Publication ☐ Publication Style
Publication Details	Wang, Y.; Kaur, G.; Zysk, A.; Liapis, V.; Hay, S.; Santos, A.*; Losic, D.*; Evdokiou, A.*: Systematic in vitro nanotoxicity study on anodic alumina nanotubes with engineered aspect ratio: Understanding nanotoxicity by a nanomaterial model. Biomaterials 2015, 46,117-130. (IF=8.312)

Principal Author

Name of Principal Author (Candidate)	Ye Wang		
Contribution to the Paper	Designed project and accomplished 80% of experiments, performed data analysis and prepared manuscript		
Overall percentage (%)	80%		
Signature		Date	31/7/2015

Co-Author Contributions

By signing the Statement of Authorship, each author certifies that:

i. the candidate's stated contribution to the publication is accurate (as detailed above);
ii. permission is granted for the candidate in include the publication in the thesis; and
iii. the sum of all co-author contributions is equal to 100% less the candidate's stated contribution.

Name of Co-Author	Gagandeep Kaur		
Contribution to the Paper	Assisted in part of experiment		
Signature		Date	3/08/2015

Name of Co-Author	Aneta Zysk		
Contribution to the Paper	Assisted in part of experiment		
Signature		Date	11/08/15

Name of Co-Author	Vasilios Liapis		
Contribution to the Paper	Assisted in part of experiment		
Signature		Date	3/8/15

Name of Co-Author	Shelley Hay		
Contribution to the Paper	Assisted in part of experiment		
Signature		Date	3/8/15

Name of Co-Author	Andreas Evdokiou		
Contribution to the Paper	Supervised development of work, helped in data interpretation and manuscript evaluation		
Signature		Date	***11/8/2015***

Name of Co-Author	Abel Santos		
Contribution to the Paper	Supervised development of work, helped in data interpretation and manuscript evaluation		
Signature		Date	31/07/15

Name of Co-Author	Dusan Losic		
Contribution to the Paper	Supervised development of work, helped in data interpretation and manuscript evaluation		
Signature		Date	10/07/2015

Biomaterials 46 (2015) 117–130

Contents lists available at ScienceDirect

Biomaterials

journal homepage: www.elsevier.com/locate/biomaterials

Systematic *in vitro* nanotoxicity study on anodic alumina nanotubes with engineered aspect ratio: Understanding nanotoxicity by a nanomaterial model

Ye Wang [a, b], Gagandeep Kaur [a, b], Aneta Zysk [b], Vasilios Liapis [b], Shelley Hay [b],
Abel Santos [a, *], Dusan Losic [a, *], Andreas Evdokiou [b, *]

[a] *School of Chemical Engineering, The University of Adelaide, Adelaide, SA 5005, Australia*
[b] *Discipline of Surgery, Basil Hetzel Institute, The University of Adelaide, Adelaide, SA 5005, Australia*

ARTICLE INFO

Article history:
Received 22 August 2014
Accepted 16 December 2014
Available online

Keywords:
Anodic alumina nanotubes
Aspect ratio
Nanotoxicity
Apoptosis
Lysosome injury
Endoplasmic reticulum stress

ABSTRACT

Here, we report a detailed and systematic approach for studying the *in vitro* nanotoxicity study of high aspect ratio (HAR) nanomaterials using anodic alumina nanotubes (AANTs) as a nanomaterial model. AANTs with bio-inert properties and tailored aspect ratios ranging from 7.8 to 63.3 were synthesized by an electrochemical pulse anodization process. Cytotoxicity studies were conducted with RAW 264.7 mouse macrophage cells and MDA-MB 231-TXSA human breast cancer cells through several toxicity parameters, including cell viability and morphology, pro-inflammatory response, mitochondrial depolarization, lysosomal membrane permeabilization (LMP), induction of autophagy and endoplasmic reticulum (ER) stress. The resulting toxicity patterns were cell-type dependent and strongly related with AANTs dose, length of time, and importantly the AR of AANTs. Long AANTs triggered enhanced cell death, morphological changes, tumor necrosis factor α (TNF-α) release, LMP and ER stress than short AANTs. The toxic AR window of AANTs was determined to be 7.8, which is shorter than that of other previously reported HAR nanomaterials. This toxic AR window provides a promising opportunity to control the nanotoxicity of HAR nanomaterials for their advanced drug delivery application.

1. Introduction

The unprecedented research on the development of engineered nanomaterials for clinical applications is characterized as one of the most significant events in the 21st century [1]. However, the increasing development of nanomaterials has at the same time raised great concerns about their potential health hazards. Recently, high aspect ratio (HAR) nanomaterials have gained special attention due to their asbestos fiber-like morphology and potential toxicity. HAR nanomaterials can have a dramatic impact when in contact with living organisms as compared to their sphere form [2,3]. Biodegradable HAR nanomaterials such as ZnO [4] can break into shorter fibers, which facilitate macrophage clearance. Nonetheless, they are suspect of other pathogenicity paradigms such as the dissolution of toxic cations [5]. Biopersistent nanofibers with stiff nanostructures can induce significant inflammation, fibrosis or granuloma when these nanostructures are too long to be phagocytized by macrophages. Carbon nanotubes (CNTs) as the most well-known HAR nanomaterial can trigger pulmonary toxicity due to fibrosis, which is mainly caused by macrophage activation, TGF-β induction and enhanced collagen deposition [6,7]. Shorter CNTs (<5 μm) are normally considered less toxic than longer ones because of their efficient macrophage clearance [8]. However, a recent study has demonstrated the carcinogenic potential of short single-wall carbon nanotubes (SWCNTs) (<1.2 μm) through chronic exposure of human lung epithelial cells to SWCNTs. SWCNTs-transformed cells exhibited many cancer hallmarks such as increased angiogenesis, apoptosis resistance and readily formed tumors when transplanted in nude mice [9]. Other inorganic biopersistent HAR nanomaterials, such as boron nitride nanotubes [10], cerium oxide (CeO_2) nanorods [3], silicon [11], nickel [12] and silver nanowires [13] also displayed length-dependent acute toxicities in both *in vitro* and *in vivo* model systems. However, these nanomaterials contain other cytotoxic factors such as active surface chemistry [14], intrinsic peroxidase-like activity [15], or metal impurities [16], which inevitably contribute to

---

[*] Corresponding authors.
E-mail addresses: abel.santos@adelaide.edu.au (A. Santos), dusan.losic@adelaide.edu.au (D. Losic), andreas.evdokiou@adelaide.edu (A. Evdokiou).

http://dx.doi.org/10.1016/j.biomaterials.2014.12.008
0142-9612/

the acute toxicity by reactive oxygen species (ROS) generation on their active surface [17]. Therefore, additional studies using other inorganic nanomaterials are required to verify whether the nanomaterial's HAR and fiber-like structure plays a greater role over their chemical composition and surface chemistry.

Oxidative stress and inflammation are well-accepted paradigms widely used as nanotoxicity benchmarks [18]. Recent fundamental studies indicated that nanotoxicity involves multiple intracellular pathways including autophagy induction, lysosome membrane permeabilization (LMP), mitochondrial depolarization and endoplasmic reticulum (ER) stress [19,20]. Autophagy is a homeostatic process in which cells respond to stress stimuli such as starvation and infection. A number of reports showed that nanomaterials may function as autophagy activators or autophagy flux inhibitors that lead to autophagosome accumulation and cell death [21]. LMP, a dysfunction of lysosomal hydrolases release, is recognized as a critical nanotoxicity paradigm of HAR nanomaterials as previously shown with CNTs [22,23]. Mitochondria as cell energy and ROS signaling generators are involved in many kinds of cell death stimuli such as apoptosis, autophagy and LMP. Recent studies indicated that ER stress may also serve as an early biomarker for screening nanotoxicity. The active surface of spherical nanoparticles such as ZnO, silver and gold nanoparticles may disturb ER homeostasis and yield misfolded or unfolded protein accumulation on the ER, ultimately resulting in cell death through a number of signaling pathways [24–26]. It must be noted that the cross talk of these four major cell stresses is commonly involved in programmed cell death. However, detailed studies to better understand the role of cell stresses in HAR nanomaterial initiated nanotoxicity are still lacking. Such studies would require screening multiple toxic factors in a dose and time dependent manner in order to provide comprehensive and comparable toxicity information for future studies.

Here, we report for the first time the use of anodic alumina nanotubes (AANTs) as a HAR nanomaterial model for assessing *in vitro* nanotoxicity. AANTs with different aspect ratio were fabricated through a well-established electrochemical process of pulse anodization [27–29]. Nanoporous anodic alumina (NAA) nanostructures have been considered as a non-hazardous biomaterial because of its proved biocompatibility and commercial use for biomedical applications [30]. AANTs are directly fabricated from NAA nanostructure, which makes it a good candidate for nanotoxicity studies due to its highly inert chemical composition [31]. Several critical toxicity paradigms were systematically assessed including cell viability, cell morphology, pro-inflammatory response, mitochondrial depolarization, LMP, autophagy induction and ER stress.

2. Materials and methods

2.1. Materials

Aluminum (Al) foils of thickness 0.32 mm and purity 99.9997% were supplied by Goodfellow Cambridge Ltd. (UK). Sulfuric acid (H_2SO_4), copper(II) chloride ($CuCl_2$), hydrochloric acid (HCl), perchloric acid ($HClO_4$), hydrogen peroxide (H_2O_2), chromium trioxide (CrO_3), paraformaldehyde, Fluorescein isothiocyanate–dextran (average mol wt 70,000), 2′,7′-Dichlorofluorescein diacetate, 4′,6-diamidino-2-phenylindole ($C_{16}H_{15}N_5$ – DAPI) and Alizarin Red S were purchased from Sigma–Aldrich (Australia). PE annexin V apoptosis detection kit, JC 1 detection kit and TNF-α ELISA detection set were purchased from BD science. ER stress marker proteins including PDI, Ero1-Lα, BiP, calnexin, IRE1α, PERK, and CHOP were purchased from Cell Signaling. Dulbecco's modified Eagle's medium, RPMI 1640 media, fetal calf serum (FCS), penicillin/streptomycin, and glutamine were purchased from Biosciences (Australia). Trypsin (Gibco); phosphate buffer solution (PBS) (HyClone Laboratories, Inc); Culture flasks, 96-well plate, 24-well plate and 6-well plate (greiner Bio-One); 8-well glass chamber slide (Thermo Fisher); AlamarBlue® and ER-Tracker Blue-White DPX (Life Technologies Corporation); Ultrapure water Option Q–Purelabs (Australia) was used for preparation of all the relevant solutions used in this study.

2.2. Fabrication of AANTs by pulse anodization

AANTs were synthesized by a modified pulse anodization process using galvanostatic mode. Briefly, Aluminum foils 1.5 cm in diameter were first sonicated in EtOH and ultrapure water for 5 min each. Aluminum foils were electropolished prior to anodization in a mixture of EtOH and $HClO_4$ 4:1 (*v*:*v*) at 20 V and 5 °C for 3 min. After this, the first step anodization was carried out in a 0.3 M aqueous solution of H_2SO_4 at 25 V and 6 °C for 20 h. The second step pulse anodization was conducted under galvanostatic conditions at 1 °C. The area exposed to the electrolyte solution was 0.95 cm^2. This anodization step consisted of a cyclic combination of mild (MA) and hard anodization (HA) pulses under galvanostatic mode. The MA-pulse was keep at 5 s with a current of 3 mA; the HA-pulse current intensity was 350 mA and the HA duration was 2 s, 6 s and 20 s respectively for fabricating AANTs-S, AANTs-M and AANTs-L. Then, the remaining aluminum substrate was removed by wet chemical etching in a mixture of 0.2 M $CuCl_2$ and 6.1 M HCl. Free-standing AANTs were obtained by immersion into the same acid solution followed by gentle ultrasonic treatment.

2.3. Physicochemical characterization

The shape and structure of AANTs were characterized by a transmission electron microscope (FEI Tecnai G2 Spirit TEM) and a field emission gun scanning electron microscope (FEG-SEM FEI Quanta 450). The length distribution was characterized by analyzing 700 to 1000 nanotubes by TEM image analysis. Zeta-potential and particle size distributions of AANTs were analyzed by a ZetaSizer Nano (Malvern Instruments Ltd., Worcestershire, UK). AANTs with a concentration 50 μg/ml were dispersed in 500 μl of the corresponding aqueous solution and sonicated for 1 min before analysis. A XS analytical balance with readability 0.01 mg (Mettler-Toledo International, Inc.) was used for sample weighting in all the experiments.

2.4. Cell culture

MDA-MB-231-TXSA and RAW 264.7 cell lines were used for toxicity study. MDA-MB-231 derivative cell line, MDA-MB-231-TXSA was kindly provided by Dr Toshiyuki Yoneda (formerly at University of Texas Health Sciences Centre, San Antonio, Texas). Cells were cultured in Dulbecco's modified Eagle's medium (DMEM), supplemented with glutamine (2 mM), penicillin (100 IU/ml), streptomycin (100 μg/ml) and 10% fetal bovine serum at 37 °C in a 5% CO_2-containing humidified atmosphere. Unless otherwise indicated, all the cell experiments in this study were repeated three times.

2.5. Cell toxicity determination

Cell toxicity was determined by Alamar blue assay. Briefly, prior to each test, cells were harvested using Trypsin-EDTA-PBS and $1*10^4$ cells per well were plated in 96-well plate setup with 200 μl of growth media. Cells were allowed to attach overnight. Next day, cells were treated AANTs with at a dose range of 20 μg/ml, 100 μg/ml, 500 μg/ml, 1000 μg/ml for 24 h and 3 days. After determined time point in study, cells were carefully washed with PBS one time, then 200 μl alamar blue solution (10% dilution in PBS) was added to each well and incubated at 37 °C for 20–40 min, after which fluorescence was measured at 560/590 nm using a plate reader (Fluostar OPTIMA, BMG Labtech).

2.6. Quantification of TNF-α production by ELISA

The TNF-α production amount was determined by mouse TNF (Mono/Mono) ELISA set (BD science) according to the manufacturer's instructions. After AANTs treatment, 100 μl cultural media was collected for ELISA. Results were expressed as pg/ml.

2.7. Cell morphology characterization by light microscope

$1*10^4$ cells were seeded on 8-well glass chamber slide overnight and treated with AANTs at a concentration 100 μg/ml. Live cell images were recorded by Nikon Eclipse TS100 and Nikon 90i. After 3 days of treatment, cells were washed one time with PBS and fixed with 4% paraformaldehyde and stained with standard hematoxyline-eosine (H&E) staining solutions. For semi-quantitative analysis of morphological alterations (Fig. S3), three images of each experiment were randomly captured and analyzed by ImageJ software. At least 800 cells per sample were counted.

2.8. Annexin-V and JC-1 assay by flow cytometry

Annexin-V and JC-1 assay was conducted according to the manufacturer's instructions. Briefly, $2*10^4$ cells were seeded in 24-well plates overnight for attachment. After 3 days of treatment, cells were trypsinized and washed one time by PBS. Then cells were stained by Annexin-V/7-AAD or JC-1 dye followed by washing step. 0.1% hydrogen peroxide and 200 nM valinomycin was used as positive control for Annexin-V/7AAD and JC-1 assay respectively. Events were acquired by a FACScalibur (BD Bioscience), and data were analyzed using FlowJo (TreeStar) software on at least 10,000–30,000 events.

2.9. Confocal microscopy characterization of AANTs cell uptake, lysosomal membrane permeabilization and endoplasmic reticulum stress

To label inner surface of AANTs with ARS, acid-etched NAA nanostructure was incubated with 0.3 mg/ml Alizarin Red S solution in pH 8.5 Tris-HCl buffer under vacuum for 0.5 h and incubated overnight. Alizarin Red S preserves ortho-substituted enediol ligand and hydroxyl groups, which have high affinity to alumina surface [32]. After ARS labeling, the NAA structure was thoroughly washed 5 times with ultra-pure water followed by gentle sonication. ARS-labeled AANTs can be obtained by several cycles of washing and centrifugation. The AANTs-ARS composite was used for later study of cell uptake and LMP determination.

To determine LMP, 2^*10^4 RAW 264.7 cells were seeded on 8-well chamber slide together with 500 μg/ml FTIC-Dextran (MW ≈ 70,000) overnight. Next day, cells were carefully washed with PBS to remove FITC-Dextran, and then incubated with three types of AANTs at a concentration of 100 μg/ml for 6 h. At the end of time point, cells were washed one time with PBS and fixed with 4% paraformaldehyde and stained with DAPI. The chamber was then visualized under a confocal microscope (Leica SP5 spectral scanning confocal microscope) using 405-nm, 488-nm, and 561-nm lasers with band-pass filters of 420–480 nm, 505–530 nm, and 570–700 nm, respectively.

For ER staining, cells were cultured on 8-well chamber slides treated with AANTs. At the end of time course, cells were washed one time with PBS and fixed by paraformaldehyde. To label the ER, the fixed cells were incubated with ER-Tracker (1 μM for 30 min at 37 °C) and then imaged using DAPI channel.

2.10. TEM microtome sample preparation

To prepare microtome samples, 1^*10^6 cells/well were seeded in a 6-well plate and allowed to attach overnight. Then, 100 μg/ml of AANTs were transferred into culture media followed by incubation overnight. After that, cells were carefully washed with sterile PBS two times, and transferred into 1.5 ml eppendorf tubes. Collected cell pellets were re-suspended in a solution of 4vol% paraformaldehyde and 1.25 vol% glutaraldehyde and fixed overnight. Then, all samples were post-fixed in a 2 vol% osmium tetroxide solution for 45 min. After this, cells were fully dehydrated and embedded in epoxy resin. Ultrathin sections of 70 nm were cut and post-stained with uranyl acetate and lead citrate [33]. Cell samples were analyzed by TEM at 100 kV.

2.11. Western blotting

4^*10^5 cells were seed in T25 flask and treated with 100 μg/ml AANTs in a three-day time course. After that, Cells were lysed in buffer containing 10 mmol/L Tris-HCl (pH 7.6), 150 mmol/L NaCl, 1% Triton X-100, 0.1% SDS, 2 mmol/L sodium vanadate, and a protease inhibitor cocktail (Boehringer Mannheim) and stored −70 °C until ready to use. The amount of protein in each sample was quantified using the BCA protein assay reagent (Pierce) according to the manufacturer's instructions. Fifty micrograms of cell lysates was separated using 12.5% SDS-PAGE. Gels were then electro-blotted onto polyvinylidene difluoride membranes (Novex, San Diego, CA) and blocked using 5% skim milk in TBST buffer (10 mM Tris-HCl, pH 7.5/150 mM NaCl/0.05% Tween-20) at room temperature for 1–3 h. Immunodetection was done overnight at 4 °C in TBST/blocking reagent, using the following primary antibodies at the dilutions suggested by the manufacturer. Primary antibodies were purchased from Cell Signaling Technology (ER stress antibody sampler kit). Anti-actin pAb (Santa Cruz, CA) was used to normalize for protein concentration. Membranes were then rinsed several times with PBS containing 0.1% Tween 20 and incubated with 1:5000 dilution of anti-mouse or anti-rabbit alkaline phosphatase conjugated secondary antibodies (Amersham) for 1 h. Visualization and quantification of protein bands was done using the Vistra ECF substrate reagent kit (Amersham) on a FluorImager (Molecular Dynamics, Inc., Sunnyvale, CA). The intensity of the band was quantified utilizing the software, NIH ImageJ (National Institutes of Health, Bethesda, MD, USA) and normalized by the band intensity of actin.

2.12. Reactive oxygen species quantification by DCF-DA assay

To determine the ROS production by DCF-DA assay, we carefully optimized the experimental protocol as shown in Fig. S4 (Supporting Information). In general, 2^*10^4 cells were seeded in 96-well plate and incubated overnight. Next day, cells were treated with hydrogen peroxide or AANTs at given doses. For AANTs ROS experiment, cells were treated with AANTs and then carefully washed by PBS once at the end of time-course (4 h and 24 h). Next, cells were incubated with freshly prepared 10 μM DCF-DA (35845, sigma-aldrich) in PBS solution for 50 min at 37 °C in a CO_2 incubator. Then cells were washed one times with PBS and took the reading at Ex 485 nm/Em 520 nm.

2.13. Statistical analysis

Data were analyzed using Origin pro and Microsoft Excel software and presented as mean values ± standard deviation (SD) from three independent measurements. Statistical comparisons between different treatments were assessed by two-tailed t-tests. The criterion for significance was $p < 0.05$ for *, $p < 0.01$ for **, and $p < 0.001$ for ***.

3. Results

3.1. Fabrication of AANTs and their physicochemical characterization

AANTs were fabricated by a pulse anodization process, in which the anodization current density was periodically switched between hard anodization (HA) and mild anodization (MA) regimes in order to create layered structures and weakened conjunctions between cells and layers [27,29]. The resulting NAA structures clearly show periodical junctions between the interfaces of each layer. The thickness of each anodized layer was directly controlled by HA pulse durations at a given current intensity. In our study, the HA pulse duration was set at 2 s, 6 s and 20 s and the corresponding anodized layer thickness was approximately 850 nm, 2.5 μm and 7 μm respectively (Fig. 1d–f). The liberation of AANTs was facilitated by acid etching, which enables selective removal of aluminum hydroxide at the cell conjunctions, followed by mild sonication. After liberation, the length of AANTs-S (short AANTs), AANTs-M (medium AANTs) and AANTs-L (long AANTs) was measured to be 0.7 ± 0.5 μm, 2.5 ± 1.5 μm and 5.8 ± 3.9 μm respectively according to TEM characterization (Fig. 2). Note that the length of AANTs measured by TEM analysis was shorter than their corresponding anodized layer thicknesses. We assume this was caused by the acid etching and mild sonication process. AANTs have an intrinsic hollow structure with an outer diameter of 90 ± 10.0 nm and an inner diameter of 33 ± 8.0 nm. The physicochemical characterization of the hydrodynamic diameter and zeta-potential of the three types AANTs is summarized in Table 1. AANTs have length-dependent hydrodynamic diameters ranging from 358 nm to 804 nm. The dispersion in cell culture medium (RPMI 1640) significantly increased the hydrodynamic diameter of AANTs due the ionic strength in this salt-containing media; while 10% fetal calf serum can efficiently disperse AANTs in cell culture media because the protein adsorbed on the AANTs surface can counter the colloidal forces among nanotubes [34]. The surface charge of AANTs in Mill-Q water was measured to be around 20 mV, but it became negative (−8 to −16 mV) in PBS and cell culture media.

3.2. Cell viability and inflammatory response to AANTs treatment is length dependent

To examine the cytotoxicity of AANTs, we first analyzed cell viability by choosing MDA-MB 231-TXSA breast cancer cells and RAW 264.7 macrophages as cell models. Cell viability was characterized by the Alamar Blue assay, in which the oxidized non-fluorescent Alamar Blue dye is reduced into a pink fluorescent dye by cellular metabolic activity [35]. AANTs decreased cell viability in a time-, dose- and length-dependent manner in both cell lines tested. (Fig. 3a and b) In general, high doses, long time of exposure and long AANTs induced significantly stronger impact on cell viability when compared to the weaker stimuli condition (lower doses, shorter exposure time and shorter AANTs). To determine the median lethal dose (LD_{50}), we tested AANTs at increasing doses of up-to 1 mg/ml at the time-course of three days. Interestingly, MDA-MB 231-TXSA cells were relatively resistant to treatment, showing approximately 70% cell viability in the AANTs-L treated group and 80% viability in the AANTs-S group at the highest dose of 1 mg/ml (Fig. 3a). In contrast, RAW 264.7 cells were highly sensitive such that the LD_{50} of AANTs in RAW 264.7 cells was approximately 500 μg/ml while toxic effects were not seen below 20 μg/ml (Fig. 3b). Considering the impact of nanotube length, a length-dependent toxicity pattern was seen at concentrations higher than 100 μg/ml at the time-course of 3 days. The order of the toxic effect of HAR AANTs was determined to be: AANTs-L > AANTs-

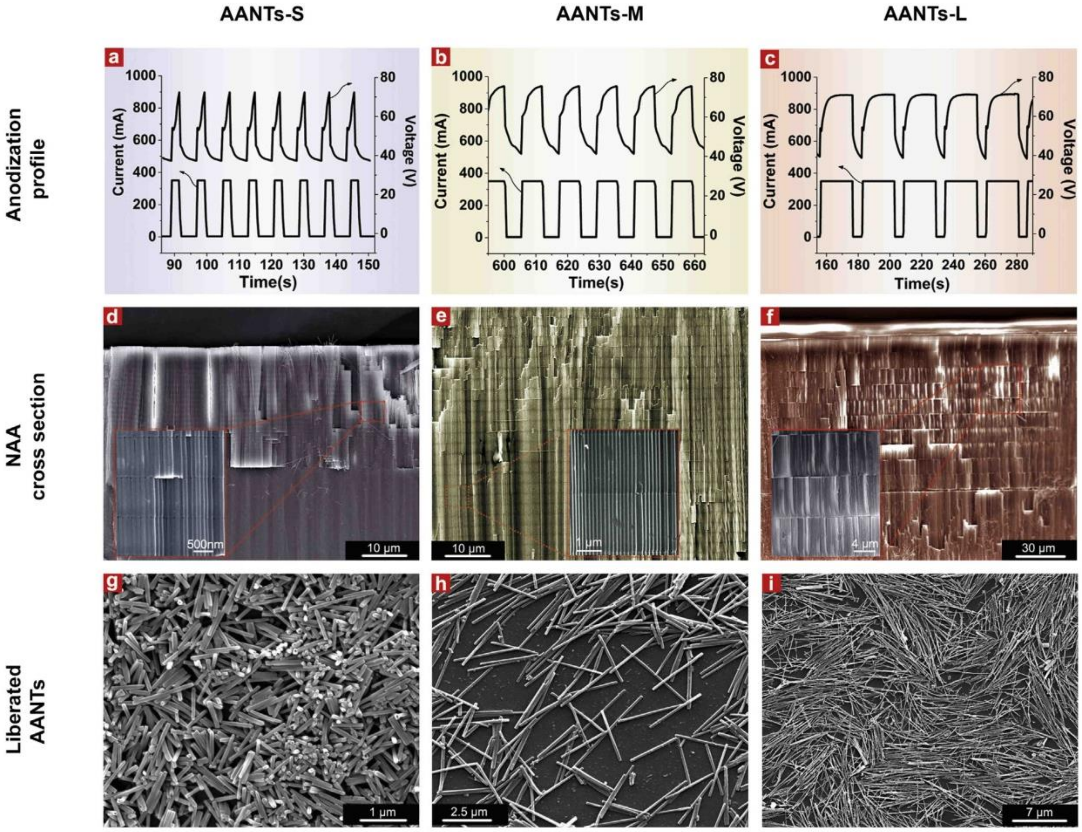

Fig. 1. Pulse anodization profile, cross-section SEM images of NAA nanostructure and liberated AANTs used in this study. (a, b and c) Typical current–voltage profile of pulse anodization by galvanostatic pulses between HA and MA regimes. The HA-pulse duration for fabricating AANTs-S, AANTs-M and AANTs-L was 2 s, 6 s and 20 s respectively at 350 mA. MA duration was maintained at 5 s at 3 mA. (d, e and f) Cross-section SEM images of the resulting NAA nanostructures showing the layered structure created by pulse anodization. Insets show magnified images of periodically spaced layers created by each current pulse; the layer thickness was directly controlled by HA pulse. (g, h and i) SEM images of three types AANTs liberated from NAA nanostructures.

M > AANTs-S. We next determined the inflammatory response of cells by an ELISA based quantification of tumor necrosis factor α (TNF-α) production. TNF-α as a proinflamatory cytokine has long been characterized as an important mediator of nanotoxicity due to its impact on system inflammation [7,11,17,33]. TNF-α release was virtually undetectable in MDA-MB 231-TXSA cells, but a significant amount of TNF-α was generated from RAW 264.7 cells at doses higher than 500 μg/ml of AANTs (Fig. 3c). Treatment with AANTs-S led to significant less TNF-α production than that of longer AANTs. Furthermore, no TNF-α release was detected in all three types of AANTs at a dose of 20 μg/ml.

We next performed double staining with Annexin-V and 7AAD to quantify the population of apoptotic and necrotic cells after a 3-day AANTs treatment (Fig. 3d and e). To determine the cell death mechanism, we chose a relatively high but non-toxic dose of 100 μg/ml for these experiments according to the LD_{50} of AANTs in both cell lines. The positive control used was 0.1% hydrogen peroxide (H_2O_2) treatment for 30 min. The representative scatter plot showed that treatment with AANTs resulted in an increase in the number of $7AAD^+$ and Annexin-V^+ cells, and that the population of necrotic cells is much larger than that of apoptotic cells (Fig. 3d). While no length-dependent toxicity pattern was observed for the AANTs-S and AANTs-M treated groups, significantly stronger necrosis, apoptosis and overall cell death was observed following treatment with AANTs-L (Fig. 3e).

3.3. *AANTs induce changes in morphology of RAW 264.6 macrophage cells*

Cell morphology was assessed by H&E-staining after cells were treated with AANTs for 3 days at a concentration of 100 μg/ml (Fig. 4, Figs. S1 and S2). The accumulation of intra-cytoplasmic AANTs was evident in both cell lines. All three types of AANTs were effectively taken up by cells due to their short length as compared to the diameter of cells. Magnified images showed a clear cytoplasmic accumulation of AANTs-L in RAW 264.7 and MDA-MB-231 cells (Fig. 4b and c). In our study, all the needle-like AANTs were localized exclusively in the cell's cytoplasm with no evidence of nuclear penetration. RAW 264.7 cells showed significant changes in morphology characteristic of cell stress such as multinucleated giant cells, pyknotic nuclei, swelling of cell bodies and loss of cell to cell contacts since these treated cells grew isolated and dispersed. The observed morphological changes were also length-dependent (Fig. S3). In contrast, no significant changes in morphology were

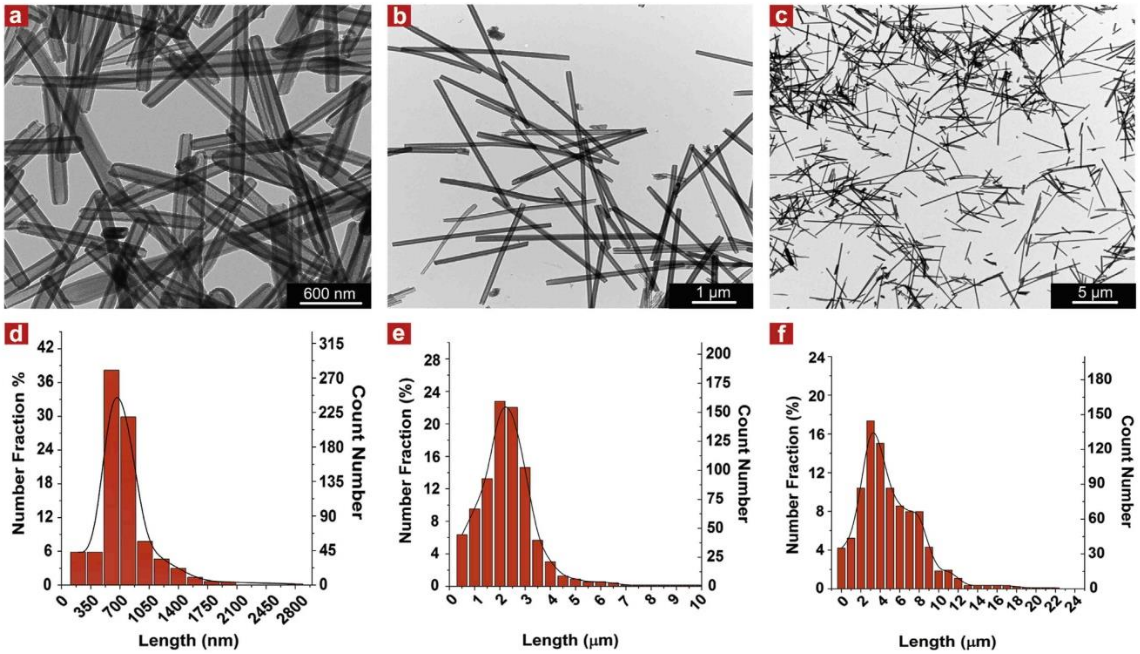

Fig. 2. TEM image analysis of AANTs-S, AANTs-M and AANTs-L. (a, b and c) TEM images and (d, e and f) length distribution of AANTs-S, AANTs-M and AANTs-L fabricated by pulse anodization with different HA duration: (a, d) 2 s; (b, e) 6 s; (c, f) 20 s.

seen in the MDA-MB-231 cell line. These results are consistent with previous reports that RAW 264.7 cells are more sensitive to morphological alternations when compared to other cell lines [10,36]. Importantly, the critical length of AANTs required for inducing such morphological changes (0.7 μm) appear to be much shorter than other previously reported HAR nanomaterials such as boron nitride nanotube [10].

3.4. *AANTs induce lysosome dysfunction through a length-dependent pattern*

Lysosome dysfunction, or lysosome membrane permeabilization (LMP) has been characterized as one of the major toxicity paradigm of nanomaterials [19,37]. To assess whether HAR AANTs can lead to LMP, FITC-Dextran was used as a lysosome marker. Healthy macrophage cells can accumulate dextran inside the lysosome characterized as bright green dots under confocal microscopy. During LMP the green fluorescence intensity is reduced significantly due to the leakage of lysosomal components into the cytoplasm [38]. Hydrogen peroxide was used here as a prototypical LMP inducer (Fig. 5b) [39]. To visualize the location of AANTs inside the cell and to avoid any chemical modification of the outer surface of AANTs, we selectively labeled the inner wall surface of AANTs with the fluorescent dye-alizarin red s (ARS) due to its high affinity to the metal oxide surface [32]. As shown is Fig. 5a, as-prepared NAA structures were first etched by acid to remove aluminum substrate, then directly incubated with ARS at pH 8.5 in Tris-HCl buffer overnight. In this way, only the inner surface of NAA was exposed to the aqueous solution and ARS molecules were selectively immobilized onto the inner surface of NAA. The cell-uptake of the three types of AANTs was confirmed by the persistence of separated red dots inside the cells (Fig. 5c). For LMP characterization, a clearly reduced green fluorescent intensity was detected only in AANTs-L and AANTs-M groups after 6 h treatment. This effect was not observed in the AANTs-S treated group, indicating that AANTs-S with average length 0.7 μm and AR 7.8 did not induce significant LMP toxicity.

Table 1
Size distribution and zeta-potential analysis in different aqueous solutions.

	AANTs-S	AANTs-M	AANTs-L
Length by TEM (μm)	0.7 ± 0.5	2.5 ± 1.5	5.8 ± 3.9
Outer diameter (nm)	90.0 ± 10.0	90.0 ± 10.0	90.0 ± 10.0
Inner diameter (nm)	33.0 ± 8.0	33.0 ± 8.0	33.0 ± 8.0
Aspect ratio	7.8 ± 0.11	27.7 ± 0.01	63.3 ± 0.01
Hydrodynamic diameter (nm)			
Mill-Q H_2O	358.6 ± 7.0	483.9 ± 11.8	804.0 ± 25.9
RPMI 1640	724.7 ± 81.8	1438.3 ± 124.0	1615 ± 59.1
RPMI 1640 with 10% FCS	467.4 ± 1.4	475.3 ± 23.7	480 ± 7.4
Zeta-potential (mV)			
Mill-Q H_2O	20.7 ± 2.6	20.3 ± 0.6	21.1 ± 0.3
RPMI 1640	−16.3 ± 0.8	−16.0 ± 0.5	−10.0 ± 0.1
RPMI 1640 with 10% FCS	−11.3 ± 0.8	−8.4 ± 0.6	−12.1 ± 0.2

RPMI: Roswell Park Memorial Institute medium.
FCS: Fetal Calf Serum.

3.5. *Characterization of mitochondrial depolarization and ROS production*

ROS generation has long been considered as a major paradigm of nanotoxicity which can lead to damage of multiple cell organelles. DCF-DA (2′,7′-Dichlorodihydrofluorescein diacetate) assay as a simple, high throughput detection method has been used extensively for the study of ROS generation and recently applied for a broad range of nanotoxicity studies [33,40]. However, some studies

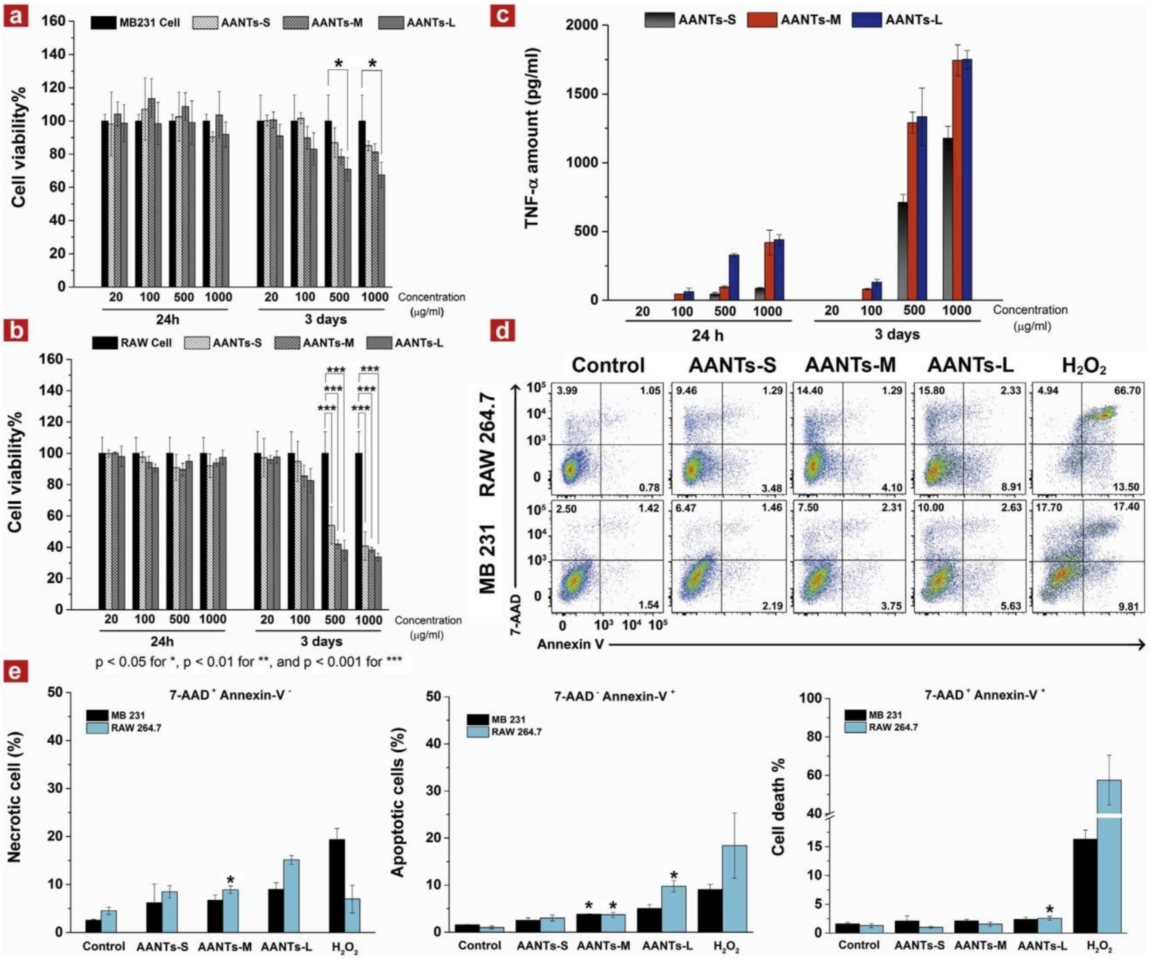

Fig. 3. Cell viability and inflammatory characterization. (a) Alamar blue assay for MDA-MB 231-TXSA and (b) RAW 264.7 cell after two time-course treatment with different doses of AANTs. AANTs treatment did not affect cell activity within the first 24 h but impact the cell viability after 3 days in a dose- and length-dependent pattern. (c) RAW 264.7 TNF-α production in respond to AANTs detected by ELISA. Cells produced significant amount of TNF-α after three days of treatment at high doses in all three types of AANTs. However, AANTs-S did not induce TNF-α generation at a concentration of 100 μg/ml after three days of treatment. No TNF-α production was found at the lowest dose treatment. (d) Representative scatter plot of Annexin-V assay and (e) statistics analysis for MDA-MB 231-TXSA cell and RAW 264.7 cell lines after 100 μg/ml AANTs treatment for 3 days. AANTs-S and AANTs-M induced necrosis but did not trigger apoptosis; AANTs-L triggered stronger necrosis and apoptosis as compared to shorter ones, although they did not induce significant cell death (late apoptosis). The level of significance was set to a probability of $p < 0.05$ for *, $p < 0.01$ for **, and $p < 0.001$ for ***.

showed that DCF-DA can give false positive amplification of fluorescence intensity due to the side reaction with cytochrome c, redox-active metals (Fe^{2+}) and self-propagating redox-cycling reactions induced by the DCF radical [41]. We attempted to optimize the protocol of microplate-based DCF-DA assay (Fig. S4). Our results showed that no significant ROS production was detected from either cell line at the highest AANTs concentration of 1 mg/ml (Fig. S4c and d) However, this may be due to the intrinsic problems associated with the detection process. The state of oxidative stress can also be evaluated by mitochondrial function. Mitochondria as the intracellular ROS generators and mediators play critical roles in many cell functions including ROS signaling, ROS generation/detoxification and programmed cell death [20]. To determine the potential mitochondrial injury, we performed a JC-1 assay using flow cytometry (Fig. 6). Valinomycin as a traditional mitochondrial depolarization inducer was used here as a positive control. JC-1 (5,5′,6,6′-tetrachloro-1,1′,3,3′-tetraethylbenzimi-dazolylcarbocyanine iodide) is a green fluorescence dye when in its monomer state but switches to red fluorescence when accumulated inside the mitochondrial membrane [42]. As shown in Fig. 6a, valinomycin induced strong mitochondrial depolarization and yielded release of JC-1 dye from the mitochondria to the cytoplasm, evident by a significant increase of green fluorescence intensity detected by flow cytomety. Cells treated with AANTs showed a slight increase of green fluorescenc intensity in both RAW 264.7 and MDA-MB 231-TXSA cell lines. JC-1 exhibits two characteristic green fluorescence peaks at the intensity around 10^3 and 10^4 respectively (Fig. 6b). AANTs treated cells showed a marginal peak shift from low to high intensity, while the valinomycin treated group only presented one peak at the high fluorescence intensity region. The

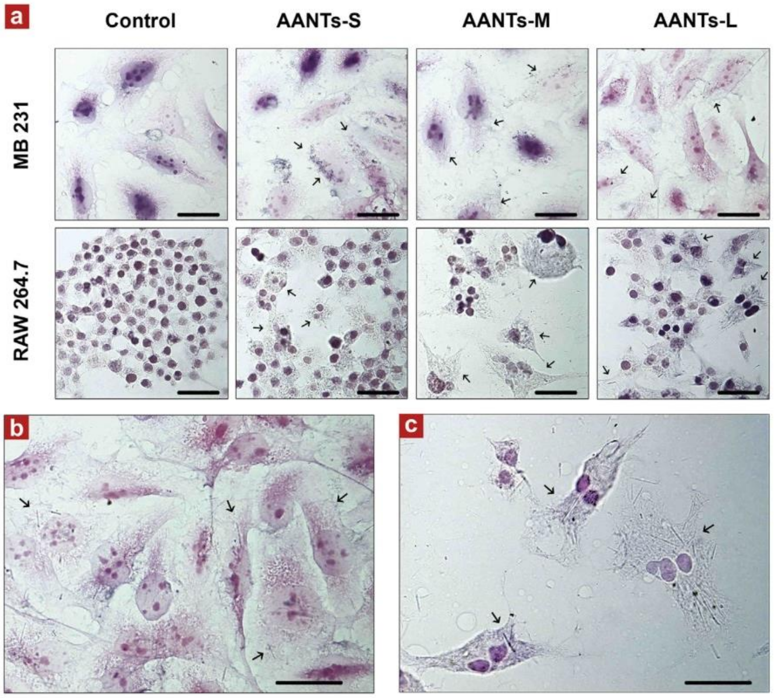

Fig. 4. Cytopathological analyses of MDA-MB 231-TXSA and RAW 264.7 macrophages treated 3 days with three types of AANTs at a concentration 100 μg/ml (a) AANTs with needle-like structure can be visualized inside the cell, where AANTs were concentrated in cytoplasm without penetrating nucleus. MDA-MB 231-TXSA did not have cell morphology change after AANTs treatment; however, RAW 264.7 cell showed loss of cell contacts, swollen cell body and increased number of multinucleate cells with a length-dependent pattern after AANTs treatment. (b) Magnified image of H&E-stained MDA-MB 231-TXSA cells and (c) RAW 264.7 cells treated with AANTs-L at a concentration 100 μg/ml for 3 days. Black arrows indicate the cell uptake of AANTs. Scale bars: 20 μm.

final mitochondrial membrane potential was characterized as the ratio of red/green fluorescence (Fig. 6c). Reduced fluorescence ratio was observed in both cell lines after AANTs treatment, indicating mitochondrial injury occurs in AANTs toxicity paradigm but not associated with AR difference.

3.6. ER stress is involved in the mechanism of HAR nanomaterial paradigm

To determine ER stress, cells after AANTs treatment were stained with the ER-tracker Blue-White DPX and examined by confocal microscopy. Thapsigargin (TG) as a traditional ER stress inducer was used as a positive control. Cells treated with the ER stress inducer have enhanced fluorescence intensity under confocal microscopy, a characteristic factor of ER stress [26,43]. As shown in Fig. 7a, TG treated cells showed prominent increased staining intensity in both cell lines but with different patterns. Specially, RAW 264.7 cells treated with 200 nM and 500 nM TG showed swollen vacuoles, loss of cell to cell contacts between neighboring cells and presence of separated bright dots located in the cytoplasm, possibly due to the aggregation of unfolded proteins on the ER membrane. In contrast, at a TG concentration of 200 nM, MDA-MB 231-TXSA cells showed increased fluorescence intensity surrounding the nuclear region, while a large number of separated bright dots appeared when cells were treated with 500 nM of TG. Treatment of MDA-MB 231-TXSA cells with AANTs at a concentration 100 μg/ml for 3 days showed increased staining intensity only in the AANTs-L treated group which was similar to that seen in the TG treatment group. Treatment with AANTs-M and AANTs-S showed no adverse effect compared to the control group. At the same time, both AANTs-M and AANTs-L treated RAW 264.7 cell showed enlarged vacuoles, isolated cells but did not appear to have separated bright dots in the cytoplasm. These findings were not only consistent with the observed cell morphological changes, but also strongly indicated that long AANTs with a relatively high AR are more likely to induce ER stress than short AANTs.

To confirm the ER staining characterization, we next assessed the expression of several well-established ER stress marker proteins by western blotting, including protein disulphide isomerase (PDI), ER chaperone GRP78 (BiP), inositol-requiring preotein-1a (IRE1α), PKR-like ER kinase (PERK), calnexin, Ero1-Lα and C/EBP homologous protein (CHOP) (Fig. 8). When unfolded proteins accumulate on the ER, the release of BiP activates three types of transmembrane signaling proteins (PERK, IRE1α, activating transcription factor 6) and thereby triggers ER stress. The down-regulation of PERK, IRE1α and up-regulation of CHOP and BiP are major indicators of ER stress [24,44,45]. In the thapsigargin treated group, the up-regulation of BiP, CHOP and down-regulation of IRE1α clearly indicated the activation of IRE1α meditated self-rescuing signaling in response to the unfold protein accumulation [44]. At the same time, AANTs-S and AANTs-M treatment showed no significant modulation of most of the ER stress markers in MB 231-TXSA cells. In contrast, treatment with AANTs-L resulted in a significant decrease in IRE1α expression and a concomitant increase in CHOP expression. This result, together with the ER-tracker imaging analysis provide evidence that AANTs-L with average AR of 63.3 induced stronger ER stress when compared to shorter AANTs.

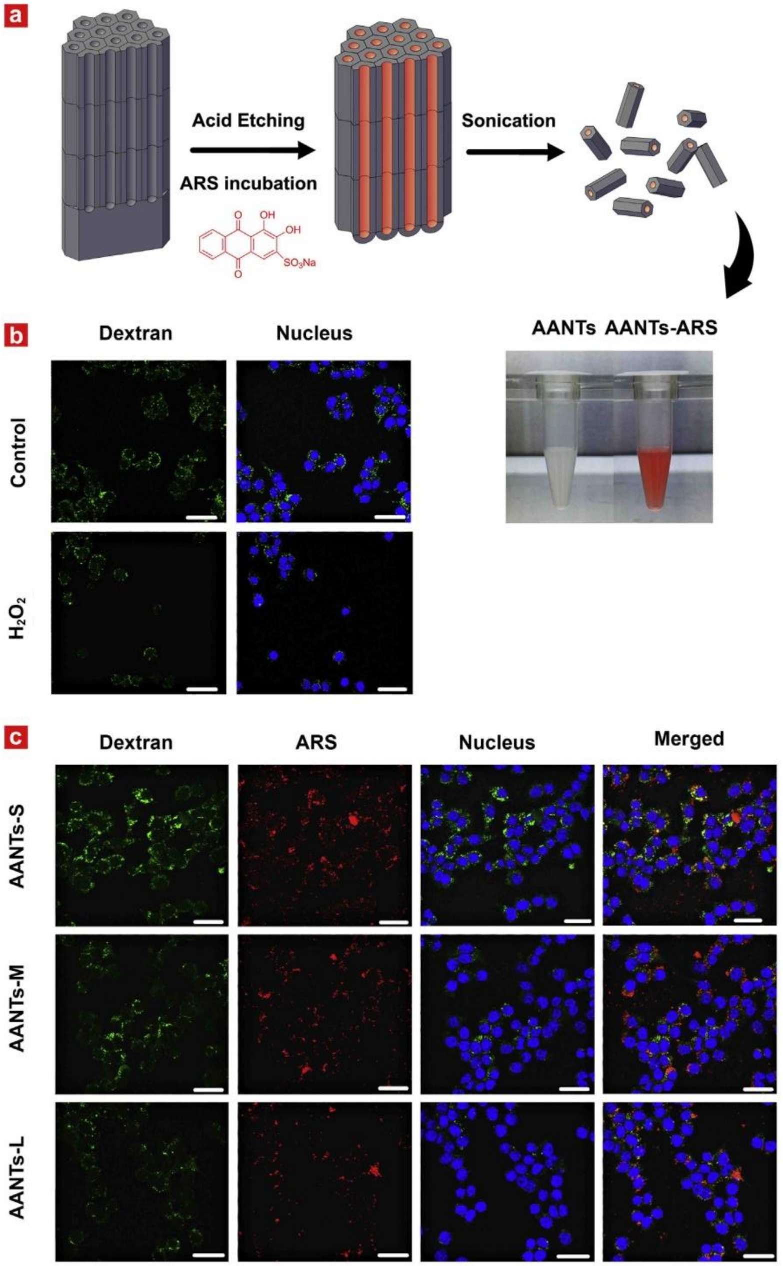

Fig. 5. Selective functionalization of AANTs inner surface with ARS and LMP characterization of RAW 264.7 macrophage cells treated with AANTs after 6 h exposure at a concentration 100 μg/ml. (a) Scheme of functionalization process of inner wall of AANTs with ARS dye. To produce ARS labeled AANTs, as-prepared NAA structures were first etched by acid to remove the Al substrate and then incubated with 0.3 mg/ml ARS overnight followed by sonication. (b) After overnight FITC-Dextran treatment in RAW 264.7 cell line, Dextran located inside lysosome was visualized by bright green dots under confocal microscopy. H_2O_2 treated sample shows significant reduced intensity of green fluorescence, indicating LMP. (c) 6 h treatment with AANTs-S did not trigger significant LMP. However, AANTs-M and AANTs-L treated groups showed reduced green fluorescence intensity, indicating LMP induction by HAR AANTs. Scale bars: 25 μm. (For interpretation of the references to color in this figure legend, the reader is referred to the web version of this article.)

To examine the morphological changes of organelles influenced by the uptake of AANTs, we prepared microtome cell sections after overnight treatment with AANTs, which were subsequently characterized by TEM (Fig. 9 and Fig. S5). AANTs uptake triggered autophagy in both cell lines evidenced by the localization of AANTs in the autophagosome and autolysosome. While the uptake of AANTs-M and AANTs-L was confirmed by our previous characterization (Figs. 4 and 5), not many AANTs were seen in the TEM

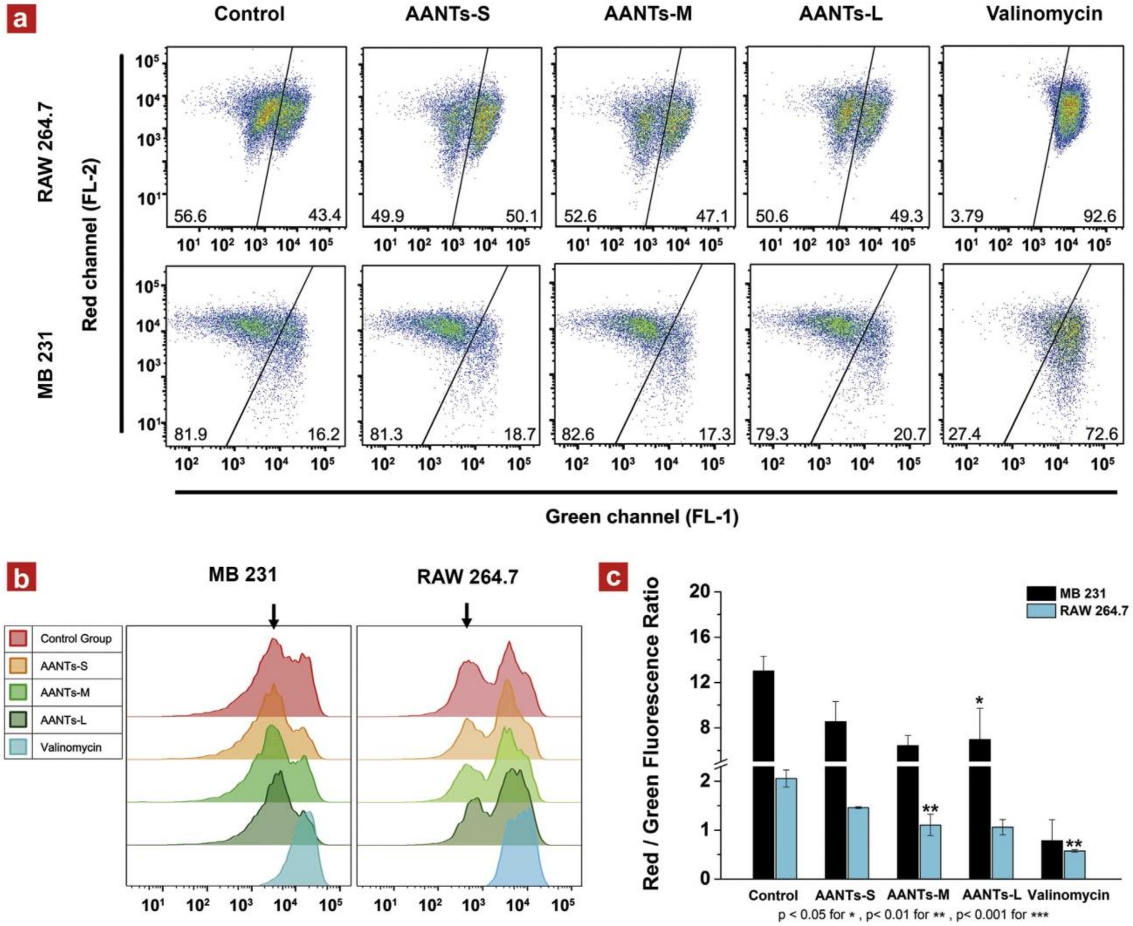

Fig. 6. JC-1 assay of MB 231-TXSA and RAW 264.1 macrophage cells treated with 100 μg/ml AANTs after 3 days. Positive control was set by 200 nM valinomycin treatment for 4 h. Mitochondrial depolarization was characterized as the increment of intensity of green channel (FL-1) as shown in (a) representative scatter plot and (b) half off-set histogram. Gating was based on green fluorescent intensity of cell population. The decreasing red/green fluorescence ratio in (c) indicated that AANTs induced mitochondrial dysfunction without having length dependent effect. (For interpretation of the references to color in this figure legend, the reader is referred to the web version of this article.)

images of RAW 264.7 cells. This can be explained by the fact that the thickness of microtome section only has around 70 nm [33], and thus the long nanotubes likely detached during the sectioning process.

Previous nanotoxicity studies reported that nanomaterial treatment can lead to the swelling of mitochondria and ER structures [18,25,46]. However, in our study, we find no significant morphological changes of these organelles in both cell lines even in the case of AANTs-L, suggesting that cells can tolerate or perhaps recover from AANTs treatment through their self-rescuing system such as autophagy [47].

4. Discussion

In this study, we fabricated AANTs and used these nanomaterials as model to systematically study their *in vitro* cytotoxicity in the context of fiber-like paradigm of HAR nanomaterials. AANTs were fabricated by a semi-industrialized process of pulse anodization. This top-down fabrication method provided a straight forward and flexible way of fabricating multilayered NAA nanostructures with controlled layer thickness as compared to the traditional two-step anodization process (Fig. 1) [48–50]. We further demonstrated the possibility to selectively label the inner surface of AANTs with ARS by utilizing close-compact NAA structure before the liberation step (Fig. 5a). This facile surface chemistry approach is expected to be useful for other inner surface functionalization without altering the surface of AANTs which is directly in contact with the biological interface.

It is widely accepted that nanotoxicity is dependent on several critical factors, including dose, surface chemistry, chemical composition and particle size/geometry in addition to being cell type dependent [17,36]. However, the broad variety of surface chemistry and nanomaterial composition makes it complicated to put forward a general model capable of associating the effect of particle size and shape on cytotoxicity. For example, zinc oxide nanoparticles trigger cytotoxicity mainly due to the particle dissolution [51], while CeO_2 nanoparticles can suppress the ROS toxicity through surface oxidation of Ce^{3+} to Ce^{4+}; CeO_2

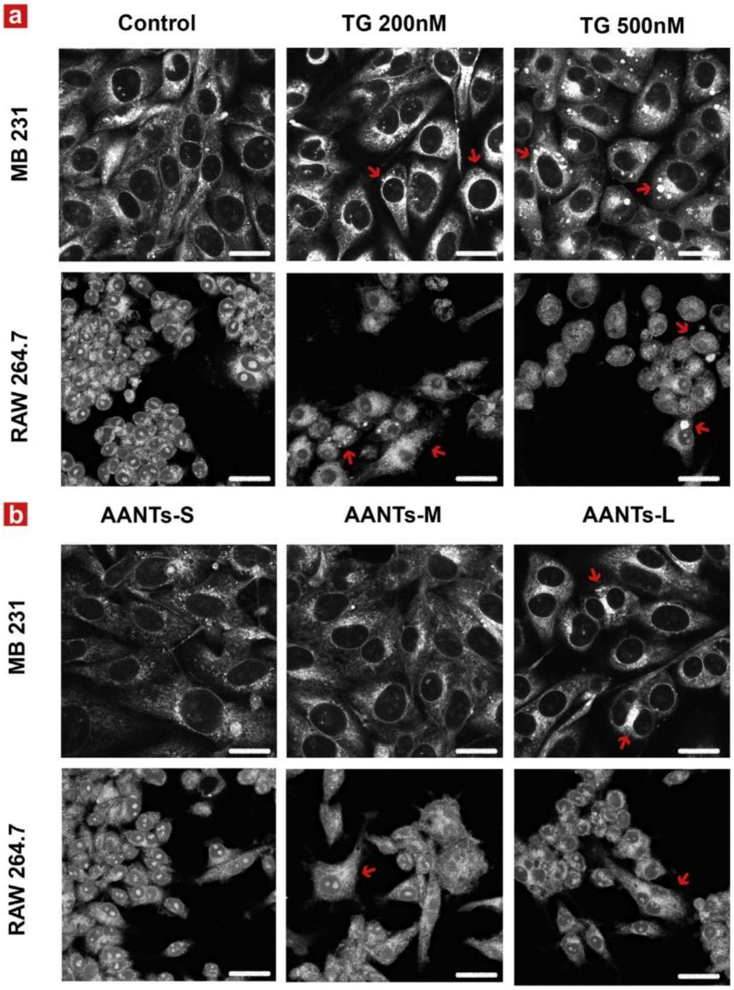

Fig. 7. ER stress characterization by ER-tracker Blue-White DPX staining. Cells were treated by AANTs and thapsigargin (TG) for three days, then stained with ER-tracker dye and examined by confocal microscopy. (a) In MB 231 cell line, ER stress induced by high concentration TG (500 nM) showed bright dots existed in the cytoplasm; 200 nM TG treatment induced clearly increased fluorescent intensity surrounding the nucleus as compared to the control group. In RAW 264.7 cell line, both 200 nM TG and 500 nM TG treatment induced aggregated protein (bright dots), loss of cell contacts and swollen vacuolar system indicated by red arrows. (b) 3-day treatment with AANTs-S at a concentration 100 μg/ml did not induce ER stress in both cell lines. Treatment with AANTs-M did not affect MB 231 cell, but induced swollen vacuolar structure in RAW 264.7 cells. Treatment with AANTs-L led to enlarged vacuolar structure in RAW 264.7 cells, and also induced enhanced staining intensity in MB 231 cells. Red arrows denote increased staining intensity. Scale bars: 20 μm. (For interpretation of the references to color in this figure legend, the reader is referred to the web version of this article.)

nanoparticles prepared by different methods, however, may have different cell responses due to their differential surface reactivity [18,52]. This kind of “cross-talk effect” among surface chemistry, material composition and biophysical interface makes it difficult to distinguish the impact of geometry paradigm of HAR nanomaterials from other parameters [5]. Even more complicated is the complexity of the cell response to nanomaterials, which makes *in vitro* nanotoxicity difficult to assess the toxic paradigm due to the cross talk of multiple cell stress signaling pathways. ER is an important organelle responsible for protein synthesis, protein folding, Ca^{2+} storage and lipid biosynthesis [44]. ER stress not only triggers a series of self-rescuing signaling events to counteract unfolded protein responses, but also can lead to mitochondrial-dependent apoptosis due to the up-regulation of cytosolic Ca^{2+} and ROS levels [26,53]. In addition, ER stress can activate autophagy to facilitate the clearance of accumulated proteins [44]. Lysosome as a cell digestion and signaling organelle is involved in the autophagy process which can be triggered after the cellular uptake of nanomaterials. Lysosome dysfunction caused by nanomaterials contribute to autophagosome accumulation due to blockage of autophagy flux; the release of cathepsins and other associated lysosomal hydrolases can directly trigger inflammation responses and mitochondrial depolarization [19,23,54]. Therefore, understanding the cross-talk mechanism among these intracellular stress signaling pathways is of imperative in clarifying the different cytotoxicity modalities of nanomaterials.

To distinguish the AR impact on nanotoxicity from the surface chemistry and material composition, we prepared AANTs with

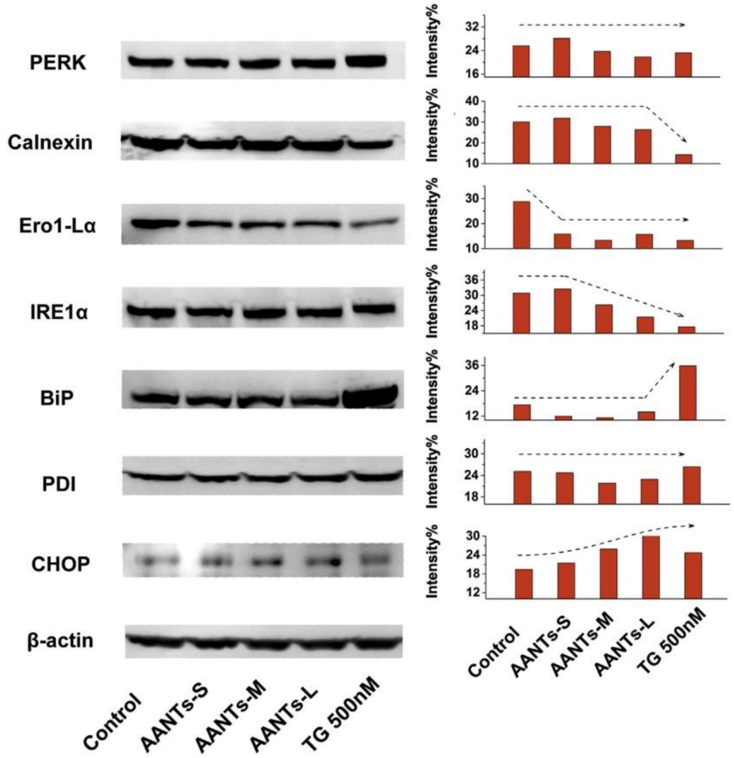

Fig. 8. Western blot of ER stress marker protein expression in MB 231-TXSA cell line treated with AANTs and thapsigargin (500 nM) after three days of exposure. The expression of protein was quantified by ImageJ software. The arrows indicate up- and down-regulation of co-responding ER stress marker. TG treated cells showed clearly up-regulation of BiP, CHOP and down-regulation of IRE1α, which are the hallmarks of ER stress. AANTs treated group did not influence ER stress marker expression except down-regulation of IRE1α, Ero1-Lα and up-regulation of CHOP in AANTs-L treated group.

controlled length by utilizing a pulse anodization process. As-prepared AANTs have no catalyst contamination, relative low surface reactivity, narrow length distribution and broad aspect ratio range, making this nanomaterial an ideal model for nanotoxicity studies. The next question is to determine the cell response and cellular consequences caused by the biophysicochemical interaction with HAR AANTs.

Establishing a dose-dependent toxicity response is a prerequisite for cytotoxicity studies, given that non-effective doses or ultrahigh doses unavoidably produce misleading results [17]. For our studies, we chose a relatively high but non-toxic dose of 100 μg/ml of AANTs as a standard concentration to systematically study the potential cell death mechanisms. Choosing suitable cell lines is another critical factor for providing comparable cytotoxicity information because the cell responses to nanomaterials are largely dependent on the cell type [10,20,36]. RAW 264.7 is a well-established macrophage cell line which is routinely used for assessing nanomaterial- associated toxicities, mainly due to its defense roles in the immune system. Cancer cell lines have also been widely used for toxicity studies, but the general apoptosis resistance property of cancer cells may compromise the objective analysis of the toxic effect associated with nanomaterials [20]. Therefore, in this study, we chose the mouse macrophage cell line RAW 264.7 as a cell model and also used the MDA-MB 231-TXSA breast cancer cell line to complement the study.

Consistent with previous reports [10,36], RAW 264.7 cells are highly sensitive to the dose impact of nanomaterials, in which the LD_{50} of AANTs was determined to be around 500 μg/ml. In contrast, MDA-MB 231-TXSA cancer cells can tolerate much higher concentrations even as high as 1 mg/ml. Under the standard AANTs dose of 100 μg/ml, a clearly length-dependent toxicity pattern was demonstrated in RAW 264.7 cells in the context of cell morphology changes, pre-inflammatory responses, necrosis and apoptosis activation, LMP and notably, ER stress. AANTs-S in general were less toxic when compared to the longer ones (Table 2). Cell viability after treatment with AANTs-S was consistently maintained above 90% after 3 days of treatment or even longer as shown in our previous study [28]. Necrosis activation is the major toxicity paradigm of AANTs-S which is likely caused by the stress of mitochondrial and autophagy systems, since LMP, ER stress and inflammatory response was not observed. In contrast, AANTs-M and AANTs-L triggered significant alternations in cell morphology, TNF-α release, LMP and ER stress. We deduce that the production of the TNF-α inflammatory cytokine was mainly caused by LMP as documented by a previous report [23]. In addition, our study demonstrated for the first time that ER stress is closely related with the AR of the nanomaterial. AANTs-M and AANTs-L with average AR 27.7 and 63.3 generated a stronger ER stress response than AANTs-S as confirmed by the ER tracker staining. As a comparison, MDA-MB 231-TXSA breast cancer cells were relatively resistant to HAR AANTs treatment than RAW 264.7 cells. However, length-dependent cell viability and ER stress was also evident in our experiment. These length-dependent cell stress patterns can in turn explain the observation that AANTs-L treated cells showed an

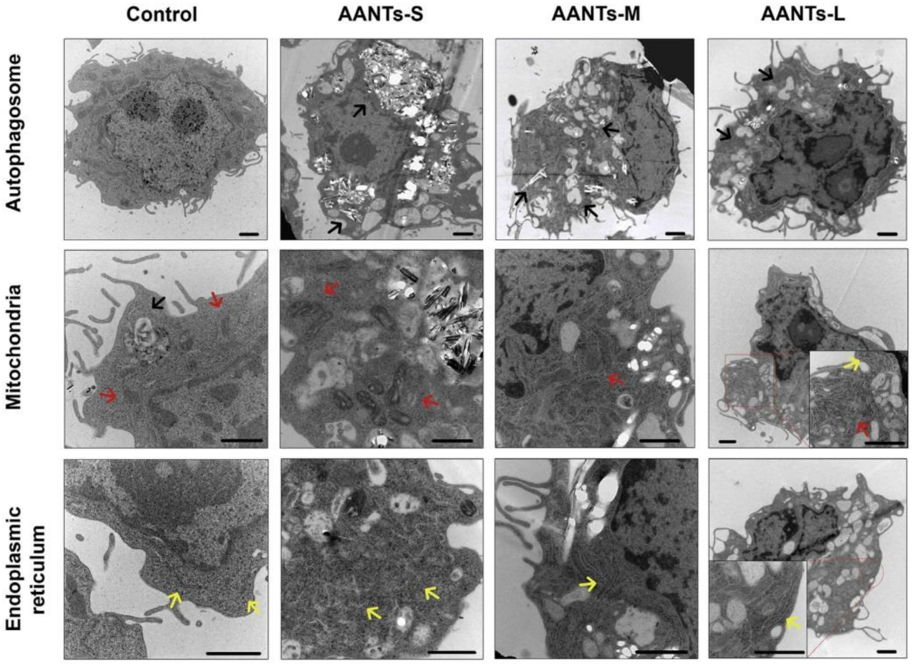

Fig. 9. TEM characterization of cell uptake and morphology of important organelles in RAW 264.7 cell line after overnight (16 h) exposure with three types of AANTs at a concentration 100 μg/ml. We found the accumulation of autophagosome after AANTs exposure. All the AANTs-S were localized inside autophagosome. AANTs-M and AANTs-L were seldom found in the microtome section of cells, probably due to the large size of nanotube compared to the ultra-thin thickness of section (70 nm). We also examined the morphology of mitochondria and endoplasmic reticulum. We did not find significant morphological change of mitochondria and endoplasmic reticulum structure. Black arrows: autophagosome; Red arrows: mitochondria; Yellow arrows: endoplasmic reticulum. Scale bar: 1 μm. (For interpretation of the references to color in this figure legend, the reader is referred to the web version of this article.)

increase in the population of necrotic and apoptotic cells when compare to short AANTs treated cells. Finally, it is worthwhile noting that both types of cells were able to counteract or tolerate various cellular stress signals induced by AANTs with different AR at a concentration of 100 μg/ml, which showed more than 80% cell viability after 3-day treatment.

Collectively the results presented in this study clearly show that AANTs-S with 0.7 μm average length/7.8 AR are non-toxic to cells, while AANTs-M with 2.5 μm length/27.7 AR trigger various cellular responses such as TNF-α release. In addition, multiple paradigms were involved with HAR nanotoxicity, including LMP, autophagy induction, ER stress and mitochondrial depolarization. While these

Table 2
Summary of Cellular Responses to AANTs at a concentration 100 μg/ml.

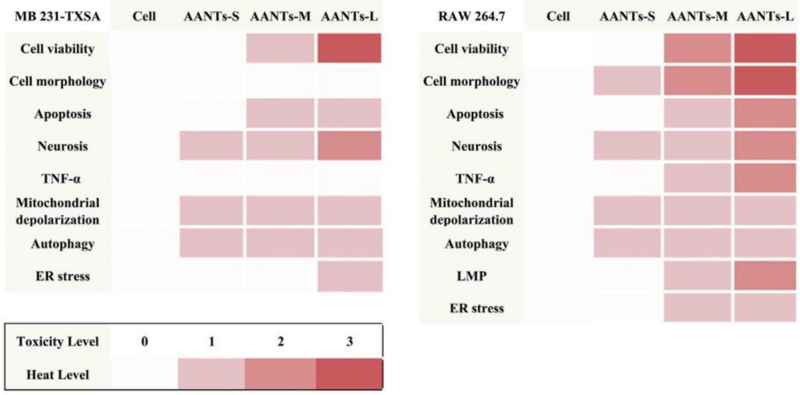

MB 231-TXSA	Cell	AANTs-S	AANTs-M	AANTs-L
Cell viability			░	▓
Cell morphology				
Apoptosis			░	░
Neurosis		░	░	▒
TNF-α				
Mitochondrial depolarization		░	░	░
Autophagy		░	░	░
ER stress				░

RAW 264.7	Cell	AANTs-S	AANTs-M	AANTs-L
Cell viability			▒	▓
Cell morphology		░	▒	▓
Apoptosis			░	▒
Neurosis		░	░	▒
TNF-α			░	▒
Mitochondrial depolarization		░	░	░
Autophagy		░	░	░
LMP			░	▒
ER stress			░	░

Toxicity Level	0	1	2	3
Heat Level		░	▒	▓

cellular responses did not lead to significant cell death after three days' treatment with a AANTs concentration of 100 μg/ml, the induction of necrosis, apoptosis and inflammatory response highlights the chronic impact of AANTs-M and AANTs-L.

5. Conclusion

In summary, our work clearly demonstrates that the AR of nanomaterials plays a critical role in nanotoxicity paradigm. To distinguish the cellular impact of AR from other toxic paradigms, we fabricated AANTs with a relatively inert surface chemistry and a wide aspect ratio range using a pulse anodization process. By selecting suitable cell types and experimental doses, our data demonstrated that AANTs with a higher AR induce significantly stronger cellular stress signals compared to low AR AANTs, evident by changes in cell morphology, pro-inflammatory responses, apoptosis/necrosis, LMP and ER stress. The critical toxic AR window of AANTs was determined here to be 7.8. Our results showed that multiple cell stress responses were involved in nanotoxicity in the context of HAR nanomaterials. More importantly, considering that the abnormal functions of lysosomes, mitochondria and ER stress are critical factors associated with various chronic diseases such as Alzheimer's disease and Parkinson's disease [44,55], the present work highlight the possibility of limiting chronic nanotoxicity by engineering and modulating the AR of nanomaterials according to their AR toxic window. Furthermore, the clarification of the fundamental AANTs toxicity paradigm in cancer cells provides additional opportunities for developing highly sophisticated and rational cancer treatments by exploiting cell responses such as autophagy activation [56]. Finally, the shortest AANTs with 0.7 μm average length and modifiable inner/outer surface chemistry exhibited the lowest toxicity impact, making this novel inorganic nanomaterial a promising candidate for future drug delivery application.

Acknowledgment

This research was supported by the Australian Research Council (ARC) through the grants DP120101680, FT110100711, DE14010054, the National Health and Medical Research Council (NHMRC) of Australia through grant APP627015, the Australian Breast Cancer Research (ABCR), The Hospital Research Foundations (THRF) and the University of Adelaide Interdisciplinary Research Fund (DVC IRF -2014). We are thankful for Adelaide Microscopy for providing microscopy facilities. This work was per-formed in part at the OptoFab node of the Australian National Fabrication Facility utilizing Commonwealth and SA State Government funding. Y.W. appreciated Ms Lyn Waterhouse, Ms Ruth Williams and Dr Agatha Labrinidis for their technique support of microscopy. Authors thank Mr. Jason Peak, Mr. Michael Jung and Mr. Jeffrey Hiorns from the mechanical workshop of the School of Chemical Engineering (UoA) for their help and support with the fabrication of the experimental set-ups used to fabricate AANTs.

Appendix A. Supplementary data

Supplementary data related to this article can be found at http://dx.doi.org/10.1016/j.biomaterials.2014.12.008.

References

[1] Chertok B, Webber MJ, Succi MD, Langer R. Drug delivery interfaces in the 21st century: from science fiction ideas to viable technologies. Mol Pharm 2013;10:3531–43.

[2] Huang X, Teng X, Chen D, Tang F, He J. The effect of the shape of mesoporous silica nanoparticles on cellular uptake and cell function. Biomaterials 2010;31: 438–48.

[3] Lin S, Wang X, Ji Z, Chang CH, Dong Y, Meng H, et al. Aspect ratio plays a role in the hazard potential of CeO_2 nanoparticles in mouse lung and zebrafish gastrointestinal tract. ACS Nano 2014;8(5):4450–64.

[4] Müller KH, Kulkarni J, Motskin M, Goode A, Winship P, Skepper JN, et al. pH-dependent toxicity of high aspect ratio ZnO nanowires in macrophages due to intracellular dissolution. ACS Nano 2010;4:6767–79.

[5] Nel AE, Madler L, Velegol D, Xia T, Hoek EMV, Somasundaran P, et al. Understanding biophysicochemical interactions at the nano-bio interface. Nat Mater 2009;8:543–57.

[6] Wang X, Xia T, Duch MC, Ji Z, Zhang H, Li R, et al. Pluronic F108 coating decreases the lung fibrosis potential of multiwall carbon nanotubes by reducing lysosomal injury. Nano Lett 2012;12:3050–61.

[7] Wang P, Nie X, Wang Y, Li Y, Ge C, Zhang L, et al. Multiwall carbon nanotubes mediate macrophage activation and promote pulmonary fibrosis through TGF-β/smad signaling pathway. Small 2013;9:3799–811.

[8] Poland CA, Duffin R, Kinloch I, Maynard A, Wallace WAH, Seaton A, et al. Carbon nanotubes introduced into the abdominal cavity of mice show asbestos-like pathogenicity in a pilot study. Nat Nano 2008;3:423–8.

[9] Wang L, Luanpitpong S, Castranova V, Tse W, Lu Y, Pongrakhananon V, et al. Carbon nanotubes induce malignant transformation and tumorigenesis of human lung epithelial cells. Nano Lett 2011;11:2796–803.

[10] Horváth L, Magrez A, Golberg D, Zhi C, Bando Y, Smajda R, et al. In vitro investigation of the cellular toxicity of boron nitride nanotubes. ACS Nano 2011;5:3800–10.

[11] Roberts JR, Mercer RR, Chapman RS, Cohen GM, Bangsaruntip S, Schwegler-Berry D, et al. Pulmonary toxicity, distribution, and clearance of intratracheally instilled silicon nanowires in rats. J Nanomater 2012;2012:2.

[12] Poland CA, Byrne F, Cho W-S, Prina-Mello A, Murphy FA, Davies GL, et al. Length-dependent pathogenic effects of nickel nanowires in the lungs and the peritoneal cavity. Nanotoxicology 2012;6:899–911.

[13] Schinwald A, Donaldson K. Use of back-scatter electron signals to visualise cell/nanowires interactions in vitro and in vivo; frustrated phagocytosis of long fibres in macrophages and compartmentalisation in mesothelial cells in vivo. Part Fibre Toxicol 2012;9:34.

[14] Qiu Y, Liu Y, Wang L, Xu L, Bai R, Ji Y, et al. Surface chemistry and aspect ratio mediated cellular uptake of Au nanorods. Biomaterials 2010;31:7606–19.

[15] He W, Liu Y, Yuan J, Yin J-J, Wu X, Hu X, et al. Au@Pt nanostructures as oxidase and peroxidase mimetics for use in immunoassays. Biomaterials 2011;32: 1139–47.

[16] Bussy C, Pinault M, Cambedouzou J, Landry M, Jegou P, Mayne-L'hermite M, et al. Critical role of surface chemical modifications induced by length shortening on multi-walled carbon nanotubes-induced toxicity. Part Fibre Toxicol 2012;9:1–15.

[17] Krug HF, Wick P. Nanotoxicology: an interdisciplinary challenge. Angew Chem Int Ed 2011;50:1260–78.

[18] Xia T, Kovochich M, Liong M, Mädler L, Gilbert B, Shi H, et al. Comparison of the mechanism of toxicity of zinc oxide and cerium oxide nanoparticles based on dissolution and oxidative stress properties. ACS Nano 2008;2:2121–34.

[19] Stern S, Adiseshaiah P, Crist R. Autophagy and lysosomal dysfunction as emerging mechanisms of nanomaterial toxicity. Part Fibre Toxicol 2012;9: 20.

[20] Andón FT, Fadeel B. Programmed cell death: molecular mechanisms and implications for safety assessment of nanomaterials. Acc Chem Res 2012;46: 733–42.

[21] Loos C, Syrovets T, Musyanovych A, Mailänder V, Landfester K, Simmet T. Amino-functionalized nanoparticles as inhibitors of mTOR and inducers of cell cycle arrest in leukemia cells. Biomaterials 2014;35:1944–53.

[22] Wan B, Wang Z-X, Lv Q-Y, Dong P-X, Zhao L-X, Yang Y, et al. Single-walled carbon nanotubes and graphene oxides induce autophagosome accumulation and lysosome impairment in primarily cultured murine peritoneal macrophages. Toxicol Lett 2013;221:118–27.

[23] Ji Z, Wang X, Zhang H, Lin S, Meng H, Sun B, et al. Designed synthesis of CeO_2 nanorods and nanowires for studying toxicological effects of high aspect ratio nanomaterials. ACS Nano 2012;6:5366–80.

[24] Tsai Y-Y, Huang Y-H, Chao Y-L, Hu K-Y, Chin L-T, Chou S-H, et al. Identification of the nanogold particle-induced endoplasmic reticulum stress by omic techniques and systems biology analysis. ACS Nano 2011;5:9354–69.

[25] Chen R, Huo L, Shi X, Bai R, Zhang Z, Zhao Y, et al. Endoplasmic reticulum stress induced by zinc oxide nanoparticles is an earlier biomarker for nanotoxicological evaluation. ACS Nano 2014;8(3):2562–74.

[26] Zhang R, Piao MJ, Kim KC, Kim AD, Choi J-Y, Choi J, et al. Endoplasmic reticulum stress signaling is involved in silver nanoparticles-induced apoptosis. Int J Biochem Cell Biol 2012;44:224–32.

[27] Lee W, Scholz R, Gösele U. A continuous process for structurally well-defined Al_2O_3 nanotubes based on pulse anodization of aluminum. Nano Lett 2008;8: 2155–60.

[28] Wang Y, Santos A, Kaur G, Evdokiou A, Losic D. Structurally engineered anodic alumina nanotubes as nano-carriers for delivery of anticancer therapeutics. Biomaterials 2014;35:5517–26.

[29] Wang Y, Santos A, Evdokiou A, Losic D. Rational design of ultra-short anodic alumina nanotube by short-time pulse anodization. Electrochim Acta 2015;154:379–86.

[30] Popat KC, Leary Swan EE, Mukhatyar V, Chatvanichkul K-I, Mor GK, Grimes CA, et al. Influence of nanoporous alumina membranes on long-term osteoblast response. Biomaterials 2005;26:4516–22.

[31] Losic D, Simovic S. Self-ordered nanopore and nanotube platforms for drug delivery applications. Expert Opin Drug Deliv 2009;6:1363–81.

[32] Chen L, Zhang B, Toborek M. Autophagy is involved in nanoalumina-induced cerebrovascular toxicity. Nanomedicine 2013;9:212–21.

[33] Bimbo LM, Mäkilä E, Laaksonen T, Lehto V-P, Salonen J, Hirvonen J, et al. Drug permeation across intestinal epithelial cells using porous silicon nanoparticles. Biomaterials 2011;32:2625–33.

[34] Xia T, Kovochich M, Liong M, Meng H, Kabehie S, George S, et al. Polyethyleneimine coating enhances the cellular uptake of mesoporous silica nanoparticles and allows safe delivery of siRNA and DNA constructs. ACS Nano 2009;3:3273–86.

[35] O'Brien J, Wilson I, Orton T, Pognan F. Investigation of the alamar blue (resazurin) fluorescent dye for the assessment of mammalian cell cytotoxicity. Eur J Biochem 2000;267:5421–6.

[36] Sohaebuddin SK, Thevenot PT, Baker D, Eaton JW, Tang L. Nanomaterial cytotoxicity is composition, size, and cell type dependent. Part Fibre Toxicol 2010;7.

[37] Tahara Y, Nakamura M, Yang M, Zhang M, Iijima S, Yudasaka M. Lysosomal membrane destabilization induced by high accumulation of single-walled carbon nanohorns in murine macrophage RAW 264.7. Biomaterials 2012;33:2762–9.

[38] Joshi G, Knecht D. Silica phagocytosis causes apoptosis and necrosis by different temporal and molecular pathways in alveolar macrophages. Apoptosis 2013;18:271–85.

[39] Boya P, Kroemer G. Lysosomal membrane permeabilization in cell death. Oncogene 2008;27:6434–51.

[40] Krejsa C, Schieven G. Detection of oxidative stress in lymphocytes using dichlorodihydrofluorescein diacetate. In: Walker J, Keyse S, editors. Stress response. Humana Press; 2000. p. 35–47.

[41] Kalyanaraman B, Darley-Usmar V, Davies KJA, Dennery PA, Forman HJ, Grisham MB, et al. Measuring reactive oxygen and nitrogen species with fluorescent probes: challenges and limitations. Free Radic Biol Med 2012;52: 1–6.

[42] Perelman A, Wachtel C, Cohen M, Haupt S, Shapiro H, Tzur A. JC-1: alternative excitation wavelengths facilitate mitochondrial membrane potential cytometry. Cell Death Dis 2012;3:e430.

[43] Abdelrahim M, Newman K, Vanderlaag K, Samudio I, Safe S. 3,3′-Diindolylmethane (DIM) and its derivatives induce apoptosis in pancreatic cancer cells through endoplasmic reticulum stress-dependent upregulation of DR5. Carcinogenesis 2006;27:717–28.

[44] Kim I, Xu W, Reed JC. Cell death and endoplasmic reticulum stress: disease relevance and therapeutic opportunities. Nat Rev Drug Discov 2008;7: 1013–30.

[45] Xu C, Bailly-Maitre B, Reed JC. Endoplasmic reticulum stress: cell life and death decisions. J Clin Invest 2005;115:2656–64.

[46] Seleverstov O, Zabirnyk O, Zscharnack M, Bulavina L, Nowicki M, Heinrich J-M, et al. Quantum dots for human mesenchymal stem cells labeling. A size-dependent autophagy activation. Nano Lett 2006;6:2826–32.

[47] Levine B, Mizushima N, Virgin HW. Autophagy in immunity and inflammation. Nature 2011;469:323–35.

[48] Lee W, Schwirn K, Steinhart M, Pippel E, Scholz R, Gosele U. Structural engineering of nanoporous anodic aluminium oxide by pulse anodization of aluminium. Nat Nano 2008;3:234–9.

[49] Masuda H, Fukuda K. Ordered metal nanohole arrays made by a 2-step replication of honeycomb structures of anodic alumina. Science 1995;268: 1466–8.

[50] Md Jani AM, Losic D, Voelcker NH. Nanoporous anodic aluminium oxide: advances in surface engineering and emerging applications. Prog Mater Sci 2013;58:636–704.

[51] Zaveri TD, Dolgova NV, Chu BH, Lee J, Wong J, Lele TP, et al. Contributions of surface topography and cytotoxicity to the macrophage response to zinc oxide nanorods. Biomaterials 2010;31:2999–3007.

[52] Dowding JM, Das S, Kumar A, Dosani T, McCormack R, Gupta A, et al. Cellular interaction and toxicity depend on physicochemical properties and surface modification of redox-active nanomaterials. ACS Nano 2013;7:4855–68.

[53] Schröder M. Endoplasmic reticulum stress responses. Cell Mol Life Sci 2008;65:862–94.

[54] Ma X, Wu Y, Jin S, Tian Y, Zhang X, Zhao Y, et al. Gold nanoparticles induce autophagosome accumulation through size-dependent nanoparticle uptake and lysosome impairment. ACS Nano 2011;5:8629–39.

[55] Lin MT, Beal MF. Mitochondrial dysfunction and oxidative stress in neurodegenerative diseases. Nature 2006;443:787–95.

[56] Zhang X, Dong Y, Zeng X, Liang X, Li X, Tao W, et al. The effect of autophagy inhibitors on drug delivery using biodegradable polymer nanoparticles in cancer treatment. Biomaterials 2014;35:1932–43.

Supporting Information

Systematic *in vitro* Nanotoxicity Study on Anodic Alumina Nanotubes with Engineered Aspect Ratio: Understanding Nanotoxicity by a Nanomaterial Model

Ye Wang [a,b], Gagandeep Kaur [a,b], Aneta Zysk [b], Vasilios Liapis [b], Shelley Hay [b], Abel Santos [a]*, Dusan Losic [a]*, Andreas Evdokiou [b]*

[a] School of Chemical Engineering, The University of Adelaide, Adelaide, SA, 5005
[b] Discipline of Surgery, Basil Hetzel Institute, The University of Adelaide, Adelaide, SA, 5005

*Corresponding authors: andreas.evdokiou@adelaide.edu, dusan.losic@adelaide.edu.au, abel.santos@adelaide.edu.au

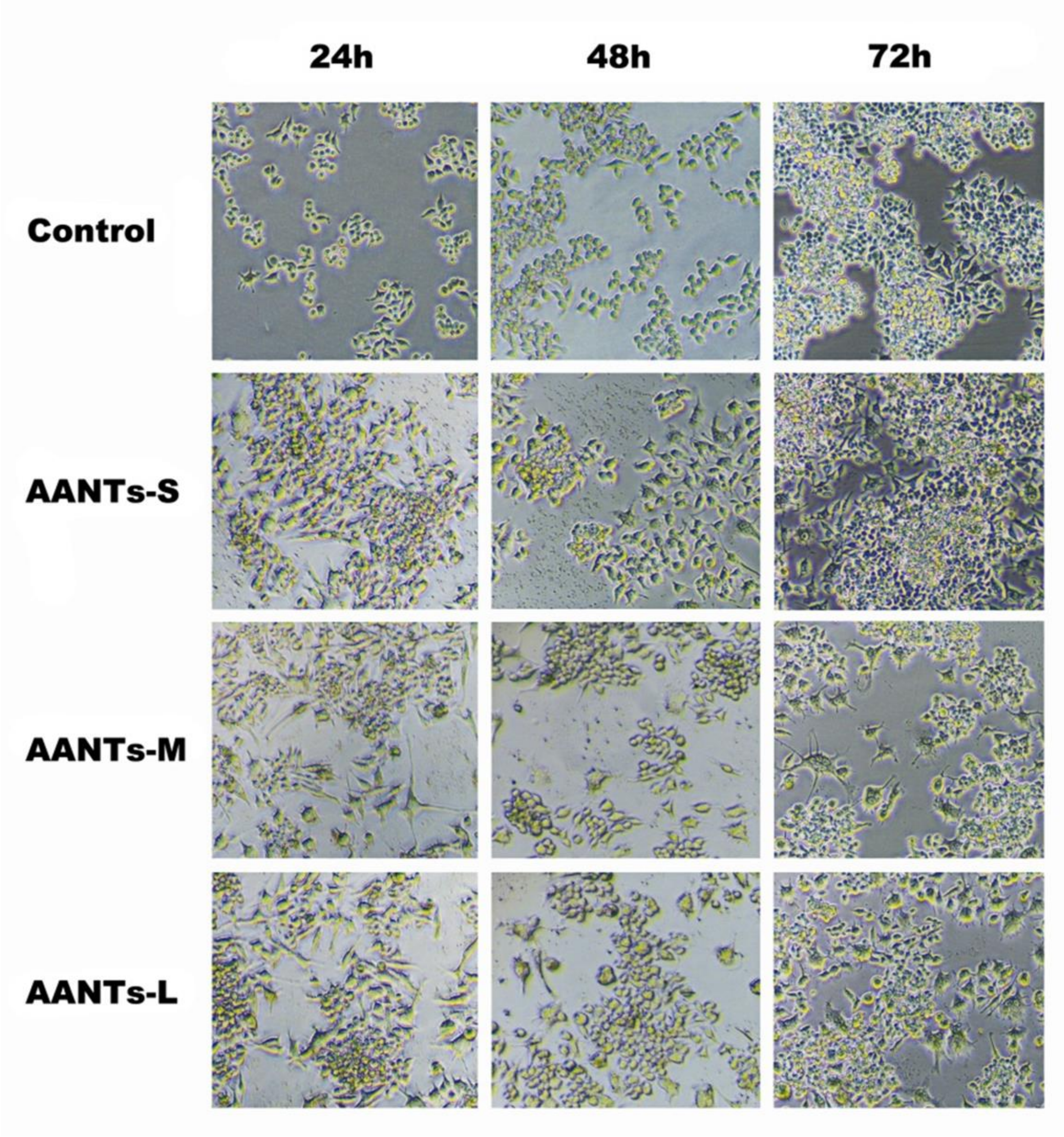

Figure S 1 Light microscopy characterization of RAW 264.7 cells after 3 days exposure to the three types of AANTs (100 μg/ml). Note that AANTs-M and AANTs-L induce significant morphological changes throughout the 3-days experiment.

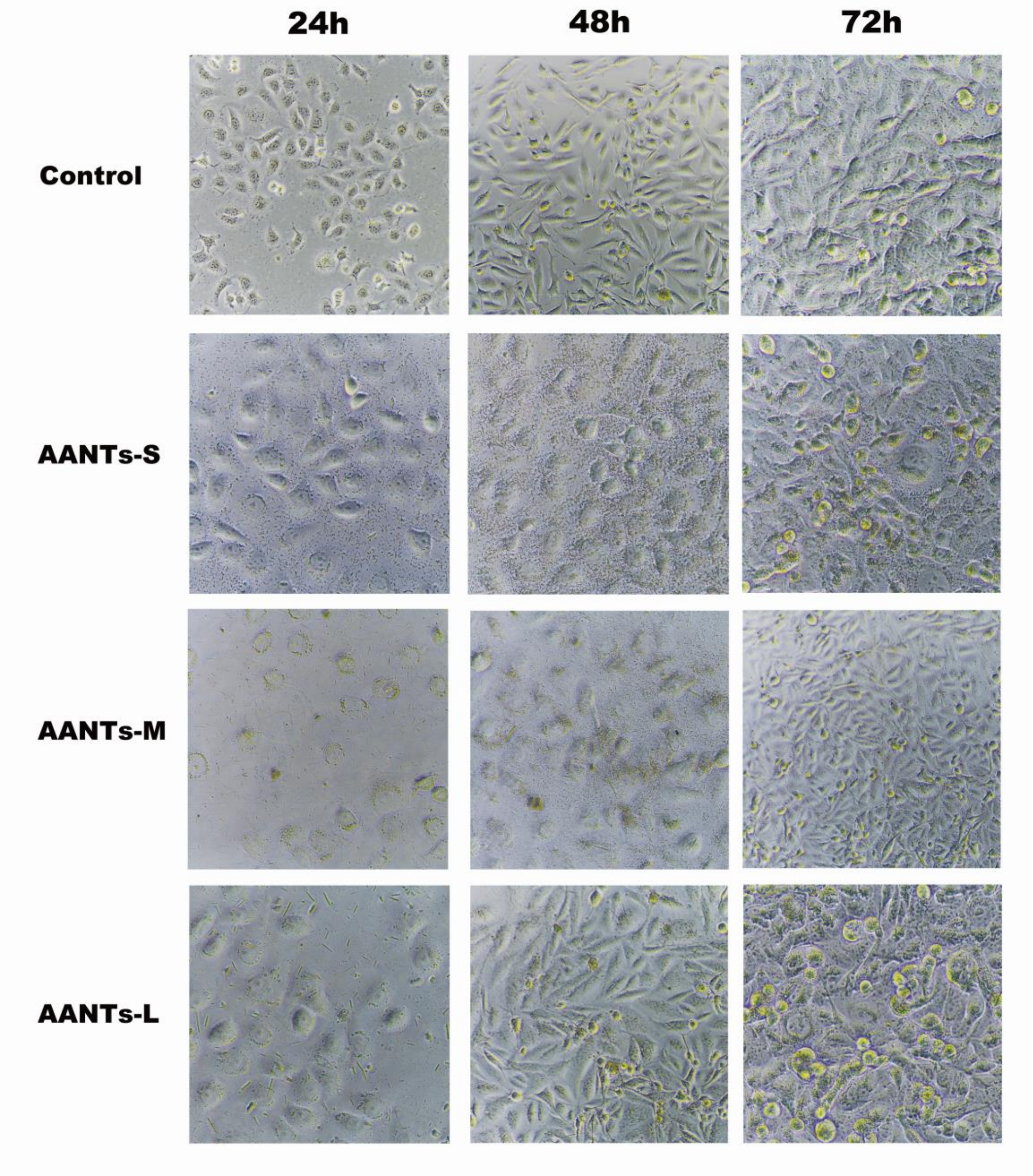

Figure S 2 Light microscopy characterization of MB 231-TXSA breast cancer cells cell after 3 days exposure to the three types of AANTs (100 μg/ml). No cell morphology change was found.

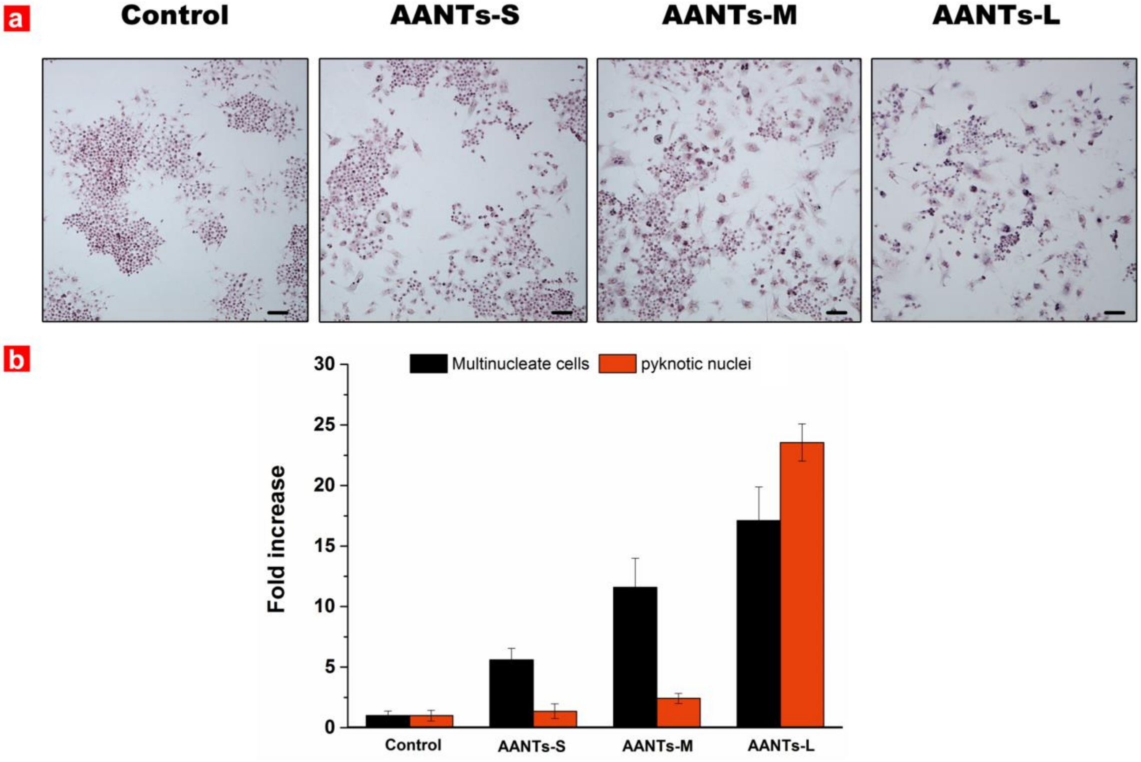

Figure S 3 Semi-quantitative statistics analysis of RAW 264.7 morphological changes after 3 days exposure to the three types of AANTs (100 μg/ml). In general, at least 800 cells were counted from three different fields of the image for the quantification of the number of multinucleated and pyknotic cells. (a) Representative H&E staining image of RAW 264.7 after AANTs treatment. Scale bar: 50 μm. (b) Quantification of morphological changes determined from optical images.

Figure S 4 ROS detection by DCF-DA assay

DCF-DA (2′,7′-Dichlorodihydrofluorescein diacetate) has been widely used for assessing nanomaterial associated ROS toxicity. Among the protocols of microplate-reader analysis, two methods were generally used for assessing nanomaterial associated ROS production. (**Scheme 1**)

In the first method, DCF-DA was incubated with cells before adding any ROS inducer. This method can minimize the influence of DCF-DA self-oxidation with air so that DCF-DA only reacts with intracellular ROS, as shown in **Method 2**. However, DCF-DA may be extracted by cells through their transport system which lead to the reaction of DCF-DA and ROS inducer outside cells. To eliminate the influence of DCF-DA extraction, a washing step was added before plate-reader detection, as shown in **Method 1**. [1-4]

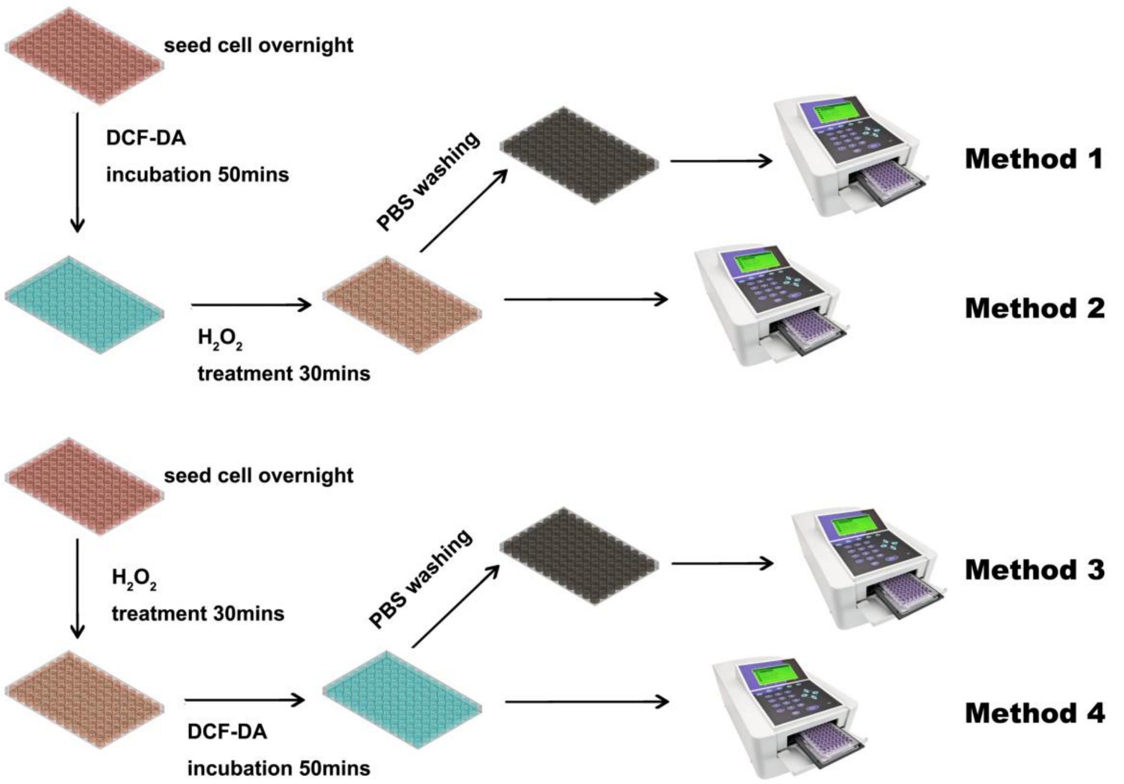

Scheme 1 schematic illustration of microplate-based ROS production protocol used in this study**.**

In another protocol, ROS inducer was first introduced to trigger intracellular ROS production, and then ROS inducer was washed away followed by DCF-DA incubation and detection, as shown in **Method 4**. [5-7] Similar to **Method 1**, we added a washing step before taking a reading in order to distinguish the influence of DCF-DA extraction and extracellular oxidation process. (**Method 3**) [8,9] H_2O_2 was used as ROS inducer in these experiments. Note that to minimize the system's error, the microplate-reader instrument was set in well-scan mode. All experiments were conducted in triplicate. We found that the cell culture media gave rise to auto-fluorescence due to the presence of factors such as folic acid which significantly increases the background. Therefore, PBS was chosen as the standard working buffer.

We first examined method 1 and 2 by using RAW 264.7 and MB 231-TXSA cells. (**Figure S 4 a)** Strikingly, RAW 264.7 cells showed a strong dose dependent ROS production in **Method 2**. The significant reduction of the signal, however, appeared after the washing step (**Method 1**), which suggested that most of the signal detected in **Method 2** is from extracellular DCF-DA through the extracellular oxidation process by hydrogen peroxide. In the case of MB 231-TXSA, no clear pattern was found no matter whether washing step was introduced. We suspected that the MB 231-TXSA cells have very active transport system so that DCF-DA cannot accumulate effectively inside the cells during the incubation step. In **Figure S 4 b**, we tested **Method 3 and Method 4**. It is clear that without the washing step (**Method 4**), the fluorescence intensity in all treatment groups were very high and did not show a dose dependent pattern. This is because DCF-DA dye was quickly oxidized with oxygen during the dark incubation step and thus led to a high background. Finally, **Method 4** was demonstrated to be a suitable method, in which an increasing fluorescence intensity corresponding to the increased dose of H_2O_2. Note that the significant reduced signal in 0.6% H_2O_2 group was caused by the detachment of cells during the washing steps due to the toxic dose. Therefore, we chose **Method 4** as a standard protocol to test ROS production in MB 231-TXSA and RAW 264.7 cells using two time-courses (**Figure S 4 c and d**) where 0.6% H_2O_2 was used as a positive control to directly react with DCF-DA without cells. No significant ROS production was detected even at highest concentration of 1 mg/ml after 24hs treatment. We argue that DCF-DA dye may not be a suitable and reliable method for ROS detection at least under our own experimental conditions. More sensitive characterization, for example flow cytometry might be a reliable approach.

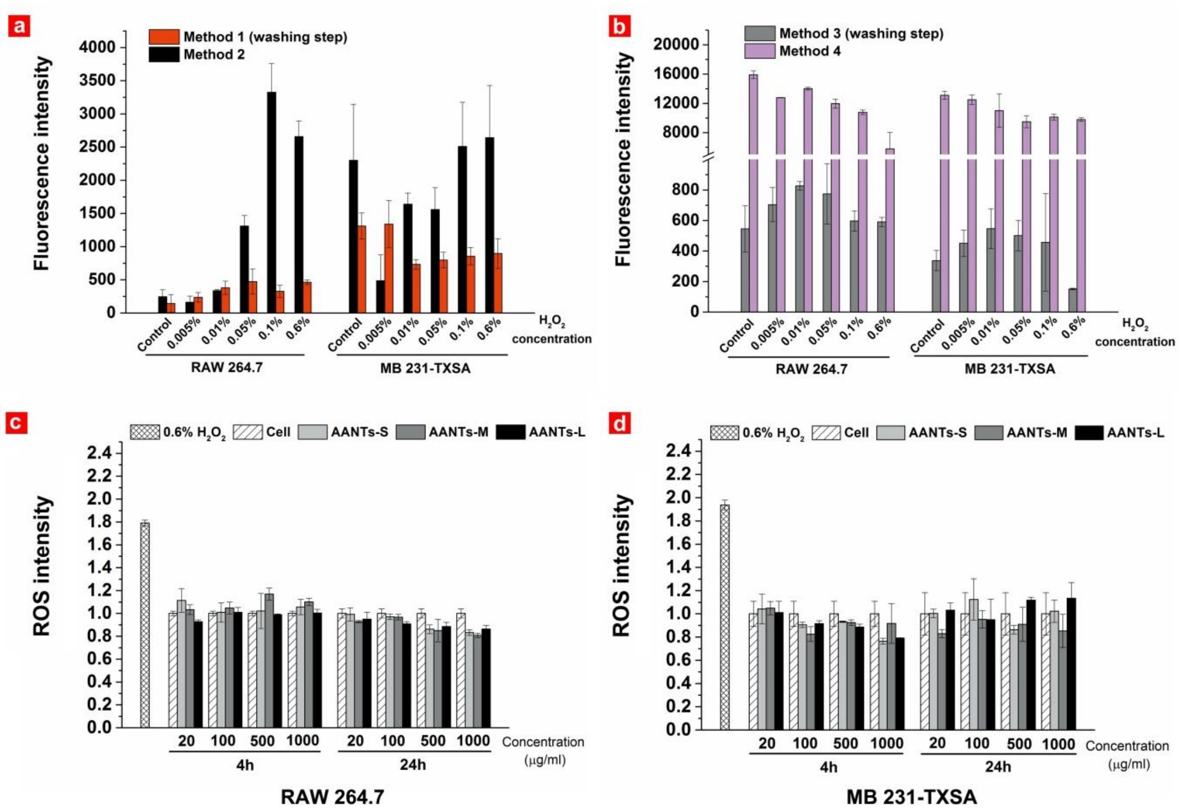

Figure S 4 (a and b**)** ROS detection with four methods mentioned in the scheme. (c and d) ROS quantification in MB 231-TXSA and RAW 264.7 cell line after AANTs treatment at the time-course of 4h and 24h.

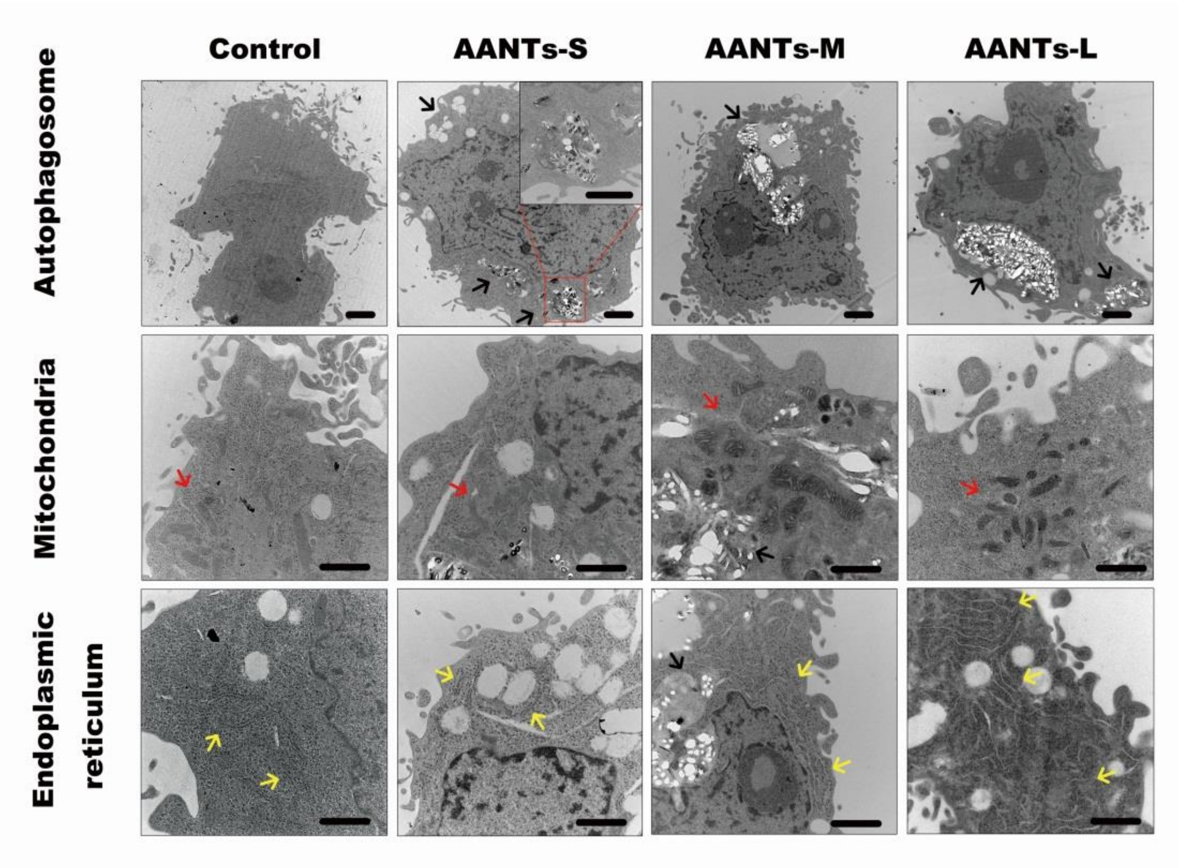

Figure S 5 TEM characterization of cell uptake and morphology of important organelles in MB 231-TXSA cell line after overnight (16h) exposure with three types of AANTs at a concentration 100 µg/ml. Similar to our observation in RAW 264.7 cell lines, we found the accumulation of autophagosome and autolysosome after AANTs exposure. AANTs were localized inside autophagosome. No significant morphological change mitochondria and endoplasmic reticulum was found. Black arrows: autophagosome; Red arrows: mitochondria; Yellow arrows: endoplasmic reticulum. Scale bar: 1 µm.

References

1. Krejsa, C. and G. Schieven, *Detection of Oxidative Stress in Lymphocytes Using Dichlorodihydrofluorescein Diacetate*, in *Stress Response*, J. Walker and S. Keyse, Editors. 2000, Humana Press. p. 35-47.
2. Bimbo, L.M., et al., *Drug permeation across intestinal epithelial cells using porous silicon nanoparticles.* Biomaterials, 2011. **32**(10): p. 2625-2633.
3. Bimbo, L.M., et al., *Biocompatibility of Thermally Hydrocarbonized Porous Silicon Nanoparticles and their Biodistribution in Rats.* ACS Nano, 2010. **4**(6): p. 3023-3032.

4. Heikkilä, T., et al., *Cytotoxicity study of ordered mesoporous silica MCM-41 and SBA-15 microparticles on Caco-2 cells.* European Journal of Pharmaceutics and Biopharmaceutics, 2010. **74**(3): p. 483-494.

5. Setyawati, M.I., C.Y. Tay, and D.T. Leong, *Effect of zinc oxide nanomaterials-induced oxidative stress on the p53 pathway.* Biomaterials, 2013. **34**(38): p. 10133-10142.

6. Jeong, Y.S., et al., *Cellular uptake, cytotoxicity, and ROS generation with silica/conducting polymer core/shell nanospheres.* Biomaterials, 2011. **32**(29): p. 7217-7225.

7. Oh, W.-K., et al., *Shape-Dependent Cytotoxicity and Proinflammatory Response of Poly(3,4-ethylenedioxythiophene) Nanomaterials.* Small, 2010. **6**(7): p. 872-879.

8. Qiu, Y., et al., *Surface chemistry and aspect ratio mediated cellular uptake of Au nanorods.* Biomaterials, 2010. **31**(30): p. 7606-7619.

9. Pulskamp, K., S. Diabaté, and H.F. Krug, *Carbon nanotubes show no sign of acute toxicity but induce intracellular reactive oxygen species in dependence on contaminants.* Toxicology Letters, 2007. **168**(1): p. 58-74.

Chapter 5 Anodic Alumina Nanotubes as Nano-Carriers for Delivery of Anticancer Therapeutics

5.1 Introduction, Significance and Commentary

The aim of this chapter is to explore the possibility of AANTs as drug carriers for drug loading and *in vitro* drug delivery. In this study, a novel therapeutic concept was developed by delivering a pro-apoptotic receptor agonist, tumor necrosis factor-related apoptosis-inducing ligand (Apo2L/TRAIL) for *in vitro* cancer cell killing. AANTs have been structurally engineered by an optimized pulsed anodization approach and subsequently employed as drug carriers. AANTs showed excellent biocompatibility, alterable geometry/surface chemistry, high drug loading capacity (104 ± 14.4 μg per mg of AANTs) and outstanding *in vitro* cancer cell killing. These results demonstrate that AANTs represent promising nano-carriers for drug delivery applications.

5.2 Publication

This section is included in the thesis as a research paper published by Ye Wang, Abel Santos, Gagandeep Kaur, Andreas Evdokiou, Dusan Losic, Structurally engineered anodic alumina nanotubes as nano-carriers for delivery of anticancer therapeutics, *Biomaterials*, **2014**, 35, 5517-5526

Statement of Authorship

Title of Paper	Systematic in vitro nanotoxicity study on anodic alumina nanotubes with engineered aspect ratio: Understanding nanotoxicity by a nanomaterial model
Publication Status	☑ Published ☐ Accepted for Publication ☐ Submitted for Publication ☐ Publication Style
Publication Details	Wang, Y.; Kaur, G.; Zysk, A.; Liapis, V.; Hay, S.; Santos, A.*; Losic, D.*; Evdokiou, A.*: Systematic in vitro nanotoxicity study on anodic alumina nanotubes with engineered aspect ratio: Understanding nanotoxicity by a nanomaterial model. Biomaterials 2015, 46,117-130. (IF=8.312)

Principal Author

Name of Principal Author (Candidate)	Ye Wang		
Contribution to the Paper	Designed project and accomplished 80% of experiments, performed data analysis and prepared manuscript		
Overall percentage (%)	80%		
Signature		Date	31/7/2015

Co-Author Contributions

By signing the Statement of Authorship, each author certifies that:

i. the candidate's stated contribution to the publication is accurate (as detailed above);

ii. permission is granted for the candidate in include the publication in the thesis; and

iii. the sum of all co-author contributions is equal to 100% less the candidate's stated contribution.

Name of Co-Author	Gagandeep Kaur		
Contribution to the Paper	Assisted in part of experiment		
Signature		Date	3/08/2015

Name of Co-Author	Aneta Zysk		
Contribution to the Paper	Assisted in part of experiment		
Signature		Date	11/08/15

Name of Co-Author	Vasilios Liapis		
Contribution to the Paper	Assisted in part of experiment		
Signature		Date	3/8/15

Name of Co-Author	Shelley Hay		
Contribution to the Paper	Assisted in part of experiment		
Signature		Date	3/8/15

Name of Co-Author	Andreas Evdokiou		
Contribution to the Paper	Supervised development of work, helped in data interpretation and manuscript evaluation		
Signature		Date	**11/8/2015**

Name of Co-Author	Abel Santos		
Contribution to the Paper	Supervised development of work, helped in data interpretation and manuscript evaluation		
Signature		Date	31/07/15

Name of Co-Author	Dusan Losic		
Contribution to the Paper	Supervised development of work, helped in data interpretation and manuscript evaluation		
Signature		Date	10/08/2015

Biomaterials 35 (2014) 5517–5526

Contents lists available at ScienceDirect

Biomaterials

journal homepage: www.elsevier.com/locate/biomaterials

Structurally engineered anodic alumina nanotubes as nano-carriers for delivery of anticancer therapeutics

Ye Wang [a], Abel Santos [a], Gagandeep Kaur [a], Andreas Evdokiou [b,*], Dusan Losic [a,*]

[a] School of Chemical Engineering, The University of Adelaide, Adelaide, SA 5005, Australia
[b] School of Medicine, Discipline of Surgery, The University of Adelaide, Adelaide, SA 5005, Australia

ARTICLE INFO

Article history:
Received 31 January 2014
Accepted 21 March 2014
Available online 14 April 2014

Keywords:
Tumor necrosis factor-related apoptosis-inducing ligand (TRAIL)
Anodic alumina nanotubes
Breast cancer
Protein/drug delivery

ABSTRACT

Here, we report a study on the biocompatibility, cell uptake and *in vitro* delivery of tumor necrosis factor-related apoptosis-inducing ligand (Apo2L/TRAIL) by new nano-carriers called anodic alumina nanotubes (AANTs) for potential cancer therapy. AANTs were electrochemically engineered by a unique pulse anodization process, which enables precise control of the nanotube geometry, and used here as nano-carriers for drug delivery. *In vitro* cytotoxicity and cell uptake of AANTs was assessed using MDA-MB231-TXSA human breast cancer cells and mouse RAW 264.7 macrophage cells. AANTs exhibited excellent biocompatibility in both cell lines over a time course of five days even at a maximum concentration of AANTs of 100 $\mu g\,mL^{-1}$. Transmission electron microscopy and fluorescence microscopy confirmed a significant uptake of AANTs by RAW 264.7 cells and breast cancer cells. AANTs loaded with the pro-apoptotic protein Apo2L/TRAIL showed exceptional loading capacity ($104 \pm 14.4\ \mu g\,mg^{-1}$ of AANTs) and demonstrated significant decrease in viability of MDA-MB231-TXSA cancer cells due to apoptosis induction. These results demonstrate that AANTs are promising nano-carriers for drug delivery applications.

1. Introduction

Delivery of bioactive drugs such as proteins and nucleic acids for cancer therapy has long faced great challenges mainly due to their poor pharmacokinetics, kidney or liver clearance and low permeability across intracellular barriers [1,2]. Rapid advances in developing nanomaterials for therapeutic drug delivery have brought new opportunities to overcome these inherent drawbacks. Their unique properties such as selective tumor targeting, limited side effects, co-delivery of different drugs, protection by encapsulation and controlled pharmacokinetics under physiological conditions make them suitable candidates for drug delivery applications [3]. For instance, Apo2L/TRAIL is a pro-apoptotic receptor agonist that belongs to the tumor necrosis factor (TNF) family of death ligands and can induce apoptosis of cancer cells with limited or no toxicity to normal cells [4]. Previous studies have demonstrated that Apo2L/TRAIL has a remarkable antitumor capability itself and a synergistic antitumor effect when combined with other chemotherapeutic agents [5,6]. However, poor pharmacokinetics (<30 min) is a major limitation of Apo2L/TRAIL for clinical applications [7]. Thus far, several preclinical studies have reported on the combination of Apo2L/TRAIL with biodegradable nanomaterials as drug carriers, including poly(lactic-co-glycolic) acid (PLGA) microparticles [8], hydrogel [9], human serum albumin nanoparticles [10] and polyethylene glycol (PEG) functionalized nanoparticles [11]. These studies showed improved stability and sustained release of Apo2L/TRAIL, suggesting that the combination of Apo2L/TRAIL and drug carriers may be a promising approach to improve current cancer therapy. However, further challenges still need to be addressed with respect to minimizing doses, enhancing drug loading capacity and better control of pharmacokinetics.

These drawbacks can be overcome by fabricating a robust nano-container capable of loading an optimal amount of Apo2L/TRAIL, preventing it from fast body clearance and maintaining a sustained release of Apo2L/TRAIL at the tumor site.

Among the broad range of nano-carrier candidates, one-dimensional (1D) nanostructures, especially carbon nanotube (CNTs), are highly desirable due to their large surface area, hollow cylindrical structure and unique property to cross cell-membrane barriers for delivering bioactive molecules [12,13]. Nevertheless, tedious purification and processing steps such as removal impurities (catalyst), CNTs cutting, surface functionalization and coating are required to make CNTs non-cytotoxic [14]. Therefore,

---

* Corresponding author.
E-mail address: dusan.losic@adelaide.edu.au (D. Losic).

http://dx.doi.org/10.1016/j.biomaterials.2014.03.059
0142-9612/Crown Copyright © 2014 Published by Elsevier Ltd. All rights reserved.

developing new and intrinsically non-toxic nanotubes through a facile and reproducible route could be an alternative approach for utilizing the advantageous 1D nanostructure in drug delivery applications.

Recently, anodic alumina nanotubes (AANTs) have been fabricated though a cost-competitive and industrialized electrochemical process called pulse anodization (PA) [15,16]. The geometry (length and diameter) of these nanotubes can be precisely engineered through PA. More importantly, nanoporous anodic alumina (NAA) has proven to be non-toxic to cells [17,18] and has been tested in various biomedical applications such as bone implants [19]. Therefore, engineered AANTs may be suitable candidates as 1D drug carriers. It is noteworthy that fibrous nanomaterials, such as asbestos fibers [17], CNTs [18] and nanowires [19] may impart significant cell toxicity by several means such as frustrated phagocytosis and oxidant injury [20]. Therefore, before AANTs become feasible nanomaterials for clinical applications, systematic cell toxicity studies are required to assess their cytotoxicity.

In this paper, we present a pioneering study on the use of AANTs as nano-carrier for drug delivery of anticancer therapeutics where Apo2L/TRAIL is used as a model drug. Scheme 1 summarizes the fabrication of AANTs, their drug loading with Apo2L/TRAIL and its mechanism of release to induce cancer cell apoptosis. AANTs 600 nm long and 100 nm in outer diameter were fabricated considering this size as optimal to provide high Apo2L/TRAIL loading and biocompatibility. Cytotoxicity and cell uptake properties of AANTs were assessed by breast cancer cell line MDA-MB231-TXSA and RAW 264.7 macrophage cells. *In vitro* drug release was performed and drug delivery capability was tested using MDA-MB231-TXSA breast cancer cells.

2. Materials and methods

2.1. Materials

Aluminum (Al) foils of thickness 0.32 mm and purity 99.9997% were supplied by Goodfellow Cambridge Ltd. (UK). Sulfuric acid (H_2SO_4), phosphoric acid (H_3PO_4), copper(II) chloride ($CuCl_2$), hydrochloric acid (HCl), ethanol (C_2H_5OH), perchloric acid ($HClO_4$), hydrogen peroxide (H_2O_2), chromium trioxide (CrO_3), fluorescein isothiocyanate (FITC), 3-aminopropyltriethoxysilane (APTES), sodium hydroxide (NaOH), acetic acid ($C_2H_4O_2$), acetone (C_3H_6O), paraformaldehyde ($OH(CH_2O)_nH$ ($n = 8-100$)), glutaraldehyde ($C_5H_8O_2$), osmium tetroxide (OsO_4), ethylenediaminetetraacetic acid ($C_{10}H_{16}N_2O_8$ − EDTA), 4′,6-diamidino-2-phenylindole ($C_{16}H_{15}N_5$ − DAPI), phalloidin ($C_{35}H_{48}N_8O_{11}S$) and crystal violet ($C_{25}N_3H_{30}Cl$) were purchased from Sigma–Aldrich (Australia) and used without further processing. Dulbecco's modified Eagle's medium (DMEM), fetal calf serum (FCS), penicillin/streptomycin, and glutamine were purchased from Biosciences (Australia). Trypsin (Gibco); phosphate buffer solution (PBS) (HyClone Laboratories, Inc); Culture flasks; 96-well plate; 8-well chamber slides and 6-well plate (greiner Bio-One); 10 v% formalin solution (Ajax Finechem); alamarBlue® (Life Technologies Corporation); non-tagged homotrimeric Apo2L/TRAIL was generously provided by Genentech Inc. (South San Francisco, CA) and Ac-DEVD-AFC (fluorogenic caspase-3(CPP32) substrate) was purchased from Kamiya Biomedical Company; Ultrapure water Option Q-Purelabs (Australia) was used for preparation of all the solutions used in this study.

2.2. Fabrication of anodic alumina nanotubes

AANTs were synthesized by a modified pulse anodization process using galvanostatic mode [16]. Briefly, Al foils 1.5 cm in diameter were first sonicated in EtOH and ultrapure water for 15 min each and dried under nitrogen stream. Aluminum foils were electropolished prior to anodization in a mixture of EtOH and $HClO_4$ 4:1 (v:v) at 20 V and 5°C for 3 min. After this, the first anodization step was carried out in a 0.3 M aqueous solution of H_2SO_4 at 25 V and 6°C for 20 h. The resulting NAA layer was dissolved by wet chemical etching in a solution of 0.2 M chromic acid (H_2CrO_4) and 0.4 M H_3PO_4 at 70°C for 3 h. The textured aluminum was first anodized at the same conditions for 5.5 h. Then, pulse anodization was conducted under galvanostatic conditions at −1°C. The area exposed to the electrolyte solution was 0.95 cm^2. This anodization step consisted of a cyclic combination of mild (MA) and hard anodization (HA) pulses under galvanostatic mode. In our study, we used a 5 s MA-

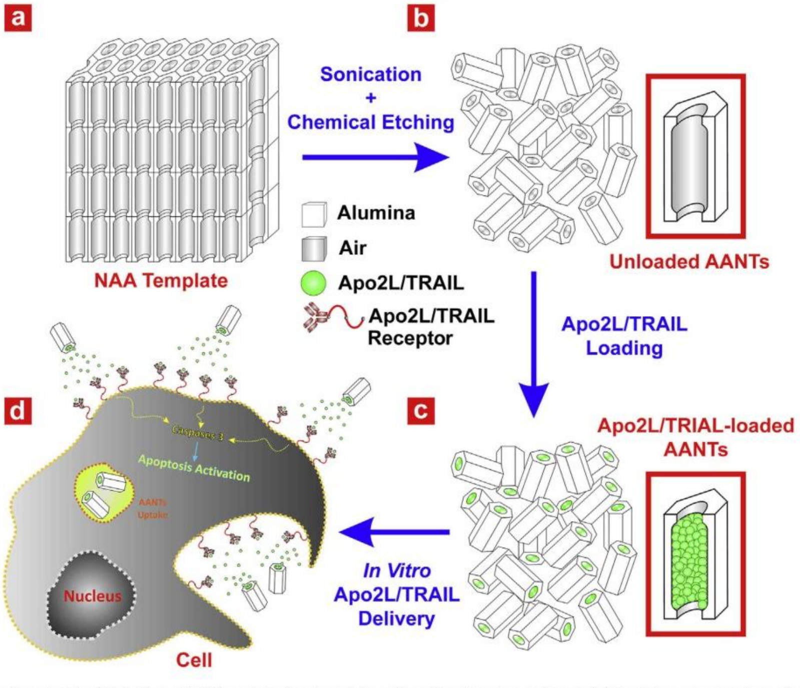

Scheme 1. Schematic illustration showing fabrication of AANTs and *in vitro* drug delivery from them for cancer therapy. (a) Resulting nanoporous anodic alumina structure obtained after pulse anodization of aluminum foil. (b) Free-standing AANTs obtained after wet chemical etching and sonication. (c) Apo2L/TRAIL loading inside AANTs. (d) *In vitro* Apo2L/TRAIL release from AANTs and apoptosis mechanism killing breast cancer cells (MDA-MB231-TXSA).

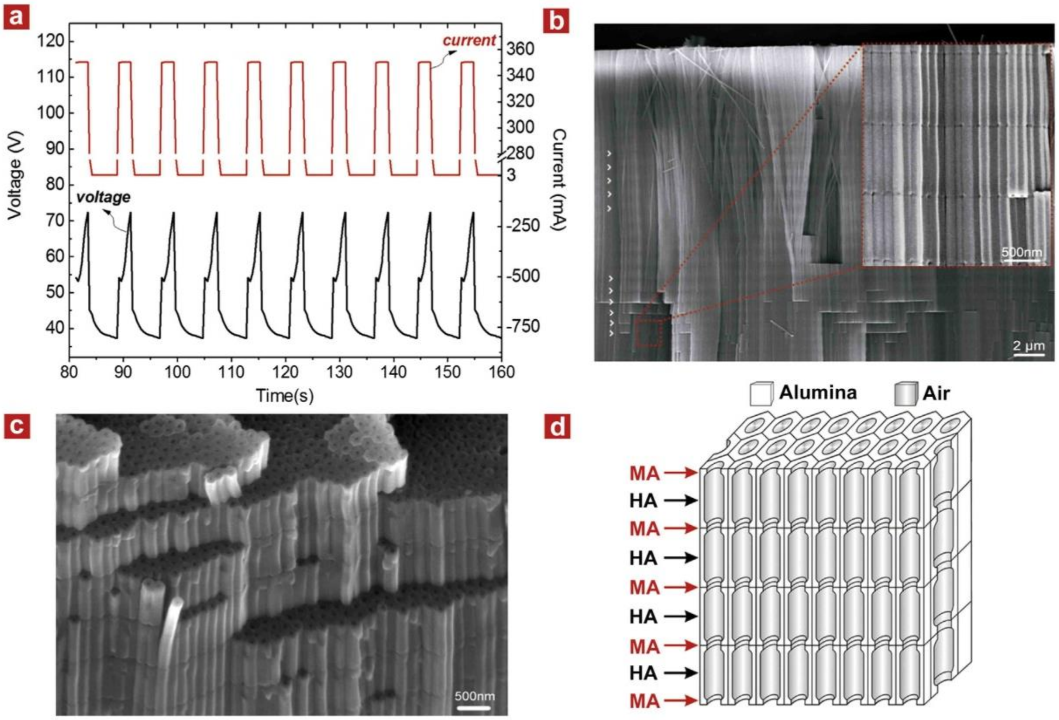

Fig. 1. Fabrication of anodic alumina nanotubes by galvanostatic pulse anodization. (a) Typical current–voltage profile used during pulse anodization of aluminum. Galvanostatic pulses consist of 5 s MA-pulse (0.003 A) and 2 s HA-pulse (0.350 A); (b) Cross-section SEM images of NAA templates prepared by pulse anodization. White arrows denote layer structures. An enlarged image clearly shows the periodically spaced layers created by each current pulse. (c) A slanted image of NAA templates. (d) Scheme illustrating cross-section view of NAA before dispersion. Nanotubes are self-organized in a hexagonal fashion (black and red arrows indicate layers created by HA- and MA-pulses, respectively). (For interpretation of the references to color in this figure legend, the reader is referred to the web version of this article.).

pulse at current of 0.003 A followed by 2 s HA-pulse at current of 0.350 A. This process was repeated for 30–50 cycles. Then, the remaining aluminum substrate was removed by wet chemical etching in a mixture of 0.2 M $CuCl_2$ and 6.1 M HCl. Free-standing AANTs were obtained by immersion into the same acid solution followed by gentle ultrasonic treatment.

2.3. Functionalization of AANTs with fluorescein isothiocyanate (FITC)

AANTs were labeled with FITC by surface modification with APTES through a well-established protocol [20]. To this end, free-standing AANTs were directly transferred into boiled hydrogen peroxide (30 wt%) for 15 min to increase the number of hydroxyl groups on the surface. After that, the solution was cooled down to room temperature followed by washing AANTs with ultrapure water and subsequent centrifugation. Next, AANTs were treated with 5 vol% APTES in absolute ethanol for 2 h and then washed repeatedly by acetone and ethanol to remove unreacted APTES molecules. APTES-functionalized AANTs were further incubated with 400 μL FITC/EtOH (2.5 mg mL^{-1}) at room temperature for 1 h. Finally, FITC-functionalized AANTs were washed several times with EtOH and stored in ultrapure water till further use. Fourier transform infrared (FTIR) spectroscopy (Spectrum 400 FTIR Spectrometer, PerkinElmer) and UV–Vis spectroscopy (Cary 300 UV–Vis, Agilent) were used to verify the labeling of AANTs.

2.4. Physicochemical characterization

The shape and structure of AANTs were characterized by a transmission electron microscope (FEI Tecnai G2 Spirit TEM) and a field emission gun scanning electron microscope (FEG-SEM FEI Quanta 450). Zeta-potential and particle size distributions of AANTs were analyzed by a ZetaSizer Nano (Malvern Instruments Ltd., Worcestershire, UK). Buffer solutions with different pH's (i.e. 3.7, 4.3, 5, 6, 7 and 8) were used in this experiment in order to analyze the effect of pH over the zeta-potential and size distribution of AANTs. The pH of these solutions was adjusted by acetic acid or NaOH solutions. AANTs with a concentration of 120 μg mL^{-1} were dispersed in 1 mL of the corresponding pH buffer solution and sonicated for 1–5 min before analysis. An XS analytical balance with readability 0.01 mg (Mettler-Toledo International, Inc.) was used for sample weighting in all the experiments.

2.5. Cell culture and toxicity assay

2.5.1. Cell culture

MDA-MB-231-TXSA and RAW 264.7 cell lines were tested for biocompatibility and cytotoxicity of AANTs. The MDA-MB-231 derivative cell line, MDA-MB-231-TXSA was kindly provided by Dr Toshiyuki Yoneda (formerly at University of Texas Health Sciences Centre, San Antonio, Texas).

Cells were cultured in Dulbecco's modified Eagle's medium (DMEM), supplemented with glutamine (2 mM), penicillin (100 IU mL^{-1}), streptomycin (100 μg mL^{-1}) and 10% fetal bovine serum at 37°C in a 5% CO_2-containing humidified atmosphere. Prior to each test, cells were harvested using trypsin–EDTA–PBS and 1×10^4 cells were plated in each well in 96-well plate setup with 200 μL of growth media. Cells were allowed to attach overnight prior to incubation with AANTs. Unless otherwise indicated, all the cell experiments were repeated three times.

2.5.2. Cell toxicity assay

To monitor cytotoxicity of AANTs, both cell lines were incubated with different concentrations of AANTs ranging from 1 to 100 μg mL^{-1}. The experimental end points were selected as 24 h and 5 days, respectively. For 5 day assay, 150 μL media was carefully replaced by fresh media after 48 h. Toxicity of AANTs was measured on the basis of cell viability after determined intervals of time via alamar blue and crystal violet assays using previously described procedures [21,22]. Briefly, after determined time point in study, culture media were removed and 200 μL alamar blue solution (10% dilution in PBS) was added to each well and incubated at 37 °C for 20–40 min, after which fluorescence was measured at 560/590 nm using a plate reader (Fluostar OPTIMA, BMG Labtech). Same cultures were subsequently washed with PBS, fixed with 10 vol % formalin and incubated with 0.1 wt% crystal violet solution [23]. After this, staining cells were carefully washed three times with PBS and imaged. Subsequently, 200 μL of 10 vol% acetic acid solution was added to each well to extract dye color and the absorbance of dissolved dye was measured at

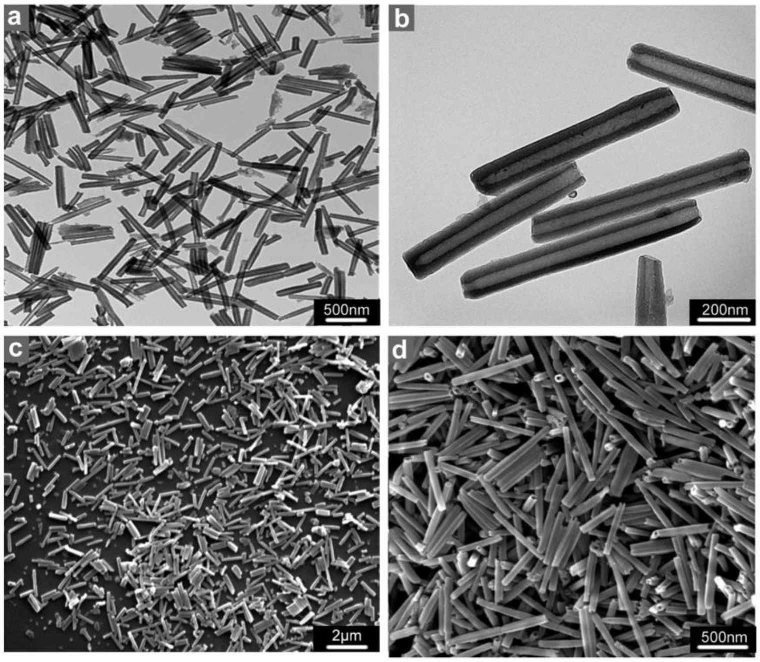

Fig. 2. Structural analysis of AANTs fabricated by pulse anodization. TEM (a and b) and SEM (c and d) characterization of AANTs. The length of AANT is around 600 nm; the inner and outer diameters of AANT are measured to be 50 and 100 nm, respectively, with 25 nm at the nanotube mouth.

570 nm. After background subtraction, the results of these two assays were normalized against viability of untreated cells, which were regarded as 100% viable. Control experimental groups were set by incubating 10 μg mL^{-1} of AANTs with DMEM media. No interruption or background error was observed.

2.6. Cell imaging

2.6.1. TEM microtome sample preparation

To prepare microtome samples, 1×10^5 cells/well were seeded in a 6-well plate and allowed to attach overnight. Then, 100 μg mL^{-1} of AANTs were transferred into culture media followed by incubation overnight. After that, cells were carefully washed with sterile PBS two times, and transferred into 1.5 mL eppendorf tubes. Collected cell pellets were re-suspended in a solution of 4 vol% paraformaldehyde and 1.25 vol% glutaraldehyde and were fixed overnight. Then, all samples were post-fixed in a 2 vol% osmium tetroxide solution for 45 min. After this, cells were fully dehydrated and embedded in epoxy resin. Ultrathin sections of 70 nm were cut and post-stained with uranyl acetate and lead citrate [24]. Cell samples were analyzed by TEM at 100 kV.

2.6.2. Fluorescence microscopy

To determine AANTs cellular uptake, 1×10^4 cells/well (MDA-MB231-TXSA and RAW 264.7) were plated in 8-well chamber slides, respectively, and allowed to attach overnight. Next morning, 40 μg mL^{-1} of AANTs and FITC-AANTs were transferred into respective wells and incubated for 24 h in culture. Cells were fixed using 4 vol% paraformaldehyde solutions for 20 min prior to phalloidin and DAPI staining. Fixed cells were permeabilized using saponin and 0.1 wt% tween surfactants for 20 min. After permeabilization, cells were incubated with 1 μg mL^{-1} red phalloidin (tetramethyl Rhodamine B isothiocynate) for 1 h. Fixed cultures were washed three times with PBS in between staining steps. Finally, cells were stained with 50 mg mL^{-1} DAPI solution for 2 min and mounted with a coverslip for imaging using anti-fade solution. Imaging was done using Axio-vision fluorescence microscope (Carl Zeiss Group, Oberkochen, Germany).

Table 1
Size distribution of AANTs in different aqueous solutions.

Media	Size (nm)[a]	PDI[b]	ζ-potential (mV)
pH 3.7	473.6 ± 38.2	0.277 ± 0.016	22.8 ± 0.4
pH 4.2	574.0 ± 37.9	0.314 ± 0.052	14.9 ± 1.6
pH 5.0	356.0 ± 11.4	0.222 ± 0.012	−25.5 ± 1.1
pH 6.0	444.6 ± 11.5	0.215 ± 0.048	−22.8 ± 0.9
pH 7.0	301.3 ± 6.6	0.139 ± 0.006	−20.0 ± 0.8
pH 8.0	302.8 ± 1.6	0.126 ± 0.023	−14.1 ± 0.7
PBS (pH 7.2)	588.4 ± 32.0	0.332 ± 0.021	−15.5 ± 0.3
DMEM	344.8 ± 11.5	0.370 ± 0.025	−10.3 ± 0.1

[a] The values represent the means of at least three experiments; ±: standard deviation.

[b] PDI: polydispersity index.

2.7. Apo2L/TRAIL loading, in vitro release and delivery

For Apo2L/TRAIL loading experiments, 250 μg of AANTs were dispersed in 100 μL of PBS solution. Then, 40 μL of Apo2L/TRAIL solution (1 mg mL^{-1}) was added followed by 10 min of sonication. The solutions were kept at room temperature overnight. Next morning, samples were centrifuged and washed with 1 mL of PBS solution to completely remove Apo2L/TRAIL residue. Drug loading capacity of AANTs was determined using 250 μg Apo2L/TRAIL-loaded AANTs sample for thermogravimetric (TGA) analysis (Hi-Res Modulated TGA 2950). The temperature was increased from room temperature to 580°C at a rate of 10 °C min^{-1} under pure nitrogen gas flow at 100 cm^3 min^{-1}.

In vitro Apo2L/TRAIL release was conducted at 37°C. In this study, 250 μg of Apo2L/TRAIL-loaded AANTs were dispersed in 1 mL PBS solution in a 1.5 mL eppendorf tube. Before reading, sample was centrifuged at 1.3×10^4 rpm for 5 min. Then, 50 μL of supernatant was drawn out and replaced by 50 μL of fresh PBS solution. The concentration of Apo2L/TRAIL in the supernatant was determined by standard bicinchoninic acid (BCA) assay [25].

For *in vitro* Apo2L/TRAIL delivery assays, 1×10^4 cells/well were seeded in a 96-well plate and incubated overnight to allow cell attachment. Then, Apo2L/TRAIL-loaded AANTs with different concentrations were added to each well. 50 ng mL^{-1} of Apo2L/TRAIL added directly into culture media were used as a positive control. Cell viability was checked after 165 min with alamar blue assay by the above-mentioned experimental procedure. A parallel experiment was done for evaluating caspase activity.

2.8. Measurement of caspase activity

To measure caspase activity, 1×10^4 cells/well were placed in a 96-well plate and were allowed to attach overnight. Next day, AANTs loaded with Apo2L/TRAIL were introduced in the media with concentration range from 1 to 100 μg mL^{-1} and cells were cultured for 165 min. After culture time, media was removed and 30 μL of NP-

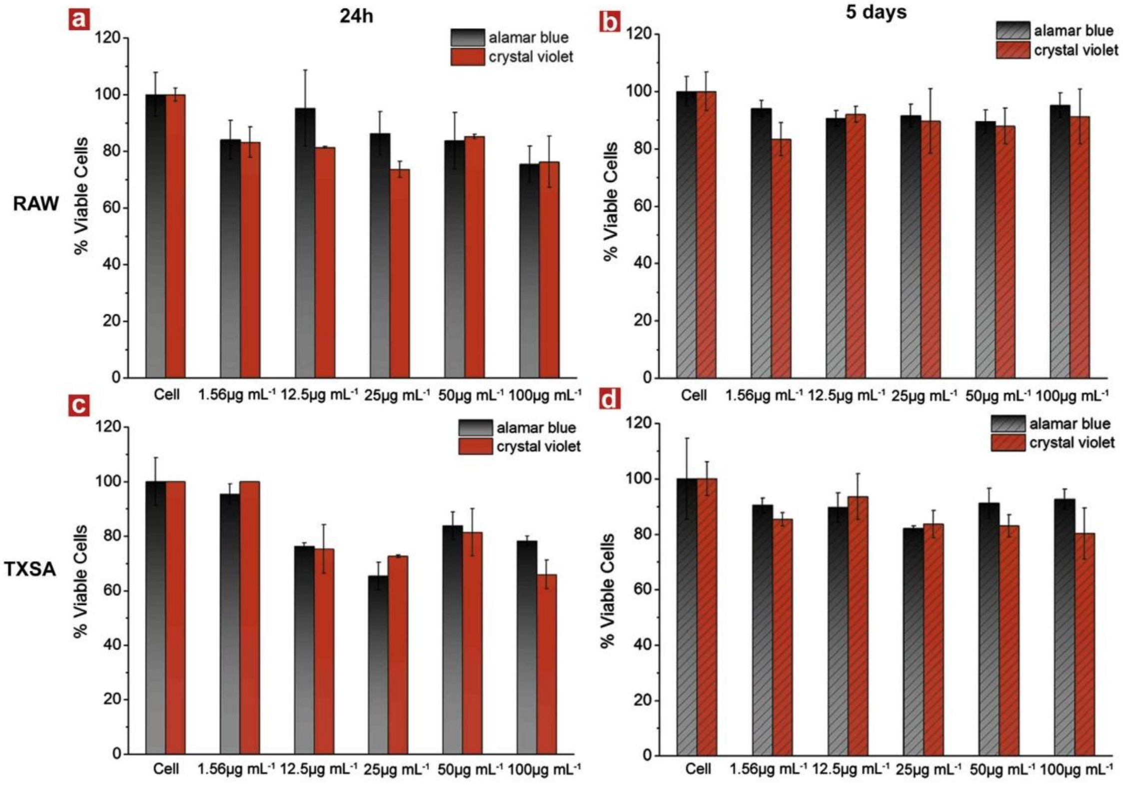

Fig. 3. Cell toxicity studies of AANTs on RAW 264.7 and MDA-MB231-TXSA cell lines within 24 h and 5 days. Cells have more than 80% viability in both cell lines, demonstrating the biocompatibility of AANTs.

40 lysis buffer containing 5 mM Tris–HCl (pH 7.5), 5 mM EDTA and 0.5 wt % NP-40 were added to lyse the cells. Cell lysates were stored at −80 °C till further processing. Caspase activity in the cells was measured using Ac-DEVD-AFC (fluorogenic caspase-3 (CPP32) substrate). Briefly, cell lysates were incubated with caspase substrate for 4 h and fluorescence caspase activity was read at 505 nm.

3. Results

3.1. Preparation and characterization of anodic alumina nanotubes (AANTs)

AANTs were synthesized by a pulse anodization process, which periodically combines high and low galvanostatic current pulses in order to switch the anodization regime between MA and HA conditions (Fig. 1a). Cross-sectional SEM images of as-prepared NAA with layered structures are presented in Fig. 1b and c. This process can create periodically spaced layers of NAA at each pulse (Fig. 1b and d) and simultaneously weaken the junction between cells and layers (Fig. 1c).

The anodization conditions were set to obtain AANTs of 600 nm in length. After selective chemical etching and gentle sonication, the close-packed NAA template was broken down into individual nanotubes with uniform size and shape. TEM and SEM images clearly show the morphology of AANTs after this process, which consist of cylindrical nanotubes of 100 nm outer diameter and 600 nm length (Fig. 2). It is noteworthy that, whereas the inner diameter is 50 nm at the lumen, it becomes narrower at the opening ends (i.e. 25 nm, approximately) [16].

Physicochemical characteristics of AANTs were analyzed under different pH and media conditions [26]. AANTs can form stable colloids within pH 5–8 without significant aggregation (Table 1). The hydrodynamic diameter was increased in PBS solution due to the ionic strength in salt-containing media, which is consistent with previous reports on other nanomaterials [27,28]. However, AANTs showed better dispersion in DMEM media containing 10% FCS due to the protein adsorption effect reported previously [26,29]. It is known that the zeta-potential of metal oxides is related with pH due to the adsorption of hydrogen ions or hydroxyl groups present on the oxide surface [29]. In our study, AANTs are positively charged when pH <4.5 and negatively charged from pH 5 to 7, with a maximum zeta-potential of −25 mV at pH 5 (see Fig. S1 – Supporting Information).

3.2. Cell toxicity analysis of AANTs on RAW 264.7 macrophages and MDA-MB231-TXSA breast cancer cells

Alamar blue and crystal violet assays were used to measure the cytotoxicity of prepared AANTs. Cell toxicity experiments were carried out for 1 and 5 days with different concentrations of AANTs, which ranged from 1.56 to 100 $\mu g\ mL^{-1}$, on breast cancer cells (MDA-MB231-TXSA) and immune response cells (RAW264.7 macrophages) (Fig. 3). No concentration dependent toxicity patterns of AANTs were evident in both cell lines. In these experiments, the survival rate was higher than 80% even at the highest dose of AANTs of 100 $\mu g\ mL^{-1}$ after 5 days.

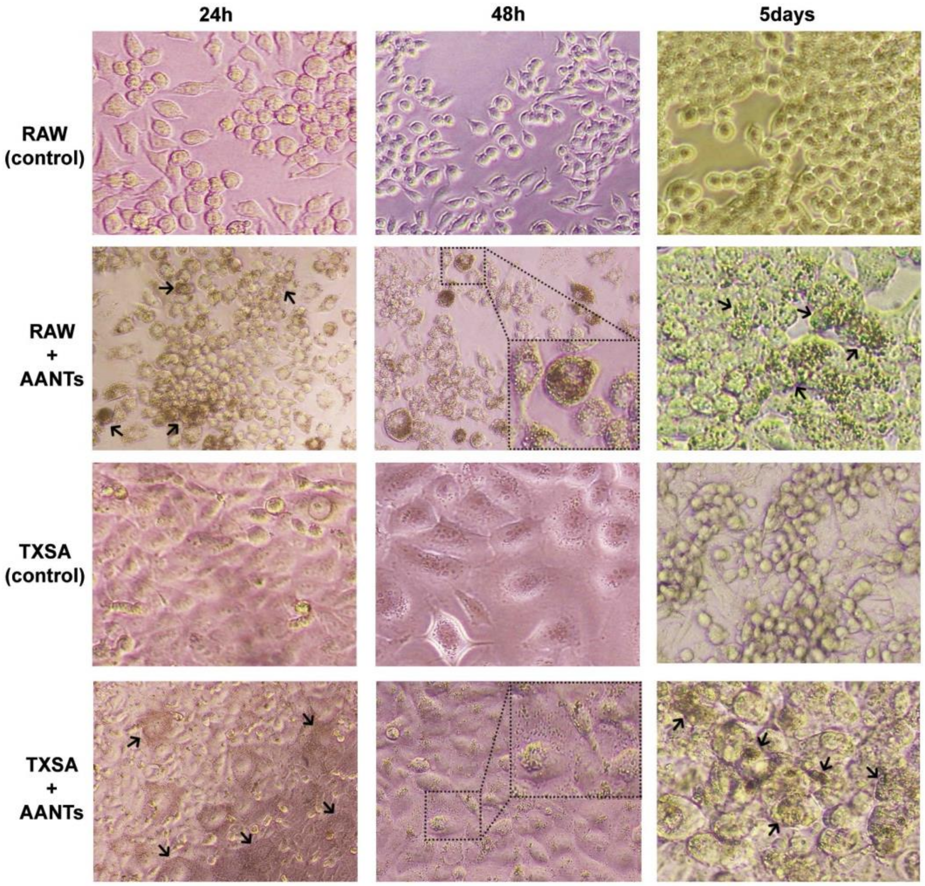

Fig. 4. Light microscope images of AANTs (100 μg mL^{-1}) incubated with two cell lines. Black arrows indicate that cells are closely surrounded by AANTs. Note that cells covered by AANTs have darker color due to the optical light refraction and adsorption of anodized alumina [30]. No cell viability inhibition was found during 5-day experiment. Insets show magnified views of individual cells after 48 h.

Light microscopy images showing the morphology of RAW 264.7 and TXSA cell lines with AANTs at the maximum concentration (100 μg mL^{-1}) are presented in Fig. 4. From this, we noted that AANTs tend to surround cells without affecting their growth. After 5 days of incubation, the number of cells increased significantly in both cell lines, revealing that AANTs do not affect cell viability, which confirms their biocompatibility.

3.3. Cellular interactions of AANTs with RAW 264.7 macrophages and MDA-MB231-TXSA breast cancer cells

The interactions between AANTs and cells after incubation overnight with 100 μg mL^{-1} of AANTs were imaged by TEM in order to examine their possible internalization (Fig. 5). TEM images proved that AANTs were readily internalized by macrophage cells and breast cancer cells. For macrophage cells, all the visible nanotubes were localized within numerous autophagic cellular vacuoles. The fusion of autophagosome with autophagic vacuoles can be found within the image area; while autophagic vacuoles containing cellular debris were also identified (Fig. 5a, b and d). Breast cancer cells also have AANTs uptake as shown in Fig. 5c and e.

AANTs were also functionalized with FTIC by APTES chemistry and functionalization was verified by FTIR and UV–Vis spectroscopy (Fig. S2 – Supporting Information). Fluorescence imaging confirmed that AANTs were internalized by macrophage cells and accumulated inside autophage vacuoles, which were shown by the separated, bright green dots surrounding the nucleus. Similar results were also found in MDA-MB231-TXSA breast cancer cells, which demonstrated the successful cell uptake of AANTs (Fig. 6).

3.4. In vitro Apo2L/TRAIL release and delivery on cells

TGA analysis established that Apo2L/TRAIL loading capacity of AANTs was 104 ± 14.4 μg mg^{-1}of AANTs (Fig. S3 – Supporting Information). *In vitro* drug release studies showed that around 40% of Apo2L/TRAIL was released after 30 min followed by a sustained release pattern extended for 240 min (Fig. 7). No burst release was evident under these conditions.

Apo2L/TRAIL delivery and Apo2L/TRAIL-induced apoptosis was tested on MDA-MB231-TXSA breast cancer cells, which are known to be highly sensitive to Apo2L/TRAIL-mediated apoptosis [6]. Cell

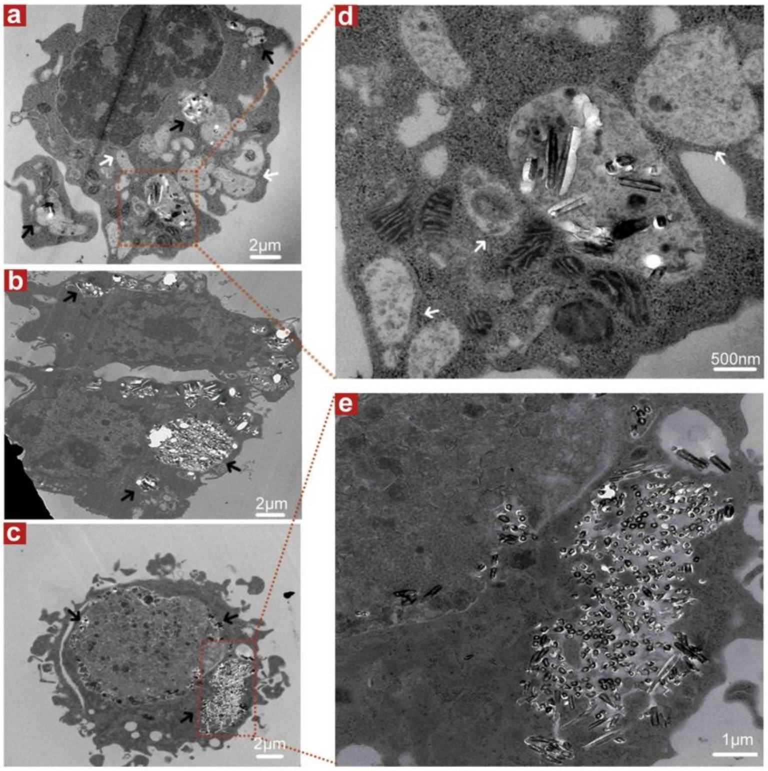

Fig. 5. TEM images of AANTs (100 μg mL^{-1}) internalized by RAW 264.7 macrophage cells (a, b, and d) and MDA-MB231-TXSA cell (c and e); (d) and (e) are magnified views of (a) and (c). The black arrows identify AANTs inside cells; white arrows indicate the fusion of autophagic vacuoles, in which cellular debris were located inside.

viability decreased significantly in a dose-dependent pattern after 165 min of incubation with Apo2L/TRAIL-loaded AANTs (Fig. 8). The decrease in cell viability was concomitant with a dose-dependent increase in caspase-3 activity. Even at the lowest dose of 1 μg mL^{-1} AANTs, caspase-3 activity was significantly higher than in those cells treated with soluble Apo2L/TRAIL, indicating effective cell apoptosis induced by Apo2L/TRAIL delivered from AANTs. Thereafter, caspase-3 activity increased with increasing dose of AANTs saturating at 200 μg mL^{-1}. Morphological changes characteristic of apoptosis assessed by light microscopy were clearly

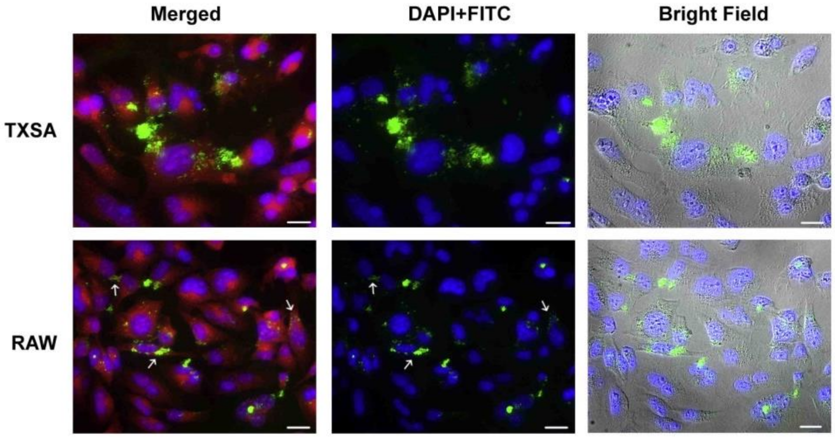

Fig. 6. Fluorescence microscopy image of AANTs-FITC with RAW 264.7 macrophage and TXSA breast cancer cells. White arrows show that AANTs were internalized and located inside autophagic vacuoles. Red: phalloidin; Blue: DAPI; Green: FITC. (Scale bar = 20 μm). (For interpretation of the references to color in this figure legend, the reader is referred to the web version of this article.).

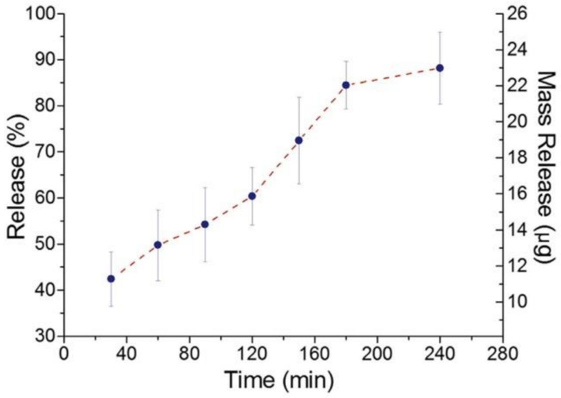

Fig. 7. *In vitro* drug release profile of AANTs loaded with Apo2L/TRAIL in PBS solution at 37 °C. The values represent the means of at least three experiments.

evident. At the same time, AANTs can be visualized surrounding the cells shown by the bright light spots in Fig. 8c.

4. Discussion

The objective of this study is to demonstrate the application of AANTs as new nano-engineered drug carriers for cancer therapy, where the pro-apoptotic receptor agonist, Apo2L/TRAIL, is used as a model anticancer drug. The fabrication of AANTs was performed by an electrochemical anodization process with galvanostatic pulsing mode. Significance of this approach is the very simple, top-down fabrication process which allows scalable and cost-competitive production of AANTs using Al foils as starting material [16]. Additionally, with the ability to alter the surface chemistry of AANTs [20], it could be possible to attach specific antibodies for targeting cancer cells selectively, or used as imaging probes or magnetic nanoparticles making AANTs highly sophisticated and multifunctional drug nano-carriers.

The concern for any new synthesized material proposed for biomedical applications is its biocompatibility and safety and therefore it was the first point to be addressed in our study. This is especially critical for nanomaterials with 1D structure, considering asbestos fibers and fiber-shaped nanoparticles, where toxicity is directly related to their length [31,32]. It is widely accepted that 1D structures longer than 20 μm are generally more toxic than shorter ones (<10 μm) [33]. Therefore, by designing the pulse anodization process, we were able to synthesize ultra-short AANTs with uniform 600 nm length. These AANTs showed excellent biocompatibility. Recently, autophagy dysfunction has been shown as an important type of cell toxicity induced by nanomaterials [34]. Autophagy, or lysosomal degradation pathway, is a homeostatic process in which cells respond to stress signals and are protected against infectious and inflammatory diseases [35]. It has been found that gold nanoparticles and quantum dots can induce size-dependent autophagy activation after cell uptake [36,37]. Graphene oxide, when internalized by RAW 264.7 mouse macrophage cells, can trigger autophagy toxicity partly regulated by the toll-like

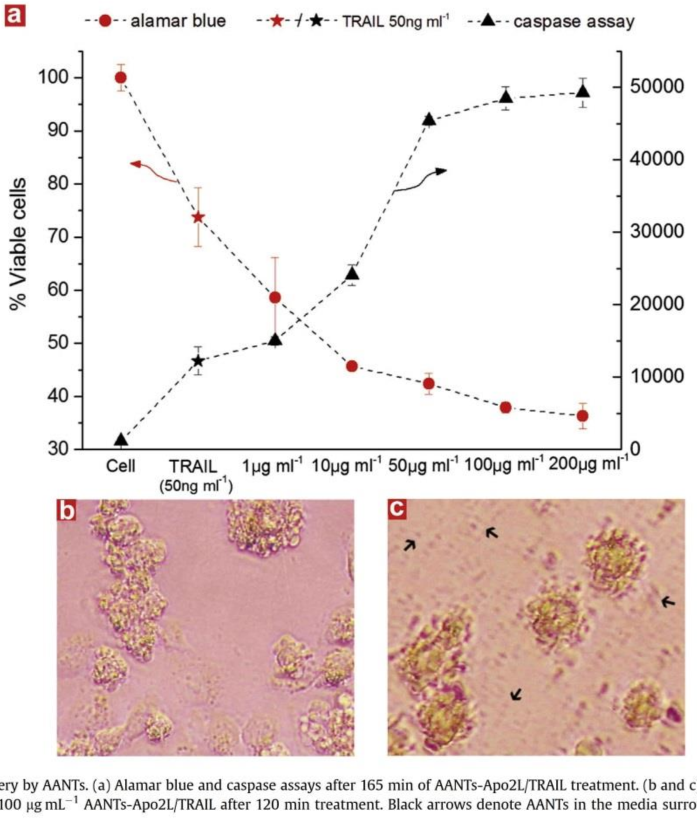

Fig. 8. *In vitro* Apo2L/TRAIL delivery by AANTs. (a) Alamar blue and caspase assays after 165 min of AANTs-Apo2L/TRAIL treatment. (b and c) Cell apoptosis images induced by (b) 50 ng ml^{-1} Apo2L/TRAIL and (c) 100 μg mL^{-1} AANTs-Apo2L/TRAIL after 120 min treatment. Black arrows denote AANTs in the media surrounding cells.

receptors pathway [38]. In our study, high-resolution TEM images of macrophage cells demonstrated significant autophagy activation induced by AANTs uptake. However, cell viability was maintained even at the highest dose of AANTs. Therefore, we conclude that RAW 264.7 macrophage cells are able to replace the damaged organelles after severe autophagy activation when internalizing AANTs.

Furthermore, engineered AANTs have a unique lumen structure and narrow-open ends, which can serve as nano-reservoirs to achieve ultra-high loading of therapeutic molecules and sustain their release. In this study, we found that the Apo2L/TRAIL loading capacity of AANTs ($104 \pm 14.4\ \mu g\, mg^{-1}$) is much higher than $\sim 30\ \mu g\, mg^{-1}$ for nanoparticles [39], $\sim 1.3\ \mu g\, mg^{-1}$ for microparticles [8] and $\sim 40\ \mu g\, mg^{-1}$ for hydrogels [27] reported in previous studies. This can be attributed to the unique ultra-large inner volume of single AANTs estimated to be $1.2 \times 10^6\ nm^3$. Compared to the general hydrodynamic volume of therapeutic proteins (approximately 4–1440 nm^3) [39], AANTs provide sufficient space for loading large amounts of protein molecules and provide high dosage and localized concentration. Since the geometry (diameter and length) of AANTs is precisely controlled, it is possible to significantly increase loading capacity required for a specific therapy.

In vitro Apo2L/TRAIL release kinetics study from AANTs showed a characteristic release pattern without burst release phase. It is worth noting that burst release is characteristic of surface-adsorbed drug molecules [40]. The absence of burst release indicates that Apo2L/TRAIL molecules are located inside the nanotubes and diffuse from the inner side of AANTs to the buffer solution (i.e. milieu). However, the release is faster (240 min) than expected, which could be associated with the fact that nanotubes are opened on both sides, allowing fast wetting of nanotubes with buffer solution and thus aiding a fast diffusion of Apo2L/TRAIL molecules to the milieu. To extend Apo2L/TRAIL release and improve drug releasing characteristics of AANTs, several approaches can be considered such as closing AANTs after drug loading or wrapping AANTs with degradable polymers.

Finally, our *in vitro* drug delivery study revealed that the AANTs-Apo2L/TRAIL nano-carrirers effectively induce cell apoptosis for MDA-MB231-TXSA cells. Due to the considerable drug loading, the high concentration of Apo2L/TRAIL triggered severe cell death within a very short time. Interestingly, we found that AANTs tend to compact on cancer cell surfaces, which may be beneficial for Apo2L/TRAIL-receptor binding through localized drug release surrounding the cell.

5. Conclusions

In summary, we have described the electrochemically engineered AANTs as new drug delivery nano-carriers and have demonstrated their biocompatibility, cell uptake and potential application for cancer therapy using Apo2L/TRAIL as a model drug. Our results have demonstrated that as-prepared AANTs have excellent biocompatibility with both immune and cancer cells at a high concentration ($100\ \mu g\, mL^{-1}$) without any chemical modification. Autophagy activation was confirmed in macrophage cells, but this phenomenon did not affect macrophage cell viability. AANTs exhibited ultra-high Apo2L/TRAIL loading capacity ($104 \pm 14.4\ \mu g\, mg^{-1}$) compared to other nanomaterials, and provided a successful release with considerable local concentration ($>24\ \mu g$) at *in vitro* simulated physiological conditions. Furthermore, our results clearly showed that the AANTs-Apo2L/TRAIL nano-carrier can efficiently reduce MDA-MB231-TXSA cancer cell viability due to cell apoptosis induced by high concentration of Apo2L/TRAIL. These findings demonstrate that AANTs is a promising biomaterial for drug delivery applications. It is expected that further innovative AANTs-based drug delivery platforms will be developed for different therapeutic applications such as targeted and remotely controlled drug delivery systems.

Acknowledgments

This research was supported by the Australian Research Council (ARC) through the grants DP120101680, FT110100711, DE14010054, the National Health and Medical Research Council (NHMRC) of Australia through grant APP627015, the University of Adelaide (DVCR Interdisciplinary Research Fund 2013-2014), the Australian Breast Cancer Research (ABCR) through Novel Concept Grant and The Hospital Research Foundations (THRF). This work was performed in part at the OptoFab node of the Australian National Fabrication Facility utilizing Commonwealth and SA State Government funding. Ye Wang acknowledges the scholarship of China Scholarship Council. Authors thank Mr. Jason Peak, Mr. Michael Jung and Mr. Jeffrey Hiorns from the mechanical workshop of the School of Chemical Engineering (UoA) for their help and support with the fabrication of the experimental set-ups used in this study.

Appendix A. Supplementary data

Supplementary data of zeta-potential, UV–Vis spectrometer, FTIR and TGA characterization associated with this article can be found in the online version at http://dx.doi.org/10.1016/j.biomaterials.2014.03.059.

References

[1] Pack DW, Hoffman AS, Pun S, Stayton PS. Design and development of polymers for gene delivery. Nat Rev Drug Discov 2005;4:581–93.
[2] Panyam J, Labhasetwar V. Biodegradable nanoparticles for drug and gene delivery to cells and tissue. Adv Drug Deliv Rev 2012;64(Suppl.):61–71.
[3] Farokhzad OC, Langer R. Impact of nanotechnology on drug delivery. ACS Nano 2009;3:16–20.
[4] Smyth MJ, Takeda K, Hayakawa Y, Peschon JJ, van den Brink MRM, Yagita H. Nature's TRAIL – on a path to cancer immunotherapy. Immunity 2003;18:1–6.
[5] Bouralexis S, Findlay DM, Atkins GJ, Labrinidis A, Hay S, Evdokiou A. Progressive resistance of BTK-143 osteosarcoma cells to Apo2L//TRAIL-induced apoptosis is mediated by acquisition of DcR2//TRAIL-R4 expression: resensitisation with chemotherapy. Br J Cancer 2003;89:206–14.
[6] Thai LM, Labrinidis A, Hay S, Liapis V, Bouralexis S, Welldon K, et al. Apo2l/Tumor necrosis factor–related apoptosis-inducing ligand prevents breast cancer–induced bone destruction in a mouse model. Cancer Res 2006;66:5363–70.
[7] Pan L-Q, Wang H-B, Lai J, Xu Y-C, Zhang C, Chen S-Q. Site-specific PEGylation of a mutated-cysteine residue and its effect on tumor necrosis factor (TNF)-related apoptosis-inducing ligand (TRAIL). Biomaterials 2013;34:9115–23.
[8] Kim I, Byeon HJ, Kim TH, Lee ES, Oh KT, Shin BS, et al. Doxorubicin-loaded porous PLGA microparticles with surface attached TRAIL for the inhalation treatment of metastatic lung cancer. Biomaterials 2013;34:6444–53.
[9] Kim Y-J, Chae SY, Jin C-H, Sivasubramanian M, Son S, Choi KY, et al. Ionic complex systems based on hyaluronic acid and PEGylated TNF-related apoptosis-inducing ligand for treatment of rheumatoid arthritis. Biomaterials 2010;31:9057–64.
[10] Bae S, Ma K, Kim TH, Lee ES, Oh KT, Park E-S, et al. Doxorubicin-loaded human serum albumin nanoparticles surface-modified with TNF-related apoptosis-inducing ligand and transferrin for targeting multiple tumor types. Biomaterials 2012;33:1536–46.
[11] Lim SM, Kim TH, Jiang HH, Park CW, Lee S, Chen X, et al. Improved biological half-life and anti-tumor activity of TNF-related apoptosis-inducing ligand (TRAIL) using PEG-exposed nanoparticles. Biomaterials 2011;32:3538–46.
[12] Liu Z, Fan AC, Rakhra K, Sherlock S, Goodwin A, Chen X, et al. Supramolecular stacking of doxorubicin on carbon nanotubes for in vivo cancer therapy. Angew Chem Int Ed 2009;48:7668–72.
[13] Kam NWS, Liu Z, Dai H. Carbon nanotubes as intracellular transporters for proteins and DNA: an investigation of the uptake mechanism and pathway. Angew Chem Int Ed 2006;45:577–81.
[14] Bianco A, Kostarelos K, Prato M. Making carbon nanotubes biocompatible and biodegradable. Chem Commun 2011;47:10182–8.

[15] Lee W, Schwirn K, Steinhart M, Pippel E, Scholz R, Gosele U. Structural engineering of nanoporous anodic aluminium oxide by pulse anodization of aluminium. Nat Nano 2008;3:234–9.

[16] Lee W, Scholz R, Gösele U. A continuous process for structurally well-defined Al_2O_3 nanotubes based on pulse anodization of aluminum. Nano Lett 2008;8:2155–60.

[17] Swan EEL, Popat KC, Grimes CA, Desai TA. Fabrication and evaluation of nanoporous alumina membranes for osteoblast culture. J Biomed Mater Res Part A 2005;72A:288–95.

[18] La Flamme KE, Popat KC, Leoni L, Markiewicz E, La Tempa TJ, Roman BB, et al. Biocompatibility of nanoporous alumina membranes for immunoisolation. Biomaterials 2007;28:2638–45.

[19] Losic D, Simovic S. Self-ordered nanopore and nanotube platforms for drug delivery applications. Expert Opin Drug Deliv 2009;6:1363–81.

[20] Jani AMM, Kempson IM, Losic D, Voelcker NH. Dressing in layers: layering surface functionalities in nanoporous aluminum oxide membranes. Angew Chem Int Ed 2010;122:8105–9.

[21] Raicevic N, Mladenovic A, Perovic M, Harhaji L, Miljkovic D, Trajkovic V. Iron protects astrocytes from 6-hydroxydopamine toxicity. Neuropharmacology 2005;48:720–31.

[22] O'Brien J, Wilson I, Orton T, Pognan F. Investigation of the alamar blue (resazurin) fluorescent dye for the assessment of mammalian cell cytotoxicity. Eur J Biochem 2000;267:5421–6.

[23] Serrano MC, Pagani R, Vallet-Regi M, Peña J, Rámila A, Izquierdo I, et al. In vitro biocompatibility assessment of poly(ε-caprolactone) films using L929 mouse fibroblasts. Biomaterials 2004;25:5603–11.

[24] Bimbo LM, Mäkilä E, Laaksonen T, Lehto V-P, Salonen J, Hirvonen J, et al. Drug permeation across intestinal epithelial cells using porous silicon nanoparticles. Biomaterials 2011;32:2625–33.

[25] Byeon HJ, Choi SH, Choi JS, Kim I, Shin BS, Lee ES, et al. Four-arm PEG cross-linked hyaluronic acid hydrogels containing PEGylated apoptotic TRAIL protein for treating pancreatic cancer. Acta Biomater 2014;10:142–50.

[26] Xia T, Kovochich M, Liong M, Meng H, Kabehie S, George S, et al. Polyethyleneimine coating enhances the cellular uptake of mesoporous silica nanoparticles and allows safe delivery of siRNA and DNA constructs. ACS Nano 2009;3:3273–86.

[27] Nel AE, Madler L, Velegol D, Xia T, Hoek EMV, Somasundaran P, et al. Understanding biophysicochemical interactions at the nano-bio interface. Nat Mater 2009;8:543–57.

[28] Bihari P, Vippola M, Schultes S, Praetner M, Khandoga AG, Reichel CA, et al. Optimized dispersion of nanoparticles for biological in vitro and in vivo studies. Part Fibre Toxicol 2008;5:14.

[29] Patil S, Sandberg A, Heckert E, Self W, Seal S. Protein adsorption and cellular uptake of cerium oxide nanoparticles as a function of zeta potential. Biomaterials 2007;28:4600–7.

[30] Santos A, Kumeria T, Losic D. Optically optimized photoluminescent and interferometric biosensors based on nanoporous anodic alumina: a comparison. Anal Chem 2013;85:7904–11.

[31] Poland CA, Duffin R, Kinloch I, Maynard A, Wallace WAH, Seaton A, et al. Carbon nanotubes introduced into the abdominal cavity of mice show asbestos-like pathogenicity in a pilot study. Nat Nano 2008;3:423–8.

[32] Hart GA, Kathman LM, Hesterberg TW. In vitro cytotoxicity of asbestos and man-made vitreous fibers: roles of fiber length, diameter and composition. Carcinogenesis 1994;15:971–7.

[33] Kostarelos K. The long and short of carbon nanotube toxicity. Nat Biotechnol 2008;26:774–6.

[34] Stern S, Adiseshaiah P, Crist R. Autophagy and lysosomal dysfunction as emerging mechanisms of nanomaterial toxicity. Part Fibre Toxicol 2012;9:20.

[35] Levine B, Mizushima N, Virgin HW. Autophagy in immunity and inflammation. Nature 2011;469:323–35.

[36] Seleverstov O, Zabirnyk O, Zscharnack M, Bulavina L, Nowicki M, Heinrich J-M, et al. Quantum dots for human mesenchymal stem cells labeling. a size-dependent autophagy activation. Nano Lett 2006;6:2826–32.

[37] Ma X, Wu Y, Jin S, Tian Y, Zhang X, Zhao Y, et al. Gold nanoparticles induce autophagosome accumulation through size-dependent nanoparticle uptake and lysosome impairment. ACS Nano 2011;5:8629–39.

[38] Chen G-Y, Yang H-J, Lu C-H, Chao Y-C, Hwang S-M, Chen C-L, et al. Simultaneous induction of autophagy and toll-like receptor signaling pathways by graphene oxide. Biomaterials 2012;33:6559–69.

[39] Hawe A, Hulse W, Jiskoot W, Forbes R. Taylor dispersion analysis compared to dynamic light scattering for the size analysis of therapeutic peptides and proteins and their aggregates. Pharm Res 2011;28:2302–10.

[40] Sinn Aw M, Kurian M, Losic D. Non-eroding drug-releasing implants with ordered nanoporous and nanotubular structures: concepts for controlling drug release. Biomater Sci 2014;2:10–34.

Supporting Information

Structurally engineered anodic alumina nanotubes as new nano-carriers for drug delivery of anticancer therapeutics

Ye Wang[1], Abel Santos[1], Gagandeep Kaur[1], Andreas Evdokiou[2]*, Dusan Losic[1]*

1. School of Chemical Engineering, The University of Adelaide, Adelaide, SA, 5005
2. School of Medicine, Discipline of Surgery, The University of Adelaide, Adelaide, SA, 5005

*Corresponding author: dusan.losic@adelaide.edu.au

Figure S1 Zeta-potential characterization of AANTs and alumina nanoparticles

AANTs have different inside and outside surface chemistry. [1] It is known that the inner wall of nanoporous anodic alumina fabricated in sulphuric acid contain sulphate groups created by HA process; while the outer wall of AANTs contains hydroxyl group which exists intrinsically on alumina surface.[2] The difference surface chemistry of inner/outer wall unavoidably influences the zeta-potential measurement, which might contribute to the increment of zeta-potential at pH above 7. We hypothesize that sulphate groups become positively charged above pH 7, which leads to the increment of zeta-potential. However, since the outer surface is still highly negatively charged, AANTs can disperse homogeneously at pH 7 and 8. To illustrate the outer surface chemistry of AANTs, alumina nanoparticles (NPs) with 1 μm diameter are used due to its similar property to AANTs.

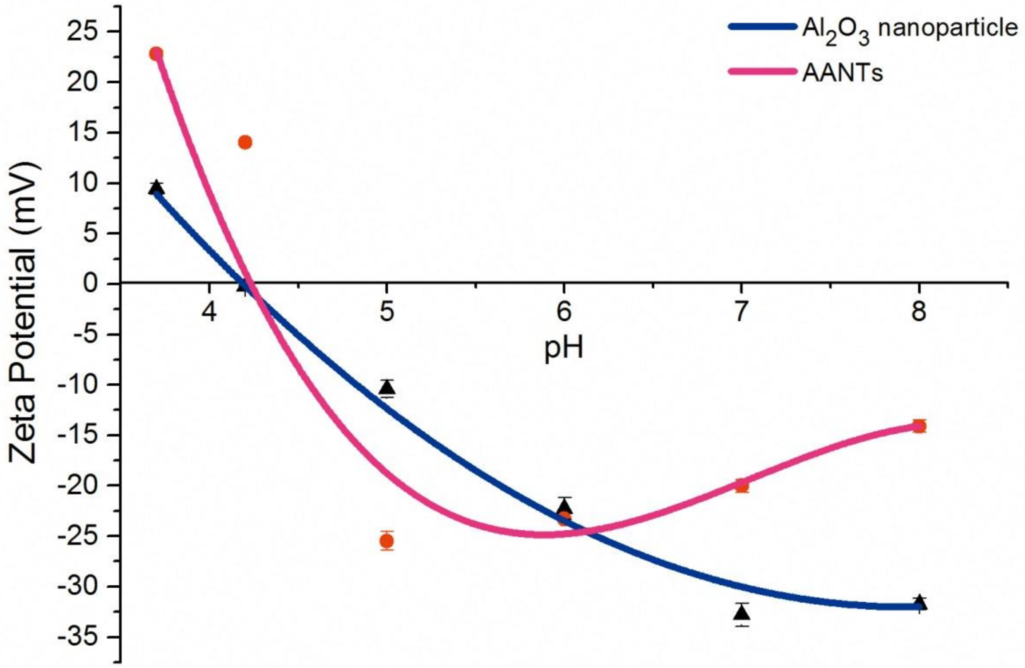

Figure S2

(a) UV-Vis spectrometer analysis of AANTs and AANTs-FITC composite.

To prove FITC was covalently bond on AANTs, we incubated FITC with AANTs at same condition without APTES functionalization. After several times washing steps, no UV adsorption was found. However, after FITC labeling by the used protocol, the AANTs-APTES-FITC solution changed to orange color and have adsorption peak at 500 nm, proving the successful functionalization of FITC.

(b) FTIR characterization of NAA template and AANTs-FITC.

Before APTES modification, as-prepared NAA template was analyzed by FTIR. Consisted with previous report, a characteristic peak of sulfate group was found at ~1096cm^{-1}.[3] Modification of APTES on AANTs surface was confirmed by –NH bending at ~1400cm^{-1}[4], CH_2 stretching at ~2883/2971 and Si-OH peak at ~804cm^{-1}[5].

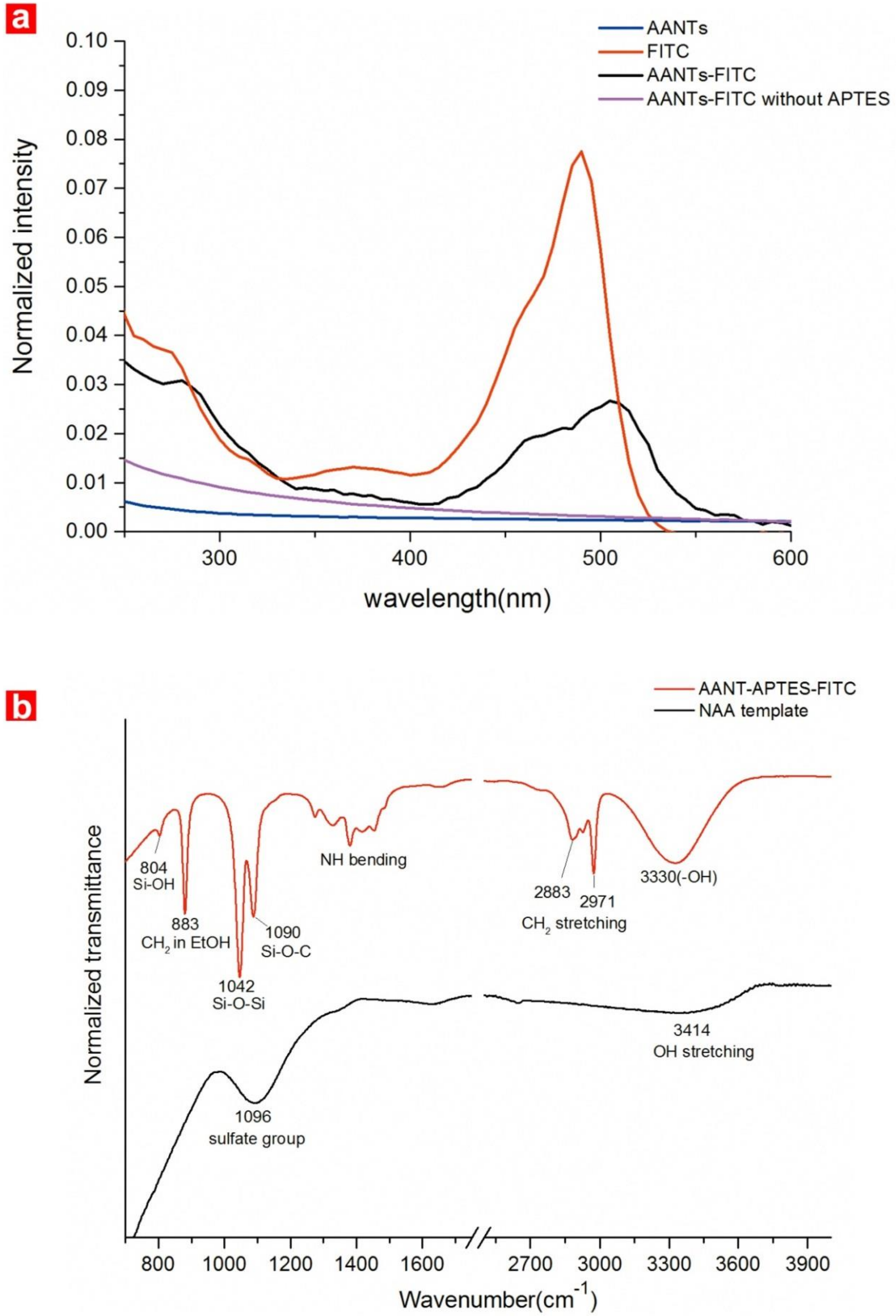
a
AANTs
FITC
AANTs-FITC
AANTs-FITC without APTES
Normalized intensity
0.10
0.09
0.08
0.07
0.06
0.05
0.04
0.03
0.02
0.01
0.00
300
400
500
600
wavelength(nm)
b
AANT-APTES-FITC
NAA template
Normalized transmittance
804
Si-OH
883
CH$_2$ in EtOH
1042
Si-O-Si
1090
Si-O-C
NH bending
2883
2971
CH$_2$ stretching
3330(-OH)
3414
OH stretching
1096
sulfate group
800
1000
1200
1400
1600
2700
3000
3300
3600
3900
Wavenumber(cm^{-1})

Figure S3 Thermogravimetric analysis of Apo2L/TRAIL drug loading on AANTs

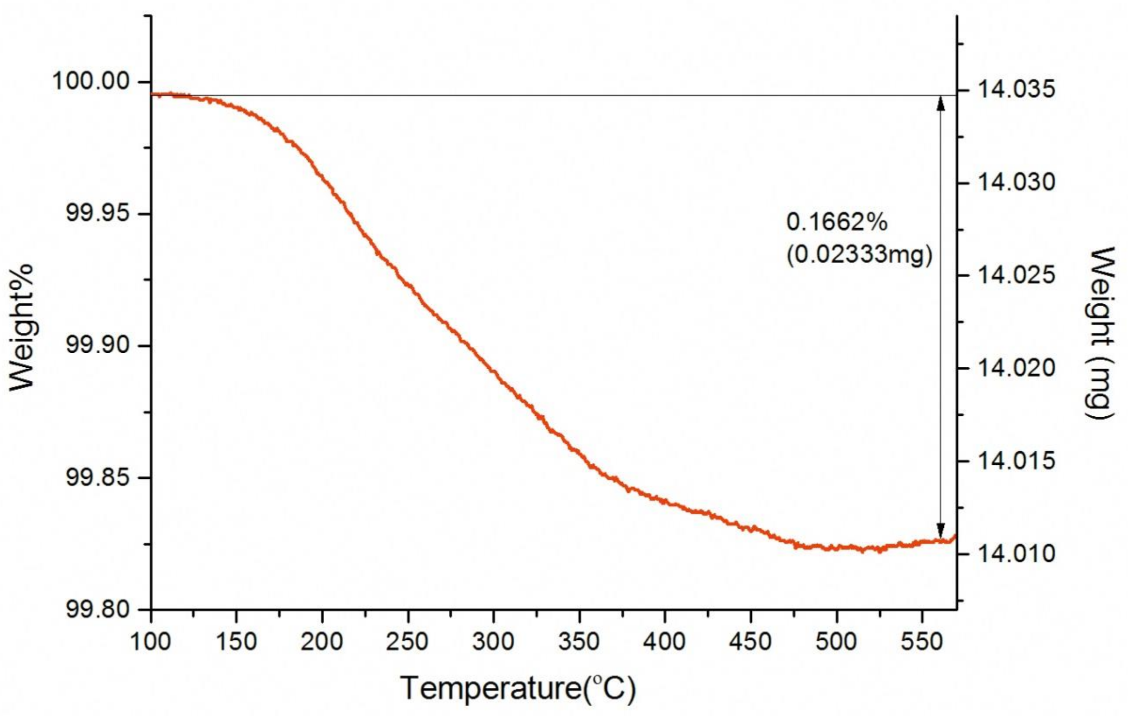

References

[1] Lee W, Schwirn K, Steinhart M, Pippel E, Scholz R, Gosele U. Structural engineering of nanoporous anodic aluminium oxide by pulse anodization of aluminium. Nat Nano. 2008;3:234-9.

[2] Tsyganenko AA, Mardilovich PP. Structure of alumina surfaces. Journal of the Chemical Society, Faraday Transactions. 1996;92:4843-52.

[3] Mata Zamora M, Saniger J. Thermal evolution of porous anodic aluminas: a comparative study. Revista Mexicana de Física. 2009;51.

[4] Lord MS, Jung M, Teoh WY, Gunawan C, Vassie JA, Amal R, et al. Cellular uptake and reactive oxygen species modulation of cerium oxide nanoparticles in human monocyte cell line U937. Biomaterials. 2012;33:7915-24.

[5] Matos MC, Ilharco LM, Almeida RM. The evolution of TEOS to silica gel and glass by vibrational spectroscopy. Journal of Non-Crystalline Solids. 1992;147–148:232-7.

Chapter 6 Targeting of Autophagic and Endoplasmic Reticulum Stress Signaling by AANTs-based Combinatorial Delivery System

6.1 Introduction, Significance and Commentary

Using nanomaterials to target cancer cell signaling is an intriguing but rarely reported concept. In chapter 4, we showed that anodic alumina nanotubes (AANTs) activated autophagy and endoplasmic reticulum (ER) stress in breast cancer cells (MDA-MB231-TXSA). ER stress signalling is a cell-rescuing process triggered by the dysfunction of ER. Autophagy is a degradation pathway that regulates the degradation of cytoplasmic material such as internalized nanoparticles and damaged organelles (e.g. ER and mitochondria). Autophagy can reduce ER stress, while inhibition of autophagy may cause ER stress signaling cascade, which can eventually lead to cell death. We hypothesised that targeting of these pathways may be an effective way to eliminate cancer.

The aim of this chapter is to target autophagic and ER stress signaling pathways by using drug loaded AANTs co-treated with an autophagy inhibitor 3-methyladenine (3-MA). We have shown that AANTs induce autophagy as a cyto-protective response in different cell types, including human fibroblast cells (HFF), human monocyte cells (THP-1) and human breast cancer cells (MDA-MB 231-TXSA). Treatment with 3-MA at a non-toxic dose inhibit autophagy, and consequently sensitized breast cancer cells to ER stress signaling without affecting apoptotic signaling. To target autophagic and ER stress signaling networking, breast cancer cells were treated with 3-MA together with AANTs loaded with the prototype ER stress inducer thapsigargin (TG). We demonstrated that 3-MA effectively enhanced the anti-cancer efficiency of AANTs loaded with TG. This effect was associated with enhanced ER stress signaling due to the combination effect of AANTs, TG and 3-MA.

These findings provide new opportunities for the development of novel ER and autophagy targeted delivery systems for the treatment of breast cancer.

6.2 Publication

This section is a research paper prepared by Ye Wang, Gagandeep Kaur, Yuting Chen, Abel Santos, Dusan Losic, Andreas Evdokiou (submitted to Journal of Material Chemistry B at 11th Auguest 2015)

Statement of Authorship

Title of Paper	Targeting of endoplasmic reticulum stress and autophagic signaling networking by a nanotube-based combinatorial delivery system: A new strategy of cancer therapy
Publication Status	☐ Published ☐ Accepted for Publication ☑ Submitted for Publication ☐ Publication Style
Publication Details	Submitted to Journal of Material Chemistry B at 11th August 2015

Principal Author

Name of Principal Author (Candidate)	Ye Wang		
Contribution to the Paper	Designed project and accomplished 80% of experiments, performed data analysis and prepared manuscript		
Overall percentage (%)	80%		
Signature		Date	11/08/2015

Co-Author Contributions

By signing the Statement of Authorship, each author certifies that:

i. the candidate's stated contribution to the publication is accurate (as detailed above);

ii. permission is granted for the candidate in include the publication in the thesis; and

iii. the sum of all co-author contributions is equal to 100% less the candidate's stated contribution.

Name of Co-Author	Yuting Chen		
Contribution to the Paper	Assisted in part of experiment		
Signature		Date	1. 8. 2015.

Name of Co-Author	Gagandeep Kaur		
Contribution to the Paper	Assisted in part of experiment		
Signature		Date	3/08/2015

Name of Co-Author	Abel Santos
Contribution to the Paper	Supervised development of work, helped in data interpretation and manuscript evaluation
Signature	Date 07-08-2015

Name of Co-Author	Andreas Evdokiou
Contribution to the Paper	Supervised development of work, helped in data interpretation and manuscript evaluation
Signature	Date **11/8/2015**

Name of Co-Author	Dusan Losic
Contribution to the Paper	Supervised development of work, helped in data interpretation and manuscript evaluation
Signature	Date 11/08/2015

Targeting of endoplasmic reticulum stress and autophagic signaling networking by a nanotube-based combinatorial delivery system: A new strategy of cancer therapy

Ye Wang[a, b], *Gagandeep Kaur*[a, b]‡, *Yuting Chen* [a]‡, *Abel Santos*[a*], *Dusan Losic*[a*], *Andreas Evdokiou*[a, b*]

[a] School of Chemical Engineering, The University of Adelaide, Adelaide, SA, 5005

[b] Discipline of Surgery, The University of Adelaide, Basil Hetzel Institute, Adelaide, SA, 5005

‡These authors contributed equally.

* ***Corresponding Authors***

Doctor Abel Santos
Postdoctoral Fellow - Lecturer
School of Chemical Engineering – The University of Adelaide
Phone: +61 8 8313 1535 – Fax: +61 8 8303 4373
Email: abel.santos@adelaide.edu.au
Web page: http://www.adelaide.edu.au/directory/abel.santos

Prof. Andreas Evdokiou
School of Medicine – The University of Adelaide
Basil Hetzel Institute
Telephone: +618 8222 7451 Facsimile: +618 8222 7872 DAX 465702
Email: andreas.evdokiou@adelaide.edu.au

Prof. Dusan Losic
School of Chemical Engineering – The University of Adelaide
Telephone: + 61 8 8313 4648 Fax: +61 8 8303 4373
E-Mail: dusan.losic@adelaide.edu.au
Personal web page: http://www.adelaide.edu.au/directory/dusan.losic

Abstract

Although nanoparticle-based targeted delivery systems have gained promising preclinical achievements for cancer therapy, the development of sophisticated strategies with effective combinatorial therapies remains an enduring challenge. Herein, we report an autophagic and endoplasmic reticulum (ER) stress signaling targeting combination delivery system by using thapsigargin (TG) loaded anodic alumina nanotubes (AANTs) co-treated with an autophagy inhibitor 3-methyladenine (3-MA) for potential chemotherapy. We showed that AANTs induce autophagy as a cyto-protective response in different cells including human fibroblast cells (HFF), human monocyte cells (THP-1) and human breast cancer cells (MDA-MB 231-TXSA). Treatment with 3-MA at a non-toxic dose reduced the level of autophagy, and consequently sensitized breast cancer cells to AANTs-induced cellular stresses. To target autophagic and ER stress signaling networking, breast cancer cells were treated with 3-MA together with AANTs loaded with the prototype ER stress inducer thapsigargin (TG). We demonstrated that low dose 3-MA (1 mM) enhanced the cancer cell killing effect of AANTs loaded with TG. This effect was associated with enhanced ER stress signaling due to the combination effect of TG and 3-MA. These findings provide new opportunities for developing novel ER and autophagy targeted delivery systems for future clinical cancer therapy.

Keywords anodic alumina nanotubes, endoplasmic reticulum stress, autophagy, cell signaling, nanotoxicity, drug delivery

1. Introduction

Our increasingly understanding of the interaction between biological entities (i.e. biomolecules, cells, tissues etc.) and nanomaterials has triggered the development of various drug delivery systems targeting specific organelles in recent years.[1-3] For example, nuclei and mitochondria targeting can be readily achieved by conjugating corresponding bio-molecular ligands, such as nuclear localization signals on nanomaterial' surfaces.[4] Cationic nanoparticles are also widely used as nanocarriers for nuclei targeting which can accumulate in the peri-nuclear region through the so-called endosomal escape pathway.[5,6] In addition, biodegradable polymers such as polylactic-co-glycolic acid can localize into lysosome, endoplasmic reticulum (ER) and Golgi as part of their intracellular degradation pathway.[7,8] Although targeting a sub-cellular organelle which drives cancer development can result in selective cancer cell killing, such a strategy may not always succeed due to the development of multi-drug resistance.[9,10] Drug resistance is mainly caused by the complex interplay of cell survival signaling pathways, which facilitate cell survival by various mechanisms including enhanced drug transport[11], over-expression of anti-apoptotic proteins[12], increased DNA damage repair[13] and autophagy[14]. An effective and specific strategy for cancer cell killing is to target subcellular compartments associated with signaling networks. Such strategies not only require a good understanding of the cell survival mechanisms induced by chemotherapy, but also demand an optimal design of drug cocktails and nano-carriers based on the biological performance of drug delivery systems.

Macro-autophagy, herein referred to as autophagy, is of growing interest in the area of nanotoxicity and cancer therapy due to its paradoxical role for both cell survival and cell death. Autophagy is a homeostatic, catabolic degradation process which regulates the degradation of cytoplasmic material to support cell preservation in response to various stress signals including those culminating from nanomaterial internalization and chemotherapy. [15,16] Nanotoxicity studies have demonstrated that a number of nanomaterials can trigger autophagy in various cell types. However, the role of autophagy can be either cyto-protective or cyto-destructive which is depended on several features of the nanomaterial including size, surface chemistry and other experimental factors such as working dose and treatment time.[19-24] At the same time, accumulating evidence clearly showed that autophagy is exemplified as a survival pathway in cancer cells when treated with anticancer drugs.[14] Therefore, utilizing autophagic signaling pathways in combination with other therapies may be a rational strategy for developing novel drug delivery systems.

The application of autophagy inhibitors such as chloroquine (CQ) in combination with other therapies is currently in clinical trials and has recently been translated into nanoparticle-based drug delivery systems.[25,26] However, increasing evidence suggests that the combination effects of CQ and 3-methyladenine (3-MA) with other anti-cancer drugs are independent of autophagy, although enhanced cancer cell killing has been achieved. This combination effect may be partially attributed to the toxicity of CQ and 3-MA when used at high working dose as well as their off-target effects acting on other survival signaling pathways.[27-29] Therefore, novel autophagic-based combination drug delivery systems are urgently required together with a systematic approach to study the combination effect at the bio-molecular level.

In this study, we report for the first time a potential combination delivery system based on the targeting of autophagic and ER stress signaling using anodic alumina nanotubes (AANTs) as a nanomaterial model. ER is an essential intracellular organelle responsible for multiple cell functions, such as intracellular calcium homeostasis, lipid biosynthesis and protein secretion.[30] Perturbation of ER functions leads to protein misfolding, which triggers a cyto-protective response so-called ER stress to re-establish the homeostasis of ER function. Importantly, ER stress is a well-established nanotoxicity paradigm associated with several types of nanomaterials including gold/silver nanoparticles[33,34] and polystyrene nanosphere[35]. Excessive ER stress leads to cell death, while autophagic pathway is interconnected with ER to ameliorate ER stress.[30,31] Therefore, we reasoned that delivering an ER stress inducer by nanocarriers while simultaneously blocking autophagic pathway may be a novel and effective strategy for enhanced cancer therapy, which has not been explored before.[32] Here we systematically investigated the impact of autophagy and AANTs on the cell function, and then utilized AANTs as drug carriers to load a prototype ER stress inducer, thapsigargin (TG) and co-treated with 3-MA for enhanced killing of breast cancer cells *in vitro*. This research highlighted the importance of manipulating signaling networks for developing advanced nanoparticle-based targeted delivery systems.

2. Materials and Methods

2.1 Materials

Aluminum (Al) foils of thickness 0.32 mm and purity 99.9997 % were supplied by Goodfellow Cambridge Ltd. (UK). Sulphuric acid (H_2SO_4), copper(II) chloride ($CuCl_2$), hydrochloric acid (HCl), perchloric acid ($HClO_4$), hydrogen peroxide (H_2O_2), chromium trioxide (CrO_3), paraformaldehyde, Fluorescein isothiocyanate–dextran (average mol wt 70,000), 2′,7′-Dichlorofluorescein diacetate, 4',6-diamidino-2-phenylindole ($C_{16}H_{15}N_5$ – DAPI), monodansylcadaverine, 2-mercaptoethanol, polystyrene sulfonic acid and poly(allylamine hydrochloride) were purchased from Sigma-Aldrich (Australia). PE annexin V apoptosis detection kit and JC 1 detection kit were purchased from BD science. Primary antibodies including LC-3, p62, p53, BiP, IRE1α, PERK, CHOP, mTOR substrates, caspase 3, 8, and 9, Bcl-2, BiD and actin were purchased from Cell Signaling Technology. Dulbecco's modified Eagle's medium (DMEM), RPMI 1640 media, fetal calf serum (FCS), penicillin/streptomycin, and glutamine were purchased from Biosciences (Australia). Trypsin (Gibco); phosphate buffer solution (PBS) (HyClone Laboratories, Inc);

Culture flasks, 96-well plate, 24-well plate and 6-well plate (greiner Bio-One); 8-well glass chamber slide (Thermo Fisher); AlamarBlue® and ER-Tracker Blue-White DPX (Life Technologies Corporation); Ultrapure water Option Q–Purelabs (Australia) was used for preparation of all the relevant solutions used in this study.

2.2 Preparation of anodic alumina nanotubes (AANTs)

AANTs were synthesized by a modified pulse anodization process using galvanostatic mode.[36,38,62] Briefly, Aluminum foils 1.5 cm in diameter were first sonicated in EtOH and ultrapure water for 5 min each. Aluminum foils were electropolished prior to anodization in a mixture of EtOH and $HClO_4$ 4:1 (*v:v*) at 20 V and 5° C for 3 min. After this, the first step anodization was carried out in a 0.3 M aqueous solution of H_2SO_4 at 25 V and 6 °C for 20 h to prepare the first NAA layer on the surface. The second step pulse anodization was conducted under galvanostatic conditions at 1°C. The area exposed to the electrolyte solution was 0.95 cm^2. This anodization step consisted of a cyclic combination of mild (MA) and hard anodization (HA) pulses under galvanostatic mode. The MA-pulse was keep at 5 s with a current of 3 mA; the HA-pulse current intensity was 350 mA and the HA duration was 2 s. Then, the remaining aluminum substrate was removed by wet chemical etching in a mixture of 0.2 M $CuCl_2$ and 6.1 M HCl. Free-standing AANTs were obtained from prepared NAA structure by immersion into the 0.2 M $CuCl_2$ and 6.1 M HCl solution for 15 mins, followed by gentle ultrasonic in ultrapure water for 1 h.

2.3 Structural and surface charge characterization of AANTs

The shape and structure of AANTs were characterized by a transmission electron microscope (FEI Tecnai G2 Spirit TEM) and a field emission gun scanning electron microscope (FEG-SEM FEI Quanta 450). The length distribution was characterized by analysing 700 to 1000 nanotubes by TEM image analysis. Zeta-potential and particle size distributions of AANTs were analyzed by a ZetaSizer Nano (Malvern Instruments Ltd., Worcestershire, UK). To measure zeta-potential and hydrodynamic diameter, AANTs at a concentration 50 μg/ml were dispersed in 500 μl of the Mill-Q water (pH 5.8) or DMEM media with 10% FCS and sonicated for 30 s before analysis. To characterize the charge difference of inner / outer surface of AANTs, the Al substrate of pulse anodized alumina nanostructures were first removed followed by chemical etching (**Figure S1 a - Supporting Information**), then incubated with 1ml PSS solution (3 mg/ml in 0.5M NaCl solution) or PAH (1 mg/ml) under vacuum at room temperature for 3 h to selectively functionalize inner surface of AANTs. After this, the modified NAA substrates were thoroughly washed several times with ultrapure water and treated with sonication to get liberated AANTs. Since the polyelectrolyte modified the inner layer surface charge without affecting outer surface, the outer surface charge can be measured. A XS analytical balance with readability 0.01 mg (Mettler-Toledo International, Inc.) was used for sample weighting in all the experiments.

2.4 Cell culture and toxicity assay

2.4.1 Cell culture

MDA-MB-231-TXSA, HFF and THP-1 cell lines were used for toxicity study. MDA-MB-231-TXSA and HFF cells were cultured in Dulbecco's modified Eagle's medium (DMEM), supplemented with glutamine (2 mM), penicillin (100 IU/ml), streptomycin (100 μg/ml) and 10 % FCS at 37 °C in a 5 % CO_2-containing humidified atmosphere. THP-1 cells were suspended in RPMI 1640 medium supplemented with 10 % FCS and 0.05 mM 2-mercaptoethanol. Unless otherwise indicated, all the cell experiments in this study were repeated three times.

2.4.2 Cell toxicity assay

Cell toxicity was determined by Alamar blue assay. Briefly, for HFF cells, cells were harvested using trypin-EDTA-PBS and $1*10^4$ cells per well were plated in 96-well plate setup with 200 μl of growth media. Cells were allowed to attach overnight before AANTs treatment. For THP-1 cells, cells were harvested by centrifuge and plated in 96-well plate $2*10^4$ per well in total volume of 200 μl. Cells were treated with AANTs at the doses of 20 μg/ml, 100 μg/ml, 250 μg/ml, 500 μg/ml for 24 hs and 3 days. After determined time point in study, 20 μl alamar blue stock solution was added to each well and incubated at 37 °C for 1 to 2h, after which fluorescence was measured at 560/590nm using a plate reader (Fluostar OPTIMA, BMG Labtech).

2.4.3 Annexin-V and JC-1 assay by flow cytometry

Annexin-V and JC-1 assay was conducted according to the manufacturer's instructions. Briefly, $2*10^4$ cells were seeded in 24-well plates overnight for attachment. After 3 days of treatment, cells were trypsinized and washed one time by PBS. Then cells were stained by Annexin-V/7-AAD or JC-1 dye followed by washing step. 0.1% hydrogen peroxide and 200nM valinomycin was used as positive control for Annexin-V/7AAD and JC-1 assay respectively. Events were acquired by a FACScalibur (BD Bioscience), and data were analyzed using FlowJo (TreeStar) software on at least 10,000–30,000 events.

2.5 Cell imaging

2.5.1 TEM microtome sample preparation

To prepare microtome samples of cells, cells were incubated with AANTs at the concentration 100 μg/ml for overnight treatment (16hs). After that, cells were carefully washed with sterile PBS twice, and transferred into 1.5 mL eppendorf tubes. Collected cell pellets were re-suspended in a solution of 4 *vol* % paraformaldehyde and 1.25 *vol* % glutaraldehyde and were fixed overnight. Then, all samples were post-fixed in a 2 *vol* %

osmium tetroxide solution for 45 min. After this, cells were fully dehydrated and embedded in epoxy resin. Ultrathin sections of 70 nm were cut and post-stained with uranyl acetate and lead citrate.[18] Cell samples were analyzed by TEM at 100 kV.

2.5.2 Fluorescence microscopy

To visualize autophagosome, $2*10^4$ cells were cultured on 8-well chamber slide with AANTs treatment, followed by incubation with freshly prepared 0.05 mM MDC in PBS at 37°C for 10 mins. Then the cell was washed one time with PBS and fixed by 4% paraformaldehyde. The chamber was then visualized under a confocal microscope (Leica SP5 spectral scanning confocal microscope) using 405-nm lasers with band-pass filters of 420–480 nm. 20 nM rapamycin and 1mM 3-MA were used as positive and negative control respectively. For ER staining, cells were treated with AANTs or TG for 24hs and then washed one time with PBS and fixed by paraformaldehyde. To label ER, the fixed cells were incubated with ER-Tracker (1 μM for 30 min at 37°C) and then imaged using DAPI channel. For imaging the localization of AANTs inside cells, Alizarin Red S labeled AANTs was incubated with AANTs overnight. Next day, cells were first stained with MitoTracker® Deep Red (500nM) for 10mins at 37 ^{o}C, then washed twice with PBS and stained with MDC for 10 mins 37 ^{o}C. Finally, the cells was fixed and visualized by confocal micscopy (Carl Zeiss LSM 700) using 405-nm, 555-nm, and 639-nm lasers with band-pass filters of 420–480 nm, 575–600 nm, and 650–700 nm, respectively. To quantifying mitochondria volume by 3D surface reconstruction, confocal slice thickness was kept at 0.3 μm consistently with twenty slices typically being taken to encompass the three-dimensional entirety of the cells in the field of view. Z-stack images were deconvoluted with ImageJ (NIH) and Z-Stack analysis of the thresholded images volume-reconstituted using the VolumeJ plug-in, and volumes of mitochondria were quantified using the ImageJ-3D Object Counter plug-in. Calculation for the adjusted total mitochondrial volume per cell was as follows: (percentage of total volume of mitochondria)/(percentage of total area of cell). This process was completed for at least 60 cells over three separate fields of view for each sample and is representative of three independent experiments.[63]

2.6 Western Blotting

1*10^6 cells were seed in T25 flask and treated with 100 μg/ml AANTs, RP, 3-MA or TG in a 24 hs time course. After that, Cells were lysed in buffer containing 10 mmol/L Tris-HCl (pH 7.6), 150 mmol/L NaCl, 1% Triton X-100, 0.1 % SDS, 2 mmol/L sodium vanadate, and a protease inhibitor cocktail (Boehringer Mannheim) and stored -70 °C until ready to use. The amount of protein in each sample was quantified using the BCA protein assay reagent (Pierce) according to the manufacturer's instructions. Fifty micrograms of cell lysates was separated using 12.5 % SDS-PAGE. Gels were then electro-blotted onto polyvinylidene difluoride membranes (Novex, San Diego, CA) and blocked using 5 % skim milk in TBST buffer (10 mM Tris-HCl, pH 7.5/150 mM NaCl/0.05% Tween-20) at room temperature for 1-3 hour. Immunodetection was done overnight at 4 °C in TBST/blocking reagent, using the following primary antibodies at the dilutions suggested by the manufacturer. Primary antibodies were purchased from Cell Signaling Technology. Anti-actin pAb (Santa Cruz, CA) was used to normalize for protein concentration. Membranes were then rinsed several times with PBS containing 0.1 % Tween 20 and incubated with 1:5,000 dilution of anti-mouse or anti-rabbit alkaline phosphatase conjugated secondary antibodies (Amersham) for 1 hour. Visualization and quantification of protein bands was done using the Vistra ECF substrate reagent kit (Amersham) on a FluorImager (Molecular Dynamics, Inc., Sunnyvale, CA). The intensity of the band was quantified utilizing the software, NIH ImageJ (National Institutes of Health, Bethesda, MD, USA) and normalized by the band intensity of actin.

2.7 Thapsigargin loading and in vitro drug delivery

For TG loading experiments, 1 mg of as-prepared AANTs were dispersed in 300 μL of TG solution (50 μg/ml) by 10 min of sonication. The solutions were kept at room temperature for 3h, followed by 3 times wash to remove TG residue. Drug loading capacity of AANTs was determined for thermogravimetric (TGA) analysis (Auto TGA Q500, TA Instruments). Disposable aluminum pan loaded with samples (AANTs or drug loaded AANTs) was used for TGA chatacterization. The drug loading amount is calculated by the average weight lost difference between AANTs and drug loaded AANTs from three independent experiments. The experiment temperature was increased from room temperature to 590 °C at a rate of 10 °C min^{-1} under pure nitrogen gas flow at 23 ml/min. For *in vitro* TG delivery assays, $1*10^4$ cells/well were seeded in a 96-well plate and incubated overnight to allow cell attachment. Then, TG-loaded AANTs with different concentrations range from 20 to 100 μg/ml were added to each well co-treated with 1 mM 3-MA. Cell viability was checked after 24hs by using alamar blue assay. To confirm the synergism of 3-MA and TG, parallel experiments was conducted by treating cells with 3-MA, TG and TG + 3-MA.

2.8 Statistical analysis

Data were analyzed using Origin pro and Microsoft Excel software and presented as mean values ± standard deviation (SD) from three independent measurements. Statistical comparisons between different treatments were assessed by two-tailed t-tests. The criterion for significance was $p < 0.05$ for *, $p < 0.01$ for **, and $p < 0.001$ for ***. The effect of drug combinations on cytotoxicity was assessed by the median-effect method as previously described.[51] Combination index (CI) values were calculated from median results of cytotoxicity assays, which were done in triplicate. CI values significantly >1 indicate drug antagonism. CI = 1 indicated summation, CI < 1 indicated synergism.

3. Results

3.1 Preparation and characterization of AANTs

AANTs were fabricated by a modified pulse anodization approach as we previously described.[37,38] (**Figure 1 a**) This electrochemical technique utilizes periodically manipulated galvanostatic current density switching between mild anodization (MA) and hard anodization (HA) to create an engineered stack-layered anodic aluminum oxide (AAO) nanostructure, in which the layer thickness is precisely controlled by current intensity at a given time. Individual AANTs were obtained by removing the aluminum substrate followed by sonication treatment to break down the AAO nanostructure into liberated nanotubes. The resulting AANTs used in this experiment have a unique hollow and open ends structure with an inner diameter of 33 nm ± 8 nm and length of 736 nm ± 460 nm. (**Figure 1 b to e**) The physicochemical characterization of the AANTs is summarized in **Table 1 – Supporting information**. AANTs are composed of Al_2O_3 with high density of oxygen groups on surface which can be protonated in deionized water (pH 5.6) to form positively charges at 27.0 ± 0.6 mV. However, it is worth stressing that AANTs have an intrinsic heterogeneous surface chemistry between the inner and outer surface due to the incorporation of electrolyte anions (i.e. sulfonate group) into the inner surface wall during the anodization process.[39,40] Consequently, a total charge of AANTs is influenced by both outer and inner charges, which have different levels of positive charges as illustrated in **Figure S1 – Supporting Information**. In our condition, AANTs exhibited a negative surface charge (-11 ± 0.9 mV) with hydrodynamic diameters of 482.4 ± 20.6 nm when used in cell culture media with 10% FCS. This difference is caused by the complex ionic composition of cell culture media and the formation of bimolecular coronas (i.e. serum proteins) on both inner / outer surfaces.[41]

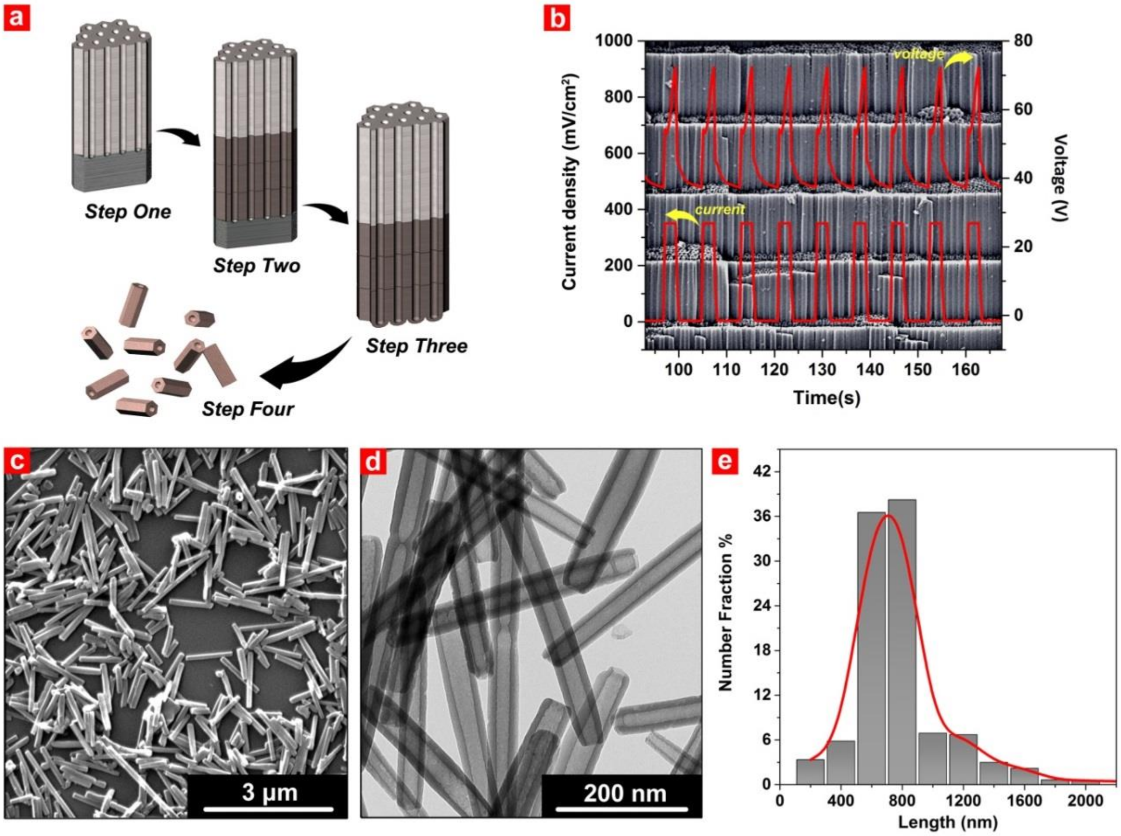

Figure 1 Preparation and characterization of AANTs. (a) Schematic illustration of AANTs fabrication by pulse anodization. Briefly, electro-polished aluminum was first anodized at MA condition to grow a certain thickness of nanoporous anodic alumina as the starting layer (step one). Pulse anodization was then applied (step two) followed by removal of aluminum substrate (step three). The liberation of AANTs was finally achieved by acid etching and mild sonication (step four). (b) Representative anodization profile of current density and voltage against time using conditions of j_{HA}=368.52 mA/cm^2 / t_{HA}= 2s, and j_{MA}= 3.26 mA/cm^2/ t_{MA}= 5s (c and d) SEM and TEM images of AANTs (e) Length distribution of AANTs characterized by TEM analysis.

3.2 AANTs induced autophagy is an intrinsic cellular response

We previously reported the effect of autophagy induction by AANTs in breast cancer cells MDA-MB 231-TXSA and mouse macrophage cells RAW 264.7.[37] For better understanding the AANTs-associated nanotoxicity pattern in various cell lines, we now show that primary human foreskin fibroblasts (HFF) and human monocytic cells (THP-1) readily internalize AANTs into autophagosome structures which contain other damaged cellular components. (**Figure 2)** Cell viability characterization by an alarmar blue assay showed that treatment with AANTs at a maximum concentration of 500 µg/ml reduced viability down to 80% in THP-1 cell line. In addition, AANTs failed to influence the cell viability of HFF cells at the highest concentration after 72hs' treatment. These results showed that AANTs as a non-degradable nanomaterial model are non-toxic to cells at a working dose of 100 µg/ml. Since autophagy has been activated after cell uptake of AANTs, we reasoned that autophagy induction may play a cyto-protective role in the contexts of AANTs induced toxicity. However, excessive autophagy may favor an apoptotic process since autophagic and apoptotic machineries share common signaling pathways that may link these two processes together.[42] Therefore, understanding the role of autophagy in AANTs associated nanotoxicity requires further detailed characterizations.

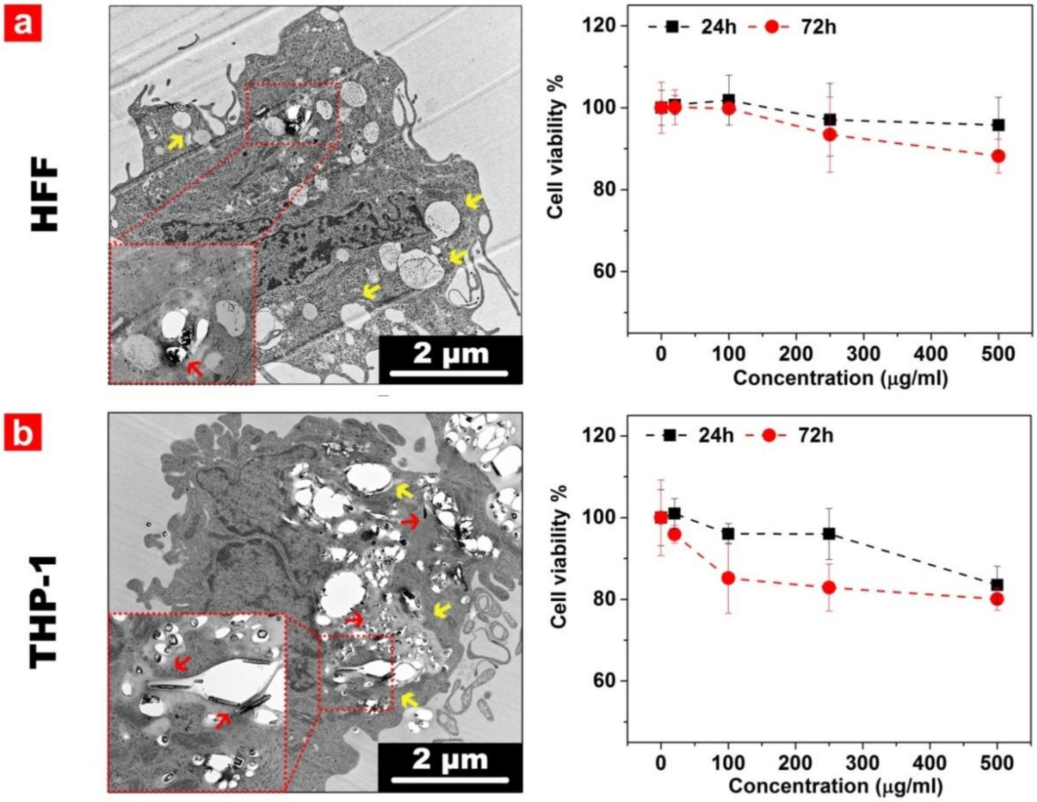

Figure 2 Cell viability and cell uptake characterization after AANTs treatment in (a) HFF and (b) THP-1 cell lines. AANTs exhibited a time-dependent and dose-dependent toxicity in both cell lines. Autophagy induction was evident in both cell lines characterized by the formulation of

autophagosome, which is depicted here as yellow arrows. AANTs were localized in the autophagosome structure, which were shown by red arrows.

3.3 Autophagy protects MDA-MB 231-TXSA breast cancer cells from AANTs induced toxicity.

To better understand the role of autophagy in cancer and nanotoxicity, we chose the breast cancer cell line MDA-MB 231-TXSA as a cell model and AANTs as a nanomaterial model. Cells were treated with AANTs at a concentration 100 μg/ml for 24 hs followed by systematic autophagy characterization, including monodansylcadaverine (MDC) staining (**Figure 3 a**), TEM imaging (**Figure 3 b**) and western blot analysis (**Figure 3 d**). Typical autophagy modulators including 3-MA and rapamycin (RP) were used here as autophagy inhibitor and promoter respectively. We found that 3-MA can induce significant type II cell death (autophagic cell death) at a commonly used dose (5 to 10 mM). (**Figure S2 – Supporting Information**) Therefore, we carefully optimized the dose and chose 1mM as a working concentration in the following experiment. Surprisingly, we found MDA-MB 231-TXSA had a relatively high basal level of autophagy. Both AANTs and RP treatment enhanced the level of autophagy, featuring the accumulated autophagosome and the lipidation of cytosolic-associated protein light chain 3 (LC-3 I) into its membrane-bound lipidated form, LC-3 II.[15] While low concentration of 3-MA did not completely abolish autophagy under these conditions, it effectively reduced the level of autophagy demonstrated here by the decreased intensity of MDC staining and reduced level of LC-3 II. Sequestosome-1 (p62), a protein targeted specific cargo (i.e. cellular waste) for facilitating autophagy, showed no significant modulation after treatment with AANTs, suggesting that treatment with AANTs at a relatively high concentration did not impair the autophagy degradation capacity.

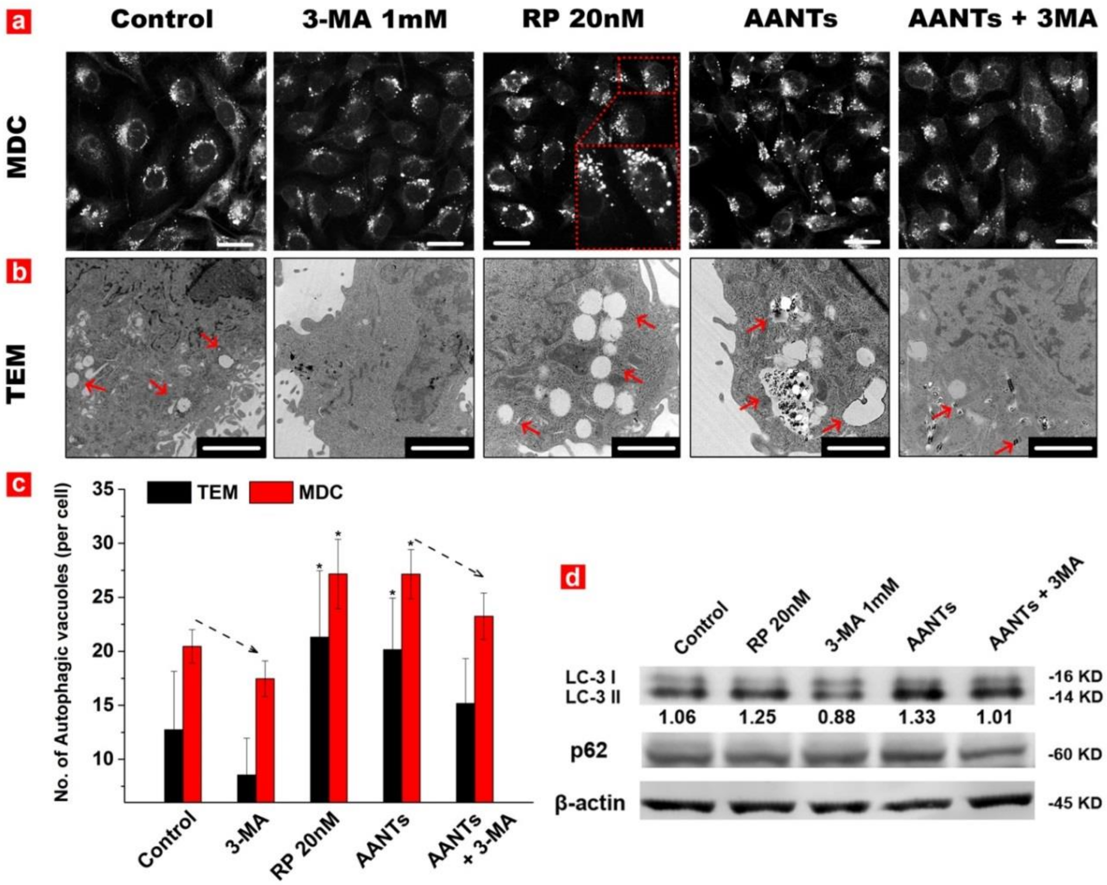

Figure 3 Autophagy characterizations of AANTs induced autophagy in MDA-MB 231-TXSA cells. (a) confocal microscopy characterization of autophagosome by MDC staining. MDA-MB 231-TXSA cells have a high basal level of autophagy, which can be inhibit by 3-MA or enhanced by rapamycin (RP) or AANTs treatment. Scale bar: 25 μm. (b) TEM characterization of autophagosome treated with 3-MA, RP and AANTs. Scale bar: 1 μm. (c) Quantitative analysis of autophagy levels by counting autophagic vacuoles from TEM and MDC staining images. AANTs and RP treatment can effectively induce autophagy. 1 mM 3-MA treatment reduced autophagy level, which is indicated by back arrows. (d) Western blot characterization of autophagy marker LC-3 and p62. The accumulation of LC-3 II is evident with RP and AANTs treatment. The ratio of LC-3 II/ LC-3 I was shown at the bottom of the LC-3 II band. The level of significance was set to a probability of $p < 0.05$ for *, $p < 0.01$ for **, and $p < 0.001$ for ***.

The impact of autophagy inhibition on cell viability was characterized by various well-established assays, including alarmar blue (**Figure 4 a**), annexin-V / 7-AAD double staining (**Figure 4 b**), and JC-1 assay (**Figure 4 c**). As shown in **Figure 4 a**, treatment with low concentration of 3-MA sensitized breast cancer cells to AANTs treatment after prolonged exposure with high doses (> 100 μg/ml). At the same time, treatment with AANTs at a concentration of 100 μg/ml did not induce significant apoptosis (annexin-V positive), necrosis (7-AAD positive) or mitochondria depolarization (JC-1positive) even after 72 hours. Such a toxicity pattern is indicative of exceptional AANTs' biocompatibility. Consistent with alarmar blue assay, 3-MA treatment enhanced the cytotoxicity of AANTs after 72 hours treatment, which further confirmed the cyto-protective role of autophagy in AANTs' triggered nanotoxicity. Further detailed characterizations of mitochondria volume, mitophagy (the specific autophagic clearance of mitochondria) and colocalization of AANTs and mitochondria inside autophagosome by confocal microscopy are shown in **Figure S3 – Supporting Information**. These results taken together demonstrated the cyto-protective function of mitophagy in degrading damaged mitochondria induced by AANTs uptake.

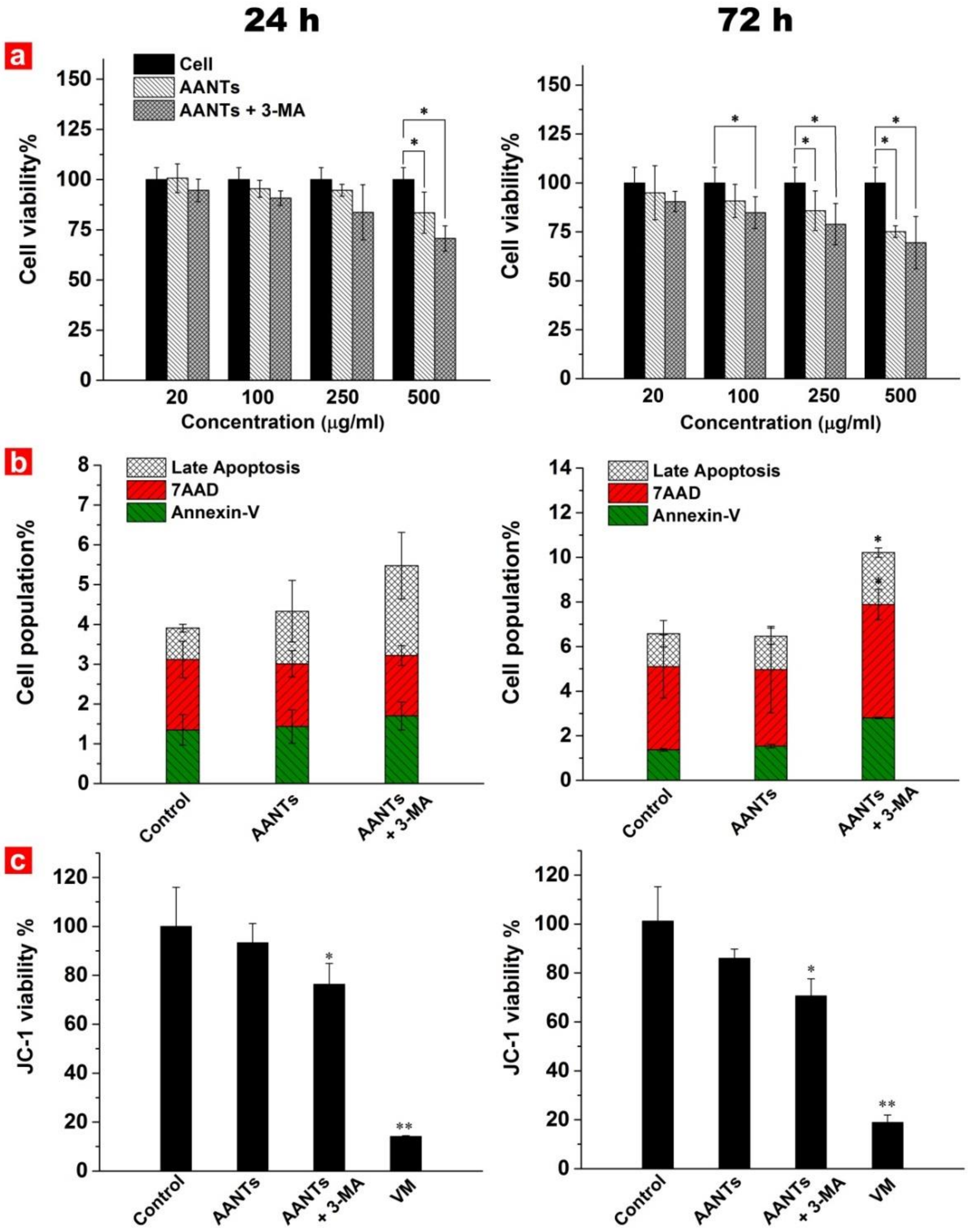

Figure 4 The impact of autophagy inhibition on MDA-MB 231-TXSA cell viability when treated with AANTs. (a) Alarmar blue assay of cell viability characterization by AANTs and 1mM 3-MA treatment. 3-MA slightly increased the AANTs induced toxicity at low dose (100 μg/ml) but significantly enhanced the toxicity of AANTs at high dose treatment (500 μg/ml) and longer time course. (b) Flow cytometry analysis of annexin-V / 7-AAD double staining and (c) JC-1 staining for quantification of cell viability treated with AANTs at a concentration 100 μg/ml. 20nM valinomycin was used as positive control. The level of significance was set to a probability of $p < 0.05$ for *, $p < 0.01$ for **, and $p < 0.001$ for ***.

Homeostasis of protein, lipid biosynthesis and energy metabolism impacts on cell function and longevity. PI3K-AKT-mTOR pathway as a key regulator of cell function (i.e. proliferation, protein synthesis and glucose metabolism) is increasingly gaining attention in cancer development and is a target for cancer therapy.[43,44] However, the impact of nanomaterials on this metabolic pathway is still unclear, although several types of nanoparticles were found to regulate PI3K-AKT-mTOR pathway by totally distinctive patterns.[45,46] As shown in **Figure 5 a**, RP, a typical mTOR inhibitor used here as a positive control, significantly down-regulated thephosphorylation of S6 kinase (p70 S6) and eukaryotic initiation factor 4E-binding protein (4E-BP1), two well-characterized mTOR substrates responsible for protein synthesis and cell cycle progression.[47] AANTs and 3-MA treatment had no effect on the downstream substrates of mTOR as well as the upstream regulators of mTOR such as class III phosphoinositide 3-kinase (PI3K III), protein kinase B (AKT) and phosphorylation of AKT at ser 473 site (phosphor-AKT (Ser 473). However, phosphorylation of mTOR at Ser-2448 (phosphor-mTOR (Ser 2448) was significantly down-regulated following treatment with AANTs + 3-MA, indicating the possible metabolic stress caused by the reducing kinase activity of p70 S6 and mTOR.[48,49] In addition, we found that 3-MA treatment up-regulated AANTs induced ER stress evidenced here by an increase in BiP and IRE1α levels (**Figure 5 b and c).** While AANTs + 3-MA triggered an ER stress response, nonetheless apoptosis signaling was not affected since the modulation of apoptosis regulators including caspase 3, p53 and Bcl-2 was virtually undetectable. Taken together these results demonstrate that inhibition of autophagy can sensitize cells to AANTs-induced ER stress leading to changes in protein biosynthesis without triggering programmed cell death.

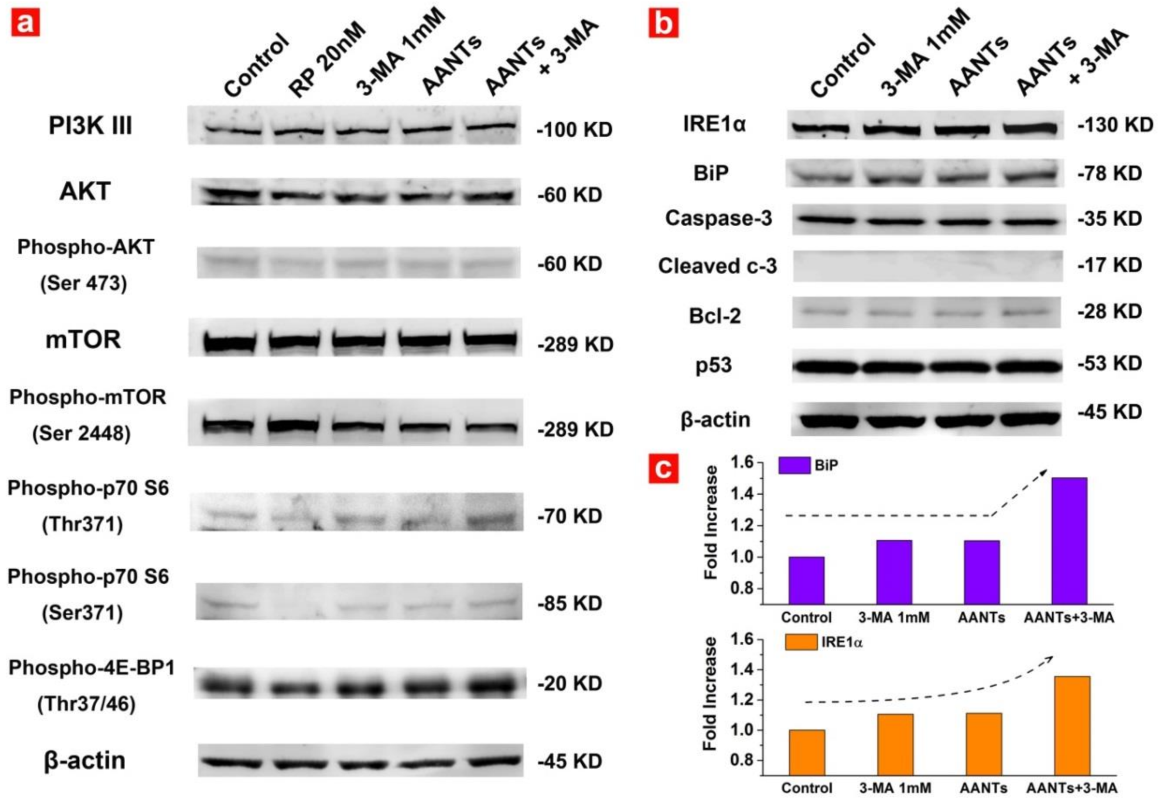

Figure 5 PI3K-AKT-mTOR, ER stress and apoptotic signaling in MDA-MB 231-TXSA exposure to AANTs. Cells were treated with AANTs at a concentration of 100 µg/ml followed by western immunoblotting analysis. (a) AANTs with or without 3-MA treatment did not influence the function of mTOR pathway. In contrast, low concentration of rapamycin down-regulated two downstream substrates of mTOR, p70 S6 and 4E-BP1. (b) AANTs treatment did not alter the pattern of apoptotic and anti-apoptotic protein expression. However, up-regulation of ER stress markers such as IRE1α and BiP is clearly evident. (c) Quantification of expression level of BiP and IRE1 α.

3.4 Autophagy inhibitor enhances cytotoxicity of thapsigargin delivered by AANTs *in vitro*

Since 3-MA increase AANTs associated nanotoxicity through ER stress, we reason that 3-MA may have synergistic effect when combined with an ER stress inducer together with AANTs for cancer killing. To rationalize our hypothesis, we chose TG as a prototype ER stress inducer and developed a TG delivery system by using AANTs as a nano-carrier model. The drug loading was conducted by incubating AANTs with high concentration of TG followed by washing and vacuum drying. The drug loading amount was quantified by thermogravimetric analysis, which was calculated to be 25.4 ± 10.2 µg per mg of AANTs. (**Figure S4 – Supporting Information**). As shown in **Figure 6 a**, treatment with TG or AANTs loaded with TG (AANTs@TG) induced significant changes in cellular morphology. Visualizing ER structures by the ER-tracker Blue-White DPX (ER tracker) under confocal microscopy showed that both TG and AANTs@TG treatment induced separated bright dots located in the cytoplasm, possibly due to the aggregation of unfolded proteins on the ER membrane.[34,50] More importantly, a clearly dose-dependent toxicity and synergistic effect of AANTs@TG and 3-MA is shown in **Figure 6 b**. After 24h treatment at a concentration of 100 µg/ml, AANTs@TG reduced cell viability to 78 %; while co-treated with 1mM 3-MA reduced cell viability even further to 60 %. The co-operative synergy analysis was confirmed using the median effect methods developed by Chou and Talalay.[51] 3-MA showed a combination index of 0.61 with AANTs@TG at the concentration 100 µg/ml. The synergy effect of 3-MA and TG was also confirmed as shown in **Figure S5 – Supporting Information**.

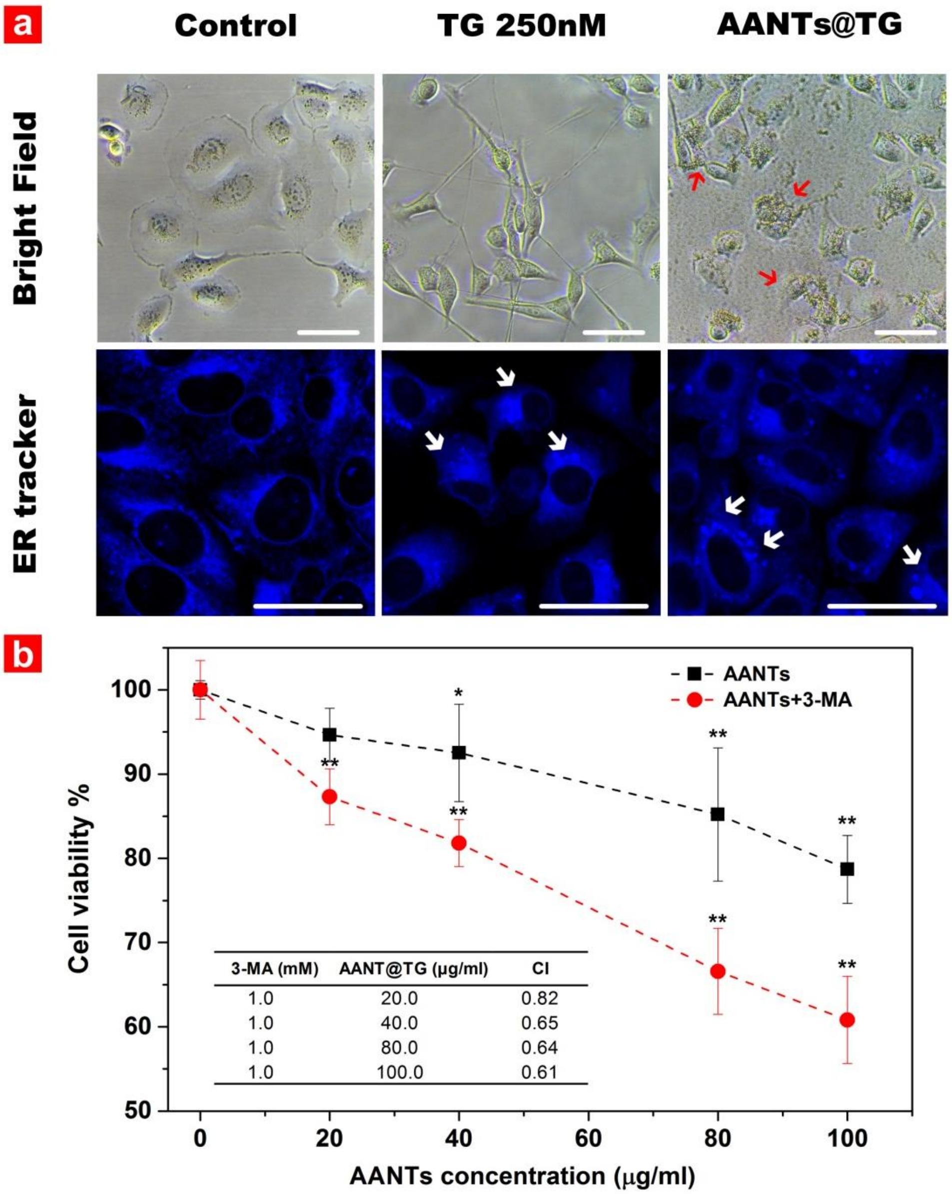

3-MA (mM)	AANT@TG (μg/ml)	CI
1.0	20.0	0.82
1.0	40.0	0.65
1.0	80.0	0.64
1.0	100.0	0.61

Figure 6 *In vitro* thapsigargin delivery by AANTs co-treated with 3-MA at the time-course of 24 hour. (a) Bright field images and ER tracker staining characterization of MDA-MB 231-TXSA cells treated with TG and AANTs@TG. Red arrows denoted the accumulation of AANTs on cell surface. White arrows showed bright dots existed in the cytoplasm of TG and AANTs@TG treated cells. Scale bar: 50 μm (b) dose dependent toxicity of AANTs@TG treatment alone and combined with 1mM 3-MA. Inset is the combination index data obtained by using Chou and Talalay method. The level of significance was set to a probability of $p < 0.05$ for *, $p < 0.01$ for **, and $p < 0.001$ for ***.

Such synergistic effect of AANTs@TG and 3-MA was further characterized at the bio-molecular level. (**Figure 7**) Treatment with TG showed significant up-regulation of several critical ER stress markers, including BiP, C/EBP homologous protein (CHOP), IRE1α and PKR-like ER kinase (PERK). Specially, treatment with 250nM TG together with 1mM 3-MA showed approximately a 13 fold increase of in BiP level and a 2 fold increase in CHOP when compared to treatment with 250nM TG alone, in which a 10 fold increase of BiP and 1.5 fold increase of CHOP were observed. Treatment with AANTs@TG and AANTs@TG + 3-MA dramatically up-regulated BiP expression. Importantly, the level of CHOP, a downstream component of ER stress signaling pathway, showed a 3.3 fold increase in AANTs@TG + 3-MA treatment when compared to 2.6 fold increase in the AANTs@TG alone group. Trans-membrane signaling proteins, IRE1α and PERK were both up-regulated by AANTs@TG and TG treatment, but such a pattern was not enhanced significantly with 3-MA co-treatment. To clarify the cell death reason, we characterized various markers of apoptosis inducers including caspase-3, 8, 9 and BiD.[52] The expression of these pro-apoptotic factors were not modulated by TG and AANTs@TG treatment within 24hs, indicating a caspase-independent mechanism of cell death. Characterization of autophagy markers LC-3 I, LC-3 II and p62 showed enhanced expression levels of LC 3-II after TG and AANTs@TG treatment, while p62 levels and the ratio of LC-3 II/LC-3 I were maintained at basal levels. However, treatment with 1mM 3-MA reduced the level of LC-3 II back to basal level. Taken together, these results strongly suggest that blocking autophagy by an autophagy inhibitor facilitates the cytotoxicity of ER stress at the molecular level and results in enhanced toxicity that is mediated by a caspase-independent cell death mechanism(s).

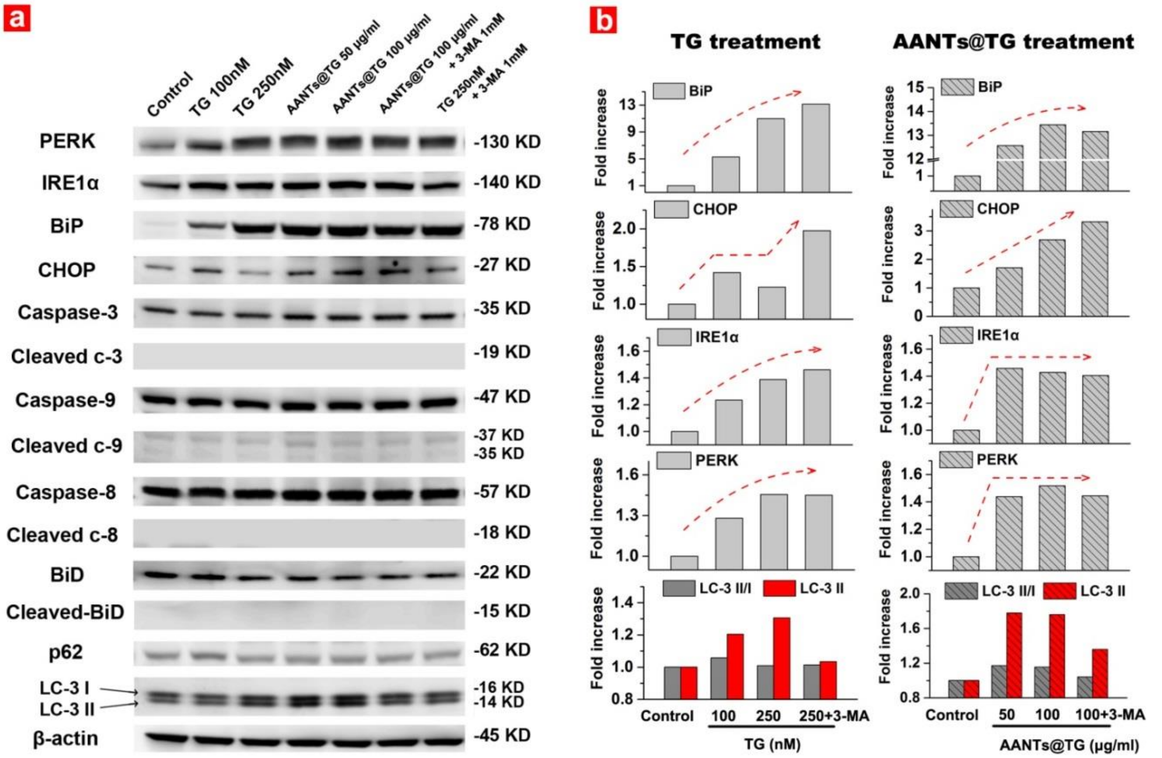

Figure 7 Synergistic effect of AANTs@TG and 3-MA treatment on the ER stress, apoptotic and autophagic signaling pathways. (a) MDA-MB 231-TXSA cells were treated with TG, AANTs@TG combined with 1 mM 3-MA for 24h followed by western immunoblotting analysis. Up-regulation of ER stress marker proteins is evident in the group of TG, AANTs@TG combined with 3-MA (b) Quantification of expression level of ER stress and autophagic marker proteins.

4. Discussion

Recent fundamental studies of nanotoxicity revealed the indispensable roles of ER stress and autophagy in the regulation of nanomaterial induced cellular stresses.[16,53] Indeed, ER stress and autophagy as two essential homoeostasis processes constitute both pro-survival mechanisms and lethal programs. ER is the major membrane source which contributes to autophagosome formation by interconnected with autophagosome through ER-associated cisternae structures.[54] Such functional connection makes autophagy an essential pro-survival pathway to reduce ER stress. It is believed that ER stress is iniciated by the release of BiP followed by the activation of three crucial transmembrane signaling proteins named IRE1α, PERK, and activating transcription factor 6 (ATF6) in respond to the misfolded proteins on ER[30]; while autophagy is functional involved for the clearance of misfoled proteins to alleviate the ER stress.[14]

However, our understanding about the cross talk between ER and autophagy molecular pathways in nanotoxicity remains limited due to the complexity of autophagy modulation by nanomaterials. Although autophagy can be cyto-protective, various nanomaterials such as graphene oxide[55] and polyethylenimine[56] were reported to induce type II cell death, in which autophagy led to cell death rather than cell survival. Therefore, the role of autophagy in cell function, like other nanotoxicity paradigms, appears to be dependent on the type of nanomaterial.[17] To clarify the role of autophagy on AANTs-associated cytotoxicity, we systematically characterized cell viability and autophagy by multiple techniques. (**Figures 3, 4 and S3**) Our results clearly demonstrate that AANTs have superior biocompatibility even under condition of autophagy inhibition. At the molecular level, such biocompatibility pattern was evidenced by the unaltered PI3K-AKT-mTOR and apoptotic signaling pathways. In addition, autophagy inhibition by 3-MA led to the induction of ER stress and down-regulation of phosphor-mTOR (Ser 2448) after AANTs treatment, which further substantiated the function of autophagy for alleviating AANTs induced cellular stress. It is worth noting that 3-MA was used here at a non-toxic dose (1 mM) due to the known cytotoxicity displayed at high concentration. (**Figure S2 – Supporting Information**) Since autophagy inhibitors such as 3-MA and CQ were routinely used at high doses in other autophagy studies, caution needs to be raised when using these drugs for nanotoxicity studies.

The complexity of cancer cell survival / death signaling pathways and their dysregulation by oncogenes have motivated the development of novel therapeutic approaches for improving therapeutic outcome.[57] It is known that a wide array of conventional chemotherapeutic agents can induce cyto-protective autophagy and ER stress responses.[14] Although the clinical transition of combining autophagy inhibitors with anti-cancer drugs for chemotherapy is in progress, the simultaneous targeting of autophagic and ER stress signaling is rarely reported.[58,59] TG is a natural compound that selectively inhibits the ER calcium-dependent ATPase pump and thus can induce extensive ER stress at nanomolar doses.[60,61] As a proof-of-concept, we chose TG as a prototype ER stress inducer and conducted TG delivery by AANTs co-treated with low concentration of 3-MA. The drug loading was conducted by utilizing the electrostatic adsorption between drug molecular and AANTs' surface. Although the drug loading was not ideal, in this instance, nonetheless AANTs@TG efficiently delivered TG into cells and consequently triggered ER stress-associated cell death when co-treated with 3-MA. (**Figure 6**) The synergistic effect of this drug delivery system was further confirmed both at the cellular and bimolecular level. (**Figure 7**) A schematic illustration of the cytotoxicity pattern of AANTs and AANTs-based drug delivery system is shown in **Figure 8**. It is anticipated that adapting this signaling network targeting strategy with other nanoparticle-based delivery systems will no doubt prove to be a promising approach for improving the drug delivery performance in targeted cancer therapy.

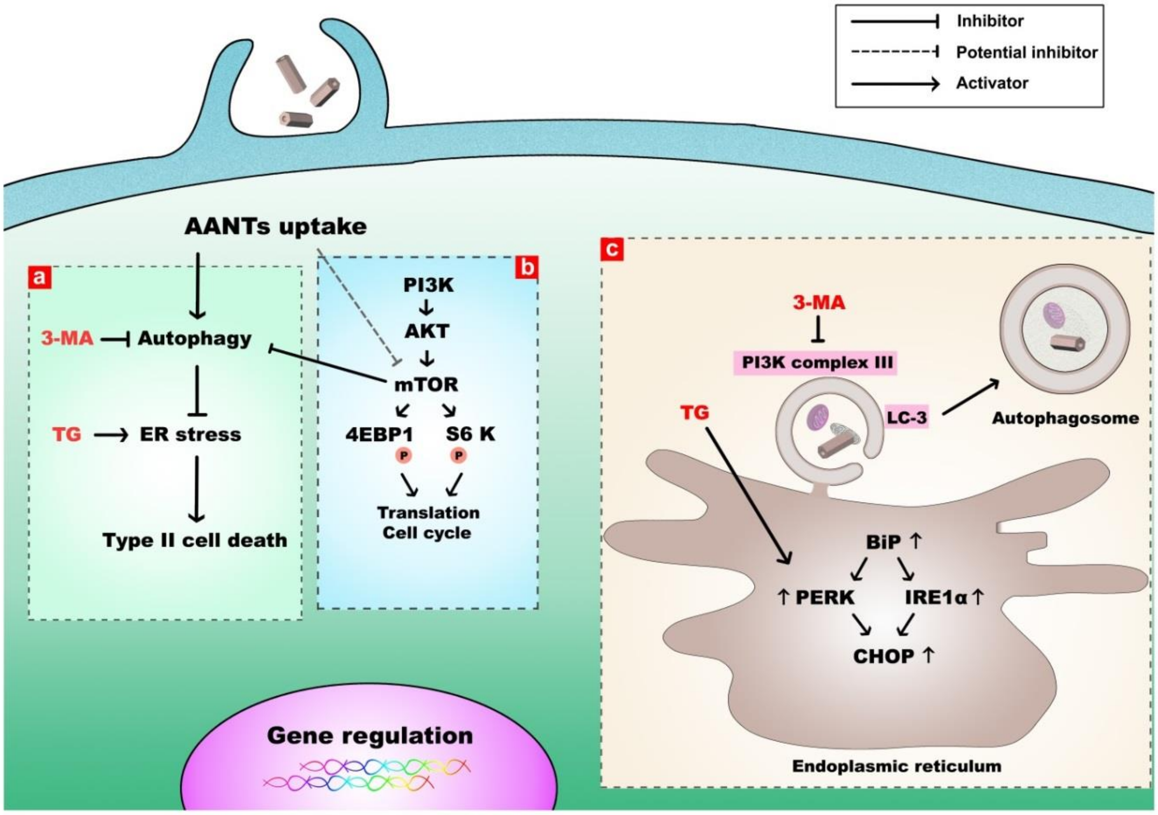

Figure 8 Schematic representations of AANTs induced toxicity pattern and ER stress – autophagic signaling targeting drug delivery system. (a) Autophagy protect cell from AANTs induced ER stress. Inhibition of autophagy and co-delivery TG together cause ER stress signaling cascade and finally lead to cell death. (b) AANTs treatment down-regulated phosphor-mTOR (Ser 2448), thus were suspected to inhibit mTOR signaling pathway. (c) A detailed illustration of signaling network connection between autophagy pathway and ER stress. 3-MA inhibited the formation of autophagosome by suppressing PI3K complex III. ER stress induced by AANTs was further enhanced by TG treatment, which up-regulated ER stress marker expression, such as BiP, PERK, IRE1α and CHOP.

5. Conclusions

With the growing knowledge of autophagic and ER stress signaling pathways in regulating cancer cell growth, survival and death, developing precise and sophisticated signaling networks targeting delivery platforms offers novel strategies for combating cancer. Herein, we addressed this challenge by developing a simple AANTs-based drug delivery platform for delivering TG and 3-MA. This stagey is based on our systematic nanotoxicity study, which clarifies the network connection between ER stress and autophagy in response to AANTs at the molecular level. Our research not only demonstrates the biocompatibility of AANTs for future advanced biomedical application, but also highlights the clinical therapeutic potential of modulating cell signaling pathways using nanoparticle-based drug delivery approaches.

Acknowledgements

This research was supported by the Australian Research Council (ARC) through the grants DP120101680, FT110100711, DE14010054, the National Health and Medical Research Council (NHMRC) of Australia through grant APP627015, the Australian Breast Cancer Research (ABCR), The Hospital Research Foundations (THRF) and the University of Adelaide Interdisciplinary Research Fund (DVC IRF -2014). We are thankful for Adelaide Microscopy for providing microscopy facilities. Ye Wang appreciated the scholarship support from China Scholarship Council. This work was per-formed in part at the OptoFab node of the Australian National Fabrication Facility utilizing Commonwealth and SA State Government funding.

Supporting Information

Supplementary data of surface charge characterization of AANTs, cytotoxicity of 3-MA, mitophagy and mitochondria characterization, thermogravimetric analysis of drug loading and synergism effect of 3-MA and thapsigargin with this article can be found in the online version.

Author Contributions

Ye Wang designed and conducted experiments assisted by Gagandeep Kaur and Yuting Chen. The manuscript was written through contributions of all authors. All authors have given approval to the final version of the manuscript.

‡These authors contributed equally.

References

1. Y. Yan, G. K. Such, A. P. R. Johnston, J. P. Best and F. Caruso, ACS Nano, 2012, 6, 3663-3669.
2. J. G. Huang, T. Leshuk and F. X. Gu, Nano Today, 2011, 6, 478-492.
3. Y. Wang, A. Santos, A. Evdokiou and D. Losic, J. Mater. Chem. B, 2015, DOI: 10.1039/c5tb00956a.
4. A. M. Derfus, W. C. W. Chan and S. N. Bhatia, Adv. Mater., 2004, 16, 961-966.
5. L. Luan, Q.B. Meng, L. Xu, Z. Meng, H.S. Yan, K.L. Liu J. Mater. Chem. B, 2015,3, 1068-1078
6. X. Du, L. Xiong, S. Dai, F. Kleitz and S. Z. Qiao, Adv. Funct. Mater., 2014, 24, 7627-7637.
7. M. S. Cartiera, K. M. Johnson, V. Rajendran, M. J. Caplan and W. M. Saltzman, Biomaterials, 2009, 30, 2790-2798.
8. X. Zhang, X. Zeng, X. Liang, Y. Yang, X. Li, H. Chen, L. Huang, L. Mei and S.-S. Feng, Biomaterials, 2014, 35, 9144-9154.
9. B. Al-Lazikani, U. Banerji and P. Workman, Nat Biotech, 2012, 30, 679-692.
10. C. Holohan, S. Van Schaeybroeck, D. B. Longley and P. G. Johnston, Nat Rev Cancer, 2013, 13, 714-726.
11. P. Borst, R. Evers, M. Kool and J. Wijnholds, J. Natl. Cancer Inst., 2000, 92, 1295-1302.
12. L. M. Thai, A. Labrinidis, S. Hay, V. Liapis, S. Bouralexis, K. Welldon, B. J. Coventry, D. M. Findlay and A. Evdokiou, Cancer Res., 2006, 66, 5363-5370.
13. L. P. Martin, T. C. Hamilton and R. J. Schilder, Clin. Cancer Res., 2008, 14, 1291-1295.
14. D. C. Rubinsztein, P. Codogno and B. Levine, Nat Rev Drug Discov, 2012, 11, 709-730.
15. B. Levine, N. Mizushima and H. W. Virgin, Nature, 2011, 469, 323-335.
16. K. Peynshaert, B. B. Manshian, F. Joris, K. Braeckmans, S. C. De Smedt, J. Demeester and S. J. Soenen, Chem. Rev., 2014, 114, 7581-7609.
17. S. Stern, P. Adiseshaiah and R. Crist, Part. Fibre Toxicol., 2012, 9, 20.
18. L. Zhu, J. Zhang, L. Xiao, S. Liu, J. Yu, W. Chen, X. Zhang and B. Peng, J. Mater. Chem. B, 2015, DOI: 10.1039/C5TB00894H

19. J. Juan, L. Cheng, M. Shi, Z. Liu and X. Mao, J. Mater. Chem. B, 2015, 3, 5769-5776.

20. H.-Y. Lu, Y.-J. Chang, N.-C. Fan, L.-S. Wang, N.-C. Lai, C.-M. Yang, L.-C. Wu and J.-a. A. Ho, Biomaterials, 2015, 42, 30-41.

21. Y. Lu, L. Zhang, J. Li, Y.-D. Su, Y. Liu, Y.-J. Xu, L. Dong, H.-L. Gao, J. Lin, N. Man, P.-F. Wei, W.-P. Xu, S.-H. Yu and L.-P. Wen, Adv. Funct. Mater., 2013, 23, 1534-1546.

22. S.L. Li, C.Q. Zhang, W.P. Cao, B.Y. Ma, X.W. Ma, S.B. Jin, J.C. Zhang, P.C. Wang, F. Li, X.J. Liang, J. Mater. Chem. B, 2015,3, 3324-3330

23. L. Dong, Y. Liu, Y. Lu, L. Zhang, N. Man, L. Cao, K. Ma, D. An, J. Lin, Y.-J. Xu, W.-P. Xu, W.-B. Wu, S.-H. Yu and L.-P. Wen, Adv. Funct. Mater., 2013, 23, 5930-5940.

24. Q. Wen, L. Liu, Q. Yang, F. Lv and S. Wang, Adv. Funct. Mater., 2013, 23, 764-769.

25. Z. J. Yang, C. E. Chee, S. Huang and F. A. Sinicrope, Mol. Cancer Ther., 2011, 10, 1533-1541.

26. X. Zhang, Y. Dong, X. Zeng, X. Liang, X. Li, W. Tao, H. Chen, Y. Jiang, L. Mei and S.-S. Feng, Biomaterials, 2014, 35, 1932-1943.

27. P. Maycotte, S. Aryal, C. T. Cummings, J. Thorburn, M. J. Morgan and A. Thorburn, Autophagy, 2012, 8, 200-212.

28. Y.-T. Wu, H.-L. Tan, G. Shui, C. Bauvy, Q. Huang, M. R. Wenk, C.-N. Ong, P. Codogno and H.-M. Shen, J. Biol. Chem., 2010, 285, 10850-10861.

29. Y. Sheng, B. Sun, W.-T. Guo, Y.-H. Zhang, X. Liu, Y. Xing and D.-L. Dong, Biochem. Biophys. Res. Commun., 2013, 432, 5-9.

30. I. Kim, W. Xu and J. C. Reed, Nat Rev Drug Discov, 2008, 7, 1013-1030.

31. C. Xu, B. Bailly-Maitre and J. C. Reed, J. Clin. Invest., 2005, 115, 2656-2664.

32. A. H. Schönthal, Cancer Lett., 2009, 275, 163-169.

33. Y.-Y. Tsai, Y.-H. Huang, Y.-L. Chao, K.-Y. Hu, L.-T. Chin, S.-H. Chou, A.-L. Hour, Y.-D. Yao, C.-S. Tu, Y.-J. Liang, C.-Y. Tsai, H.-Y. Wu, S.-W. Tan and H.-M. Chen, ACS Nano, 2011, 5, 9354-9369.

34. R. Zhang, M. J. Piao, K. C. Kim, A. D. Kim, J.-Y. Choi, J. Choi and J. W. Hyun, J. Biochem. Cell Biol., 2012, 44, 224-232.

35. H.-W. Chiu, T. Xia, Y.-H. Lee, C.-W. Chen, J.-C. Tsai and Y.-J. Wang, Nanoscale, 2015, 7, 736.

36. Y. Wang, G. Kaur, A. Zysk, V. Liapis, S. Hay, A. Santos, D. Losic and A. Evdokiou, Biomaterials, 2015, 46, 117-130.

37. Y. Wang, A. Santos, G. Kaur, A. Evdokiou and D. Losic, Biomaterials, 2014, 35, 5517-5526.

38. Y. Wang, A. Santos, A. Evdokiou and D. Losic, Electrochim. Acta, 2015, 154, 379-386.

39. A. M. Md Jani, D. Losic and N. H. Voelcker, Prog. Mater. Sci., 2013, 58, 636-704.

40. D. Losic and S. Simovic, Expert Opin. Drug Deliv., 2009, 6, 1363-1381.

41. M. P. Monopoli, C. Aberg, A. Salvati and K. A. Dawson, Nat Nano, 2012, 7, 779-786.

42. M. C. Maiuri, E. Zalckvar, A. Kimchi and G. Kroemer, Nat Rev Mol Cell Biol, 2007, 8, 741-752.

43. E. Blanco, T. Sangai, S. Wu, A. Hsiao, G. U. Ruiz-Esparza, C. A. Gonzalez-Delgado, F. E. Cara, S. Granados-Principal, K. W. Evans, A. Akcakanat, Y. Wang, K.-A. Do, F. Meric-Bernstam and M. Ferrari, Mol Ther, 2014, 22, 1310-1319.

44. B. T. Hennessy, D. L. Smith, P. T. Ram, Y. Lu and G. B. Mills, Nat Rev Drug Discov, 2005, 4, 988-1004.

45. J. Duan, Y. Yu, Y. Yu, Y. Li, P. Huang, X. Zhou, S. Peng and Z. Sun, Part. Fibre Toxicol, 2014, 11, 50.

46. B. Wang, N. Chen, Y. Wei, J. Li, L. Sun, J. Wu, Q. Huang, C. Liu, C. Fan and H. Song, Sci. Rep., 2012, 2.

47. N. Hay and N. Sonenberg, Genes Dev., 2004, 18, 1926-1945.

48. G. G. Chiang and R. T. Abraham, J. Biol. Chem., 2005, 280, 25485-25490.

49. L. H. P. Caro, P. J. A. M. Plomp, E. J. Wolvetang, C. Kerkhof and A. J. Meijer, Eur. J. Biochem., 1988, 175, 325-329.

50. M. Abdelrahim, K. Newman, K. Vanderlaag, I. Samudio and S. Safe, Carcinogenesis, 2006, 27, 717-728.

51. T.-C. Chou, Cancer Res., 2010, 70, 440-446.

52. I. Zinonos, A. Labrinidis, M. Lee, V. Liapis, S. Hay, V. Ponomarev, P. Diamond, A. C. W. Zannettino, D. M. Findlay and A. Evdokiou, Mol. Cancer Ther., 2009, 8, 2969-2980.

53. F. T. Andón and B. Fadeel, Acc. Chem. Res., 2012, 46, 733-742.

54. P. Ylä-Anttila, H. Vihinen, E. Jokitalo and E.-L. Eskelinen, Autophagy, 2009, 5, 1180-1185.

55. G.-Y. Chen, H.-J. Yang, C.-H. Lu, Y.-C. Chao, S.-M. Hwang, C.-L. Chen, K.-W. Lo, L.-Y. Sung, W.-Y. Luo, H.-Y. Tuan and Y.-C. Hu, Biomaterials, 2012, 33, 6559-6569.

56. X. Gao, L. Yao, Q. Song, L. Zhu, Z. Xia, H. Xia, X. Jiang, J. Chen and H. Chen, Biomaterials, 2011, 32, 8613-8625.

57. Michael J. Lee, Albert S. Ye, Alexandra K. Gardino, Anne M. Heijink, Peter K. Sorger, G. MacBeath and Michael B. Yaffe, Cell, 149, 780-794.

58. X.-H. Ma, S.-F. Piao, S. Dey, Q. Mcafee, G. Karakousis, J. Villanueva, L. S. Hart, S. Levi, J. Hu and G. Zhang, T J. Clin. Invest., 2014, 124, 1406-1417.

59. A. H. Schönthal, Biochem. Pharmacol., 2013, 85, 653-666.

60. S. R. Denmeade, A. M. Mhaka, D. M. Rosen, W. N. Brennen, S. Dalrymple, I. Dach, C. Olesen, B. Gurel, A. M. DeMarzo, G. Wilding, M. A. Carducci, C. A. Dionne, J. V. Møller, P. Nissen, S. B. Christensen and J. T. Isaacs, Sci. Transl. Med., 2012, 4, 140ra186.

61. C. M. Jakobsen, S. R. Denmeade, J. T. Isaacs, A. Gady, C. E. Olsen and S. B. Christensen, J. Med. Chem. 2001, 44, 4696-4703.

62. W. Lee, R. Scholz and U. Gösele, Nano Lett., 2008, 8, 2155-2160.

63. L. Liu, D. Feng, G. Chen, M. Chen, Q. Zheng, P. Song, Q. Ma, C. Zhu, R. Wang, W. Qi, L. Huang, P. Xue, B. Li, X. Wang, H. Jin, J. Wang, F. Yang, P. Liu, Y. Zhu, S. Sui and Q. Chen, Nat Cell Biol, 2012, 14, 177-185.

Graphical Abstract

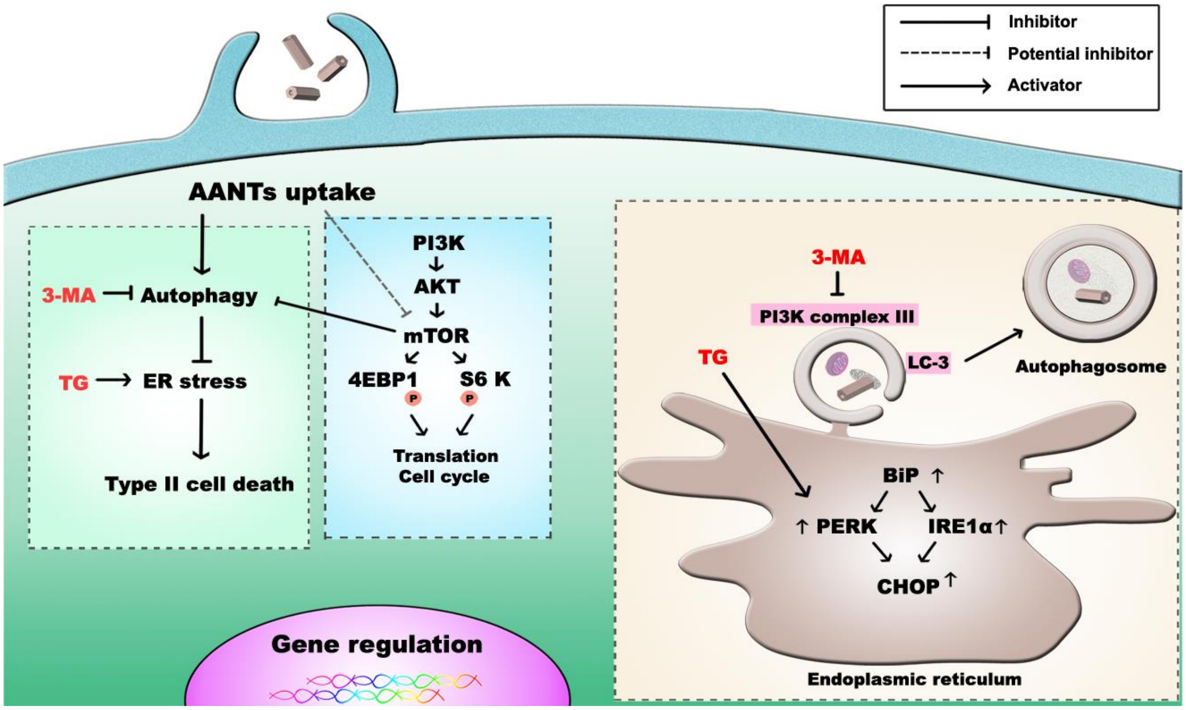

Cancer cell signaling targeting strategy is achieved by using anodic alumina nanotubes (AANTs) as nanocarriers to deliver an endoplasmic stress inducer, thapsigargin, co-treated with an autophagy inhibitor 3-methyladenine. Autophagy inhibition not only sensitizes cancer cells to AANTs-induced nanotoxicity, but also contributes to the synergism effect when combined with the AANTs-based thapsigargin delivery system.

Supporting Information

Targeting of endoplasmic reticulum stress and autophagic signaling networking by a nanotube-based combinatorial delivery system: A new strategy of cancer therapy

Ye Wang[a, b], Gagandeep Kaur[a, b†], Yuting Chen[a†], Abel Santos[a*], Dusan Losic[a*], Andreas Evdokiou[b*]

[a] School of Chemical Engineering, The University of Adelaide, Adelaide, SA, 5005

[b] Discipline of Surgery, The University of Adelaide, Basil Hetzel Institute, Adelaide, SA, 5005

[†] These authors contributed equally to this work.

* E-mails: abel.santos@adelaide.edu.au / dusan.losic@adelaide.edu.au / andreas.evdokiou@adelaide.edu

Figure S1 Surface charge measure of AANTs in deionized water

It is known that electrolyte anions (i.e. sulfonate group) can incorporate into the inner-wall surface of AAO during anodization. Therefore, the charge of inner surface should be taken into account when measuring the outer surface charges. To clarify the charges of outer surface which directly in contact with physiological environment, we selectively coated inner surface with positive or negative charged polymer (i.e. polystyrene sulfonic acid (PSS) and poly(allylamine hydrochloride) (PAH)) by a template-assisted functionalization protocol. (**Figure S1 a**) We denoted the inner surface coating of AANTs as AANTs-inner PSS / AANTs-inner PAH in contrast to the unselective polymer coating as AANTs-PSS / AANTs-PAH. As shown in **Table 1**, such polymer coating protocol have no effect on the DLS diameter, but significantly modulated the total surface charge pattern of the resulting AANTs. As-prepared AANTs had a positive surface charge of 27.0 mV, while AANTs-inner PSS showed a reduced ζ-potential of –1.8 mV. Interestingly, the sample of AANTs-PSS, which contained polymer coated on both inner / outer surface of AANTs, showed an enhanced negative surface charge of -33.1 mV. In contrast, AANTs-inner PAH did not alter the surface charge as compared to AANTs. However, AANTs-PAH showed a strong positive charge + 54.8 mV. Taken together, these analyses demonstrated that the inner and outer surface are both positively charged but at different levels due to the heterogeneous surface chemistry.

Table 1 surface charge and size distribution analysis of AANTs

	Size (nm) [a]	**PDI** [b]	**ζ-potential (mV)** [c]
AANTs	475.6 ± 38.2	0.21 ± 0.03	27.0 ± 0.6
AANTs-inner PSS	485.4 ± 57.9	0.28 ± 0.05	-1.8 ± 0.4
AANTs-PSS	450.4 ± 4.9	0.24 ± 0.01	-33.1 ± 0.5
AANTs-inner PAH	456.8 ± 21.4	0.23 ± 0.02	26.8 ± 0.6
AANTs-PAH	496.2 ± 11.0	0.26 ± 0.04	54.8 ± 0.9

a. The values represent the means of at least three experiments; **±:** standard deviation

b. PDI: polydispersity index

c. Analysis of size distribution and ζ-potential was conducted within ultrapure water at pH 5.8.

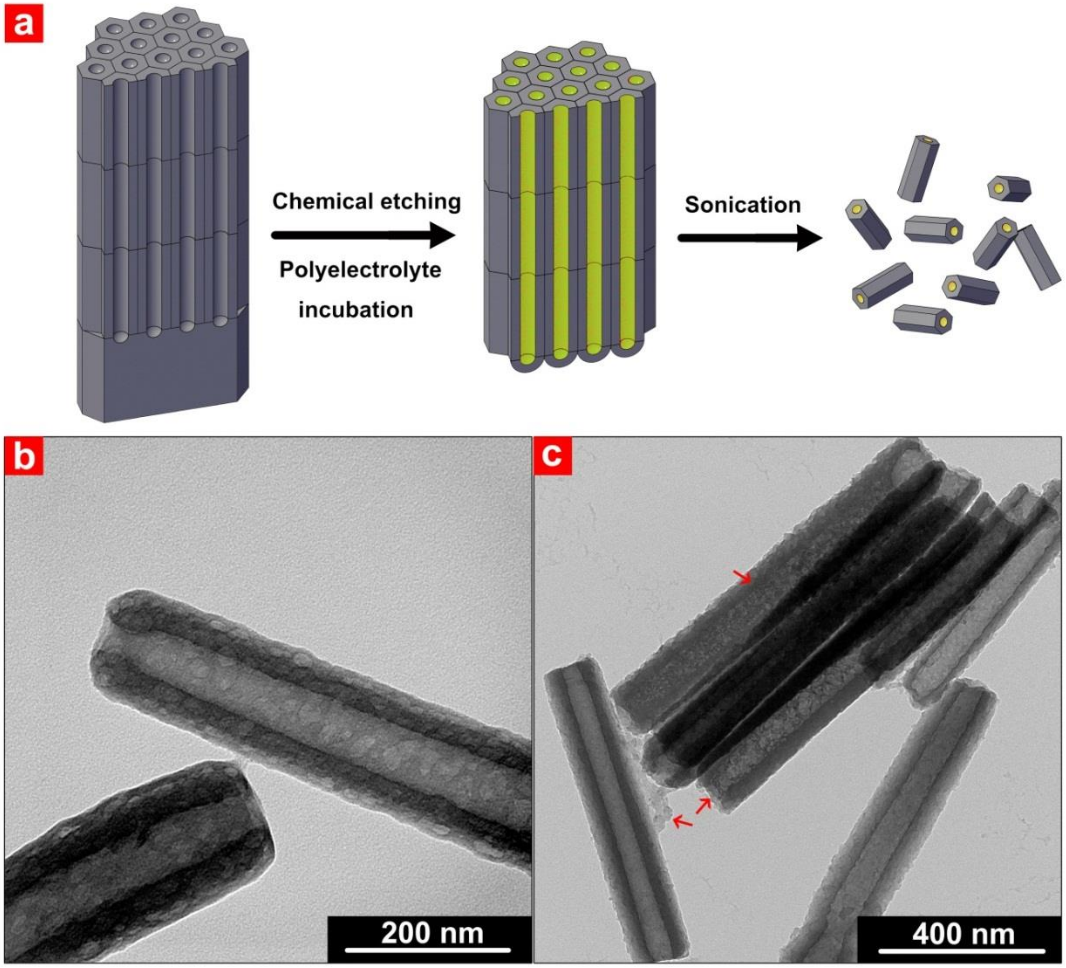

Figure S1 Coating AANTs inner surface with polyelectrolyte. (a) schematic illustration of inner AANTs coating with polystyrene sulfonic acid (PSS). Briefly, after pulse anodization, the aluminum substrate was removed by acid etching followed by polyelectrolyte incubation. After several cycles of washing, AANTs were obtained by sonication treatment. (b) TEM characterization of as-prepared AANTs. (c) TEM images of AANTs with inner surface coating of PSS. The existence of polymer is evident inside nanotube, which is denoted by red arrows.

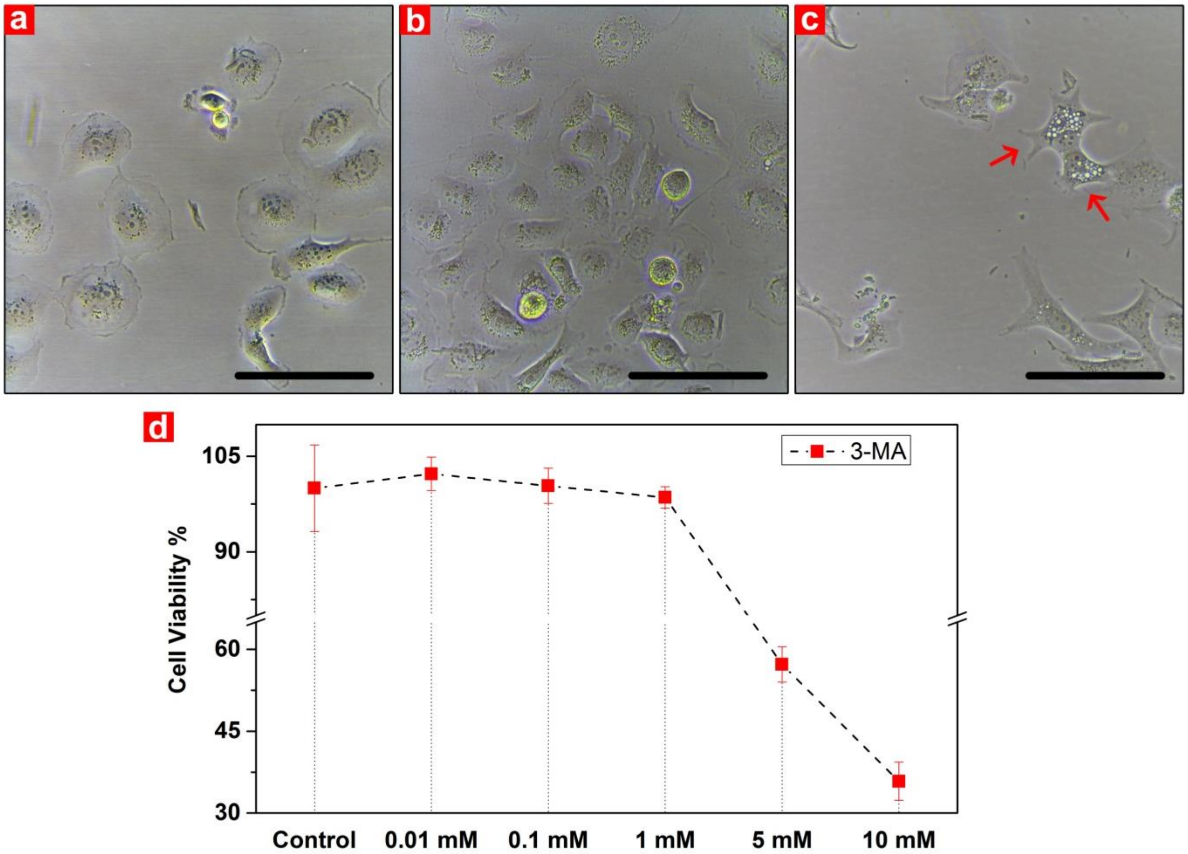

Figure S2 3-methyladenine (3-MA) induced cytotoxicity at high concentration. (a-c) light microscope characterization of MDA-MB 231-TXSA cells treated with (a) 0 mM, (b) 1mM and (c) 10mM 3-MA. High concentration of 3-MA induced autophagy cell death, which were denoted by red arrows. Scale bar: 50 µm. (d) cell viability of 3-MA after 24h treatment with gradient dose.

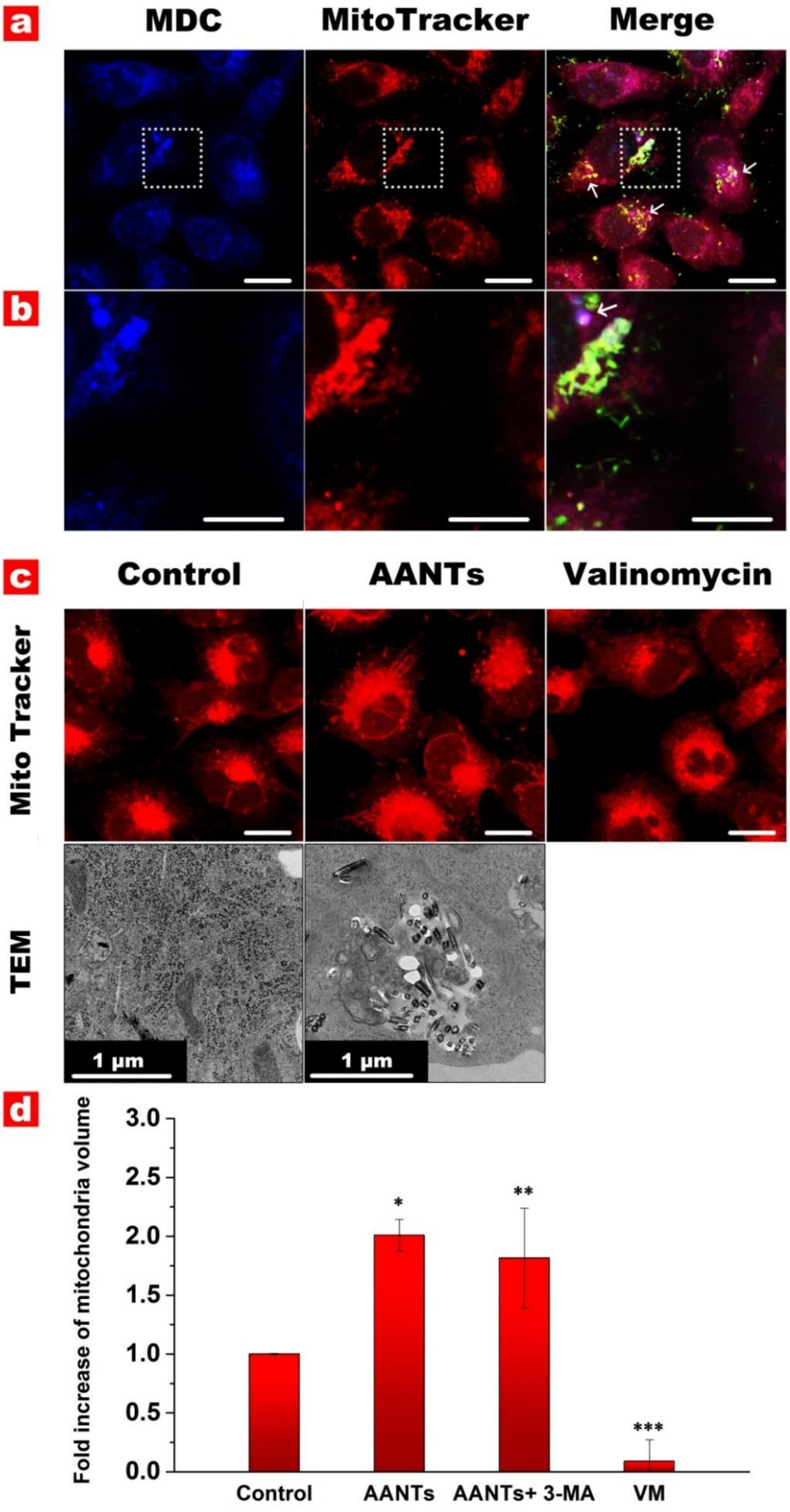
a
MDC
MitoTracker
Merge
b
c
Control
AANTs
Valinomycin
Mito Tracker
TEM
1 µm
1 µm
d
Fold increase of mitochondria volume
3.0
2.5
2.0
1.5
1.0
0.5
0.0
*
**
***
Control
AANTs
AANTs+ 3-MA
VM

Figure S3 Mitochondria characterization by confocal microscopy and TEM.

(a) AANTs and mitochondria were colocalized inside autophagosome. AANTs: green; Autophagosome: blue; Mitochondra: red. AANTs were labeled with Alizarin Red S. Mitochondria were stained with MitoTracker deep red. Autophagogome was stained with MDC. White arrows denote the co-localization of AANTs and mitochondria inside autophagosomes. Scale bar: 10 μm

(b) Enlarged area in (a) which is indicated by dash square. Scale bar: 5 μm.

(c) Representative images of mitochondria staining and TEM characterization. It is evident that the morphology of mitochondria in healthy cells was worm-like. Valinomycin induced mitochondria depolarization significantly changed the mitochondria morphology into circle shape. AANTs did not induce morphology change. From TEM, we were not able to identify the mitochondria volume change in AANTs samples. However, the debris of mitochondria inside autophagosome is identified, indicating the cyto-protective role of autophagy in degrading damaged mitochondria. 20nM valinomycin was used as positive control. Scale bar: 10 μm.

(d) Mitochondria volume calculation by 3D surface reconstruction of z-stack images. 50nM Valinomycin (VM) was used as positive control. Although mitochondria morphology change was not evident by TEM and confocal characterization, AANTs treatment showed around 1 fold volume increase. 3-MA treatment did not significantly enhance the volume change in this case. We found 50nM VM induced strong toxicity to cells and thus significantly reduced the staining intensity, thus the volume was virtually undetectable by confocal microscopy. The level of significance was set to a probability of $p < 0.05$ for *, $p < 0.01$ for **, and $p < 0.001$ for ***.

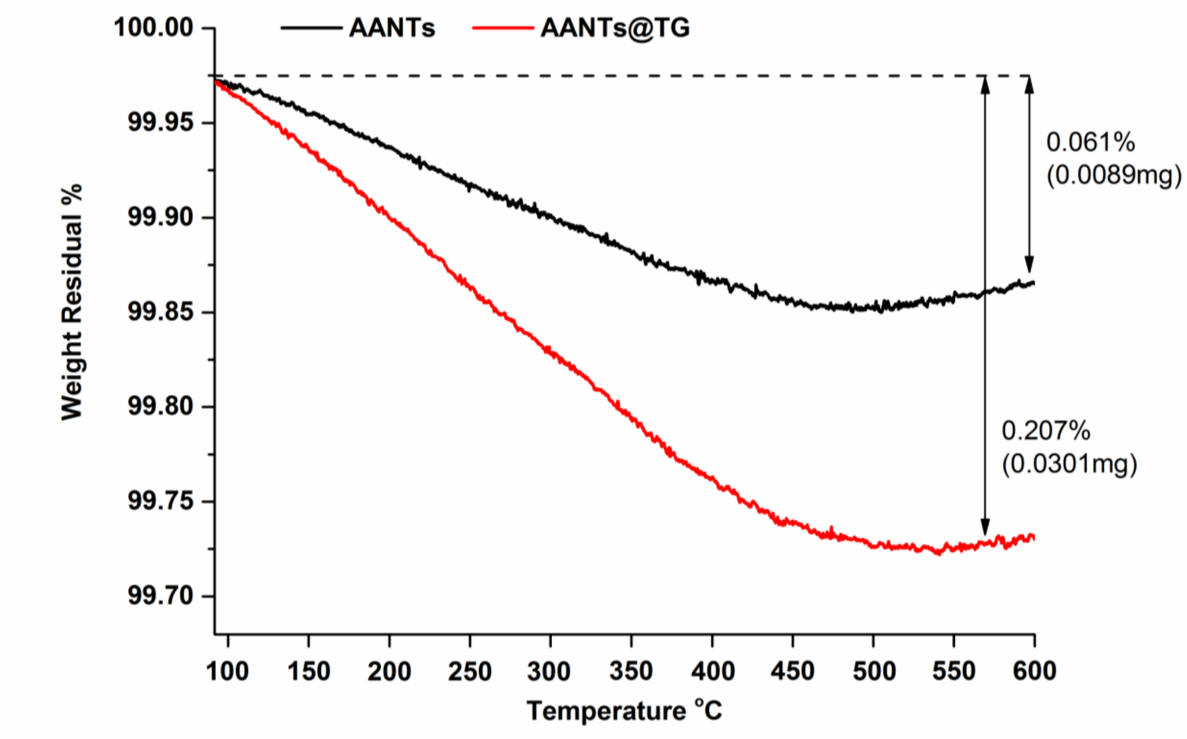

Figure S4 Thermogravimetric analysis (TGA) of thapsigargin loading on AANTs. Drug loading amount was calculated by the average weight lost difference between control group (AANTs) and drug loaded group (AANTs@TG) .

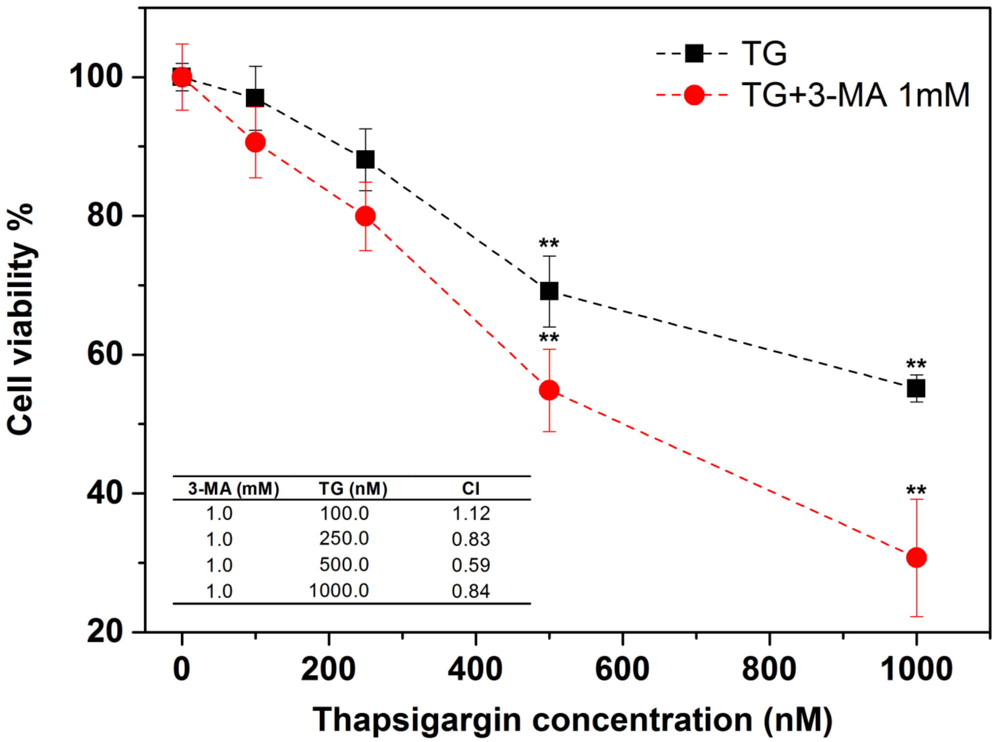

3-MA (mM)	TG (nM)	CI
1.0	100.0	1.12
1.0	250.0	0.83
1.0	500.0	0.59
1.0	1000.0	0.84

Figure S5 Synergism effect of 1mM 3-MA and thapsigargin (TG) after treatment with MDA-MB 231-TXSA cells for 24hs. The level of significance was set to a probability of $p < 0.05$ for *, $p < 0.01$ for **, and $p < 0.001$ for ***.

Chapter 7 Conclusions and Perspectives

7.1 Conclusions

This thesis aims at utilizing advanced anodization techniques to structural engineer anodic aluminium oxide (AAO), and to fabricate anodic alumina nanotubes (AANTs) for the study of drug delivery and nanotoxicity. Highlights and conclusions of this thesis are summarized below:

In **chapter 3**, detailed research of pulse anodization was performed in order to elucidate fundamental mechanisms of electrochemical anodization. This enabled feasible synthesis of anodic aluminium oxide (AAO)-based nanostructures including AAO-microcavities and AANTs. These novel nanomaterials are proven to be valuable tools for the research of interactions occurred at physical, chemical and biological interfaces due to the excellent properties of anodic alumina. The fundamental studies of pulse anodization in this thesis also paved the way for synthesizing other advanced anodic nanostructures in the future.

Besides material fabrication, this thesis considerably expands our knowledge of AANTs at bio-nano interfaces. In **chapter 4**, we showed for the first time a systematic toxicological study of AANTs with differing aspect ratios. The results showed that AANTs with low aspect ratios (7.8) are non-toxic to cells, while AANTs with high aspect ratio trigger cellular stresses and cell death. Clarifying the paradigm of nanotoxicity provides guidelines of the safe design of functional AANTs for drug delivery application. The establishment of high-throughput toxicity screening platform in this study is of useful for the rapid assessment of nanotoxicity of various nanomaterials. It is worth noting that AANTs showed superior biocompatibility as compared to other nanomaterials (e.g. carbon nanotubes, gold nanorods etc.). This is because AANTs are intrinsically stable with the absence of toxic paradigms such as reactive oxygen species generation and chemical ions dissolution.

Mapping the toxicity pattern of AANTs in this thesis paves the way for potential biomedical applications of this novel nanomaterial.

To explore the applicability of AANTs on drug delivery, two drug delivery systems were designed by using AANTs to deliver pro-apoptotic receptor agonists and cell signaling modulators for *in vitro* cancer cell killing. In **chapter 5**, tumor necrosis factor-related apoptosis-inducing ligand (Apo2L/TRAIL) was selected to demonstrate the drug delivery concept for *in vitro* cancer killing. Inspired by the intrinsic toxicity paradigms of autophagy and endoplasmic reticulum (ER) stress as illustrated in **chapter 4**, in **chapter 6** a novel cell signaling targeting approach was proposed by delivering cell signaling modulators to simultaneously targeting autophagic and ER stress signaling networks. The understanding of autophagy and ER stress in the context of nanotoxicity and drug delivery opens new opportunities for the design of novel nanoparticle-based therapeutic concepts. More importantly, the therapeutic concepts developed in this thesis can be feasibly adapted to commercialized and clinical-approved nanomedicine platforms for realizing clinical transitions.

7.2 Recommendations for Future work

1. Structural engineering of AAO requires continuous translation of programmed electrochemical profile into nanopore structures in real time. The delay of this “translating process” can interfere the quality of structural engineering. However, since the barrier layer of AAO is composed of anodic alumina, which is a dielectric material, a delayed electric recovery is unavoidable during pulse anodization. The restricted electric recovery is unfavourable for producing AAO-based nanophotonics as well as AANTs as discussed in **chapter 3**. Further experimental optimizations are required to achieve better performance

of structurally engineering AAO for producing high-quality photonic nanostructures such as Thue−Morse and Fibonacci structures.[1-2]

2. Short AANTs are ideal for drug delivery applications, but precise length control of AANTs is still challenging based on current techniques. Although we attempt to reduce the length of AANTs by optimizing electrolyte compositions, further shortening AANTs would be possible by taking advantage of the current oscillation, acid etching and sonication process.[3-4] In addition, the productivity of AANTs is limited at lab-scale due to the requirement of applying high current intensity during fabrication. It would be preferred to explore conditions that utilize low current intensity to produce AANTs, possibly through the modification of electrolyte.

3. The toxicological studies and drug delivery experiments of AANTs are at the level of cell culture in this thesis. Future work of animal experiments (e.g. mice model) should be conducted to address the long-term toxicity issue of this new nanomaterial. The study of bio-distribution of AANTs with stealth surface functionalization (e.g. polyethylene glycol) is necessary to clarify the cancer targeting property *in vivo*.[5-6] In addition, more sophisticated surface chemistry should be conducted to control and optimize the drug loading / release both *in vitro* and *in vivo*.[7-8]

4. With the maturation of nanofabrication and drug delivery techniques, personalized nanomaterial-based cancer therapy may become possible in the long-term to meet the requirements of individual cancer patients. To address the visionary concept of personalized therapy, it becomes increasingly important for chemical engineers and material scientists to understand the cancer biology and cancer genome in order to design suitable nanomedicine-based therapeutics for targeted therapy. New opportunities are

emerging by establishing high-throughput nanomedicine fabrication platforms to enable rapid nanomedicine formulation in respond to personalized cancer targets.[9-10]

References

1. Agarwal, V.; Soto-Urueta, J. A.; Becerra, D.; Mora-Ramos, M. E., Light propagation in polytype Thue–Morse structures made of porous silicon. *Photonics and Nanostructures - Fundamentals and Applications* **2005,** *3* (2–3), 155-161.

2. Moretti, L.; Rea, I.; Rotiroti, L.; Rendina, I.; Abbate, G.; Marino, A.; De Stefano, L., Photonic band gaps analysis of Thue-Morse multilayers made of porous silicon. *Opt. Express* **2006,** *14* (13), 6264-6272.

3. Lee, W.; Kim, J.-C.; Gösele, U., Spontaneous Current Oscillations during Hard Anodization of Aluminum under Potentiostatic Conditions. *Advanced Functional Materials* **2010,** *20* (1), 21-27.

4. Losic, D.; Lillo, M.; Losic, D., Jr., Porous Alumina with Shaped Pore Geometries and Complex Pore Architectures Fabricated by Cyclic Anodization. *Small* **2009,** *5* (12), 1392-1397.

5. Krug, H. F.; Wick, P., Nanotoxicology: An Interdisciplinary Challenge. *Angewandte Chemie International Edition* **2011,** *50* (6), 1260-1278.

6. Knop, K.; Hoogenboom, R.; Fischer, D.; Schubert, U. S., Poly(ethylene glycol) in Drug Delivery: Pros and Cons as Well as Potential Alternatives. *Angewandte Chemie International Edition* **2010,** *49* (36), 6288-6308.

7. Mura, S.; Nicolas, J.; Couvreur, P., Stimuli-responsive nanocarriers for drug delivery. *Nat Mater* **2013,** *12* (11), 991-1003.

8. Srinivasarao, M.; Galliford, C. V.; Low, P. S., Principles in the design of ligand-targeted cancer therapeutics and imaging agents. *Nat Rev Drug Discov* **2015,** *14* (3), 203-219.

9. Oliva, N.; Unterman, S.; Zhang, Y.; Conde, J.; Song, H. S.; Artzi, N., Personalizing Biomaterials for Precision Nanomedicine Considering the Local Tissue Microenvironment. *Advanced Healthcare Materials* **2015,** *4* (11), 1584-1599.

10. Davies, M. C.; Alexander, M. R.; Hook, A. L.; Yang, J.; Mei, Y.; Taylor, M.; Urquhart, A. J.; Langer, R.; Anderson, D. G., High throughput surface characterization: A review of a new tool for screening prospective biomedical material arrays. *Journal of Drug Targeting* **2010,** *18* (10), 741-751.